POLYTECHNIQUE MONTRÉAL
affiliée à l'Université de Montréal

On-chip Fabry-Pérot microcavity for refractive index cytometry and deformability characterization of single cells

ANTOINE LEBLANC-HOTTE
Département de génie physique

Thèse présentée en vue de l'obtention du diplôme de *Philosophiæ Doctor*
Génie physique
Avril 2019

POLYTECHNIQUE MONTRÉAL
affiliée à l'Université de Montréal

Cette thèse intitulée :

On-chip Fabry-Pérot microcavity for refractive index cytometry and deformability characterization of single cells

présentée par **Antoine LEBLANC-HOTTE**
en vue de l'obtention du diplôme de *Philosophiæ Doctor*
a été dûment acceptée par le jury d'examen constitué de :

Thomas GERVAIS, président
Yves-Alain PETER, membre et directeur de recherche
Jean-Sébastien DELISLE, membre et codirecteur de recherche
Frédéric LEBLOND, membre
Frédéric ZAMKOTSIAN, membre externe

DEDICATION

To Jessica and my daughter, Stella,
To my mother,
And to my father who would have been proud to see me complete this PhD

À Jessica et ma fille, Stella,
À ma mère
Et à mon père qui aurait été fier de me voir terminer ce doctorat

ACKNOWLEDGEMENTS

My foremost acknowledgment is directed towards my supervisor, Professor Yves-Alain Peter. Exactly ten years ago you welcomed me, a young and naive bachelor student, into your group. You granted me such creative liberty, cleverly guided my actions, provided countless opportunities to promote my work and was always present at my side along this winding path. Undoubtedly, over a decade, personal challenges are bound to surface. In these times, your empathy extended beyond the boundaries of our professional relationship. I cannot thank you enough for your consistent support.

I would also like to express my absolute gratitude to my co-supervisor Dr. Jean-Sébastien Delisle and to our precious collaborator Professor Sylvie Lesage. Your implication and support over the last six years has been more than helpful, it was essential to the success of this project. I am truly grateful for your engagement throughout this work and I salute your audacity to reach beyond your medical expertise and into the field of engineering physics.

I also want to thank the Microfabrication Laboratory staff, especially Christophe Clément and Yves Drolet. Your valuable input and hard work is the foundation for the achievement of not just my research but many others. I hope you realize the extent of your impact on students' researches. Thereby, I thank my colleagues, from the past and the present, whom all have a part into this accomplishment. I bethink of past group members such as Alexandre Poulin, Alireza Hajhosseini Mesgar, Annabelle Gascon, Cecilia La Mela, Ahmad Hayat, Pablo Bianucci, Léandro Acquaroli, Thomas Lazzara, Antoine Ramier, Philippe Jubinville, Joseph André Bélanger, Hubert Camirand, Émile Beaulieu, Julianne Desforges and Guillaume Emond. I would like to specifically thank Raphaël St-Gelais for his headmost guidance which allowed me to carry on his work. I also hold a special thank to Francis Vanier, Hala Ghali, Kazem Zandi and Samir Saïdi with whom I felt like I could discuss anything. Your befriending allowed me to find my place. I also thank the newest members of our research group, Régis Guertin, Marc-Antoine Bianki and Cédric Lemieux-Leduc. Your arrival has brought a fresh and dynamic perspective and I have no doubt you will brilliantly carry out your respective PhD. I thank our collaborators from Polytechnique Montreal Chi-Yuan Chang and Mohamad-Gabriel Alameh as well as from Maisonneuve-Rosemont Hospital Professor El Bachir Affar, Manon Richaud, Nadine Sen Nkwe, Mikhail Sergeev and Livia Odagiu. I would like to specifically thank Geneviève Chabot-Roy for her hard work and immediate motivation into this project, it is very appreciated.

I also thank the Department of Engineering Physics which provided the ideal environment for me to become a mature and rigorous engineer. The academic training provided by the faculty and its professors is unique and has allowed me to engage into international scientific communities. I thank the funding agencies, in particular the Fonds de recherche du Québec – Nature et technologies (FRQNT) and the Natural Sciences and Engineering Research Council of Canada (NSERC) which provided most of the funding for this research as well as a generous doctoral scholarship.

I also want to thank the members of the jury whom graciously agreed to examine this thesis. This work gains from your valuable scientific expertise and I am grateful for your contribution.

I thank my family who has always been supporting and encouraging even if sometimes they did not fully understand the technicalities of my research subject.

Last but not least, I wish to thank my spouse Jessica. You have made a great deal of sacrifices and compromises in the pursuit of my dream. You have supported me through the rough times and shared my burden. Thank you from the bottom of my heart.

RÉSUMÉ

Une identification correcte et précise du phénotype et des fonctions cellulaires est fondamentale pour le diagnostic de plusieurs pathologies ainsi qu'à la compréhension de phénomènes biologiques tels que la croissance, les réponses immunitaires et l'évolution de maladies. Conséquemment, le développement de technologies de pointe offrant une mesure multiparamétrique à haut débit est capital. À cet égard, la cytométrie en flux est l'étalon de référence due à sa grande spécificité, sa grande sensibilité et ses débits élevés. Ces performances sont atteintes grâce à l'évaluation précise du taux d'émission de fluorophores, conjugués à des anticorps, ciblant certains traits cellulaires spécifiques. Néanmoins, sans ce précieux étiquetage, les propriétés physiques caractérisées par la cytométrie sont limitées à la taille et la granularité des cellules. Bien que la cytométrie en flux soit fondamentalement un détecteur optique, elle ne tire pas avantage de l'indice de réfraction, un paramètre reflétant la composition interne de la cellule. Dans la littérature, l'indice de réfraction cellulaire a été utilisé comme paramètre phénotypique discriminant pour la détection de nombreux cancers, d'infections, de la malaria ou encore de l'anémie. Également, les structures fluidiques de la cytométrie sont conçues afin d'empêcher une déformation cellulaire de se produire. Cependant, les preuves que la déformabilité est un indicateur de plusieurs pathologies et d'état de santé cellulaire sont manifestes. Pour ces raisons, l'étude de l'indice de réfraction et de la déformabilité cellulaire en tant que paramètres discriminants est une avenue prometteuse pour l'identification de phénotypes cellulaires.

En conséquence, de nombreux biodétecteurs qui exploitent l'une ou l'autre de ces propriétés cellulaires ont émergé au cours des dernières années. D'une part, les dispositifs microfluidiques sont des candidats idéaux pour la caractérisation mécanique de cellules individuelles. En effet, la taille des structures microfluidiques permet un contrôle rigoureux de l'écoulement ainsi que de ses attributs. D'autre part, les dispositifs microphotoniques excellent dans la détection de faibles variations d'indice de réfraction, ce qui est critique pour un phénotypage cellulaire correcte. Par conséquent, l'intégration de composants microfluidiques et microphotoniques à l'intérieur d'un dispositif unique permet d'exploiter ces propriétés cellulaires d'intérêt. Néanmoins, les dispositifs capables d'atteindre une faible limite de détection de l'indice de réfraction tels que les détecteurs à champ évanescent souffrent de faibles profondeurs de pénétration. Ces dispositifs sont donc plus adéquats pour la détection de fluides ou de molécules. De manière opposée, les détecteurs interférométriques tels que les Fabry-Pérots sont sensibles aux éléments présents à l'intérieur de leurs cavités, lesquelles peuvent mesurer jusqu'à plusieurs dizaines de micromètres. Les cavités Fabry-Pérot sont donc par-

faitement appropriées pour la mesure de cellules entières. Cependant, la plupart de ces détecteurs volumiques présentent une limite de détection trop grande ou encore requièrent un montage hors plan incompatible avec une solution entièrement intégrée. Bref, l'amalgame d'une grande sensibilité et d'une profondeur d'interaction adéquate en plus d'assurer un débit élevé, le tout sur un seul dispositif, est un défi contemporain. En outre, la littérature ne rapporte aucune caractérisation simultanée de l'indice de réfraction et de la déformabilité réalisée sur des cellules entières.

Incidemment, la première contribution de cette thèse traite de la conception et de la fabrication d'un biodétecteur intégré capable de détecter de faibles variations d'indices de réfraction tout en atteignant un haut débit de mesure. Ces objectifs sont atteints grâce à une cavité Fabry-Pérot intégrée, composée de réflecteurs de Bragg à alternance de couches de silicium et d'air, qui engendre une limite de détection de 1.2×10^{-5} unité d'indice de réfraction. Une condition essentielle au fonctionnement d'un tel résonateur intégré réside dans le comportement monomode des guides d'onde en silicium à l'entrée et à la sortie. L'importante différence d'indice de réfraction entre le cœur et la gaine d'air combinée aux larges dimensions requises pour l'analyse de cellules entières entraîne un comportement multimode. La propagation concurrente de plusieurs modes optiques génère ainsi une distribution spectrale non uniforme de la puissance, laquelle masque les résonances de la cavité Fabry-Pérot. À cet effet, l'ingénierie de guides d'onde en côte surdimensionnés exhibant un comportement quasi monomode est critique. Toutefois, pour de telles dimensions, le respect des critères de conception préalablement établis dans la littérature ne suffit pas pour assurer un comportement monomode. À ce titre, une portion substantielle de cette première contribution scientifique consiste à l'amendement de ces critères. Enfin, l'approche de focalisation inertielle adoptée produit un débit de mesure de 5000 cellules par seconde. Cette méthode ne nécessite qu'un seul canal microfluidique et de surcroît permet d'homogénéiser l'espace longitudinal entre les cellules.

La seconde contribution de cette thèse aborde la caractérisation de cellules individuelles basée sur l'indice de réfraction et la déformabilité. Lorsque l'écoulement est faible, les modestes forces de cisaillement appliquées sur les cellules ne provoquent pas de déformation considérable. Ainsi, la caractérisation est basée uniquement sur l'indice de réfraction. À l'opposé, lorsque l'écoulement est fort, les cellules se déforment sous l'effet des forces fluidiques et sont par conséquent simultanément caractérisées selon leur indice de réfraction et leur déformabilité. Une telle opérabilité implique que la déformation cellulaire peut être réduite ou accentuée en variant le débit du fluide. Par ailleurs, l'asymétrie des courbes produites par le passage de cellules déformées à l'intérieur de la cavité s'avère indiquer la position relative du noyau au sein de la cellule. Cette particularité biomécanique en lien direct avec la déformabilité

cellulaire n'est pas évoquée dans la littérature.

La dernière contribution majeure porte sur la discrimination accrue d'un type de globules blancs particuliers, les cellules myéloïdes. En effet, les neutrophiles, les basophiles et les promyélocytes ne sont pas discriminables en cytométrie sans l'utilisation d'un étiquetage fluorescent. Cette thèse démontre sans ambiguïté que ces cellules sont explicitement distinguées par notre biodétecteur. Une telle contribution scientifique a des répercussions au sein de plusieurs autres applications biologiques telles que le diagnostic du cancer, la détection de cellules précancéreuses, la thérapie par lymphocytes T, l'identification de pathologies des globules blancs et beaucoup d'autres.

ABSTRACT

Accurate identification of cellular phenotype and function is fundamental to the diagnostic of many pathologies as well as to the comprehension of biological phenomena such as growth, immune responses and diseases development. Consequently, development of state-of-the-art technologies offering high-throughput and multiparametric single cell measurement is crucial. Therein, flow cytometry has become the gold standard due to its high specificity and sensitivity while reaching a high-throughput. Its marked performance is a result of its ability to precisely evaluate expression levels of antibody-fluorophore complexes targeting specific cellular features. However, without this precious fluorescence labelling, characterized physical properties are limited to the size and granularity. Despite flow cytometry fundamentally being an optical sensor, it does not take full advantage of the refractive index (RI), a valuable label-free measurand which reflects the internal composition of a cell. Notably, the cellular RI has proven to be a discriminant phenotypic parameter for various cancer, infections, malaria and anemia. Moreover, flow cytometry is designed to prevent cellular deformation but there is growing evidence that deformability is an indicator of many pathologies, cell health and state. Therefore, cellular RI and deformability are promising avenues to discriminate and identify cellular phenotypes.

Novel biosensors exploiting these cellular properties have emerged in the last few years. On one hand, microfluidic devices are ideal candidates to characterize single cells mechanical properties at large rates due to their small structures and controllable flow characteristics. On the other hand, microphotonic devices can detect very small RI variations, critical for an accurate cellular phenotyping. Hence, the integration of microfluidic and microphotonic components on a single device can harness these promising cellular physical properties. However, devices achieving very small RI limit of detection (LOD) such as evanescent field sensors suffer from very short penetration depths and thus are better suited for fluid or single molecule detection. In opposition, interference sensors such as Fabry-Pérots are sensitive to the medium inside their cavity, which can be several tens of micrometers in length, and thus are ideally suited for whole-cell measurement. Still, most of these volume sensors suffer from large LOD or require out-of-plane setups not appropriate for an integrated solution. Such a complex integration of high-throughput, sensitivity and large penetration depth on-chip is an ongoing challenge. Besides, simultaneous characterization of whole-cell RI and deformability has never been reported in the literature.

Thereupon, the first contribution of this thesis is the design and fabrication of an integrated

biosensor able to detect small RI variations while achieving a large cellular measurement rate. This task is accomplished by an integrated Fabry-Pérot cavity, constructed of air-silicon distributed Bragg reflectors (DBRs), which reports a LOD of 1.2×10^{-5} refractive index unit (RIU). An essential operating condition of such an integrated resonating sensor is the single-mode behavior of its input and output silicon rib waveguides. However, the combination of high core-cladding RI difference and large dimensions required for whole-cell analysis allow multiple optical modes to propagate. This concurrent propagation generates a non-uniform spectral power distribution which masks the resonances. Therefore, the engineering of large cross-section rib waveguides exhibiting single-mode like behavior is of utmost importance. At these dimensions, the previously established single-mode design rules do not apply anymore. As such, a substantial part of this first scientific contribution is the formulation of modernized design guidelines. Lastly, with respect to throughput, the adopted inertial focusing scheme allows for a measurement rate of 5000 cells per second. Furthermore, inertial focusing requires a single straight microchannel and organize cells longitudinally with regular spacing.

The second contribution of this thesis is the characterization of single cells based on their RI and deformability. At small flow rates, fluidic shear forces are not large enough to deform significantly the cells. Thus, cells are characterized based on their RI alone. Oppositely, at large flow rates, cells experience deformations allowing simultaneous RI and deformability characterization. Such microfluidic operationality implies that cellular deformation can be minimized or stimulated by varying the applied flow rate. Moreover, an in depth analysis of the cells curve reveals that the asymmetry is an indicator of the relative nucleus position, an unconsidered parameter until now in other studies.

The last and most influential contribution is the realization of enhanced discrimination of specific types of white blood cells, namely myeloids. Neutrophils, basophils and promyelocytes are indiscriminated by flow cytometry without fluorescent labelling. This thesis demonstrates a clear discrimination of these cells by the proposed biosensor. Such a scientific contribution has extensive potential applications in many other cellular research fields such as cancer diagnostic, precancerous cell detection, T lymphocytes therapy, white blood cells pathology and more.

TABLE OF CONTENTS

DEDICATION iii

ACKNOWLEDGEMENTS iv

RÉSUMÉ vi

ABSTRACT ix

TABLE OF CONTENTS xi

LIST OF TABLES xv

LIST OF FIGURES xvii

LIST OF ACRONYMS xxiv

LIST OF SYMBOLS xxvi

LIST OF APPENDICES xxix

CHAPTER 1 INTRODUCTION 1
- 1.1 Biological context 1
- 1.2 Principles of flow cytometry 4
- 1.3 Refractive index and deformability as phenotypic biomarkers 7
- 1.4 Problem statement & motivation 9
- 1.5 Achieved objectives & original contributions 11
- 1.6 Thesis structure 12

CHAPTER 2 LITERATURE REVIEW 13
- 2.1 Cell focusing in microchannels 13
  - 2.1.1 Sheathed hydrodynamic focusing 13
  - 2.1.2 Microvortices 15
  - 2.1.3 Inertial focusing 17
- 2.2 Miniaturized flow cytometry 21
- 2.3 Refractive index sensing 23
  - 2.3.1 Evanescent field 25

2.3.2 Interference . . . 26
2.3.3 Phase microscopy . . . 28

CHAPTER 3 OPTICAL PROPERTIES OF IN-PLANE SILICON FABRY-PÉROT CAVITIES . . . 29
3.1 Distributed Bragg reflectors . . . 29
3.2 Fabry-Pérot cavity . . . 31
3.3 Fabry-Pérot cavity for cell sensing . . . 36

CHAPTER 4 ARTICLE 1 - THE IMPORTANCE OF SINGLE-MODE BEHAVIOR IN SILICON-ON-INSULATOR RIB WAVEGUIDES WITH VERY LARGE CROSS SECTION FOR RESONANT SENSING APPLICATIONS . . . 40
4.1 Authors and affiliations . . . 40
4.2 Abstract . . . 41
4.3 Introduction . . . 41
4.4 Rib Waveguide Modal Analysis . . . 42
4.5 Microfabrication . . . 44
4.6 Experimental Setup . . . 46
4.7 Results and Discussion . . . 47
4.7.1 Stand-alone rib waveguide . . . 47
4.7.2 Rib Waveguide coupled to a Fabry-Perot cavity . . . 49
4.7.3 Fabry-Perot resonance properties . . . 51
4.8 Conclusion . . . 53
4.9 Supplementary information: Unpublished results and discussion on rib waveguide modal analysis and Fabry-Pérot properties . . . 54
4.9.1 Fundamental mode attenuation map . . . 54
4.9.2 Odd higher order modes attenuation maps . . . 54
4.9.3 Considerations on the Fabry-Pérot sensitivity . . . 57

CHAPTER 5 ARTICLE 2 - HIGH-THROUGHPUT REFRACTIVE INDEX-BASED MICROPHOTONIC SENSOR FOR ENHANCED CELLULAR DISCRIMINATION 59
5.1 Authors and affiliations . . . 59
5.2 Abstract . . . 60
5.3 Introduction . . . 60
5.4 Materials and methods . . . 62
5.4.1 Microfabrication . . . 62
5.4.2 Single-mode like Rib waveguide . . . 63

5.4.3 Microfluidic operation . . . 64
5.4.4 Cell culture . . . 65
5.4.5 Experimental setups . . . 66
5.4.6 Flow cytometry measurements . . . 67
5.4.7 Single cell analysis . . . 67
5.5 Results and discussion . . . 68
5.5.1 Single-mode like Rib Waveguides . . . 68
5.5.2 Resonant cavity sensing . . . 68
5.5.3 Promyelocytic leukemia biological model . . . 71
5.6 Conclusion . . . 75

CHAPTER 6 ARTICLE 3 - ON-CHIP REFRACTIVE INDEX CYTOMETRY FOR WHOLE-CELL DEFORMABILITY DISCRIMINATION . . . 76
6.1 Authors and affiliations . . . 76
6.2 Abstract . . . 77
6.3 Introduction . . . 77
6.4 Materials and methods . . . 80
6.4.1 RIC devices . . . 80
6.4.2 Cell culture . . . 81
6.4.3 Single cell analysis . . . 82
6.4.4 Cellular population discrimination . . . 82
6.4.5 Numerical simulations . . . 83
6.5 Results and discussion . . . 84
6.5.1 Single cell analysis . . . 84
6.5.2 Cytochalasin B treated HL-60 cells model . . . 87
6.5.3 Parameters variations with flow . . . 91
6.5.4 Differentiated cells model . . . 92
6.6 Conclusion . . . 95
6.7 Published electronic supplementary information . . . 97
6.7.1 Examples of numerical simulation curve . . . 97
6.7.2 Inertial focusing length and cells spread . . . 97
6.7.3 Curve parameters dependencies to relative nucleus position . . . 99
6.7.4 Curve parameters dependencies to deformed cell length . . . 100
6.7.5 Confocal microscopy . . . 101
6.7.6 Flow cytometry measurement of control and cytochalasin B treated HL-60 cells . . . 102

6.7.7 Measured curve parameters dependencies to flow rate 102
6.7.8 Derivation of particle velocities 104
6.7.9 Coefficients of variation of flow cytometry and RIC measurements . . 106
6.7.10 OLR of myeloid cells populations 107

CHAPTER 7 GENERAL DISCUSSION – LIMITATIONS AND POSSIBILITIES OF ON-CHIP REFRACTIVE INDEX CYTOMETRY 108
7.1 Device performance 108
7.1.1 *TE* and *TM* propagating modes 108
7.1.2 Cellular deformation profile 109
7.1.3 Small particle detection 110
7.2 Towards integration in flow cytometry 112
7.3 Biological applications 114

CHAPTER 8 CONCLUSIONS AND RECOMMENDATIONS 117

REFERENCES 120

APPENDICES 141

LIST OF TABLES

Table 2.1 Comparison of particle focusing techniques. 20
Table 2.2 Comparative of benchmark on-chip flow cytometry devices. 22
Table 2.3 RI sensors comparison based on LOD and magnitude of the penetration depth. 24
Table 3.1 Comparison of ideal and expected reflectivity and bandwidth of DBRs depending on the number of periods. 31
Table 3.2 Comparison of ideal (a) and expected (b) Fabry-Pérot cavities properties at λ_0 calculated from Fig. 3.4a and 3.4b. 34
Table 3.3 Experimental optical properties of a microfabricated Fabry-Perot cavity ($l_{air} = l_{Si} = 1.7\ \mu m$ and $l_{cav} = 40\ \mu m$) in oil ($n_{oil} = 1.412$) reproduced from Chapter 5. Theoretical and expected values are also reported for comparison. 35
Table 3.4 Range of values of the in-plane silicon Fabry-Pérot cavities properties. 38
Table 4.1 Fabry-Pérot resonance properties calculated from the experimental spectra for a rib waveguide width of 5 μm. 53
Table 4.2 Experimental Fabry-Pérot resonances properties for $n_{oil} = 1.412$. . . . 58
Table 5.1 Fabry-Pérot resonances properties calculated from experimental spectra for the *TE* and *TM cavities* 71
Table 5.2 OLR coefficients comparison between the flow cytometer and the microsystem for each experiment 74
Table 6.1 Calculated areas, heights, volumes and suspended sphere radii (mean $\pm$ standard deviation) of cytospun ($N = 5$) control and ($N = 5$) cytochalasin B treated HL-60 cells using confocal fluorescence microscopy images. Measured suspended cell radius of ($N = 336$) control and ($N = 379$) cytochalasin B treated HL-60 cells using bright field images. Coefficients of variation (CV) are reported for suspended cells radii. P-values are from t-test. 88
Table 6.2 Calculated lift coefficients, required focusing lengths and resulting spreads in width for a cavity placed 1.2 mm away from the beginning of the straight channel for cells of 12 μm in a $W = 40\ \mu m$ by $H = 15\ \mu m$ channel at different flow rates. 98

Table 6.3 Calculated lift coefficients, required focusing length and resulting spread in width for a cavity placed 1.2 mm away from the beginning of the straight channel for cells of 12 μm in a $W = 30\ \mu m$ by $H = 15\ \mu m$ channel at 15 μl/min. 98
Table 6.4 Total number of cells and subset at each flow rate for control and Cytochalasin B treated HL-60 cells. 104
Table 6.5 Calculated average fluid and particle velocities, Re and Re_p at the different imposed flow rates for $W = 40\ \mu m$, $H = 15\ \mu m$ and $D_{cell} = 12\ \mu m$ using $\gamma = 0.45$. 105
Table 6.6 Calculated average fluid and particle velocities, Re and Re_p at a flow rate of 15 μl/min for $W = 30\ \mu m$, $H = 15\ \mu m$ and $D_{cell} = 12\ \mu m$ using $\gamma = 0.40$. 106
Table 6.7 Calculated coefficients of variation of FSC-A and SSC-A measurements for control and Cytochalasin B treated HL-60 cells. 106
Table 6.8 Calculated coefficients of variation of Max, FW, Area, RT, FT and Ratio Time measurements for control and Cytochalasin B treated HL-60 cells at all flow rates. 106
Table 6.9 Calculated coefficients of variation of FSC-A and SSC-A measurements for neutrophils, basophils and baseline conditions. 107
Table 6.10 Calculated coefficients of variation of Max, FW, Area, RT, FT and Ratio Time measurements for neutrophils, basophils and baseline conditions at a flow rate of 15 μl/min. 107
Table 6.11 Calculated 1D OLR values of all combinations of myeloid cells for discrimination. 107

LIST OF FIGURES

Figure 1.1 Simplified hematopoiesis diagram in humans showing WBC classification by structure (granulocytes and agranulocytes) and lineage (myeloids and lymphoids). 2

Figure 1.2 Schematic of the working principles of optical flow cytometry. 5

Figure 2.1 Diagram of simple lateral sheathed hydrodynamic focusing. 14

Figure 2.2 Dean microvortices generated in a curved rectangular microchannel. . 16

Figure 2.3 Two-stage inertial focusing mechanism in a rectangular microchannel. 18

Figure 3.1 Scheme of a 1.5 period DBR on the top layer of an SOI. Light is input and output by rib waveguides. Structures are sliced at their center for better viewing. 30

Figure 3.2 Simulated DBRs reflection spectra when varying the number of periods for (a) the ideal case and (b) the expected case. 31

Figure 3.3 Scheme of a Fabry-Pérot consisting of 2 periods DBRS separated by a microfluidic channel on the top layer of an SOI. Light is input and output by rib waveguides. Structures are sliced at their center for better viewing. 32

Figure 3.4 Simulated Fabry-Pérot cavities transmission spectra when varying the number of periods for (a) the ideal case and (b) the expected case. . . 34

Figure 3.5 Simulated ideal and expected (a) normalized power variation, (b) sensitivity and (c) LOD of a 2 periods Fabry-Pérot cavity ($m_{air} = 5$, $m_{Si} = 17$ and $m_{cav} = 50$) in function of RI variation (Δn). 36

Figure 3.6 Computed (a) sensitivity and (b) LOD in function of the cavity length for a typical HL-60 cell. RI variations were computed using the simulation model presented in Chapter 6. 37

Figure 3.7 Stable (white areas) and unstable (gray areas) conditions in function of the cavity length to cell radius ratio (l_{cav}/R_{cell}) and the relative position of the cell along the cavity (0.5 is at the center of the cavity). 39

Figure 4.1 Rib waveguide on SOI cross-section dimensions and variables used for modal analysis. 43

Figure 4.2 Lowest attenuation coefficient recorded for (a) HE_{20} mode, (b) HE_{40} mode, and (c) combined HE_{20} and HE_{40} at all simulated operating wavelengths in function of ratios h/H and W/H. Plain line corresponds to Soref's single-mode boundary whereas the dashed line is associated to Pogossian's correction. 45
Figure 4.3 SEM images of a microfabricated device showing (a) rib waveguide facet geometry and (b) structure of a rib waveguide coupled to a Fabry-Perot cavity composed of two DBRs. 46
Figure 4.4 NIR images of the output mode for stand-alone optical rib waveguides showing presence of higher order mode profile for widths of (a) 20 μm, (b) 15 μm, (c) 7.5 μm, and (d) 5 μm respectively. 48
Figure 4.5 Output spectra for stand-alone optical rib waveguides showing intensity variation for widths of (a) 20 μm and (b) 15 μm whereas widths of (c) 7.5 μm and (d) 5 μm exhibits lower fluctuations. 49
Figure 4.6 NIR images of the output mode for cavity coupled rib waveguides showing higher mode profile for widths of (a) 20 μm, (b) 15 μm, and (c) 7.5 μm and single-mode profile for width of (d) 5 μm. 50
Figure 4.7 Output spectra for Fabry-Perot cavity coupled rib waveguides showing intensity profile for widths of (a) 20 μm, (b) 15 μm, and (c) 7.5 μm and exhibiting an isolated resonance peak for a width of (d) 5 μm. . . 51
Figure 4.8 Spectral comparison between simulated, dashed line, and experimental, plain line, single-mode Fabry-Perot cavity for a rib waveguide width of 5 μm. 52
Figure 4.9 Measurement points for single-mode cavity coupled rib waveguide resonance peak displacement with certified refractive index oils superposed with a linear fit. 52
Figure 4.10 Highest attenuation coefficient recorded for the HE_{00} mode at all simulated operating wavelengths in function of ratios h/H and W/H. The plain line corresponds to Soref's single-mode boundary whereas the dashed line corresponds to Pogossian's correction. Black and white dots represent the fabricated devices. 54

Figure 4.11 Lowest attenuation coefficient recorded for the (a) HE_{10} mode, (b) HE_{30} mode, and (c) combined HE_{10}, HE_{20}, HE_{30} and HE_{40} modes at all simulated operating wavelengths in function of ratios h/H and W/H. The plain line corresponds to Soref's single-mode boundary whereas the dashed line is corresponds to Pogossian's correction. Black and white dots represent the fabricated devices. The white "x" in (c) marks the region for the second generation of rib waveguides reported in Chapter 5 and 6. 56

Figure 4.12 (a) Measured Fabry-Pérot spectra in function of the oil refractive index. The $n = 1.412$ spectrum has been substituted by a second measurement. (b) Fitted linear sensitivities for each resonance. 57

Figure 5.1 Illustrations of the microphotonic cell sensor with (a) 3D rendering of the assembled device using Blender Software and (b) SEM image of the microfabricated rib waveguides, DBRs, Fabry-Pérot cavities and microfluidic channel. 63

Figure 5.2 Combined attenuation map for modes HE_{10}, HE_{20}, HE_{30} and HE_{40} at wavelengths of $\lambda = 1.50\ \mu m$, $1.575\ \mu m$ and $1.65\ \mu m$. Onsets showing a schematic of the rib waveguide cross-section with corresponding variables and the single-mode like NIR output mode profile of the fabricated $5.5\ \mu m$ rib waveguide. 64

Figure 5.3 (a) Experimental spectrum of the Fabry-Pérot cavity with DBRs widths of $2.0\ \mu m$, microchannel width of $35\ \mu m$ and rib waveguide width of $5.5\ \mu m$ (solid line) and simulated spectra for the *TE cavity* (dashed line), *TM cavity* (dotted line) and combined cavities (dashed-dotted line). (b) Superimposed spectra of the Fabry-Pérot resonance peaks shifts with corresponding refractive index value and (c) fitted linear regressions used to calculate the sensitivity of the *TE* and *TM cavities*. (d) Typical voltage variation in time curve for a single cell passage with corresponding extracted parameters. 70

Figure 5.3 HL-60 differentiated into basophils and neutrophils cannot be distinguished by typical FSC-SSC flow cytometry profiles. (a) Typical FSC-SSC profiles of HL-60 cells differentiated neutrophils (middle) or basophils (right). The baseline culture condition is also shown (left). The total number of measured cells and the percentage of gated cells is shown. (b) and (c) respectively depict overlays for baseline vs neutrophil-differentiating conditions and basophil- vs neutrophil-differentiating conditions; in dot plot (left), in FSC histogram (middle) and in SSC histogram (right) for baseline in green, neutrophils in blue and basophils in red. One representative of at least three experiments. (d) HL-60 cells were differentiated for 7 days into neutrophils (middle) or basophils (right). The baseline culture condition is also shown (left). Arrows on the right panel point to cells bearing vacuoles, typical of basophils, while arrows on the middle panel point to cells bearing a segmented nucleus characteristic of neutrophils. One representative of at least three experiments. (e) Color-coded density scatter plots in function of Maximum and FWTM for separately measured baseline culture conditions (left), HL-60 cells differentiated neutrophils (middle) and basophils (right) solutions and (f) combined cellular populations for baseline vs neutrophil-differentiating conditions (left), basophil- vs neutrophil-differentiating conditions (middle) and baseline vs basophil-differentiating conditions (right). The total number of measured cells and the percentage of gated cells is shown. One representative of at least two experiments. 73

Figure 6.1 3D rendering of the silicon-on-insulator (SOI) RIC device. 81

Figure 6.2 Numerical simulation scheme of the cell interaction with optical modes and the reference spherical cell. 84

Figure 6.3 Measurement of losses vs time showing (a) a typical single cell at higher velocity corresponding to a ratio time < 1 (15 μl/min in a 15 μm $\times$ 30 μm channel cross-section, average flow velocity 0.56 m/s, average cell velocity 0.22 m/s), (b) a single cell at midrange velocity corresponding to a ratio time $\sim$1 (10 μl/min in a 15 μm $\times$ 40 μm channel cross-section, average flow velocity 0.28 m/s, average cell velocity 0.13 m/s) and (c) the particular case of a single cell at lower velocity corresponding to a ratio time > 1 (5 μl/min in a 15 μm $\times$ 40 μm channel cross-section, average flow velocity 0.14 m/s, average cell velocity 0.06 m/s). Average cell velocities are approximated using a conversion factor from the average flow velocities $U_p = \gamma U_f$, where γ =0.45 for 12 μm cells in a 15 μm $\times$ 40 μm channel and γ =0.40 for a 15 μm $\times$ 30 μm channel. See ESI for derivation.† 85

Figure 6.4 Computed ratio time values from simulated curve when varying (a) the nucleus offset in the x-axis and (b) the nucleus deformation in the x-axis. Red dashed lines mark the centered nucleus position in (a) and the undeformed nucleus in (b). Full black line marks the equal 4% deformation of the nucleus and the cell in the x-axis. Each steps in (a) are 25% offset except for the two points closest to the centered position which are $\pm$10%. Each steps in (b) are 2.5% deformation. 86

Figure 6.5 (a) RIC Area and ratio time density-colored dot plot combination for control and Cytochalasin B treated HL-60 cells (2D OLR=0.3) at a flow rate of 15 μl/min. Cytochalasin B treated HL-60 cells have a smaller ratio time value than HL-60 control cells, in line with their higher degree of whole-cell deformability. Histograms of control and Cytochalasin B treated HL-60 cells for (b) Area (1D OLR=1), (c) ratio time (1D *overlaprate* (OLR)=0.4), (d) full width (FW) (1D OLR=1), (e) rising time (RT) (1D OLR=1), (f) falling time (FT) (1D OLR=1) and (g) Max (1D OLR=1). Subset is used for OLR calculations. One representative of at least four experiments. 90

Figure 6.6 (a) Flow cytometry FSC-A and SSC-A dot plot superimposition of HL-60 cells maintained in baseline conditions and differentiated into neutrophils and basophils. (b) FSC-A histograms and (c) SSC-A histograms of subsets. 2D OLR for any combination of two myeloid cell populations is 1. One representative of at least three experiments. . . 92

Figure 6.7 RIC ratio Max/FW and rising time density-colored dot plot at a flow rate of 15 μl/min for (a) HL-60 differentiated into neutrophils, (b) HL-60 differentiated into basophils, (c) HL-60 baseline conditions and (d) combination. One representative of at least three experiments. 93

Figure 6.8 Histograms of HL-60 cells maintained in baseline conditions (total cells: 48 154) and differentiated into neutrophils (total cells: 66 589) and basophils (total cells: 48 200) at a flow rate of 15 μl/min for (a) maximum, (b) full width, (c) Area, (d) ratio time, (e) rising time and (f) falling time. 94

Figure 6.9 Examples of numerically simulated RI variation curve for different relative positions of the nucleus. 97

Figure 6.10 Inertial equilibrium positions in a rectangular channel and focusing area due to the spread in width. 98

Figure 6.11 Computed parameter values from simulated curve when varying the relative nucleus position for (a) max, (b) full width (FW), (c) Area, (d) rising time (RT), (e) falling time (FT) and (f) ratio time. Red dashed lines indicates a centered nucleus position. Each steps are 25% offset except for the two points closest to the centered position which are $\pm$10%. 99

Figure 6.12 Computed parameter values from simulated curve when varying the deformed cell length in the x-axis for (a) max, (b) full width (FW), (c) Area, (d) rising time (RT), (e) falling time (FT) and (f) ratio time. Deformed cell length is $dx_{cell}/2R_{cell}$ where dx_{cell} is the diameter of the cell ellipsoid in the x-axis. A fixed 10% contraction deformation was imposed on the cell membrane ellipsoid in the y-axis. The nucleus radius was matched to the one of the cell in the y-axis by a 0.9% contraction deformation. For each step of 2.5% deformation, both the cell and the nucleus ellipsoids were deformed in the x-axis. The nucleus relative position was kept at $x_{off}/(dx_{cell} - dx_{nuc}) = -0.5$. Other nucleus relative position yielded similar results. 100

Figure 6.13 Confocal fluorescence microscopy images of cytospun immunostained control and cytochalasin B treated HL-60 cells. F-actin is stained with Alexa Fluor 488 phalloidin (green) and nuclei is stained with DAPI (blue). Top view of the fluorescence composite for (a) HL-60 cells control and (b) cytochalasin B treated HL-60 cells. Treated cells present clumps of phalloidine fluorescence associated to grouped broken-down actin filaments, responsible for the larger whole-cell deformability. Scale bars are 20 μm. 101

Figure 6.14 Flow cytometry measurements of control and cytochalasin B treated HL-60 cells. (a) Flow cytometry FSC-A and SSC-A dot plot superimposition (2D OLR=1). (b) FSC-A histogram (1D OLR=1) and (c) SSC-A histogram (1D OLR=1) of subsets. One representative of at least two experiments. 102

Figure 6.15 Measured curve parameters dependencies to flow rate for (a) max, (b) full width (FW) normalized by velocity, (c) Area normalized by velocity, (d) rising time (RT) normalized by velocity, (e) falling time (FT) normalized by velocity and (f) ratio time. Each error bar is ± one standard deviation derived from the normal distribution fitted over the corresponding parameter at a particular flow rate for a specific cell type. Parameters with time dependence, FW, Area, RT and FT were multiplied by the particle velocity to represent values in terms of length rather then time. The total mode field diameter (MFD) of the fiber, or a fraction for RT and FT, was subsequently subtracted. Total number of cells and subset at each flow rate for control and Cytochalasin B treated HL-60 cells are reported in Tab. 6.4. 103

Figure 7.1 Spectral and power measurements comparison in function of the cavity length l_{cav} based on (a) the LOD and (b) the smallest detectable particle diameter having an RI of $n_{cyt} = 1.447$. 111

LIST OF ACRONYMS

AFM	atomic force microscopy
Area HM	area under the curve at half maximum
Area TM	area under the curve at one third of the maximum
BAS	basophils
BOX	buried oxide
CBC	complete blood count
CD	cluster of differentiation
CW	continuous wave
DBR	distributed Bragg reflector
DC	deformability cytometry
DHM	digital holographic microscopy
DPSS	diode-pumped solid-state
DRIE	deep reactive ion etching
EOS	eosinophils
FBG	fiber Bragg grating
FBS	fetal bovine serum
FCS	fetal calf serum
FD	finite difference
FMO	fluorescence-minus-one
FSC	forward scattered light
FSR	free spectral range
FT	falling time
FW	full width
FWHM	full width at half maximum
FWTM	full width at one third of the maximum
HGB	hemoglobin
HIV/AIDS	human immunodeficiency virus and acquired immune deficiency syndrome
HTC	hematocrit
LOD	limit of detection
LP	lowpass
LPFG	long-period fiber grating
LYM	lymphocytes

MCH	mean corpuscular hemoglobin
MCHC	mean corpuscular hemoglobin concentration
MCV	mean corpuscular volume
MON	monocytes
MPV	mean platelet volume
NEU	neutrophils
NIR	near infrared
OCM	optical coherence microscopy
ODT	optical diffraction tomography
OLR	*overlaprate*
PBS	phosphate buffered saline
PDF	probability density function
PDMS	polydimethylsiloxane
PLT	platelet
PML	perfectly matched layer
PMT	photomultiplier tube
PSI	phase-shifting interferometry
QPM	quantitative phase microscopy
RBC	red blood cells
RDW	red cell distribution width
RI	refractive index
RIC	refractive index cytometry
RIU	refractive index unit
RT	rising time
RT-DC	real-time deformability cytometry
SEM	scanning electron microscopy
SNR	signal-to-noise ratio
SOI	silicon on insulator
SPR	surface plasmon resonance
SSC	side scattered light
TE	transverse electric
TM	transverse magnetic
TPM	tomographic phase microscopy
WBC	white blood cells
WGM	whispering gallery mode

LIST OF SYMBOLS

a	cell diameter [μm]
C_L^-	negative inertial lift coefficient
C_L^+	positive inertial lift coefficient
dx_{cell}	diameter of the cell in the flowing direction [μm]
dx_{nuc}	diameter of the nucleus in the flowing direction [μm]
D_{cell}	cell diameter [μm]
D_h	hydraulic diameter [μm]
De	Dean number
EH	vertically polarized (TM) mode
$\overline{FW}$	average measured FW [s]
$\mathcal{F}$	Finesse
G_i	Gaussian probability density function of population i
h	rib waveguide slab height [μm]
H	microchannel height AND rib waveguide total height [μm]
H_f	focused fluid height [μm]
H_o	output channel height [μm]
HE	horizontally polarized (TE) mode
I	identity matrix
l_{air}	DBR air layer thickness [μm]
l_{cav}	Fabry-Pérot cavity length [μm]
l_{Si}	DBR silicon layer thickness [μm]
L	characteristic length OR focusing length [μm]
m_{air}	DBR air odd integer
m_{cav}	cavity integer
m_{Si}	DBR silicon odd integer
M_i	row vector of means of population i
M_i'	row vector means of population i after 1 transformation
M_i''	row vector means of population i after 2 transformations
n_{air}	refractive index of air
n_{cav}	refractive index in the Fabry-Pérot cavity
n_{cell}	average refractive index of the whole cell
n_{cyt}	refractive index of the cytoplasm
n_{H_2O}	refractive index of water

n_i	number of observation of population i
n_{nuc}	refractive index of the nucleus
n_{PBS}	refractive index of PBS
n_{Si}	refractive index of silicon
n_{SiO_2}	refractive index of silicon dioxide
N_{RT}	number of round trips
Q	quality factor OR flow rate $[\mu l/min]$
Q_i	inlet flow rate $[m^3/s]$
Q_{i*}	lateral inlet flow rate $[m^3/s]$
Q_{ls}	lateral sheaths flow rate $[m^3/s]$
Q_o	output flow rate $[m^3/s]$
Q_s	sheaths flow rate $[m^3/s]$
Q_{vs}	vertical sheaths flow rate $[m^3/s]$
R	reflectivity
R_{cell}	cell radius $[\mu m]$
R_{curv}	microchannel radius of curvature $[\mu m]$
R_h	hydrodynamic resistance $[Pa/m^3/s]$
R_{nuc}	nucleus radius $[\mu m]$
Re	Reynolds number
Re_p	particle Reynolds number
S_{exp}	expected sensitivity $[nm/RIU]$
S_{theo}	theoretical sensitivity $[nm/RIU]$
T	throughput $[cells/s]$
U_f	average flow velocity $[m/s]$
U_{foc}	average focused flow velocity $[m/s]$
U_p	average particle velocity $[m/s]$
W	microchannel width (rib waveguide width in Chap. 4) $[\mu m]$
W_f	focused fluid width $[\mu m]$
W_o	output channel width $[\mu m]$
W_{spread}	cell spread in width $[\mu m]$
x_d	symbolic variable
x_d^i	columns vector of observations of variable d and population i
x_{off}	absolute offset of the nucleus from cell center $[\mu m]$
X_i	matrix of observations for all variables of population i
X_i'	matrix of observations for all variables of population i after 1 transformation

X_i''	matrix of observations for all variables of population i after 2 transformations
X_{tot}	matrix of observations for all variables of combined populations
$\mathcal{X}$	row vector of symbolic variables
α	hydrodynamic focusing velocity ratio
α_l	lateral hydrodynamic focusing velocity ratio
α_v	vertical hydrodynamic focusing velocity ratio
γ	ratio of particle velocity on average fluid velocity
Δn	refractive index variation
Δx_{cell}	separation between adjacent cells $[\mu m]$
ΔP	applied pressure drop $[Pa]$
$\Delta\lambda$	resonance shift $[nm]$
ε	microchannel geometrical factor
ζ	eigenvectors of $\left(\Sigma_{tot}^{-1}\Sigma_1'\right)$
λ_0	wavelength in vacuum $[nm]$
μ	fluid viscosity $[Pa \cdot s]$
μ_d^i	distribution mean of variable d and population i
ρ	fluid density $[kg/m^3]$
σ_d^i	distribution standard deviation of variable d and population i
σ_i	row vector of standard deviations of population i
σ_{res}	standard deviation of the measured resonance position $[nm]$
Σ_i	covariance matrix of population i
Σ_i'	correlated covariance matrix of population i
Σ_i''	covariance matrix of population i after 2 transformations
Σ_{tot}	covariance matrix of combined populations
$CORR[\Sigma_i]$	correlation matrix of Σ_i

LIST OF APPENDICES

Appendix A LIST OF SCIENTIFIC CONTRIBUTIONS 141

Appendix B CELLULAR THROUGHPUT OF SHEATHED HYDRODYNAMIC AND INERTIAL FOCUSING 143

Appendix C *OVERLAPRATE* (OLR) COEFFICIENT 146

CHAPTER 1 INTRODUCTION

Undoubtedly, expanding our knowledge on cells phenotype and function deepens our understanding of the human body and its complex biological interactions. Accurate identification of a cell composition, shape, size, granularity or stiffness leads to a larger comprehension of biological phenomenon such as growth, immune responses, diseases and pathologies development. Phenotypically classified and sorted cell populations allows researchers to individually study their biochemical function and thus evaluate their biological impact. In routine health status assessment, analysis of circulating blood cells subpopulations is the initial source of information. This method offers a minimally invasive collection method, needle sampling, while providing abundant health markers. Medical research and clinical laboratories have access to high-end apparatus, namely hematology analyzers, to precisely count and classify these circulating cells. Its main technology, flow cytometry, although being a well implanted and powerful tool, is limited in terms of physical properties measurement. Despite being an optical measurement system, it does not take full advantage of other valuable biomarkers such as refractive index (RI) and deformability. In counterpart, the evolution of integrated miniaturized optical and fluidic structures has fueled the emergence of novel biosensors for single cell manipulation and characterization which can exploit these untapped cellular properties. This thesis details the engineering of an on-chip Fabry-Pérot microcavity for refractive index cytometry (RIC) and deformability characterization of large cell populations and reveals its resulting application on human myeloid cells. In this chapter, the background biological context is first described, then principles of flow cytometry and its underlying technologies are revealed and RI and deformability are introduced as novel biomarkers. Lastly, the motivation and problem statement supporting this research are defined, the objectives are specified and the thesis structure is outlined.

1.1 Biological context

It is well known that the main function of white blood cells (WBC) is to protect our body against infectious diseases or foreign invaders. These protection phenomena, generally encompassed under the term immune response, involve five types of WBC: neutrophils, lymphocytes, monocytes, eosinophils and basophils. Perhaps the most well-known and most present in an adult body, around 60% of WBC, are the neutrophils. These cells, exhibiting a distinctive lobed nucleus, represent the first line of defense against microbial infection. In second place are lymphocytes, around 30% of WBC including B, T and Natural Killer cells.

Lymphocytes are responsible for the adaptive immunity of our body, for example learning to recognize viruses. Next are monocytes, around 5%, cleaning the system by phagocytosis and often becoming macrophages, then eosinophils, around 2%, fighting parasitic infections and finally basophils, around 0.5%, responsible for histamine release in allergic reactions. Despite their very different immune functions, all WBC can be traced back to a single common parent: the hematopoietic stem cell. This stem cell produces two main hematopoietic lineages in which it can further differentiate: lymphoids and myeloids. These lineages constitute the first general classification method for WBC. The second classification is based upon cellular structure and separates between granulocytes, distinguished by their multi-lobed nucleus and presence of granules in the cytoplasm, and agranulocytes, distinguished by their one-lobed nucleus and absence of granules. Thus, using these classification methods, neutrophils, eosinophils and basophils are granular myeloid cells, monocytes are agranular myeloid cells and T and B lymphocytes are agranular lymphoid cells. Figure 1.1 shows a simplified hematopoiesis diagram in humans and the WBC classification methods.

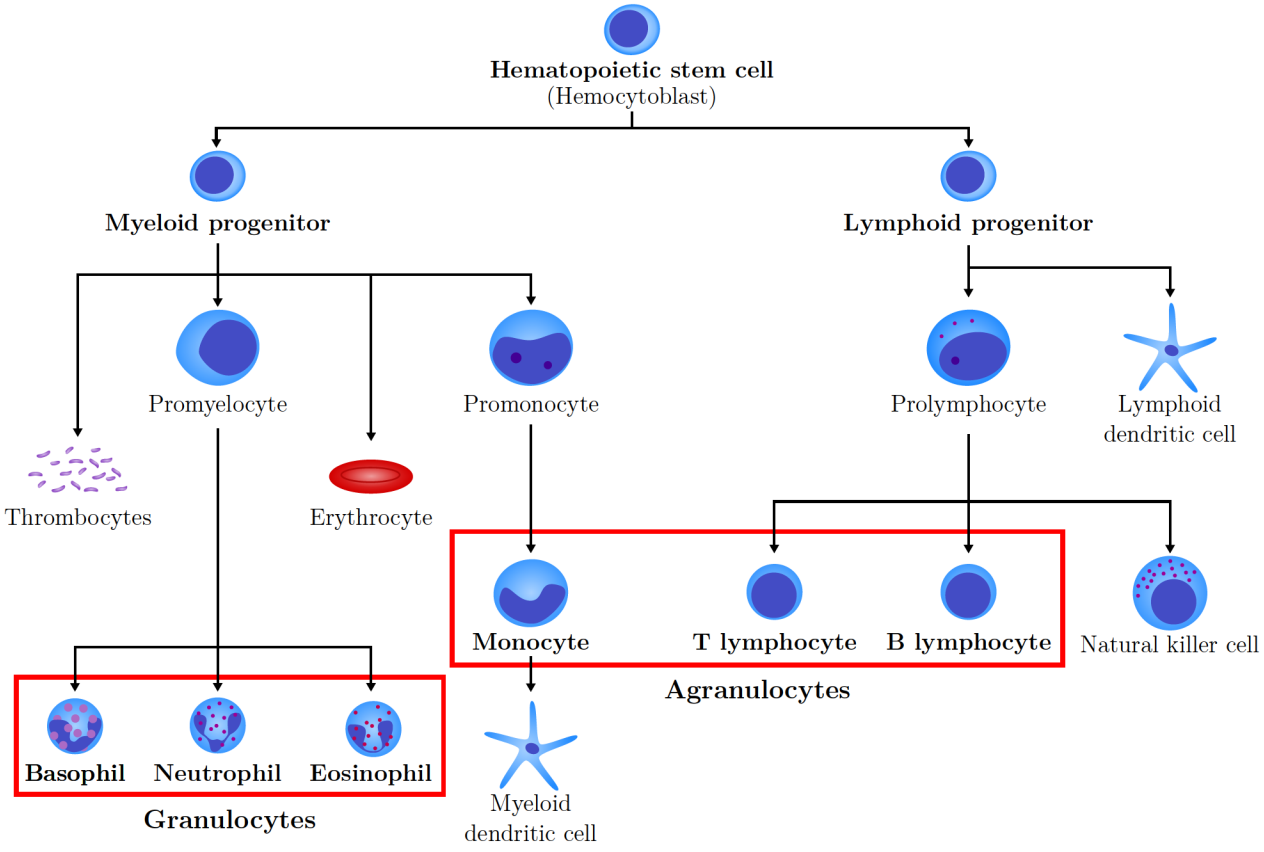

Figure 1.1 Simplified hematopoiesis diagram in humans showing WBC classification by structure (granulocytes and agranulocytes) and lineage (myeloids and lymphoids).

To assess a patient general health, a complete blood count (CBC) is commonly required. A low count of one type of WBC may indicate a depressed immune system whereas a high count may represent symptoms of a disease. Accurate discrimination of WBC types is critical to correctly diagnose a patient's condition or pathology. Therefore, high-performance hematology analyzers are routinely used to count and characterize blood cells, as well as some specific proteins, for patients health monitoring. The CBC analysis reports an impressive list of parameters and indicators relevant to identify the potential source of a health disease. Most recent hematology analyzers can report up to 50 parameters,[1] from which the most common ones are:

- the total WBC, which includes the number of neutrophils (NEU), lymphocytes (LYM), monocytes (MON), eosinophils (EOS) and basophils (BAS)
- the total red blood cells (RBC)
- the hemoglobin (HGB) amount
- the fraction of RBC in the whole blood, known as the hematocrit (HTC)
- the average volume of RBC, known as the mean corpuscular volume (MCV)
- the average amount and concentration of HGB per RBC, known as mean corpuscular hemoglobin (MCH) and mean corpuscular hemoglobin concentration (MCHC) respectively
- the spread of RBC size, known as the red cell distribution width (RDW)
- the number and average size of platelets, known as platelet (PLT) and mean platelet volume (MPV) respectively

In the next section, technologies employed in hematology analyzers to measure and identify common circulating blood cells are detailed. The principal and most powerful constituent of hematology analyzers is flow cytometry. Consequently, flow cytometers are often used and sold alone since they are mostly utilized for cellular research purposes and not CBC. Indeed, they can identify and isolate precise and rare cellular subpopulations, allowing to better understand their function and behavior.

[1] HORIBA, Pentra DX Nexus SPS Evolution

1.2 Principles of flow cytometry

Hematology analyzers rely on two methods for analyzing cells: electrical and optical. The electrical-based method measures impedance to count cells, calculate their volume, membrane capacitance and viability in a label-free manner. Briefly, cells suspended in an electrolyte solution are drawn through the microchannel of a flow cell. Strategically embedded electrodes apply an electric field perpendicular to the flow. Since cells are poorly conductive, their transition in the sensing region produces an impedance pulse. The measured current drop is proportional the amount of displaced solution, thus the cell volume. These impedance-based measurement systems, better known as Coulter counters, were developed in the 50's and are now well established technologies actively used in clinics and research centers around the world.

The optical-based method relies on either absorbance of a protein solution or the interaction of a laser beam with a single cell. In the first case, light absorbance of a diluted target protein sample, for example HGB, is compared, at a precise wavelength, against a reference sample to determine its concentration. Using the Beer-Lambert law, the concentration of the target protein can be found. In the second case, the interaction of a laser beam with a single cell allows to measure its size and granularity. The granularity of a cell is representative of its inner complexity and is evaluated by the extent to which it scatters light at large angular values. Indeed, Mie scattering predicts that smaller particles scatter light at higher angular values than larger ones. Thus, the granularity measurement is influenced primarily by the amount of particles or vesicles inside of the cell that are smaller or in the same order of magnitude as the probing wavelength. Large angular scattering is also influenced by the nucleus shape or the membrane roughness. Small nucleus lobes or extrusions scatter light at large angles whereas rough membranes produce diffuse reflection which contributes to the higher angular light. These optical-based measurement systems, better known as flow cytometers, can characterize cells at a throughput in the order of 10 000 cells/s. Reaching a high-throughput is of utmost importance for detection of rare cells in a reasonable time period. Typical flow cytometers have a detection level of 0.1% for rare events, which conveniently corresponds to the concentration of hematopoietic stem cells in peripheral blood. Though, some rare cells such as circulating tumor cells (CTCs) in peripheral blood can be at concentration as lows as 1 cell per 10^7 cells [1]. Thereupon, flow cytometry is the result of complex engineering to achieve accurate and high-throughput analysis of large cell populations. Its apparatus can be divided into three essential systems: the fluidic components, the optical components and the analysis tools. Figure 1.2 shows a schematic of a typical flow cytometer essential systems and their corresponding components.

First, the fluidic components align cells in a single file using a sheathed flowing liquid stream for accurate measurements. The size of the core stream containing the cells is controlled by the hydrodynamic pressure difference between the sheath and the sample fluids. Thus, to squeeze the core stream at the size of the analyzed cells, its pressure needs to be lower than the one of sheath fluids. Since, the sheath pressure on flow cytometer is fixed at a certain value to ensure proper operation, it limits the maximum reachable cell measurement throughput. To overcome this limit, higher-end flow cytometers add acoustic focusing to their flow cell. Acoustic radiation pressure allows cells focusing in larger core stream flows thus reaching throughput up to 35 000 cells/s.[2]

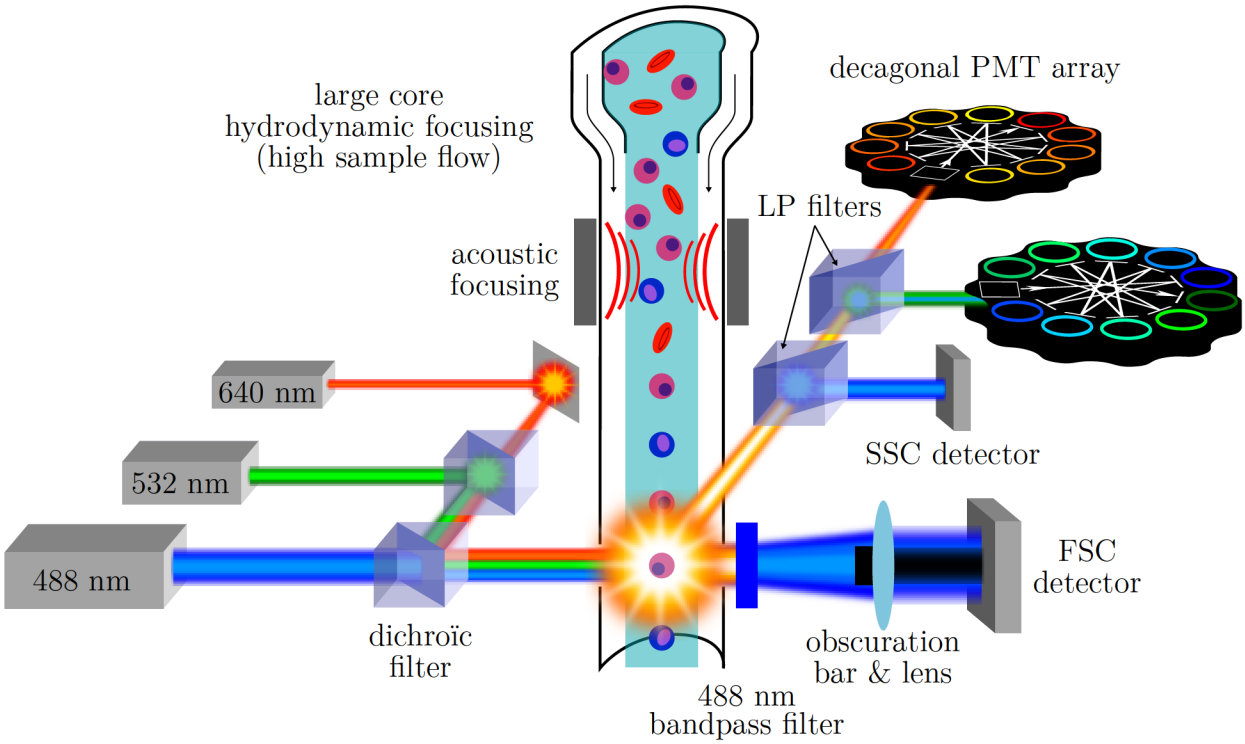

Figure 1.2 Schematic of the working principles of optical flow cytometry.

The optical components can be further subdivised into three categories: lasers, detectors and light guiding components such as lenses, filters and mirrors. Combined lasers beam are aimed at the focused cell flow for individual cell sensing. Typically, a continuous wave (CW) diode-pumpe solid-state (DPSS) laser emitting at 488 nm interrogates physical cellular properties, namely the size and granularity. The intensity of light scattered by a cell at small angular values, forward scattered light (FSC), is directly proportional to its size. Synchronously,

[2]ThermoFisher Scientific, Attune NxT Cytometer.

the intensity of light scattered at large angular values, side scattered light (SSC), is directly proportional to its granularity. Other DPSS lasers emitting at wavelengths ranging from 350 nm to 980 nm are usually included to interrogate more cellular properties by the means of fluorescence. Indeed, carefully labeling cells with fluorescent antibody complexes allows to evaluate specific antigen production levels. Common measured parameters using fluorescence include intracellular or surface protein expression, cell cycle analysis and other DNA-based phenomena, cell death by apoptosis or necrosis and enzymatic activity, to name a few. Flow cytometry companies have developed numerous specialized organic fluorochromes specific for each DPSS laser. Though, quantum dots have been increasingly adopted because of their larger excitation band and narrower emission peaks.

Following cell-light interaction, the FSC signal unblocked by the obscuration bar is directly collected by a lens and projected onto a photodiode. Meanwhile, each emitted fluorescent spectrum, as well as SSC, is guided to its specific detector using a set of dichroic and bandpass filters. Usually, the whole emitted spectra is chromatically divided along its path into optical bands using precise lowpass (LP) filters, as schematized in Fig.1.2. For each optical band, an array of photomultiplier tube (PMT), featuring a complex combination of dichroic and bandpass filters, further isolates and measures the light signal into separate channels. Weak fluorescent signal are captured by PMT which are better suited than photodiode because of their higher sensitivity. Most recent flow cytometers can simultaneously measure up to 50 different channels for a single cell, using a maximum of 10 laser lines and 5 circular decagonal PMT arrays.[3]

Lastly, the analysis tools calibrate the collected fluorescent data to ensure correct values of the measured cell characteristics. To certify proper data analysis and results, critical calibrations should be performed on each experiment. In particular, autofluorescence, spectral overlap and non-specific antibody binding effects can contribute to the background signal and need to be corrected [2, 3]. Autofluorescence is caused by the excitation of naturally occurring cellular entities, especially recurrent at 488 nm. A non-treated cell population will help to determine the amount of autofluorescence in each channel and thus can be software corrected. Spectral compensation corrects the spillover signal from adjacent fluorochrome emission into the selected bandpassed PMT. If uncorrected, spectral overlap can falsely report the presence of the target entity or artificially increase the measured expression level. Wisely chosen, minimally overlapping fluorochromes can minimize the need and effect of spectral compensation, if the experiment at hand allows it.

Non-specific binding of a fluorochrome-antibody complex can occur through a variety of

[3]Becton Dickinson, FACSymphony.

phenomema. For example, simple adsorption, undesired antigen expressing the same target portion and receptors binding to other portions of the antibody or directly to the fluorochrome. Non-specific binding is the hardest effect to calibrate in flow cytometry and is part of many debates amongst specialists. Nevertheless, commonly applied calibration procedures for non-specific binding consist of isotope control, isoclonic control, internal negative control and fluorescence-minus-one (FMO) control. Isotope control employs an isotope antibody, perfectly matching the working antibody, for which no antigen is expressed on the cell to deduce all non-specific binding. Isotope control applicability is fiercely argued since the isotope might itself have different binding dynamics. Indeed, finding an isotope matching an antibody on protein chains, type and number of fluorochromes as well as manufacturing process and solution formulation is not realistic. Isoclonic control identifies the level of fluorochrome direct binding. It introduces an excess of unlabeled antibodies to block all target antigen and then, if any relative fluorescence increase is measured after treating cells with the flurorochrome-antibody complex, it is related to direct fluorochrome binding. The internal negative control introduces a population of cells that do not express the target antigen, if it exists, inside the cellular population at test. This included cell population undergoes the same experimental protocol and thus defines the fluorescence intensity negative threshold value. At last, the FMO control, typically used when 4 antibodies complexes or more are under study, is a series of multicolor test in which cells have been treated with all the different antibodies except one. Each negative FMO test measures the nonspecific binding of other antobodies and spectral overlap into the channel in study.

This laborious description of calibration procedures might seem excessive but it is intended to show the complexity and lengthly process users have to go through for tests that are performed every day. It also sets the background need for other easily accessible phenotypic biomarkers.

1.3 Refractive index and deformability as phenotypic biomarkers

Apart from size and granularity, other physical phenotypic biomarkers, such as RI and deformability, can discriminate cells and are growing in interest. In this thesis, effective RI measurement is implemented to discriminate some myeloid cell populations. In addition, RI can help in the diagnosis process since it reflects the internal composition of a cell. In most studies, a single cellular effective refractive index is measured and variations from a normal cell line are correlated to various cancers [4–8], infections or anemia [9]. Its only recently that sub-cellular entities, particularly the nucleus and cytoplasm, were investigated based on their RI. The nucleus, which contains DNA, was always believed to have a higher RI than

the surrounding cytoplasm [10, 11]. Interestingly, Schürmann et al. reported beforehand the opposite, *i.e.* lower RI values for the nucleus than the cytoplasm [12]. Their results, enforced in this thesis, were later confirmed by another group using the same technique [13]. This important development has repercussions for many prior research conclusions and implies that proteins and vesicles inside the cytoplasm have a larger role in defining the effective RI than previously assumed.

Likewise, deformability is also an information rich physical phenotypic biomarker. Deformability reflects the cytoskeleton organization as well as health and state of the cells. In the literature, variations of deformability from normal RBC correlates to numerous pathologies such as malaria, anemia and diabetes [14]. Similarly, deformability deviation in WBC is associated to diseases, such as chronic lymphocytic leukemia[15], changes in cytoskeleton[16], cell cycle phases and cellular differentiation [17–20]. In this thesis, deformability measurement provides the missing piece to achieve complete discrimination of the selected myeloid cells: neutrophils, basophils and promyelocytes.

Integrated technologies measuring RI and deformability are reviewed in Chapter 2 and 6 respectively. Notably, combining cellular RI and deformability in a single measurement has never been reported elsewhere and represents one solution addressing the issues exposed in the next section.

1.4 Problem statement & motivation

Accurate identification of cellular phenotypes can determine effective immunity or predict diseases, especially for WBC. Consequently, clinicians and research professionals alike strive to obtain state-of-the-art technology that offers a high-throughput, multiparametric and diversified single cell measurement, ideally in a unique system. Flow cytometers have been developed accordingly to become high performance, specific and sensitive systems allowing high-throughput of cells. However, the measured physical properties are limited to the size, FSC, and granularity, SSC.

A direct implication of this limitation is that correctly discriminating all WBC is not easily done. Indeed, FSC-SSC can only yield a 3-part WBC count which identifies lymphocytes, monocytes and granulocytes. It means that neutrophils, basophils and oesinophils are mixed into the granulocytes scatter and thus are not discriminated. To achieve a complete 5-part WBC count, specificity can be enhanced using fluorescent labeling of cells combined with advanced flow cytometry calibration and analysis. The multiple antibodies necessary to properly discriminate WBC need to be measured in separate channels. It implies a complex organization of optical components as well as precise optimization to reduce artifacts such as autofluorescence, overlapping spectra and non-specific binding. Hence, as exposed previously, more fluorescent spectra might also mean more problems. Also, the fluorescent antibodies can be expensive, easily a couple of hundreds dollars per 100 μl, labeling procedures are time consuming and impact cell viability. Furthermore, fluorescence labeling does not rely on physical properties of the cells. It is rather an evaluation of a function, *i.e.* the level of production of a specific antigen, which may not truly reflect phenotypic populations. This 3-part *vs* 5-part WBC populations count example is a well-known matter amongst biologist and research professionals. The provided fluorescence solutions are so well implanted that they are believed to be inescapable methods.

Additionally, accessibility to a benchtop flow cytometer is restricted since it is usually shared between users to divide its high acquisition, installation and maintenance cost. Besides, its large size makes it necessary to be permanently installed in a dedicated room. The considerably large number of electronic, optical and fluidic components required for flow cytometry inevitably comes with its lot of troubleshooting problems and hardware failure which requires time consuming and costly service contracts. Flow cytometry also uses large volumes of liquids and reagents which adds up to the operational cost. Microsystems, featuring highly miniaturized components, can overcome these issues. Indeed, fully integrated devices could be afforded by individual groups or point-of-care users since their mass production, lower liquid volume and simple replacement all dramatically lower costs. Their portability reduces

the time between the sample collection and measurement for more consistent results and allows to deliver the technology to remote or underdeveloped regions. In particular, integrated miniaturized single cell analysis devices represent compact, portable and low-cost solutions specifically related to flow cytometry.

Miniaturized flow cytometers report good performances but measure the same physical (impedance, FSC and SSC) and fluorescent parameters as conventional benchtop flow cytometers or hematology analyzers. Besides, no integrated on-chip flow cytometer reported throughput reaching the ones of their benchtop equivalent. Limited to only one or two excitation laser, most microflow cytometers can excite a lower number of fluorochromes. Their versatility and capacity to discriminate cell populations is thus hindered. In the past decades, miniaturized biomedical devices have opened the way to new physics phenomena, novel functionalities and applications, for which flow cytometry has not taken advantage of yet. Adding other physical biomarker measurements can mitigate long lasting cellular identification issues, such as the 3-part *vs* 5-part WBC populations count. Indeed, even though flow cytometry is fundamentally an optical sensor, it does not take advantage of the cellular RI which has proven to be a discriminant phenotypic parameter. Equally, fluidic structures in flow cytometers have been fabricated to prevent cell deforming forces but there is growing evidence that deformability is an indicator of pathologies, cell state and population belonging. Consequently, cellular RI and deformability are promising avenues to discriminate and identify cells of interest. The motivation for enhancing discrimination, by adding complementary measurements, extends to more than the presented immune system context. Other important applications benefiting from complementary phenotypic parameters may include: rare cell detection, identification of cancerous or precancerous cells, T-cell phenotyping, human immunodeficiency virus and acquired immune deficiency syndrome (HIV/AIDS) infection research, stem cells research, identification of RBC pathologies, drug treatment analysis to assess efficiency and toxicity or cell cycle analysis and total DNA content. The goal of this research project is not to replace existing flow cytometers but rather to include complementary measurements, cellular RI and deformability, in a compact device for which portability and low-cost are easily reachable.

1.5 Achieved objectives & original contributions

Based on these exposed issues, the purpose of this thesis is to propose an integrated biosensor yielding enhanced cellular discrimination based on specific physical properties, RI and deformability, at a throughput comparable to flow cytometry. To achieve such a device, this thesis is divided into three main objectives.

Objective 1: Development of an integrated biosensor

In the development of this biosensor, optical and microfluidics components were fully integrated on a single chip. Microfluidic structures allows control over position and velocity of the cells for reproducible measurements as well as a throughput up to 5 000 cells/s. Integrated waveguides were engineered to generate low losses while maintaining a single-mode like behavior in propagation. The sensor is an in-plane Fabry-Pérot, chosen for its higher interaction with cells due to its resonant nature. Geometry of the distributed Bragg reflectors (DBRs) composing the Fabry-Pérot cavity were engineered to yield resonances in the near infrared (NIR) electromagnetic spectrum, conveniently matching the transparency window of silicon. The final integrated biosensor offers high sensitivity, high-throughput and compatibility with existing flow cytometers.

Objective 2: RI and deformability characterization of single cells

To demonstrate the working principle, on-chip RI and deformability characterization of single cells is realized. Optical resonances of the Fabry-Pérot are highly sensitive to RI, enabling effective volume refractive index measurement of cells at a resolution as small as 1.2×10^{-5} refractive index unit (RIU). Shear stress induced on cells is tunable through volumetric flow control to either promote or inhibit cellular deformation.

Objective 3: Enhanced discrimination of myeloid cells

To confirm the improved discrimination feature of the device, myeloid cells are measured and compared against flow cytometry. The RIC device reports complete discrimination of neutrophils, basophils and promyelocytes when measuring both RI and deformability. As expected, FSC-SSC measurement cannot discriminate any of these myeloid cells. The developed analysis algorithm provides a simple coefficient to assess the discrimination efficiency, the OLR.

1.6 Thesis structure

Chapter 2 exposes the important concepts, through a literature review, necessary to understand on-chip single cell measurement. First, cell focusing techniques are reviewed and, when necessary to the comprehension of this thesis, governing equations are laid out. It is a prerequisite to review, classify and expose the main miniaturized flow cytometry devices presented subsequently. In the last section, a comprehensive review of existing on-chip RI sensing technologies is presented. Chapter 3 lays out the mathematical equations and optical principles describing the operation of the DBRs as well as the Fabry-Pérot cavity employed in this thesis. A comparative scheme between ideal and expected properties is employed to explain the effects of losses and thus serves as a guideline for Fabry-Pérot cavity design.

Chapter 4 addresses the optical part of the first objective. It describes the methodology to achieve single-mode like propagation in very large cross-section rib waveguides and highlights its importance for resonant sensing applications. Importantly, it shows that previously established equations are no longer valid when using large silicon rib waveguides. This chapter also contains complementary results and considerations that were not included in the published article. Chapter 5 completely fulfills the first objective and part of the second and third. It describes the fully integrated biosensor but only exploits the cellular RI to discriminate some of the myeloid cell populations. In this chapter, the complete microfabrication process, microfluidic operation and experimental setup are detailed. Chapter 6 completes the second and third thesis objectives. It reports the addition of deformability measurements to achieve complete discrimination of the selected myeloid cells. Chapter 4 to 6 were published in peer-reviewed journals.

Chapter 7 presents a discussion on the limitations and possibilities of the proposed integrated biosensor which focuses on device performance, integration into flow cytometry and potential biological applications. Chapter 8 concludes this thesis, exposes remaining challenges and expresses recommendations for future work directions.

CHAPTER 2 LITERATURE REVIEW

Microsystems propose highly miniaturized components able to accomplish most of the biological measurements done by their macroscale equivalent. In this chapter, published microtechnologies mimicking flow cytometry are reviewed. Manipulating cells in microscaled devices inevitably introduces microfluidic mechanics and concepts. In particular, microfluidic systems have proven their outstanding ability to precisely focus cells into the sensing area, at a high-throughput while preventing coincidental events. Thus, before reviewing existing miniaturized flow cytometer devices, a necessary overview of the main cellular focusing methods is presented. Finally, integrated systems exploiting another physical cellular property of interest, refractive index, are also described here to provide a more contemporary review than Chapter 4 and 5. To avoid repetition, devices achieving on-chip cellular deformability measurement are reviewed in the latest published article (Chapter 6).

2.1 Cell focusing in microchannels

To obtain reproducibility, consistency and high-throughput of a dedicated biosensor, cells must be positioned and ordered when passing through the optical detection volume. A precise control over the position of each cell ensures a steady trajectory at a constant speed. This is particularly important for signal comparison since flowing time is an underlying parameter for most optical biosensors. Additionally, it reduces the setup induced variability, leaving the measured variations to be primarily influenced by biological disparities. In this section, only cell focusing strategies purely acting upon microfluidic effects are described. They are grouped into three main categories: sheathed hydrodynamic focusing, microvortices and inertial focusing.

2.1.1 Sheathed hydrodynamic focusing

Sheated hydrodynamic focusing was the first technique to be integrated on-chip and is an in-plane reproduction of what can be found in flow cytometry. Different flows are brought into the same pipe which squeezes the sample solution into a narrow stream. Turbulent mixing of the different solutions is prevented by the strong viscous forces at this scale. This phenomenon is referred as laminar flow and is characterized by small Reynolds number (Re). The Re is an adimensional number calculated as the ratio of inertial over viscous forces:

$$Re = \frac{inertial forces}{viscous forces} = \frac{\rho U_f L}{\mu} \tag{2.1}$$

where ρ and μ are the fluid density and dynamic viscosity respectively, U_f is the average flow velocity and L is the characteristic length. The characteristic length is usually the hydraulic diameter $D_h = 2WH/(W + H)$ where W and H are the width and height of the rectangular microchannel cross-section respectively. Thus, for $Re < 1$, viscous forces are dominant and inertial effects are neglected. In flow cytometry, the sample solution is completely sheathed using imbricated cylindrical tubes. Contrarily, achieving sheathed 3D hydrodynamic focusing in microscale devices has been a challenging task. Knight et al. were the first to experimentally and theoretically describe simple lateral hydrodynamic focusing in rectangular microfluidic channels as depicted in Fig. 2.1.

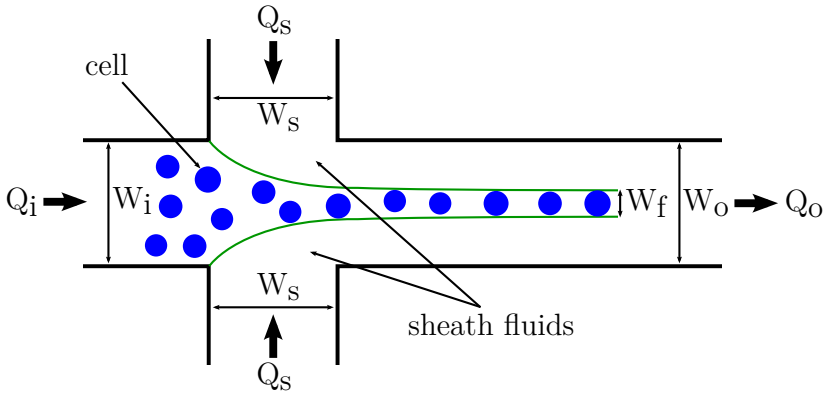

Figure 2.1 Diagram of simple lateral sheathed hydrodynamic focusing.

Later on, Lee et al. characterized and developed the sheathed hydrodynamic focusing theory for cylindrical [22] and rectangular [23] micromachined flow cytometers. Concurrently, Wu and Nguyen proposed an equivalent theory for laterally sheathed hydrodynamic focusing, specifying the velocity profile for liquids of different viscosity and also taking into consideration diffusion effects [24]. The simplified equation form describing symmetric lateral sheathed focusing for in-plane rectangular channels takes the following form:

$$\frac{Q_s}{Q_i} = \frac{1}{2\alpha} \cdot \left(\frac{W_f}{W_o}\right)^{-1} - \frac{1}{2} \qquad \text{where} \quad \alpha = \frac{U_{foc}}{U_f} = [1.0, 1.5] \tag{2.2}$$

where Q_s and Q_i are the sheaths and inlet flow rates respectively, W_f and W_o are the focused fluid and channel output widths respectively and α is the ratio of the average focused fluid velocity U_{foc} over the average output flow velocity U_f. A derivation of the velocity ratio α can be found in ref. [23]. Notably, the velocity ratio α can only vary from 1.0 to 1.5 depending

on the geometrical factor $\varepsilon = H/W_o$. For $\varepsilon \to \infty$, $\alpha = 1.5$ whereas for $\varepsilon \to 0$, $\alpha = 1.0$. This equation also applies to hydrodynamic focusing in flow cytometers, where $\alpha = 1.5$ since channels are cylindrical and $W_f << W_o$. Typically, in flow cytometers, W_o and Q_s are fixed. Thus by varying only the inlet flow rate Q_i, generally specified as the inlet pressure, precise control over the focused width W_f can be achieved.

The equation for the maximum cell throughput under the $Re < 1$ condition, as presented in Annex B, is:

$$T < \frac{\mu}{\rho L} \cdot \frac{\alpha}{\Delta x_{cell}} \tag{2.3}$$

where Δx_{cell} is the separation between the beginnings two adjacent cells. To compare the focusing methods, this distance will be set to $\Delta x_{cell} = 2a$, where a is the diameter of the cell. This is the minimal distance for cells to be measured separately and provides the largest theoretical throughput. For the limit case where no focusing is required ($L = a = W_o = W_f$ and $\alpha = 1$), the maximum throughput is then $T < \mu/2\rho a^2$. For typical $a = 15$ μm cells, this yields a maximum reachable throughput around 2200 cells/s. Any sheathed hydrodynamic focusing applied would then result in a smaller throughput, if the $Re < 1$ condition is respected.

3D sheathed hydrodynamic yields a similar mathematical description and conclusion on the maximum throughput, as explained in Annex B. Polymers, such as polydimethylsiloxane (PDMS), allowed multi-layered 3D focusing devices to be manufactured [25–29]. However, these devices require more complex fabrication, precise alignment and may not account for deformation of the polymer channels under pressure. To eliminate alignment, direct writing of 3D microchannels in silica using femtosecond laser has been proposed [30]. Although achieving complex 3D microfluidic structures and reducing the number of inlets, integration of other components is difficult. Single-layer 3D focusing reduces the fabrication complexity and eliminates the necessary alignment [31]. Still, 3D sheathed hydrodynamic focusing requires larger volumes of liquid, multiple inlets and is known to be very sensitive to flow rate perturbations.

2.1.2 Microvortices

Contrarily to sheathed hydrodynamic focusing, microvortices focusing is a passive method which usually requires less pumps. Microvortices are generated in curved microchannel or in abrupt geometry variations such as expansion-contraction regions. More precisely, these structures produce secondary flows, perpendicular to the mainstream flowing direction,

namely the microvortices. Despite the generally assumed purely laminar behavior of fluids in microchannels, inertial effects cannot be neglected in these cases. Indeed, microvortices are associated to centrifugal pressure gradients. This effect is better understood using the simple curved microchannel model first described by W. R. Dean [32]. Due to the parabolic velocity profile of a flowing liquid, the fluid particles at the center of the microchannel have the largest velocity and thus more inertia. In a curved microchannel, these high-velocity particles are pushed outwards by the pseudo-centrifugal force thus generating a pressure gradient in the radial direction. The relatively stagnant fluid particles at the channel walls are then forced to recirculate producing two symmetric microvortices, called Dean vortices or Dean flows [33]. Figure 2.2 illustrates Dean microvortices in a curved rectangular microchannel. The Dean number (De) is an adimensional number describing the amplitude of the microvortices.

$$De = \frac{\sqrt{\frac{1}{2}\ inertial forces \times centripetal forces}}{viscous forces} = Re\sqrt{\frac{L}{2R_{curv}}} \tag{2.4}$$

where R_{curv} is the radius of curvature of the channel. For stable Dean flows to appear, the De must be between 40 and 100.

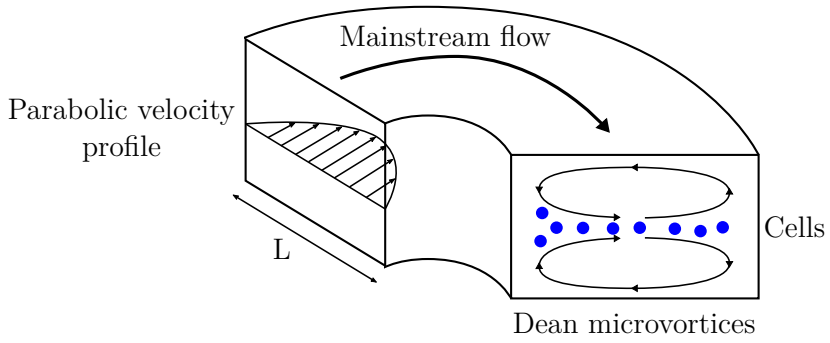

Figure 2.2 Dean microvortices generated in a curved rectangular microchannel.

Similarly, contraction regions along a microfluidic channel generate centrifugal forces, thus microvortices. Many devices have been using sheaths combined with microvortices in curved channels [34–36] or contraction-expansion regions [37–40] to achieve 3D hydrodynamic focusing. Importantly, larger particles are less affected by microvortices, hence other devices have used this effect to sort particles of different sizes [41–45]. However, microvortices focusing is better suited for small particles in large channels at very large flows. Indeed, the square root term in the De equation is smaller than 1 which means that the Re must be large. Such Re is associated to turbulent flows in straight channels which imply losing the stable velocity profile.

2.1.3 Inertial focusing

Inertial focusing is also a passive method which rely on inertial phenomena occurring on the particles rather than on the fluid itself. It was first observed by Segré and Silberberg in 1961 where particles focused on an annulus approximately 0.6 times the radius of a cylindrical pipe [46]. It's only years later that Schonberg and Hinch as well as Asmolov explained this effect in a Poiseuille flow. They investigated two counteracting forces governing the equilibrium positions of particles, namely the shear-induced and wall lift forces [47, 48]. The parabolic nature of a bounded flow induces a local shear lift force on the particles pushing them away from the centerline. In addition, particles near a wall build up a pressure in the vicinity between the wall and the particle due to the constricted flow. This pressure acts as a force pushing particles away from the wall. Consequently, the net lift force in cylindrical channels allows to predict the focusing length [33, 48–50]. However, these equations fail to predict the observed behavior in rectangular microchannels. In square microchannels, 4 stable equilibrium positions centered at each face have been observed [50–52]. Moreover, in high aspect ratio rectangular channel ($W/H \geq 2$), only 2 equilibrium positions centered along the long faces exist [53–57].

Up to this day, the inertial microfluidic phenomena in rectangular channels are still subject to debate and are not fully understood. However, Zhou and Papautsky have done an outstanding work in summarizing the governing parameters for each inertial lift phenomenon [58]. They have also proposed a third inertial lift force, the rotation-induced force, responsible for the migration of particles from unstable position near the corners into the stable face-centered equilibrium positions. This weak lift force becomes dominant where shear-induced and wall lift forces are balanced, hence the two-stage focusing mechanism proposed by the authors [58]. At these balanced points, a shear rate exists along the walls and thus induces rotation of the particle. This yields a force parallel to the wall and directed against the flow velocity gradient. Figure 2.3 shows this two-stage focusing mechanism in a rectangular channel.

In this two-stage inertial focusing, the length L required for complete focusing of particles is:

$$L = \frac{3\pi\mu D_h^2}{4\rho U_f a^3}\left(\frac{H}{C_L^-} + \frac{W}{C_L^+}\right) \qquad \text{when} \quad W > H \tag{2.5}$$

where C_L^- and C_L^+ are the negative and positive lift coefficients [58]. The sign of the lift coefficient is attributed based on the migration down (negative) or up (positive) the velocity gradient. In the first stage the shear-induced and wall lift forces act to migrate particles away from the centerline, down the velocity gradient, thus the lift coefficient is negative. Conversely, in the second stage, the rotation-induced force acts to migrate particle to the center

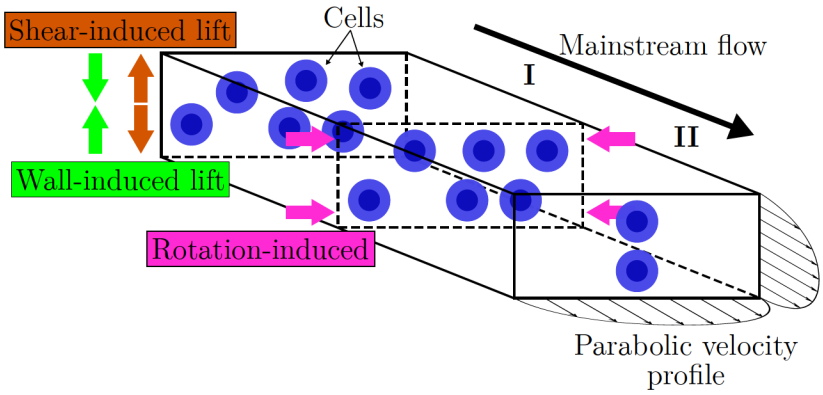

Figure 2.3 Two-stage inertial focusing mechanism in a rectangular microchannel.

of the faces, up the velocity gradient thus the lift coefficient is positive. The experimental data reported in ref. [58] can be used to evaluate these coefficients.

Furthermore, particles have also been found to be longitudinally ordered, generating trains with regular spacing in the flow direction [53–57, 59, 60]. Although not fully understood, Lee et al. suggested that the interplay between viscous repulsive forces and inertial lift forces act to produce regular interparticle spacing in the flow direction [55]. Their main conclusion, is that there is no long range nor short range attraction forces, only local repulsive forces between two particles which can be transfered down the train and ultimately lead to longitudinal organization.

By precisely engineering the microchannels geometries, one can achieve stable, ordered and controlled 3D focusing of particles at quite impressive throughputs. Hur et al. have reported an inertial focusing device using 456 parallel channels to capture images of cells at a total throughput of 1×10^6 cells/s. Concurrently, Mach and di Carlo developed a blood filtration device exploiting the dominant inertial forces on larger particles to sort bacteria from RBC. Their 40 channels device achieved a total throughput of 4×10^6 cells/min [61]. Many other sorting devices exploiting this size effect [56, 62] or a combination of Dean flows and inertial lift [42, 43, 63–65] were reported. Inconveniently, focused streamlines are located closer to walls than to the centerline which may not be suited for integrated optical measurement. However, an interesting combination of Dean flows and inertial focusing was implemented by Di Carlo et al. in a serpentine channel. Using successive asymmetrical curves in a rectangular channel, authors were able to focus cells on a single streamline, effectively eliminating other equilibrium focusing [60]. Concurrently, Zhang et al. investigated a symmetric rectangular corner serpentine able to focus particles in a single centered streamline [66]. However, this device could only focus larger particles, required very large Re and suppressed the regular

interparticle spacing. For further reading on the inertial focusing phenomena and description of the related forces, review articles in ref. [33, 67, 68] are suggested.

To compare inertial focusing against hydrodynamic focusing, the throughput equation is presented. Inertial migration of particles occurs for particle Reynolds number (Re_p) in the order of 1. The Re_p represents the ratio of inertial to viscous force at the particle length scale:

$$Re_p = Re\left(\frac{a}{L}\right)^2 \tag{2.6}$$

The throughput equation for inertial focusing when imposing Re_p ($5>Re_p>1$) [54] is (see Annex B for derivation):

$$T < \frac{5\gamma\mu L}{\rho\Delta x_{cell}a^2} \tag{2.7}$$

where γ is the velocity factor of the lagging particle velocity over the average fluid velocity ($U_p = \gamma U_f$). Taking the same typical values as sheathed hydrodynamic focusing of $\Delta xcell = 2a$, $a = 15$ μm, a rectangular channel of $Dh = 50$ μm with an aspect ratio $W/H = 2$ and $\gamma = 1 - a/Dh = 0.7$ (see Chapter 6 for derivation) yields a maximum throughput around 26 000 cells/s. This throughput is one order of magnitude larger than hydrodynamic focusing.

On a final note, elasto-inertial focusing using non-Newtonian fluids is of growing interest in the community. Particles suspended in viscoelastic fluids and flowing through a microchannel have been observed to focus near the centerline in some conditions [69–71]. Non-Newtonian fluids used for 3D focusing characteristically exhibit shear-thinning and elasticity. By tuning the fluid composition, a dominant elastic force, which pushes the particles away from the walls, can be developed to balance the inertial forces and thus successfully focus particles around a centerline region [72–74]. A thorough analysis of elasto-inertial focusing was recently published, further highlighting its complexity and the different behaviors observed experimentally [75]. Elasto-inertial focusing requires adding polymer to the solution, is mostly limited to Re close to 0, requires very dilute solutions, weak shear-thinning fluids and small particles compared to the channel. Also, the focusing efficiency is intrinsically weaker since focusing only occurs on a centerline region and not on precise equilibrium position as it is the case for inertial focusing. Thus it might not be compatible with the cells in hand nor be suited for high-throughput applications. Table 2.1 summarizes and compares the presented particle focusing methods.

Table 2.1 Comparison of particle focusing techniques.

Technique	**Governing effect**	**Working range**	**Particle size**	**Pros**	**Cons**	**References**
Sheathed hydrodynamic	pinched laminar flows	$Re < 1$	any size	• Precise 3D focusing • Established equations	• Multiple pumps • Sensitive to perturbations • Limited throughput	[21–31]
Microvortices	secondary perpendicular flows	$40<De<100$	small	• Less pumps • Integration with other focusing structures	• Large Re • Large flow rates • Weaker forces for large particles	[33–45]
Inertial	inertia of particles	$1<Re_p<5$	small & large	• Single pump • Regular interparticle spacing • Integration with other focusing structures	• Not fully understood • Long length to focus • Focused streams near walls	[42, 43, 46–49, 51–68]
Elasto-inertial	fluid viscoelasticity	$Re \sim 0$	small	• Single pump • Centerline focusing	• Complexity & not understood • Addition of polymer • Dilute solutions • Larger focused region	[69–75]

To summarize, inertial focusing, although not fully understood, has undeniable advantages over other focusing methods. It requires a single pump, easily integrates on-chip, naturally produces regular interparticle spacing and can achieve high-throughput. Moreover, for a rectangular channel height similar to the focused cell size, the two equilibrium positions largely overlap thus yielding a single streamline behavior. For these reasons, inertial focusing is enforced in the devices presented in Chapters 5 and 6. Still, multiple entries are designed to support sheathed 3D hydrodynamic focusing of small cells ($a/H < 2/3$) for which equilibrium positions do not overlap enough.

2.2 Miniaturized flow cytometry

This section reviews integrated miniaturized flow cytometry devices reproducing FSC, SSC and fluorescence measurements developed and reported in the literature. Miniaturized on-chip flow cytometers have aroused great interest considering their smaller cost and portability. However, the complex integration of high-throughput, sensitive and reproducible optical detection of cells on-chip is an ongoing challenge. Different strategies are used to deliver light onto the single stream focused cells. The main reported optical methods either consist of out-of-plane excitation [76–86], direct delivery using embedded optical fibers [87–93] or integrated waveguides and two-dimensional lenses to guide light [94–99]. Out-of-plane excitation usually requires bulky apparatus and do no represent a true integrated solution. Collecting FSC signals using embedded optical fibers can be challenging since it is easily hidden in the excitation signal. Integrated waveguides and light shaping components can be precisely patterned and engineered to enhance cell excitation and light collection. However, their microfabrication can be more challenging and patterned materials might degrade, react or present autofluorescence with the typical 488 nm interrogation laser.

To focus cells precisely, devices either use acoustic focusing [79, 80], sheathed hydrodynamic focusing [76, 77, 82, 83, 85–88, 90, 92, 94–96, 98, 99], inertial focusing [78, 84, 93, 97], microvortices or a combination [91]. Devices reported in ref. [85, 88, 99] are more representative of miniaturized hematology analyzers since they also integrate electrodes for cellular impedance measurement. Table 2.2 categorizes the benchmark on-chip flow cytometry devices, reports their specifications and achieved throughput. Commercial flow cytometry specifications are reported for comparison.

Commercialization of high-end cameras providing high sensitivity and extreme frame rate has favored the emergence of on-chip imaging flow cytometry. Using similar optical components as conventional flow cytometry this technology is able to realize complementary multiparametric measurement of single cells. In addition to morphological measurement such as size

Table 2.2 Comparative of benchmark on-chip flow cytometry devices.

Optical setup	**Cell focusing**	**Achieved throughput**	**Discriminated cells**	**References**
Embedded fibers	elasto-inertial	2 500 s^{-1}	No	[93]
	3D sheaths	1 800 s^{-1}	1. PLT *vs* RBC 2. granulocytes, MON and CD4+ T-LYM	[88]
Integrated waveguides and lenses	3D sheaths	not mentioned	live/dead T-LYM	[96]
	inertial	not mentioned	PLT and RBC	[97]
	No	300 s^{-1}	NEU, MON and CD4-/CD4+ T-LYM	[99]
Out-of-plane excitation	3D sheaths	12 000 - 20 000 s^{-1}	No	[76, 77, 86]
	3D sheaths	not mentioned	granulocytes, MON and CD4-/CD4+ T-LYM	[82]
	lateral sheaths	1 000 s^{-1}	granulocytes, MON, LYM, RBC and PLT	[85]
	acoustic	$\sim$ 3 000 s^{-1}	granulocytes, LYM	[79, 80]
	COMMERCIAL FLOW CYTOMETRY			
	3D sheaths	35 000 s^{-1}	CBC	[1] footnotes 1-3
Imaging	inertial	50 000 s^{-1}	promyelocytes, NK cells, cell cycles and apoptosis	[100]

and shape, it can quantify and more importantly localize common fluorescent probes. Another undeniable advantage rests upon the marginally larger throughput it can achieve. Single cell focusing is ultimately limited by destructive fluidic forces, maximal cell concentration and coincident events, which state-of-the-art devices are actually reaching. Thus, single cell interaction devices are also limited to this throughput whereas imaging flow cytometry can simultaneously capture multiple parallel microchannels. However, imaging flow cytometry is limited by the trade-off between the field of view (number of pixels), the sensitivity of the camera and the frame rate. Indeed, weak fluorescent signals that are usually captured by a PMT require highly sensitive cameras, or larger exposure time, which comes at the expense of a smaller frame rate. Equally, a large field of view requires more pixels and thus a greater

time to collect all the pixels data, thus decreasing the frame rate. Subsequently, a smaller frame rate suffers from blurring of the cells if flowing speeds are to large. Thus commercially available imaging flow cytometers have a throughput actually limited between 1 000 to 5 000 cells/s, depending on the magnification, while supporting up to 12 simultaneous optical channels.[1]

Recently, an on-chip imaging flow cytometry device using two colors, out-of plane excitation and multiple inertial focusing channels reported a throughput of 50 000 cells/s and a theoretical one of 96 000 cells/s [100]. Authors discriminated promyelocytes (HL-60) from Natural Killer cells (K-562), some cell cycle phases and apoptotic stages. Another recently published work reported an out-of-plane optical setup simultaneously exciting 16 acoustically focused stream lines which yielded a throughput of 100 000 beads/s [101]. However, imaging flow cytometry technology requires out-of-plane bulky optical components which can be very expensive, in particular high-end high-speed cameras (>150 000$). These technologies face their own separate challenges, require massive off-line computation limiting the real time analysis and do not consist of true integrated solutions. Recently published review articles detailing these latest imaging flow cytometry technologies are recommended for further reading [102–104].

2.3 Refractive index sensing

Flow cytometry FSC measurements have been know to report larger absolute particle diameters than their true values due to the influence of the RI [105]. Smaller particles are more affected by this error than larger ones. Instead of dealing with the undesired optical refractive effects of cells, efforts have been made to quantify it in flow cytometry [8, 105–107]. Indeed, RI has proven to be a remarkable label-free biomarker for numerous pathologies, diseases and thus can also be used for cell populations discrimination. However, technologies embedded in flow cytometers have reported large limit of detection (LOD) around 10^{-2} RIU and do not constitute good RI sensors. In opposition, many other optical sensing mechanisms have been reported, yielding LOD as small as $\sim 10^{-9}$ RIU. Still, not all allow penetration depths in the order of 10 μm suited for whole cells detection. To lighten this thesis, RI sensors have been grouped into three main categories: evanescent field, interference and phase microscopy. In this section, reviewed devices were limited to the ones which showed applications in fluid, particle or cell RI measurement. Reviewed technologies in each category are compared in terms of LOD and interaction depth in Tab. 2.3.

[1] EMD Millipore, FlowSight and ImageStreamX Mark II.

Reported sensitivities in published papers differ greatly from one another, in terms of absolute values and units. Furthermore, some papers only focus on sensitivity enhancement without explicitly detailing the achievable LOD. Depending on the accuracy of the experimental setup, the LOD may differ considerably. There is an evident need for a common comparison ground and in particular a standard definition of the LOD. This concern was previously raised and a standard method was proposed, although not widely applied yet [152]. The proposed definition of the LOD is 3 standard deviation of the measured entity over the sensitivity of the device $LOD = 3\sigma/S$. From a general point of view, the sensitivity of an RI sensor depends on the fraction of its optical probing mode interacting with the sample. Larger fractions yield larger sensitivities. Still, most optical sensors are inherently limited to a sensitivity $S = \lambda_0/n$ where λ_0 is the interrogation wavelength and n is the refractive index of the sample, as shown in Chapter 3. Hence, for a given wavelength, the only method achieving smaller LOD is to reduce the standard deviation, namely the accuracy. The standard deviation can be reduced either by reducing the signal-to-noise ratio (SNR) of the system or by achieving larger

Table 2.3 RI sensors comparison based on LOD and magnitude of the penetration depth.

Category	**Technology**	**LOD* (RIU)**	**Penetration depth**	**References**
Refraction	FSC	1.3×10^{-2}	1 mm	[8]
Evanescent field	waveguides	1.2×10^{-4} – 1.0×10^{-5}	↑	[108, 109]
	(interference)	2.0×10^{-5} – 9.0×10^{-9}		[110–113]
	fibers	5.0×10^{-4} – 6.0×10^{-6}	1 μm	[114–117]
	Bragg gratings	9.8×10^{-5} – 1.4×10^{-5}		[118–123]
	(LPFG)	3.0×10^{-4} – 1.4×10^{-5}	↓	[124–126]
	SPR	1.9×10^{-6} – 2.8×10^{-8}	↑	[127–131]
			100 nm	
	WGM	2.0×10^{-6} – 3.4×10^{-8}	↓	[132–135]
Interference	Mach-Zehnder and Young	9.5×10^{-5} – 9.7×10^{-7}	100 μm – 1 mm	[136, 137]
	photonic crystal	2.0×10^{-3} – 7.8×10^{-6}	1 μm	[138, 139]
	Fabry-Pérot	1.0×10^{-4} – 1.0×10^{-5}	10 – 100 μm	[7, 140–145]
	(differential)	8.4×10^{-7} – 2.0×10^{-9}	100 μm – 1 mm	[146, 147]
	(this work)	1.2×10^{-5}	10 μm	[148]
Phase microscopy	Hologram	$\sim 10^{-2}$ – 10^{-3}	10 – 100 μm	[10–13, 149–151]

* Some LOD may have been calculated using $3\sigma = 0.01$ nm.

confinement of the optical probing mode. The confinement of an optical mode is quantified by the Q factor. Larger Q factors yield thinner spectral widths thus thinner full width at half maximum (FWHM). However, a larger confinement typically reduces the interaction fraction, thus reducing the sensitivity and the penetration depth.

2.3.1 Evanescent field

Technologies grouped in the evanescent field sensors category include waveguides and optical fibers, surface plasmon resonance (SPR), Bragg gratings and whispering gallery mode (WGM). The core sensing mechanism in all of these is an evanescent wave, at the interface between the sample and the optical structure, for which properties are affected by the surrounding RI. Despite the various implemented strategies, evanescent wave sensors show very short penetration depth compared to other technologies. Indeed, the rapid exponential decay of optical modes outside the structures inevitably limits the penetration depth. Hence, evanescent field sensors are better suited for fluid or single molecule detection than cell sensing.

Waveguides and optical fibers can either adopt very small cross-section [108–110, 114, 153] or higher order propagation modes [115–117] to expand the evanescent field into the surrounding liquid sample. However, the penetration depth is still limited to a few microns ($\sim 1\ \mu m$). The light which interacts with the sample is either directly measured for differential losses [114, 115] or is forced to generate interference using various schemes [108–110, 116]. Typical LOD for waveguides and optical fibers using differential losses varies between 10^{-4} and 10^{-5} RIU. Smaller LOD are achieved using Young or Mach-Zehnder interferometers [113]. Young interferometers have reported the smallest LOD of 9.0×10^{-9} RIU [112] compared to Mach-Zehnder 9.0×10^{-8} RIU [111]. However, Young interferometers require up to a few centimeters of free space ray propagation to produce an appropriate interference pattern thus are not adapted for complete on-chip integration. Futhermore, Mach-Zehnder interferometers using phase modulation to achieve small LOD require longer integration time, in the order of 1 ms, thus is not suited for high-throughput measurement.

Bragg gratings are periodic RI variations of the light guiding material which produces a wavelength band reflection. The reflected Bragg wavelength band, or resonance band, is determined by interference phenomena described in the next Chapter (3). The most popular configuration is within a stripped optical fiber core, namely fiber Bragg grating (FBG). FBG are sensitive to the surrounding environment through the evanescent fraction of their resonance. A change in the surrounding RI directly affects the resonance of the Bragg grating. Most FBG achieve LOD around 10^{-5} RIU. One particular form of FBG, long-period fiber

grating (LPFG), couples light into a specific cladding mode which is also determined by the surrounding environment RI. This configuration is usually easier to manufacture and can achieve similar LOD in the range of 10^{-4} to 10^{-5} RIU. One notable device used porous silicon to design an on-chip Bragg grating which can be partially filled with the sample fluid. It allowed a greater fraction of the light to interact with the sample and thus reported a larger sensitivity than others [122]. However, authors did not specify the LOD nor the accuracy.

SPR are resonances of electrons, *i.e.* a plasmon, at the surface of a metal thin layer on top of a dielectric. A specific wavelength at a specific angle will excite a SPR at the metal-dielectric boundary. Thus, most systems have adopted configurations where either different angles are scanned at a fixed wavelength or conversely where different wavelengths are scanned at a fixed angle. Due to the very thin metal layer, SPR are highly confined and have an extended evanescent fraction of their resonance in the sample thus reporting smaller LOD in the range $10^{-6} - 10^{-8}$ RIU [154]. However, these sensors suffer from even smaller penetration depth, typically in the order of 100 nm [155].

WGM are optical resonance modes inside a circular-shaped cavity such as a microsphere [135, 156], microtube [157], microring [132–134], microdisk or microtoroid. Trapped light recirculates around the geometry, bouncing off the interface due to total internal reflection, thus generating unique interference modes [158]. Similarly to the other devices, the evanescent field of the resonance modes expands in the surrounding environment. Contrarily to the technologies above, light interacts multiple times with a single point on the interface. The time decay of the resonance light, *i.e.* the number of interactions, is dictated by the quality factor Q. A larger Q means a longer time decay but also larger confinement and thus smaller LOD are achieved ranging from 10^{-6} to 10^{-8} RIU. However, their large Q factors implies a very short interaction depth typically in the order of 100 nm.

2.3.2 Interference

Technologies grouped in the interferometric sensors category include Mach-Zehnder and Young interferometers, photonic crystals and Fabry-Pérot cavities. Some of these interferometric sensors can have a larger fraction of their optical mode interacting with the fluid sample, thus better suited for particle or cell measurement. Mach-Zehnder and Young interferometers, are based on the interference of a reference beam with a probing beam which has a single interaction with the sample. Due to the difficulty of conserving the sample beam properties while propagating in a liquid volume, most Mach-Zehnder and Young interferometers use evanescent field sensing. From the few devices reported in the literature using volume interaction, one has reached a LOD of 9.7×10^{-7} RIU [136]. However, this

device requires several centimeters to project its Young interference pattern thus limiting its compact integration.

Contrarily, integrated microcavities such as photonic crystal and Fabry-Pérot have multiple interaction with the probed sampled due to the resonant nature of these sensors. Photonic crystals are periodic dielectric structures at the scale of the working wavelength. This periodicity produces an optical reflection band, also known as the photonic bandgap. In fact, the previously introduced Bragg gratings, or distributed Bragg reflector (DBR), are 1D photonic crystals. Introducing a defect by removing a couple of alternating structures generates a resonance in the disallowed photonic bandgap. The silicon Fabry-Pérot cavity presented in this thesis is an example of such a defect in a 1D photonic crystal. When extending to the 2D case, these periodic structures are typically sub-micrometric to micrometric holes on a thin slab. By introducing a precise defect, *i.e.* removing some of the holes, one can achieve large Q resonances and reach LOD in the order of 10^{-6} RIU [138, 139, 159]. However, 2D photonic crystal cavities have smaller sensitivities since a smaller fraction of their optical mode is interacting with the small liquid filled holes. Additionally, their highly confined resonant mode confers these sensors a limited penetration depth, typically in the order of 1 μm.

Coming back to Fabry-Pérot cavities, these structures generate optical resonance modes between two reflective mirrors facing one another. These mirrors can be DBR, as mentioned above. Likewise, the quality factor Q of the cavity describes the time decay of the resonance, thus the resonance spectral width. A more detailed description of Fabry-Pérot cavities and DBR properties is provided in Chapter 3. Importantly, Fabry-Pérots are sensitive to the medium inside their cavity, where the optical resonance is confined. The cavity can be several tens of micrometers in length, ideally suited for cellular measurement. Some Fabry-Pérot sensors have reported LOD up to 2.0×10^{-9} RIU [147]. The numerous on-chip configurations have been reported and can be divided into two main branches: out-of-plane setups an in-plane integration.

Out-of-plane Fabry-Pérot setups require microscope objectives to precisely input and collect light into the microcavities [143, 146, 160] which is not convenient for an integrated solution. However, out-of-plane setups allow for deposition of very high quality surfaces yielding enhanced Q factors, thus achieving much smaller LOD. Contrarily, most integrated in-plane Fabry-Pérots use optical fibers to input and collect light in the plane of the microchip. This greatly reduces the space and represents a more integrated solution. Still, in-plane integrated Fabry-Pérot for RI sensing have been reported in a wide range of configurations. The simplest configuration consist of optical fibers alone [7, 142, 161] but suffers from small reflection coefficients, thus small Q factors. Larger reflection coefficient are achievable using internal FBG

[6, 162] or deposited multilayers [141]. However, optical fibers require precise alignment and call for complex integration if using a microfluidic channel smaller than the fiber radius. Fully integrated optical structures such as gold coated sidewalls [140], vertically etched silicon-air planar DBR [144] with integrated waveguides [148] or cylindrical DBR with focusing fiber rod before the cavity [145] or inside the cavity [163] are auto-aligned and can accommodate for smaller microfluidic channels. Two notable configurations reported in ref. [146] and [147] achieved smaller LOD than the other reported Fabry-Pérot devices. The first one utilizes two cascaded Fabry-Pérot cavities, one sensing cavity and one Fabry-Pérot etalon, to produce a Vernier effect. Using this technique, which can theoretically be reproduced for any of the devices mentioned above, the authors achieve a LOD of 8.4×10^{-7} RIU. The second one performs differential detection using a high surface quality out-of-plane Fabry-Pérot and further reduces the system noise using phase-lock detection. This setup can achieve an impressive LOD of 2.0×10^{-9} RIU. However, the added equipment heavily impacts the detection time, reaching 3 seconds, thus is not suited for high-throughput measurement.

2.3.3 Phase microscopy

Phase microscopy or quantitative phase microscopy (QPM) is a general term encompassing many different techniques such as tomographic phase microscopy (TPM), optical coherence microscopy (OCM), optical diffraction tomography (ODT), phase-shifting interferometry (PSI) or digital holographic microscopy (DHM). The variety of terms and definitions can become rapidly confusing. Nevertheless, all of these techniques use the same basic principle: phase shift measurement. In all cases, a single wavelength source, usually a laser, is divided into a reference beam and a probing beam, interacting with the sample. When recombined and projected onto a camera, these beams generate interference patterns. These interference patterns can either be recorded as phase (hologram) or as intensity, much like the Mach-Zehnder and Young interferometers presented above. The absolute phase shift of the probing beam from the reference for each pixel can be directly unwrapped from the hologram or computed from the intensity image using wave optics theory. However, intensity images may be affected by other intensity modulating effects and thus are less used to quantify the phase shift. Nonetheless, the phase shift is directly related to the optical path (refractive index $\times$ length), thus knowing the height or shape of the object under test is essential to decouple the absolute refractive index. While these techniques can be applied to homogeneous liquids, they are well suited for the measurement of an object, in particular a biological cell [10–13, 149–151]. Indeed, they advantageously provide small lateral resolution allowing refractive indices of sub-cellular entities to be measured. However, when probing an object, their LOD is considerably larger around 10^{-3} RIU.

CHAPTER 3 OPTICAL PROPERTIES OF IN-PLANE SILICON FABRY-PÉROT CAVITIES

This chapter describes the ideal and expected optical properties of in-plane silicon Fabry-Pérot cavities for which the reflective structures are distributed Bragg reflectors (DBRs). The imperfections of the microfabricated device induce losses which deviates the experimental properties from the ideal case. A previously published work detailed these sources of loss occurring in deep-etched multilayer optical resonators [164]. Using the recommended transfer matrix model, both ideal and expected optical properties can be simulated. Four sources of loss were considered in the published work:

1) Divergence of the optical beam
2) Surface roughness at the interfaces
3) Verticality of the DBRs layers
4) Misalignment of the input and output beams

In the present work, misalignment is eliminated since light is coupled using integrated rib waveguides. Similarly, losses induced by non-vertical DBR layers are neglected since the microfabricated devices achieve high verticality ($< 0.1°$). However, losses due to the divergence of the optical beam and the surface roughness are inherent to device and must be included. For the first source of loss, it is the dimensions of the rib waveguides required to have a single-mode like behavior which produce divergence. Details about rib waveguides dimensions and behavior are presented in Chapter 4. For the second source of loss, it is the microfabrication method used in this work, also detailed in Chapter 4, which produces surface roughness. In the following, surface roughness is included by adding lossy layers of 30 nm at each interface (measured surface RMS of 30 nm in ref. [164]). Simulated divergence and surface roughness may not be exactly matched experimentally. Still, the presented results serve as guidelines for the design of the Fabry-Pérot cavity.

3.1 Distributed Bragg reflectors

DBRs are periodic variation of dielectric materials, which are silicon and air in this work, in one dimension. Figure 3.1 illustrates an integrated DBR of 1.5 period structured on the top layer of a silicon-on-insulator (SOI) wafer, namely the device layer, for which incident and output light is guided in rib waveguides.

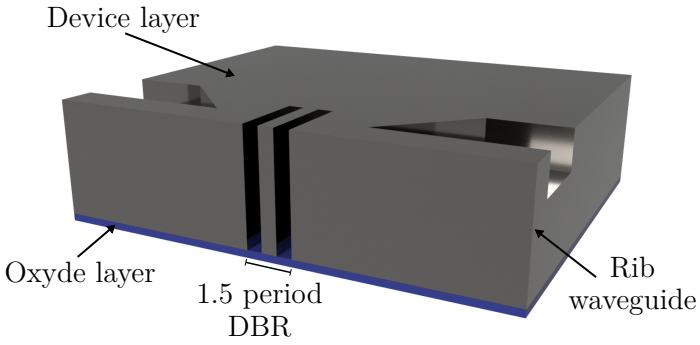

Figure 3.1 Scheme of a 1.5 period DBR on the top layer of an SOI. Light is input and output by rib waveguides. Structures are sliced at their center for better viewing.

For a DBR to achieve reflectivity at a given wavelength λ_0, the phase condition on each dielectric layer thickness is:

$$l_{air} = \frac{m_{air}\lambda_0}{4n_{air}} \qquad and \qquad l_{Si} = \frac{m_{Si}\lambda_0}{4n_{Si}} \tag{3.1}$$

where λ_0 is the wavelength in vacuum, l_{air} and l_{Si} are the thicknesses, m_{air} and m_{Si} are the odd integers and n_{air} and n_{Si} are the refractive indices of the air and silicon layers respectively.

Quantitatively, DBRs are characterized by their peak reflectivity and their reflection bandwidth. The reflectivity depends on the difference between the refractive indices of the dielectric materials as well as the number of periods. As such, an increase in either the refractive indices difference or the number of periods yields a higher reflectivity. The bandwidth is the spectral width over which the DBR achieves $> 0.5\ dB$ from peak reflectivity. Moreover, the bandwidth depends on the odd integers of each dielectric layer, m_{air} and m_{Si}. Smaller odd integers, hence smaller thicknesses, yield larger bandwidth.

For all presented simulations, the wavelength λ_0 is fixed to 1600 nm ($n_{air} = 1.0003$ and $n_{Si} = 3.4719$) and odd integers are fixed to $m_{air} = 5$ and $m_{Si} = 17$, corresponding to typical microfabricated layers of approximately 2 μm. The diameter of the guided mode was set to 15 μm which corresponds the SOI device layer thickness used throughout this work. Simulated spectra for DBRs of 1.5, 2.5 and 3.5 periods for the ideal and expected case are reported in Fig. 3.2a and 3.2b respectively. Calculated peak reflectivities, occurring at λ_0, and bandwidths are reported in Tab. 3.1.

From these simulation results, it is clear that the added losses lower the peak reflectivity as well as the bandwidth of DBRs. Contrarily, the number of periods has a limited effect on

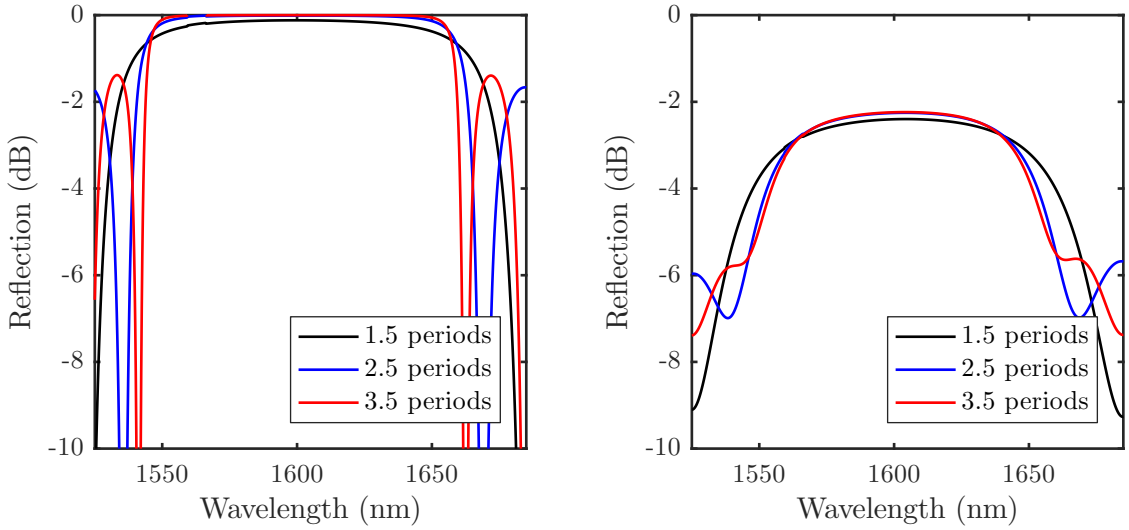

Figure 3.2 Simulated DBRs reflection spectra when varying the number of periods for (a) the ideal case and (b) the expected case.

Table 3.1 Comparison of ideal and expected reflectivity and bandwidth of DBRs depending on the number of periods.

Number of periods	**Peak reflectivity (%)**		**Bandwidth (nm)**	
	ideal	**expected**	**ideal**	**expected**
1.5	97.28	57.57	113	81
2.5	99.77	59.52	113	74
3.5	99.98	59.74	111	72

both the peak reflectivity and bandwidth. This is due to the large refractive index difference between silicon and air which yields high reflectivity even for a small number of periods. Thus, based only on DBR properties, attention should be directed towards reducing the sources of loss, such as the surface roughness, during microfabrication rather than the number of periods used for design.

3.2 Fabry-Pérot cavity

The fabricated Fabry-Pérot cavities consist of two DBRs facing one another across the width of a microfluidic channel. Figure 3.3 illustrates such a Fabry-Pérot cavity structured on the device layer of an SOI wafer. Light entering the cavity is trapped by successive reflections on each DBR. Higher DBR reflectivity leads to more round trips (N_{RT}), thus better confinement. For a fixed optical length (refractive index times the cavity length, $n_{cav}l_{cav}$), only particular

wavelengths will possess a phase allowing for constructive interference, namely the resonant modes. Out of phase wavelengths interact destructively leaving only the resonating phase-matched wavelengths to be transmitted.

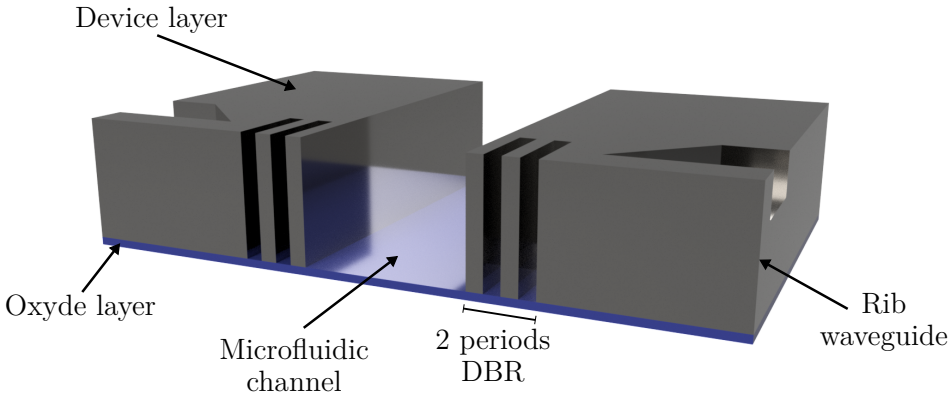

Figure 3.3 Scheme of a Fabry-Pérot consisting of 2 periods DBRS separated by a microfluidic channel on the top layer of an SOI. Light is input and output by rib waveguides. Structures are sliced at their center for better viewing.

For a Fabry-Pérot cavity to achieve resonance at λ_0, the phase condition on the cavity length is:

$$l_{cav} = \frac{m_{cav}\lambda_0}{2n_{cav}} \tag{3.2}$$

where l_{cav} is the Fabry-Pérot cavity length, m_{cav} is the cavity integer and n_{cav} is the refractive index of the cavity.

Fabry-Pérot cavities output distinctive spectra exhibiting repeated peaks of transmission inside the reflection bandwidth of the DBRs. The spectral distance between two consecutive peaks is the free spectral range (FSR) whereas the width of a peak is the full width at half maximum (FWHM). The equation describing the FSR of a Fabry-Pérot at normal incidence is:

$$\text{FSR} = \frac{\lambda_0^2}{2n_{cav}l_{cav} + \lambda_0} \approx \frac{\lambda_0^2}{2n_{cav}l_{cav}} = \frac{\lambda_0}{m_{cav}} \tag{3.3}$$

However, for the presented devices, the resonant mode extend into the DBRs which yields longer effective cavity lengths, thus a smaller effective free spectral range (FSR_{eff}). This extension effect is reduced for mirrors that are very thin compared to the cavity length and thus approach the theoretical value.

As mentioned in Chapter 2, most resonant cavities are quantitatively characterized by their Q factor. However, the finesse is a widely used parameter as well, especially for Fabry-Pérot cavities. These quantities are calculated from the spectrum as:

$$Q = \frac{\lambda_0}{\text{FWHM}} \qquad \text{and} \qquad \mathcal{F} = \frac{\text{FSR}}{\text{FWHM}} \tag{3.4}$$

The finesse $\mathcal{F}$ is related to the Q factor such that:

$$\mathcal{F} = Q \times \frac{\text{FSR}}{\lambda_0} \approx \frac{Q}{m_{cav}} \tag{3.5}$$

There is an important difference between the quality factor Q and the finesse $\mathcal{F}$. Indeed, contrarily to the Q factor, the theoretical finesse does not depend on the cavity length but only on the reflectivity.

$$\mathcal{F} \approx \frac{\pi\sqrt{R}}{1-R} \tag{3.6}$$

This means that a longer cavity, which is associated to a smaller FWHM, yields a higher Q factor, a reduced dynamic range (FSR) and thus a constant finesse. Since the quality factor only relies on the FWHM, it essentially represents how well the spectral peak can be resolved. Contrarily, the finesse represents how well the range between peaks can be resolved.

To evaluate the impact of loss and number of periods on our Fabry-Pérot cavities, simulated spectra for the ideal and expected cases are reported in Fig. 3.4a and 3.4b respectively. The cavity integer was set to $m_{cav} = 50$ and the refractive index of the cavity to the one of water $n_{cav} = 1.3142$. These values are chosen considering a cell sensing application and correspond to a cavity length of approximately 30 μm. Table 3.2 reports the corresponding calculated losses, FWHM, FSR, Q factor and finesse $\mathcal{F}$ at the central resonance.

From these simulation results, it is clear that the added losses lower the resonance peak transmission and enlarge the FWHM, thus yielding drastically smaller Q factors and finesse. The slight FSR reduction, when including sources of loss, is only due to the additional thin lossy layers. Moreover, the theoretical FSR is $FSR = 31.4\ nm$ whereas the simulated one is around $FSR_{eff} = 27.0\ nm$. This corresponds to an extension of the resonant mode into each DBR of approximately 2.5 μm.

Interestingly, the large increase of Q factor and finesse related to the increase in number of periods reported for the ideal case does not apply to the expected case. Indeed, more than 2 periods only further increase the loss of the resonance peak while the other quantities remain

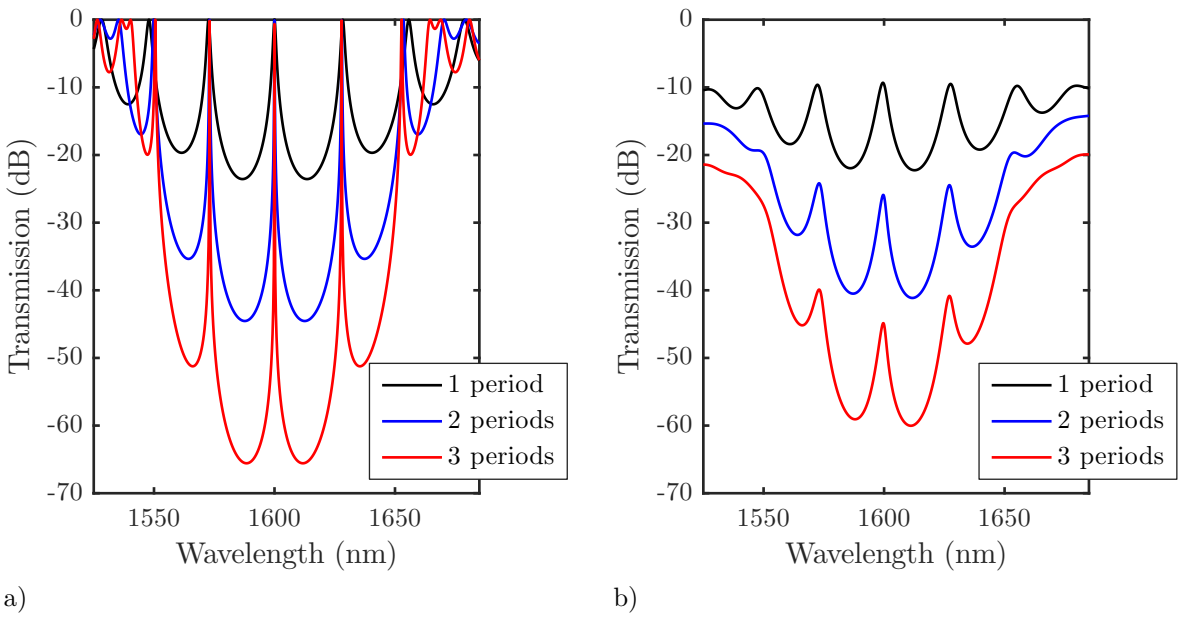

Figure 3.4 Simulated Fabry-Pérot cavities transmission spectra when varying the number of periods for (a) the ideal case and (b) the expected case.

mostly the same. The $\sim 30\%$ reduction of the FWHM from 1 to 2 periods yields a slightly higher finesse of 9, better suited for RI sensing. Thus, the presented devices in the following chapters are 2 periods DBRs. These Fabry-Pérot cavities have a very small number of round trips N_{RT} of 1.4 ($\mathcal{F} = 2\pi N_{RT}$, where N_{RT} is the number of round trips after which $\sim 60\%$ $(1 - e^{-1})$ of the circulating power has left the cavity).

Table 3.2 Comparison of ideal (a) and expected (b) Fabry-Pérot cavities properties at λ_0 calculated from Fig. 3.4a and 3.4b.

Periods	**Loss (dB)**		**FWHM (nm)**		**FSR (nm)**		**Q**		$\mathcal{F}$	
	a	**b**	**a**	**b**	**a**	**b**	**a**	**b**	**a**	**b**
1	0	9.3	1.13	4.31	27.4	27.2	1.4×10^3	3.7×10^2	24	6
2	0	25.9	0.09	3.1	27.0	26.7	1.7×10^4	5.2×10^2	2.9×10^2	9
3	0	44.9	0.008	3.0	26.9	26.7	2.1×10^5	5.4×10^2	3.5×10^3	9

As mentioned in Chapter 2, RI sensors must maximize both the accuracy and the sensitivity to yield better limit of detection (LOD). The theoretical sensitivity is defined as the displacement of the resonance peak ($\Delta\lambda$) in function of the RI variation (Δn). For very thin mirrors compared to the cavity length, the relative displacement of the resonance peak ($\Delta\lambda/\lambda_0$) is

equal to the relative RI variation in the cavity ($\Delta n/n_{cav}$). Combining these relations yields the maximal theoretical sensitivity:

$$\frac{\Delta\lambda}{\lambda_0} = \frac{\Delta n}{n_{cav}} \quad \rightarrow \quad S_{theo} = \frac{\Delta\lambda}{\Delta n} = \frac{\lambda_0}{n_{cav}} \tag{3.7}$$

For our considered sensor operating at 1600 nm in water ($n_{H_2O} \sim 1.3$), the maximum achievable sensitivity is approximately 1200 nm/RIU. The calculated sensitivities for the ideal and expected case are 1057 and 1040 nm/RIU respectively. This is because a fraction of the resonant mode lies inside the DBR and thus cannot sense the cavity variation. Subsequently, the expected sensitivity is a fraction of the theoretical sensitivity such that:

$$S_{exp} = \frac{\Delta\lambda}{\Delta n} = \frac{\lambda_0}{n_{cav}} \frac{\mathrm{FSR}_{eff}}{\mathrm{FSR}_{theo}} \tag{3.8}$$

Considering an experimentally measured accuracy of $3\sigma = 0.015$ nm, the corresponding LODs ($LOD = accuracy/sensitivity$) are 1.25×10^{-5} for the theoretical case and approximately 1.4×10^{-5} for both the simulated ideal and expected cases.

Optical properties of a microfabricated Fabry-Pérot cavity ($l_{air} = l_{Si} = 1.7\ \mu m$ and $l_{cav} = 40\ \mu m$) in oil ($n_{oil} = 1.412$) reported in Chapter 5 are summarized in Tab. 3.3 and compared to the theoretical and expected values. Based on this comparison, the only way to achieve better LOD is to obtain better accuracy. This implies reducing the surface roughness below 10 nm to insure more defined resonance peaks. However, this is not currently possible using the proposed microfabrication process.

Table 3.3 Experimental optical properties of a microfabricated Fabry-Perot cavity ($l_{air} = l_{Si} = 1.7\ \mu m$ and $l_{cav} = 40\ \mu m$) in oil ($n_{oil} = 1.412$) reproduced from Chapter 5. Theoretical and expected values are also reported for comparison.

	FSR (nm)	**Sensitivity (nm/RIU)**	**LOD (RIU)**
Experimental	21.2	965	1.6×10^{-5}
Theoretical†	22.5	1143	1.3×10^{-5}
Expected*	19.0	964	1.6×10^{-5}

† Theoretical FSR and Sensitivity are calculated using Eq. 3.3 and 3.7 respectively.

* Expected FSR and sensitivity are calculated using a simulated spectrum and Eq. 3.8 respectively.

3.3 Fabry-Pérot cavity for cell sensing

Lastly, for a high-throughput cellular sensing application, measuring part of the spectrum to identify the peak shift is not realistic due to the very short period of time the cells reside in the cavity. Thus, the proposed experimental setup is based on a power variation measurement in time for which detectors have very short response time (< 1 ns). In this section, the ideal as well as the expected sensitivity and LOD using a power measurement scheme are detailed.

When a cell flows through the cavity, the peak is shifted towards longer wavelength. Thus the two possible power measurement setups are either to lock the sampling wavelength on the longer-wavelength slope of the resonance or at the peak position. In the first case, passage of a cell yields an increase of power whereas in the second case a decrease of power. However, the presence of a cell produces additional sources of loss such as absorption and scattering. These supplementary losses have been found to sufficiently affect the measurement such that very small power variations (if any) were experimentally recorded. Thus, the adopted strategy is to lock the sampling wavelength at the peak position of the resonance and measure the decrease in power generated by cells. Figure 3.5 compares the simulated ideal and expected power variation, sensitivity and LOD in function of RI variation for the same previous 2 periods DBR Fabry-Pérot cavity. LODs are obtained considering an experimentally measured accuracy of $3\sigma = 0.1\ dB$.

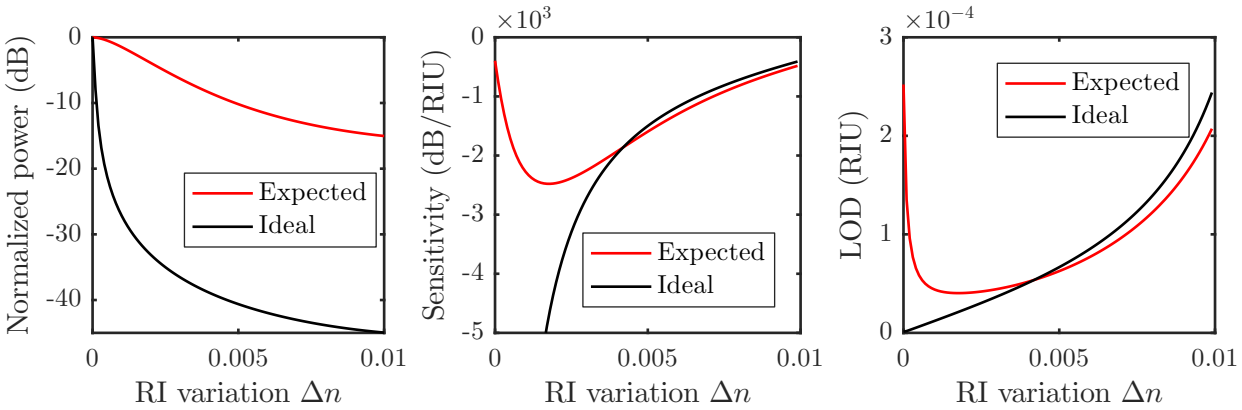

Figure 3.5 Simulated ideal and expected (a) normalized power variation, (b) sensitivity and (c) LOD of a 2 periods Fabry-Pérot cavity ($m_{air} = 5$, $m_{Si} = 17$ and $m_{cav} = 50$) in function of RI variation (Δn).

Differently from the previous method, the normalized power does not have a linear dependency to the RI variation (Fig. 3.5a). This yields sensitivities and LOD which depend on the RI variation as well, as shown in Fig. 3.5b and 3.5c respectively. Interestingly, the

ideal simulated case achieves better sensitivity and LOD only for RI variation smaller than $\sim 4 \times 10^{-3}$ RIU.

The question now is: what is the RI variation induced by the presence of a cell. For a given cell, it depends on its relative volume in the cavity. If the cell is small compared to the cavity, then the RI variation induced by the cell is also small. Intuitively, the length of the cavity should then be the one for which the RI variation caused by the cell optimizes the LOD ($\Delta n \sim 2 \times 10^{-3} RIU$ in Fig. 3.5c). However, as mentioned above, longer cavities have smaller FWHM which changes all the curves presented in Fig. 3.5 such that the minimal LOD is shifted towards smaller RI variation. To better understand this issue, the RI variation produced by a cell centered in the cavity was first computed in function of the cavity length (l_{cav}). The simulation model used to determine cellular RI variation is presented in Chapter 6. Then, the normalized power, sensitivity and LOD curves for each cavity length was computed. Lastly, for each cavity length, the sensitivity and LOD corresponding to the computed cellular RI variation was identified. Figures 3.6a and 3.6b report these sensitivity and LOD in function of the cavity length l_{cav}. RI variations were calculated using the typical HL-60 cell presented in Chapter 6.

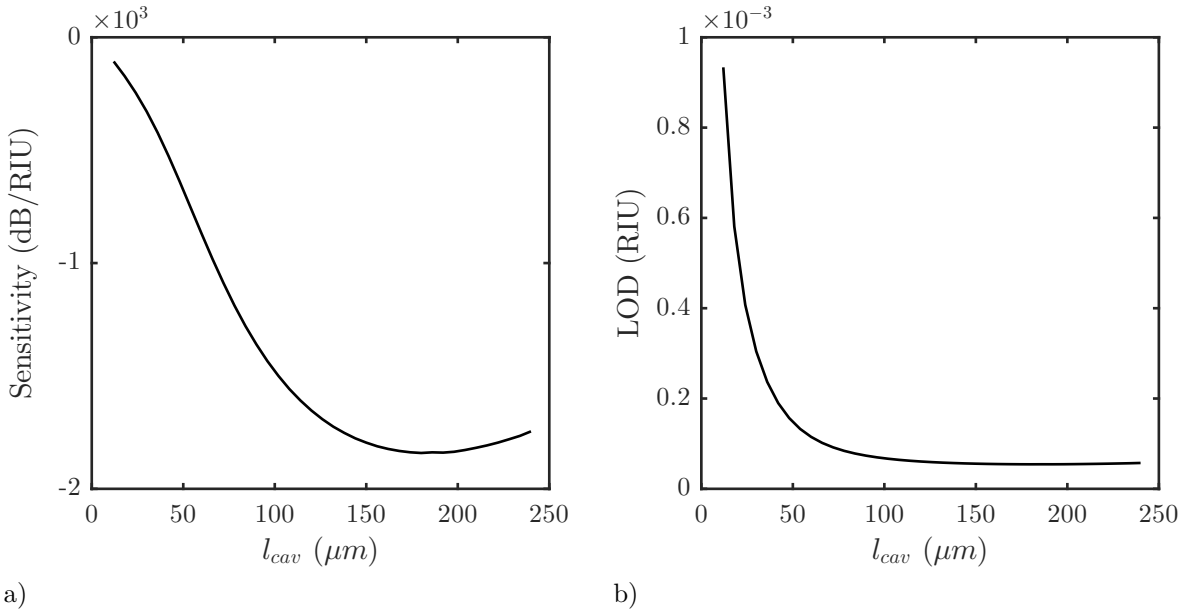

Figure 3.6 Computed (a) sensitivity and (b) LOD in function of the cavity length for a typical HL-60 cell. RI variations were computed using the simulation model presented in Chapter 6.

The optimized sensitivity and LOD (5.5×10^{-5} RIU) are reached for a cavity length of 185 μm. This implies that the proposed power measurement setup cannot achieve a LOD as small as a the spectral setup (1.2×10^{-5} RIU). Still, the LOD lies below 10^{-3} RIU for any cavity

length which is appropriate for cellular populations discrimination. Furthermore, for cavity lengths longer than $\sim 50\ \mu m$ the gain on the achievable LOD is not substantial and may complexify the microfluidics operation. At last, these results were simulated using a typical cellular model which may not occur in practice. Indeed, smaller or less refractive cells will yield smaller refractive index variation thus potentially better LOD whereas larger or more refractive cells do the opposite. Moreover, the simulated power on which the LOD relies do not include the absorption and scattering losses induced by the cell. Still these results allow to gain an understanding on the working principle and portray the dynamic range of the sensor. Table 3.4 summarizes the range of values of the in-plane silicon Fabry-Pérot cavities properties reported throughout this thesis.

Table 3.4 Range of values of the in-plane silicon Fabry-Pérot cavities properties.

Parameter	**Range**	**Parameter**	**Range**
$\mathcal{F}$	$4.8 - 6.4$	m_{Si}	$13 - 22$
FSR	$21.2 - 21.55\ nm$	n_{air}	1.0003
$FWHM$	$3.3 - 4.5\ nm$	n_{cav}	$1.0003 - 1.418$
H	$15\ \mu m$	n_{Si}	3.4719
l_{air}	$1.5 - 2.5\ \mu m$	N_{RT}	$0.75 - 1$
l_{cav}	$30 - 40\ \mu m$	Q	$3 - 4 \times 10^{-2}$
l_{Si}	$1.5 - 2.5\ \mu m$	R	$53 - 62\%$
LOD_{power}	$4.1 - 6.7 \times 10^{-5}$	S_{power}	$1500 - 2435\ dB/RIU$
$LOD_{spectral}$	$1.2 - 1.6 \times 10^{-5}$	$S_{spectral}$	$930 - 1278\ nm/RIU$
m_{air}	$4 - 6$	$3\sigma_{power}$	$0.1\ dB$
m_{cav}	$44 - 62$	$3\sigma_{spectral}$	$0.015\ nm$

On a final thought, the presence of a cell may hinder the resonance stability of the cavity. To establish the stability conditions of the system, the ones which maintain geometrical rays inside the cavity, the transfer matrix of the optical cavity is used. The general condition for stability is:

$$-1 \leq \frac{Trace(M)}{2} \leq 1 \tag{3.9}$$

where M is the transfer matrix of the entire system for one round trip. Using the schematize system in Fig. 3.7a, the stable and unstable regions were determined for three crucial variables: the cavity length to cell radius ratio (l_{cav}/R_{cell}), the relative position of the cell in the cavity ($d/(l_{cav} - 2R_{cell})$) and the nucleus to cell radius ratio (R_{nuc}/R_{cell}). Figure 3.7b and 3.7c show the stable and unstable regions for these variables. It is interesting to note that for $l_{cav}/R_{cell} <\sim 50$ any relative position of the cell yields a stable cavity (Fig. 3.7b).

This result is especially important since the inertially focused cells presented in the following chapters may not always be in the center of the cavity. An equally important result is that for $R_{nuc}/R_{cell} <\sim 0.8$, corresponding to a volume ratio of approximately 50%, no stability is observed. Fortunately, most cells have a nucleus large enough to fit this criteria, including the HL-60 myeloid cells measured in this thesis which usually present a ratio R_{nuc}/R_{cell} around 0.9.

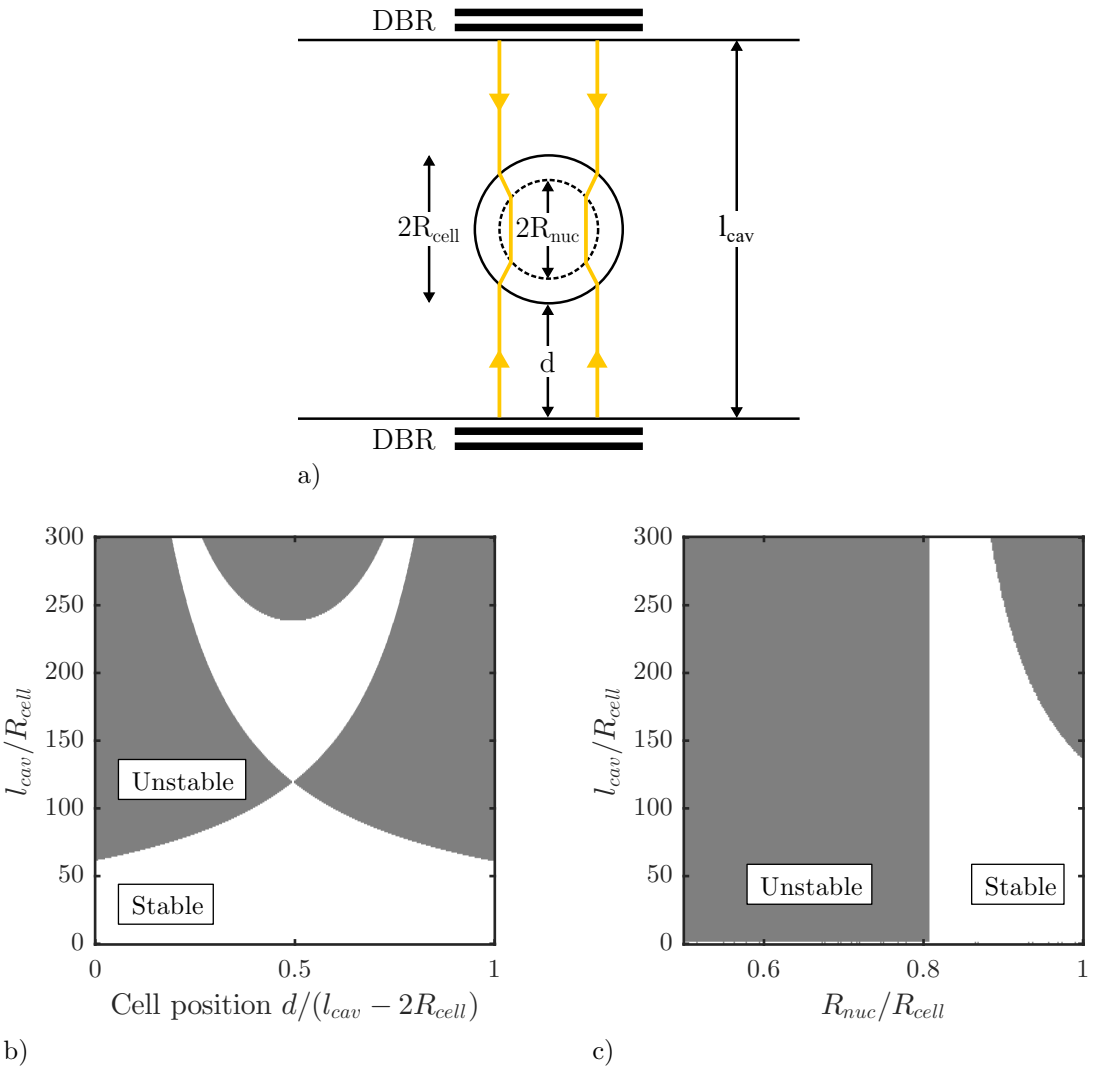

Figure 3.7 Stable (white areas) and unstable (gray areas) conditions in function of the cavity length to cell radius ratio (l_{cav}/R_{cell}) and the relative position of the cell along the cavity (0.5 is at the center of the cavity).

CHAPTER 4 ARTICLE 1 - THE IMPORTANCE OF SINGLE-MODE BEHAVIOR IN SILICON-ON-INSULATOR RIB WAVEGUIDES WITH VERY LARGE CROSS SECTION FOR RESONANT SENSING APPLICATIONS

This chapter presents simulations and experimental results highlighting the importance of single-mode propagation in rib waveguides for resonant sensing applications. Sections 4.1–4.8 are a reproduction of an article published in the IEEE Journal of Selected Topics in Quantum Electronics.[1] For very large cross-section silicon rib waveguides, satisfying the previously established design rules by Soref et al. and Pogossian et al. does not guarantee single-mode operation. The presented in-depth modal analysis reveals which rib dimensions attenuate higher order modes propagation sufficiently to provide the sought single-mode behavior. Subsequently, this modal analysis is applied for the design of cell sensing devices, described in the following chapters. Predicted conditions for single-mode like behavior are experimentally confirmed using a series of fabricated devices for which the complete microfabrication process is detailed. Some terms have been replaced to consistently preserve the definitions presented in the previous chapters.

Section 4.9 presents unpublished results and discussion on rib waveguide modal analysis and Fabry-Pérot cavity. Specifically, the contribution of odd higher order modes yields an alternative combined attenuation map employed in Chapters 5 and 6. Also, amendments and explanations regarding the reported Fabry-Pérot sensitivity and LOD provide a more rigorous characterization.

4.1 Authors and affiliations

A. Leblanc-Hotte,[a] J.-S. Delisle,[b] S. Lesage,[c] and Y.-A. Peter [a]

[a] *Department of Engineering Physics, École Polytechnique de Montréal, Montreal, QC H3T 1J4, Canada.*

[b] *Division of Hematology-oncology, Department of medicine, Centre de recherche de l'Hôpital Maisonneuve-Rosemont, Université de Montréal, Montreal, QC H1T 2M4, Canada.*

[c] *Department of Microbiologie, Infectiologie et Immunologie, Centre de recherche de l'Hôpital Maisonneuve-Rosemont, Université de Montréal, Montreal, QC H1T 2M4, Canada.*

4.2 Abstract

Control of light properties through propagation in large cross-section optical rib waveguides is of utmost importance to obtain the desired behavior, especially with resonant cavities. We have simulated, fabricated and experimentally tested optical rib waveguides to evaluate the advantages of single-mode properties against multimode. Modal analysis of very large cross-section rib waveguides showed that only particular dimensions allow a single-mode behavior. Furthermore, on-chip Fabry-Perot cavities were coupled to rib waveguides to assess impacts for a typical resonator. Experimental results are in good agreement with simulation guidelines, effectively highlighting the importance of single-mode behavior for resonant sensing applications.

Index Terms – Microphotonics, Rib Waveguide, Sensing, Single-Mode.

4.3 Introduction

Microphotonics technologies find numerous applications in the biomedical and chemical fields. A growing number of devices using on-chip integrated microphotonic structures are being designed as tools to facilitate the work of specialists in biology and medicine. These structures can use evanescent waves of an optical waveguide as a sensor [109], arrayed waveguide grating for multiplexed sensing [167] or even take advantage of optical resonant cavities for enhanced photon life time [168]. Integrated sensors combining microfluidics and microphotonics commonly use waveguides to bring light from optical fibers to the on-chip sensing structure. Control over light properties through waveguide propagation is of utmost importance to obtain the desired behavior, especially with resonant cavities. As an example, previous work reported a microfabricated optical waveguide coupled to a Fabry-Perot resonant cavity for single cell sensing with abnormally high losses [169]. This device employed a resonant spectroscopic measurement which exploits small differences in cells refractive index. This measurement can improve the discriminative resolution of medical devices used for diagnosis, such as flow cytometers, for more reliable cellular identification. It could also permit the identification of new cellular parameters or even novel cell types.

Large particle analysis, as in [169] with cells of approximately 10-12 μm in diameter, requires waveguides of at least a few micrometers in height. However, on-chip rib waveguides made out of silicon exhibit large refractive index difference with its cladding (air). Consequently, waveguides with large dimensions and high core-cladding refractive index difference theoretically support multiple optical modes. In this paper, we suggest that single-mode rib waveguides yield optical properties better suited for resonating sensors spectroscopy. Indeed,

propagation of two or more modes in a waveguide with close modal refractive index generates a beating effect. Thus, modal power distribution at a fixed length is different for each wavelength, which renders a non-uniform spectrum and hides resonance peaks in its background. Moreover, since the optical path in a coupled cavity changes with the presence of a particle, the whole beating pattern also changes making very hard deducing the resonator response. Finally, the intensity measurement based on peak shifting reported in [169] is better suited for a smooth slope of the resonance. Even if multimode resonances occur at the same wavelength for a Fabry-Perot, the total peak profile is composed of multiple resonances each possessing a different height, full width at half maximum (FWHM) and slope. This yields a final peak shape and resonance sensitivity not suitable for practical measurements.

It has been shown previously first by Soref [165] and then by Pogossian [166] that rib waveguides on silicon-on-insulator (SOI) with a cross-section of a couple micrometers (around 4 μm $\times$ 4 μm) can be effectively defined as single-mode. In these particular cases, interpretation of the single-mode behavior for an optical rib waveguide must be carefully defined. In theory, these waveguides support more than one mode, making them multimode by definition. However, after one or two millimeters of propagation only the fundamental mode remains because losses for higher order modes are superior. This phenomenon makes these studied optical rib waveguides practically single-mode for experimentations. Then, Lousteau [170] showed that for slightly higher rib waveguides (around 7.5 μm) single-mode behavior is not as simple as following the established design rules by Soref and Pogossian. Therefore, precaution must be taken when working with large cross-section optical rib waveguides. We have tested this theory and evaluated the advantages of single-mode properties against multimode for resonators. We have simulated, fabricated and experimentally tested isolated rib waveguides as well as coupled to a typical resonating cavity: an integrated in-plane Fabry-Perot. This paper reports simulation, fabrication and optical characterization of very large cross-section optical rib waveguides on SOI for resonant sensing applications.

4.4 Rib Waveguide Modal Analysis

This section describes the technique used for modal analysis of the rib waveguides and reports the results obtained for different dimensions. The cross-section dimensions of the rib waveguide are defined in Fig. 4.1

where W is the width of the rib, H is the total height of the rib and h is the height of the surrounding slab. Refractive indices for air, silicon, and silicon dioxide (SiO_2) are represented by the common variable n and their respective subscript. In this design, air is the top cladding, silicon dioxide is the bottom cladding and silicon is the core of the rib waveguide.

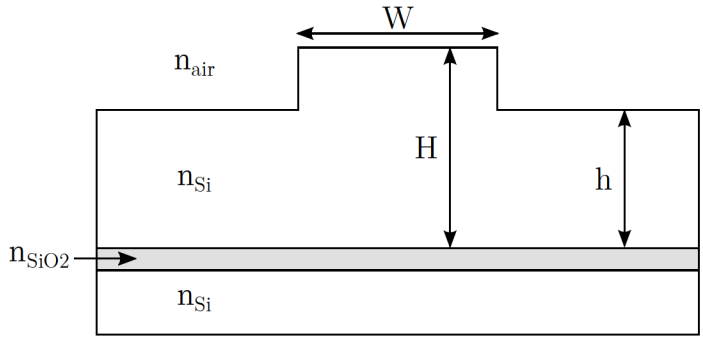

Figure 4.1 Rib waveguide on SOI cross-section dimensions and variables used for modal analysis.

Equations (4.1) and (4.2) are the proposed formulas for design purposes established by Soref [165] and later corrected by Pogossian [166]. These equations need to be jointly satisfied in order to have a single-mode behavior of the rib waveguide.

$$\frac{h}{H} \geq 0.5 \tag{4.1}$$

$$\frac{W}{H} \leq \alpha + \frac{h/H}{\sqrt{1-(h/H)^2}} \tag{4.2}$$

where $\alpha = 0.3$ for Soref's formulation and $\alpha = 0$ with Pogossian's correction. The variables h/H and W/H are introduced for uniformity with other published work [165, 166, 170].

Performed simulations are based on the technique used by Lousteau [170]. We used a standard finite difference (FD) method to design the waveguide geometry and a direct matrix mode solver with perfectly matched layers (PMLs) as boundary conditions. This method outputs the complex refractive index of the supported modes and the imaginary part was used to calculate the modes respective attenuation coefficient. We follow Lousteau's notation for rib waveguide modes: HE_{nm} and EH_{nm}. Where HE modes are horizontally polarized (quasi-transverse-electric (TE)) and EH modes are vertically polarized (quasi-transverse-magnetic (TM)). For compactness, we only discuss horizontally polarized modes, HE, without loss of generality. Modes with pure vertical symmetry are represented with $m = 0$ whereas modes with $n = 0$ have pure horizontal symmetry. Also, we have voluntarily disregarded horizontally symmetric modes, HE_{0m}, assuming that they couple into the slab and do not propagate [170]. Furthermore, modes with an odd integer n were disregarded considering simulation results. These modes never reach an attenuation coefficient low enough to add meaningful information to the final attenuation map. Finally, we have stopped our investigation to the HE_{40} mode since higher order modes are considerably affected by the surface roughness in

the propagation direction and do not have enough power coupled into them. This study evaluates single-mode advantages for resonant sensing application over multimode and is not intended to be an exhaustive modal analysis of optical rib waveguides. Therefore modes order higher than HE_{40} would not be meaningful in this case.

In this work, the value of H was fixed to 15 μm considering a biomedical sensing application and typical cells diameter. Values of h/H ranged from 0.5 to 1 whereas values of W/H ranged from 0.25 to 1.33. Operating wavelengths were chosen to be $\lambda_1 = 1.50$ μm, $\lambda_2 = 1.575$ μm, and $\lambda_3 = 1.65$ μm covering a large part of the near infrared (NIR) transparent region for silicon. The losses recorded for HE_{20} and HE_{40} modes were then computed and reported in an attenuation coefficient map. Fig. 4.2 reports the lowest attenuation coefficients recorded, out of the three simulated wavelengths, in function of the h/H and W/H ratios for a) the HE_{20} mode, b) the HE_{40} mode, and c) both modes combined. Dark regions in these maps represent high attenuation of the corresponding optical modes over the three wavelengths. Thus, for combined HE_{20} and HE_{40} modes, black regions highlight geometries for which the fundamental mode should be dominant (Fig. 4.2c). As references, Soref's and Pogossian's boundary condition are also plotted onto these graphics, single-mode behavior is expected below the boundary condition.

Accordingly with Lousteau's conclusion, simulation results of Fig. 4.2c tends to advise that *"satisfying the design formulas* (4.1) *and* (4.2) *is not in itself sufficient to ensure effective single-mode operation"* [170]. To further test this theory, we fabricated on-chip stand-alone rib waveguides to assess the predicted behaviors. Additionally, rib waveguides coupled to an integrated in-plane Fabry-Perot cavity were simultaneously fabricated to evaluate the effect in a resonant cavity. Since all structures are microfabricated in a single process, the slab height h is the same for all rib waveguides, thus only the width W was varied. Chosen geometries are represented by black (or white for better contrast) dots in Fig. 4.2c. These four geometries are correlated to: one multimode rib waveguide according to Pogossian's formula and to our simulation (top dot with $W \geq H$), one multimode rib waveguide according to our simulation but single-mode in Pogossian's theory (second dot from top with $W = H$) and two rib waveguides less multimode, *i.e.* with potential single-mode like behavior, according to our simulations and single-mode according to Pogossian (third from top with $W = H/2$ and bottom dot with $W = H/3$).

4.5 Microfabrication

A SOI wafer with a 600 μm handle, 0.5 μm oxide layer, and 15 μm silicon top layer was employed. Final devices are achieved in a two-phase production which both includes standard

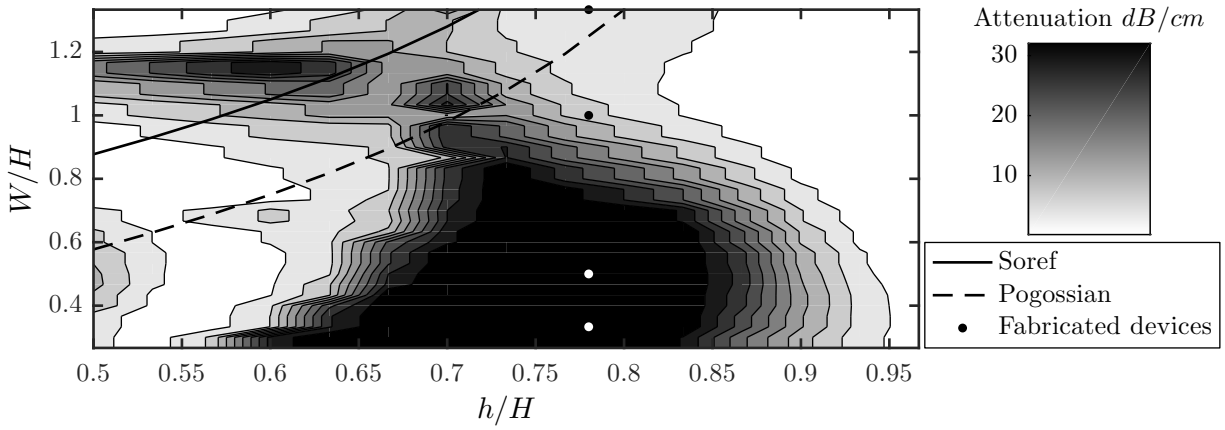

a)

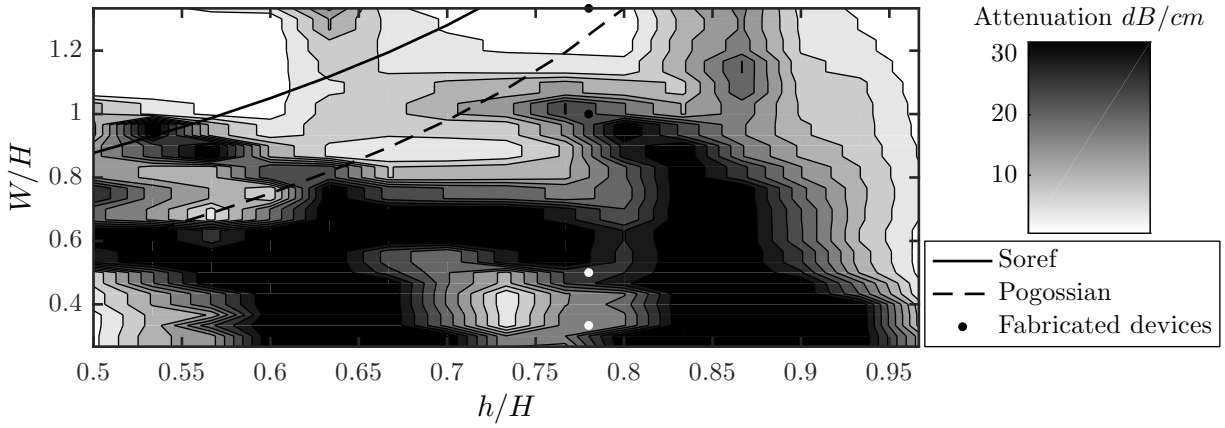

b)

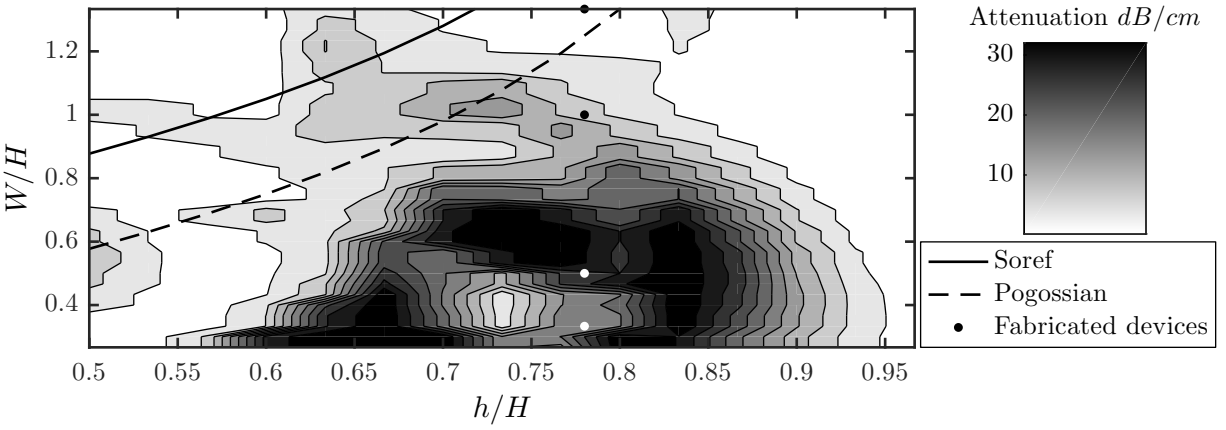

c)

Figure 4.2 Lowest attenuation coefficient recorded for (a) HE_{20} mode, (b) HE_{40} mode, and (c) combined HE_{20} and HE_{40} at all simulated operating wavelengths in function of ratios h/H and W/H. Plain line corresponds to Soref's single-mode boundary whereas the dashed line is associated to Pogossian's correction.

photolithography and deep reactive ion etching (DRIE). In the first microfabrication phase, Fabry-Perot cavities are photolithographically defined and etched down to the buried oxide layer using a DRIE-BOSCH process with alternating SF_6 and C_4F_8 plasmas. These Fabry-Perot cavities are composed of two distributed Bragg reflectors (DBRs) facing one another and separated by a microfluidic channel acting as the cavity gap. Design and microfabrication of the DBRs was based on previously published work [164]. In the second phase, rib waveguides are photolithographically defined and etched with the same DRIE-BOSCH process but at a lower depth to achieve the rib geometry. The SOI wafer is subsequently cut into separate chips using a dicing saw (ADT, Provectus 7100) and an engineered resin/diamond blade yielding diced facets of optical quality. Roughness measurement on these facets reported a mean value of 5.5 nm which provides low scattering losses for coupling. Then, the separated devices are cleaned in a piranha solution (H_2SO_4 + H_2O_2) followed by a final decontamination in oxygen plasma. Fig. 4.3 shows scanning electron microscopy (SEM) images of a microfabricated rib waveguide facet geometry and a Fabry-Perot cavity structure. Measurements reported a value of $h = 11.7$ μm for all waveguides, widths of 5 μm, 7.5 μm, 15 μm, and 20 μm (all within $\pm$250 nm) and waveguides length of 7.5 mm.

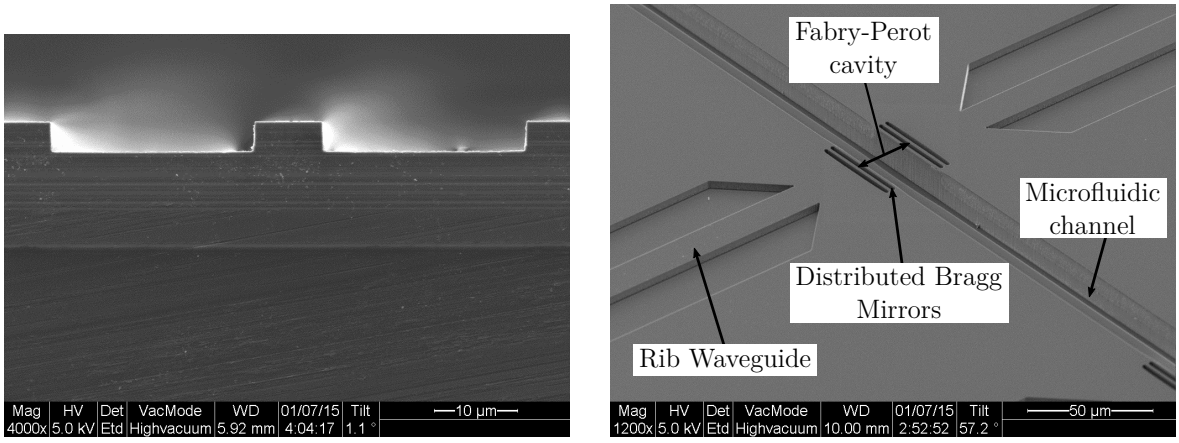

a) b)

Figure 4.3 SEM images of a microfabricated device showing (a) rib waveguide facet geometry and (b) structure of a rib waveguide coupled to a Fabry-Perot cavity composed of two DBRs.

4.6 Experimental Setup

In this study, two different experimental setups were used: one to analyze the output NIR mode profile of the rib waveguide and another to analyze the spectral response from the photonic structure. In both cases, stand-alone and Fabry-Perot cavity coupled rib waveguides

were experimentally tested. The NIR mode profile analysis setup uses a wide band laser source (Newport, BBS-430) with a standard SMF-28 fiber output butt coupled into the rib waveguide inlet facet. At the output facet, a mirror is set at angle of 45 ° from the horizontal axis to reflect NIR light to an InGaAs camera (VDS Vosskühler GmbH, NIR-610PGE) through an objective lens. Camera exposure time was set to allow small features of the mode profile to be spatially defined. The spectral analysis setup uses the same wide band laser source jointly with standard SMF-28 optical fibers butt coupled in and out of the rib waveguide. This setup difference resides in the fact that an optical spectrum analyzer (Hewlett Packard, 86142A) collects the NIR light and records the differential spectrum (raw spectrum normalized with the reference signal) on a log scale in dB units.

4.7 Results and Discussion

NIR mode profile analyses as well as spectral analyses for the four fabricated stand-alone rib waveguides geometries are reported in the first subsection. In addition, both analyses are presented for these selected rib waveguides coupled to a Fabry-Perot cavity in the second subsection. The last subsection reports Fabry-Perot resonance properties for single-mode like rib waveguide.

4.7.1 Stand-alone rib waveguide

NIR mode profile

Fig. 4.4 shows the different output NIR mode profiles, after a propagation of 7.5 mm, in their respective stand-alone rib waveguide geometry. Features of the output NIR mode profile images of Fig. 4.4a, 4.4b, 4.4c, and 4.4d show that rib waveguides widths of 20 μm, 15 μm, 7.5 μm, and 5 μm respectively, present a higher order optical mode at the end facet. In all cases, the captured mode profile is similar to the one of a HE_{40} mode. It is important to point out that exposure time of the infrared camera was lowered until small features of higher order optical modes could be seen even if multiple modes are simultaneously present, including the fundamental one.

Spectral analysis

Fig. 4.5 shows the output spectra of the different stand-alone rib waveguide widths. These spectra show arbitrary variation of intensity in function of wavelength. The amplitude of these variations for Fig. 4.5a and 4.5b is estimated to be around 13 dB whereas for Fig. 4.5c

and 4.5d it is estimated to 3.5 dB.

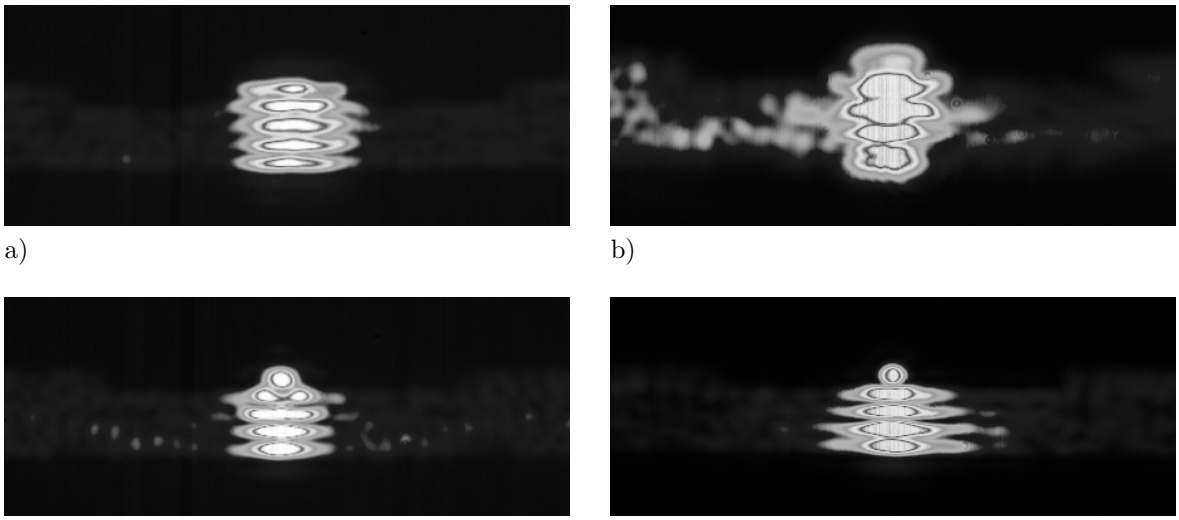

a) b)

c) d)

Figure 4.4 NIR images of the output mode for stand-alone optical rib waveguides showing presence of higher order mode profile for widths of (a) 20 μm, (b) 15 μm, (c) 7.5 μm, and (d) 5 μm respectively.

For multimode rib waveguides, a beating effect between propagating modes is expected. Since the characteristic beating length is dependent on the propagating wavelength, a fixed length waveguide will output more or less power in the fundamental mode. Because the output light is butt coupled into a single-mode optical fiber, most collected light power will come from the fundamental mode. Thus, recorded intensity in function of wavelength for highly multimode rib waveguides are expected to show more variation than practical single-mode waveguides. In the cases of rib waveguides width of 7.5 μm and 5 μm, spectral measurements exhibits less variation, associated to single-mode like behavior, whereas NIR mode profile images show a higher order profile. These geometries correspond to greater losses than other fabricated waveguides for both simulated HE_{20} and HE_{40} modes as shown in Fig. 4.2c. Thus, even if higher order mode features can be seen in the NIR mode profile image, most of the power remains in the fundamental mode for all recorded wavelengths. Based on results from Fig. 4.4 and Fig. 4.5 rib waveguides with widths of 20 μm and 15 μm are practically multimode whereas rib waveguides of widths 7.5 μm and 5 μm can be considered as practically single-mode.

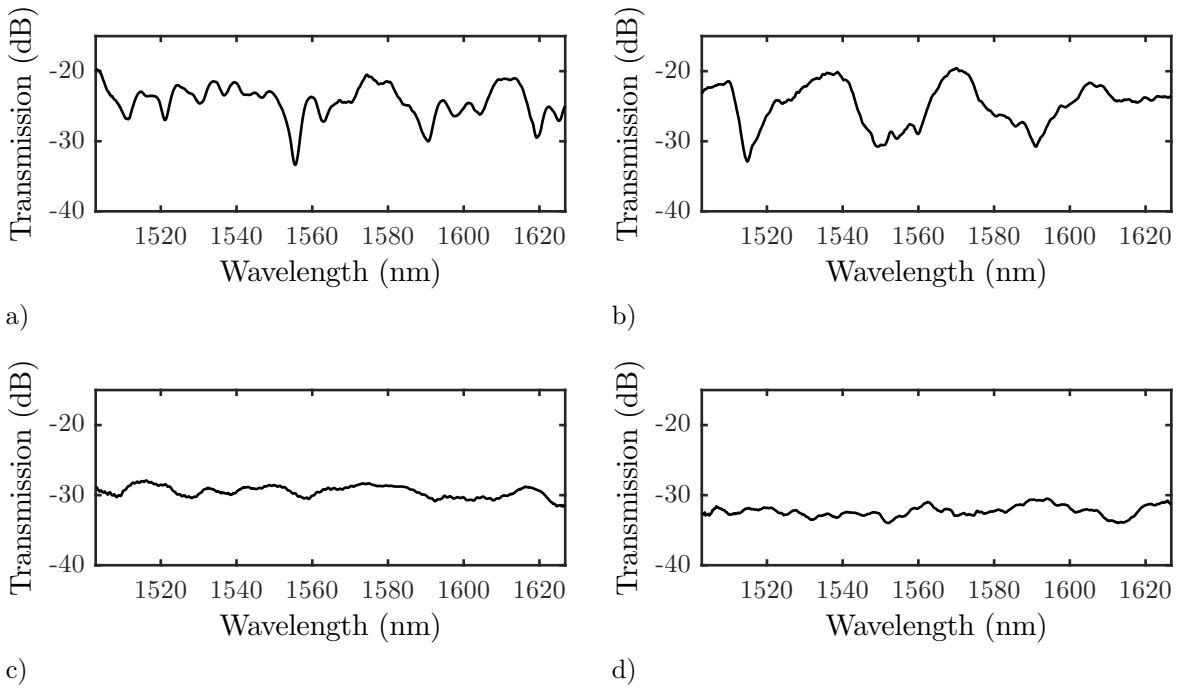

Figure 4.5 Output spectra for stand-alone optical rib waveguides showing intensity variation for widths of (a) 20 μm and (b) 15 μm whereas widths of (c) 7.5 μm and (d) 5 μm exhibits lower fluctuations.

4.7.2 Rib Waveguide coupled to a Fabry-Perot cavity

NIR mode profile

Fig. 4.6 shows the NIR output mode profiles for Fabry-Perot cavity coupled rib waveguides with different geometries. Features of the mode profile images for Fig. 4.6a, 4.6b, and 4.6c show that rib waveguides widths of 20 μm, 15 μm, and 7.5 μm, respectively, present higher order optical modes profile at the end facet. On the other hand, Fig. 4.6d for a rib waveguide width of 5 μm exhibits features similar to a single-mode like profile. The cavity coupled rib waveguide output mode profiles are different from each other unlike stand-alone rib waveguide ones in Fig. 4. Indeed, the Fabry-Perot's DBRs roughness, inherited from the DRIE-BOSCH process's scalloping, mainly lowers higher order optical modes relative intensities and contrasts. Consequently, the infrared camera renders a more noticeable superimposition of optical modes.

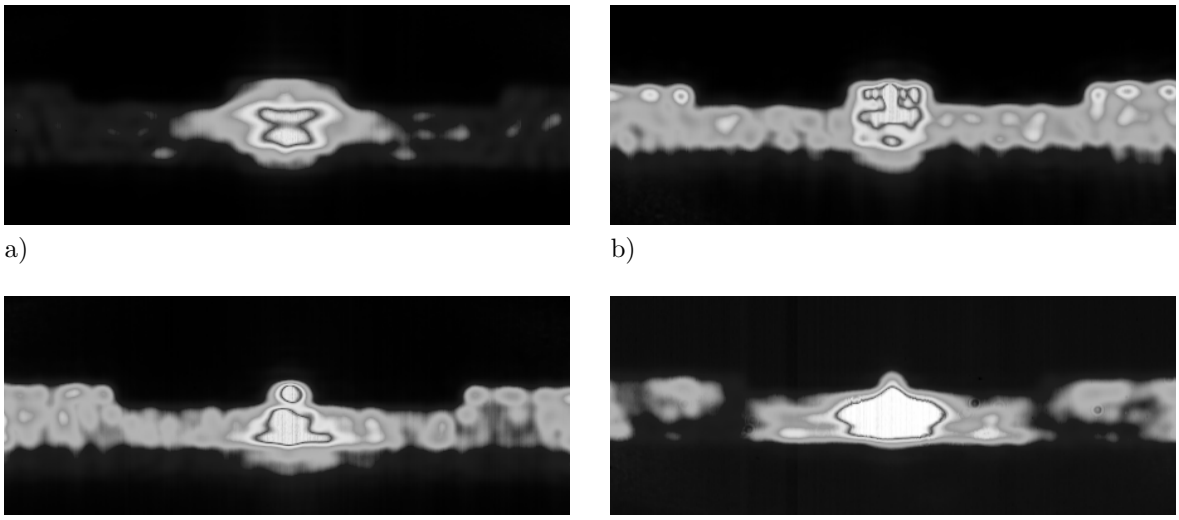

a) b)

c) d)

Figure 4.6 NIR images of the output mode for cavity coupled rib waveguides showing higher mode profile for widths of (a) 20 μm, (b) 15 μm, and (c) 7.5 μm and single-mode profile for width of (d) 5 μm.

Spectral analysis

Fig. 4.7 presents the output spectra for Fabry-Perot cavity coupled rib waveguides with different geometries. For rib waveguide widths of 20 μm, 15 μm, and 7.5 μm the spectra do not exhibit easily identifiable resonance peak. The intensity in function of wavelength seems erratic and presents no useful information as a resonant sensor device. On the other hand, the spectrum on Fig. 4.7d for a width of 5 μm exhibits an isolated resonance peak, identified by an arrow.

These results for resonant cavity coupled rib waveguides support the initial hypothesis that only single-mode behavior enables identifiable resonance peaks and provide useful information. Indeed, on-chip integrated silicon multimode rib waveguides tend to generate beating between supported propagating modes and render a complex spectrum without even being conjugated to a resonant cavity. When coupled, the cavity's resonance peaks are "lost" in the intensity variations background, thus not identifiable, and no sensing features can be extracted *a priori*. Therefore, achieving single-mode like behavior in integrated rib waveguides, with very large cross-section, coupled to a resonant cavity is crucial. To our knowledge, this paper reports the first study to experimentally achieve it.

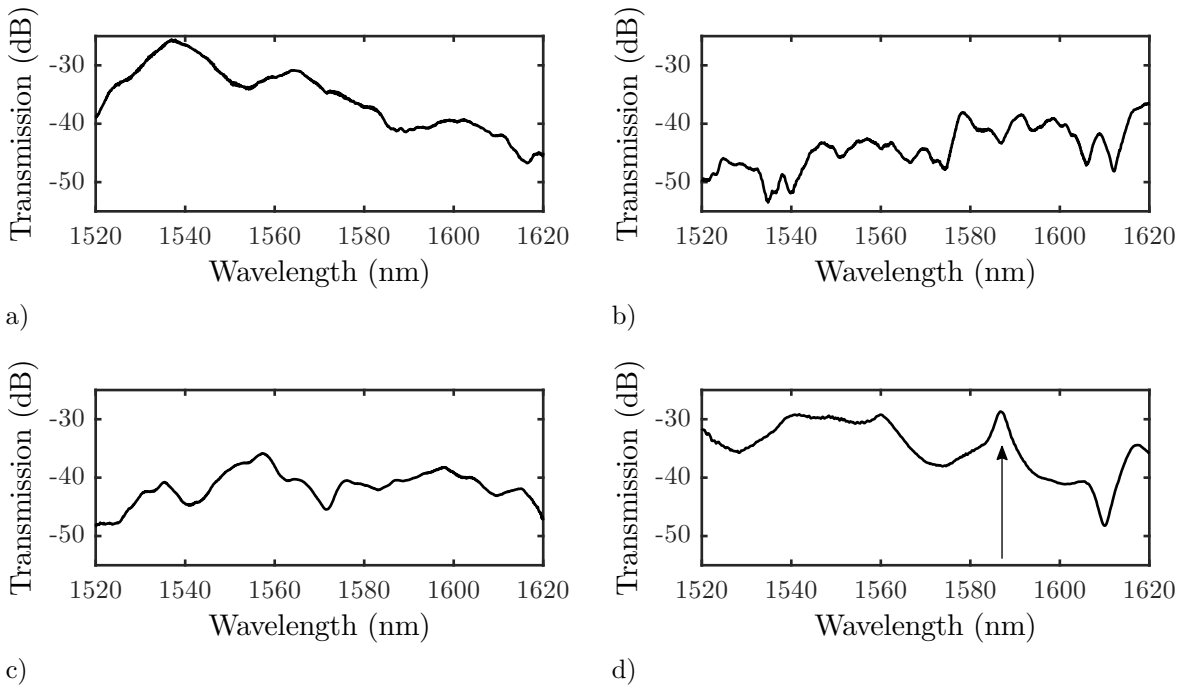

Figure 4.7 Output spectra for Fabry-Perot cavity coupled rib waveguides showing intensity profile for widths of (a) 20 μm, (b) 15 μm, and (c) 7.5 μm and exhibiting an isolated resonance peak for a width of (d) 5 μm.

4.7.3 Fabry-Perot resonance properties

In this section, information on the Fabry-Perot resonance peak for single-mode cavity coupled rib waveguide with a width of 5 μm is reported. First, a simulation based on optical matrices with an incident Gaussian beam was performed. The incident Gaussian beam is decomposed into multiple plane waves and then propagated through the simulated Fabry-Perot cavity made of silicon-air layered DBRs (see Fig. 4.3b). Fig. 4.8 shows the comparison between simulated and experimental results on the same graphic. The simulated result, dashed line, is in good agreement with the measured spectrum, plain line, for this 35 μm long cavity gap. Properties of these resonance peaks were calculated from the experimental and simulated spectra and are reported in Table 4.1, where FWHM is the Full Width at Half Maximum, FSR is the Free Spectral Range and the finesse is $FSR/FWHM$. Differences between experimental and simulated spectra properties are mainly due to the simulated roughness of the interfaces. The simulated roughness, approximated as an absorption layer, affects the sharpness of resonance peaks. It lowers the intensity at the resonant wavelength, increases the FWHM value and thus yields a smaller finesse. Furthermore, simulations do not accommodate for light re-entering the cavity from reflections elsewhere on the device and neither

for multimode resonance nor multimode coupling behavior.

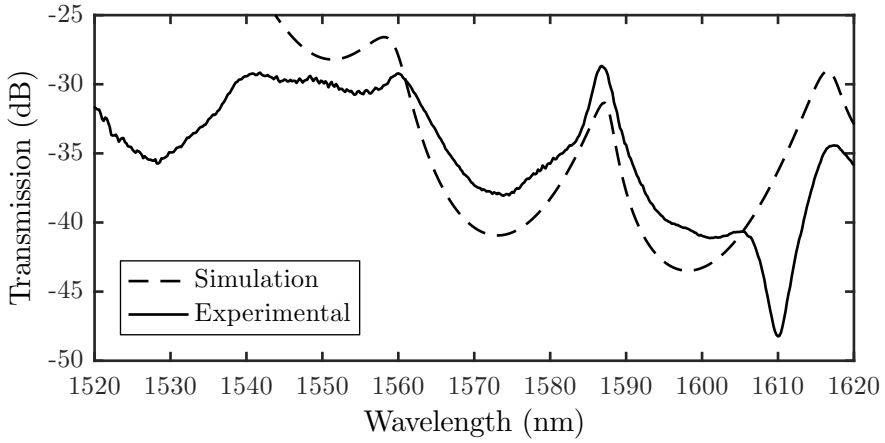

Figure 4.8 Spectral comparison between simulated, dashed line, and experimental, plain line, single-mode Fabry-Perot cavity for a rib waveguide width of 5 μm.

As mentioned previously, a rib waveguide coupled to a Fabry-Perot cavity can be used in a resonant spectroscopic measurement. This technique enables detection of small variations of refractive index. Although, before handling biological cells measurement, characterization of the sensor response with homogeneous liquids must be performed. The calculated sensitivity, in units of nm per refractive index unit (RIU), was derived from the peak displacement for different certified refractive index oils. Fig. 4.9 shows the graphical linear fit with the measurement points used to obtain this value of 1392 nm/RIU. Measurements on the resonance wavelength position had a standard variation of $\sigma = 0.005$ nm corresponding to an accuracy of $3\sigma = 0.015$ nm. Considering this accuracy and the sensitivity, this sensor has a limit

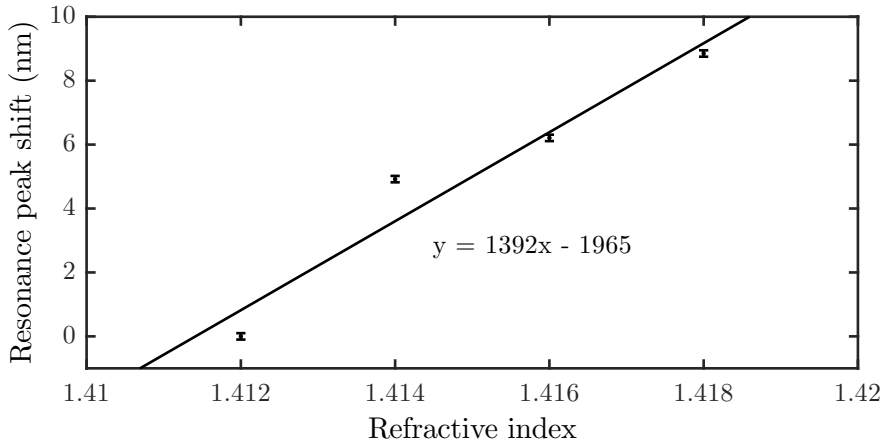

Figure 4.9 Measurement points for single-mode cavity coupled rib waveguide resonance peak displacement with certified refractive index oils superposed with a linear fit.

of detection (LOD) of $\Delta n = 1.1 \times 10^{-5}$. This small LOD over the refractive index could represent a discriminant parameter when measuring biological cells.

Table 4.1 Fabry-Pérot resonance properties calculated from the experimental spectra for a rib waveguide width of 5 μm.

	Experimental	Simulated
Loss at maximum (dB)	-28.7	-31.3
FWHM (nm)	3.56	4.41
FSR (nm)	30.6	29.3
Finesse	8.6	6.6
Sensitivity (nm/RIU)	1392	N/A
LOD (RIU)	1.1x10^{-5}	N/A

4.8 Conclusion

In summary, we have presented results for optical rib waveguides with very large cross-sections supporting the hypothesis that single-mode behavior is better suited for resonant spectroscopy measurement, especially for sensing application. Achieving single-mode propagation in these waveguides may not be as easy as following the previously established design rules. Therefore, caution must be taken when dealing with very large cross-section optical rib waveguides. Indeed, mutimode rib waveguides tend to hide the resonance peak when coupled to a resonator. Conditions for a single-mode optical rib waveguide were found by modal simulation and experimentally tested for a stand-alone rib waveguide as well as for an on-chip in-plane Fabry-Perot resonant cavity coupled structure. Resonance properties for single-mode behavior were evaluated and employed in a simple refractive index sensor device with homogeneous liquids.

Acknowledgment

The authors would like to thank R. St-Gelais for sharing simulation code and the Microfabrication Laboratory at Polytechnique Montreal for helpful insight in microfabrication.

4.9 Supplementary information: Unpublished results and discussion on rib waveguide modal analysis and Fabry-Pérot properties

4.9.1 Fundamental mode attenuation map

The fundamental mode HE_{00} attenuation map presented in Fig. 4.10 reports the highest attenuation coefficient recorded. Considering that the fundamental mode is always propagating, using the highest attenuation coefficient recorded instead of the lowest, as for the other presented attenuation maps, allows to determine the extent of attenuation to be expected. Thereupon, for all considered geometries of the rib waveguide, the attenuation is always smaller than 3 dB/cm. Furthermore, the attenuation increases for larger h/H ratio and smaller W/H ratio.

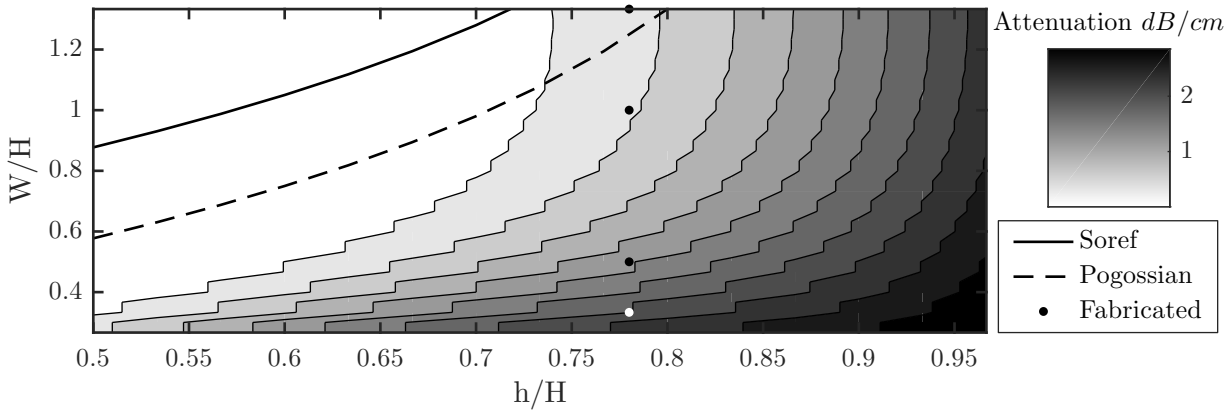

Figure 4.10 Highest attenuation coefficient recorded for the HE_{00} mode at all simulated operating wavelengths in function of ratios h/H and W/H. The plain line corresponds to Soref's single-mode boundary whereas the dashed line corresponds to Pogossian's correction. Black and white dots represent the fabricated devices.

4.9.2 Odd higher order modes attenuation maps

The odd higher order modes HE_{10} and HE_{30} were initially thought to *"never reach an attenuation coefficient low enough to add meaningful information to the final attenuation map"*. However, after careful investigation, attenuation maps were found to have an inverted x-axis due to a simulation artifact. The published attenuation maps, presented in Fig. 4.2, were corrected. Importantly, this artifact does not change the conclusions of the article. Following the established design rules is not sufficient to ensure single-mode like behavior of large cross-section rib waveguides. Furthermore, fabricated rib waveguides having widths of 7.5 μm and 5 μm have less power in higher order modes, show less spectral variations and thus

are better suited for resonant sensing applications.

However, the corrected odd higher order modes HE_{10} and HE_{30} attenuation coefficients can influence the predicted rib waveguide behavior. These modes can contribute to the spectral variations and overall low transmission observed in Fig. 4.5. For the fabricated devices, mode HE_{10} has a greater impact than mode HE_{30} following the attenuation maps presented in Fig. 4.11a and 4.11b respectively. Furthermore, the combined attenuation map of all higher order modes for all operating wavelengths presented in Fig. 4.11c reveals that the fabricated devices, although serving well this investigation, are clearly not optimized. In Chapters 5 and 6, new devices are fabricated based upon this combined attenuation map. These new devices are marked by a single "x" over the corresponding region in Fig. 4.11c. This second generation of rib waveguides report spectral transmission mean standard deviations below 1 dB, total coupling losses of -15.5 dB and propagation losses below 1.5 dB/cm (see Chapter 5). These properties are associated to single-mode like behavior of the rib waveguides and match the expected attenuation of the fundamental mode presented in Fig. 4.10.

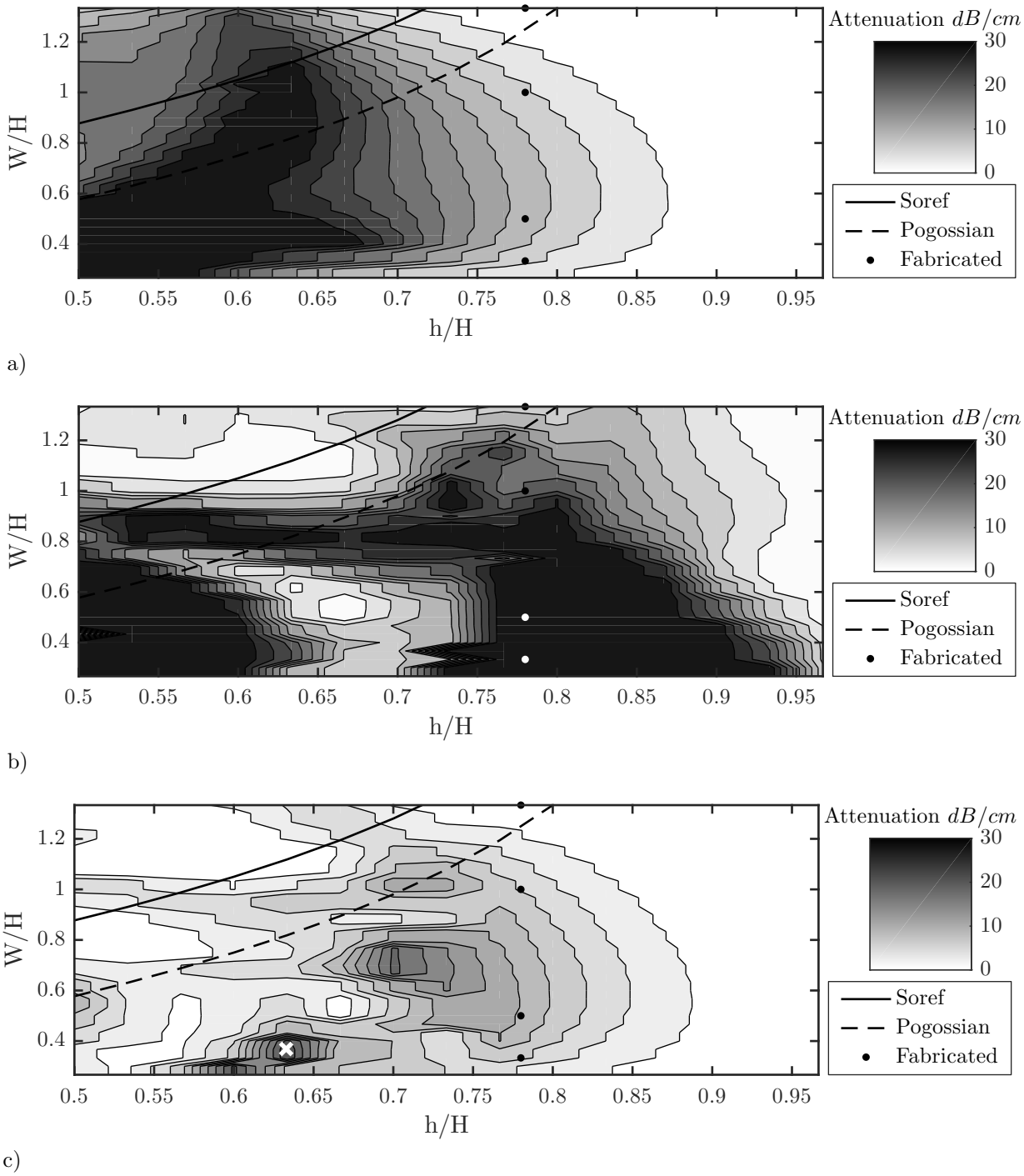

Figure 4.11 Lowest attenuation coefficient recorded for the (a) HE_{10} mode, (b) HE_{30} mode, and (c) combined HE_{10}, HE_{20}, HE_{30} and HE_{40} modes at all simulated operating wavelengths in function of ratios h/H and W/H. The plain line corresponds to Soref's single-mode boundary whereas the dashed line is corresponds to Pogossian's correction. Black and white dots represent the fabricated devices. The white "x" in (c) marks the region for the second generation of rib waveguides reported in Chapter 5 and 6.

4.9.3 Considerations on the Fabry-Pérot sensitivity

Refractive index sensing originally performed on a Fabry-Pérot cavity coupled to a 5 μm wide rib waveguide reported a sensitivity of 1392 nm/RIU and a LOD of 1.1×10^{-5} RIU (see Tab. 4.1). However, explaining the larger offset of the resonance shift for $n = 1.414$ and the calculated coefficient of determination $R^2 = 0.9385$ in Fig. 4.9 requires further considerations. Using a substituted measured spectrum for $n = 1.412$ and excluding the resonance shift for $n = 1.414$ result in strong coefficients of determination ($R^2 = 0.9999$ and $R^2 = 0.9997$). Figure 4.12a shows the measured Fabry-Pérot spectra, which includes the proposed substitution, in function of the oil refractive index. It is clear that the $n = 1.414$ spectrum does not follow the resonances shift tendencies and thus is excluded from the following sensitivity calculations. Figure 4.12b presents the linear fits of each resonance. The corrected sensitivities are 1195 nm/RIU and 1278 nm/RIU yielding LODs of 1.3×10^{-5} RIU and 1.2×10^{-5} RIU for the first and second resonance respectively. Compared to the initially reported values, the corrected LODs are only slightly larger and thus have a negligible impact on the claimed Fabry-Pérot performance. Still, these considerations provide a more rigorous analysis of the sensitivity. Table 4.2 summarizes these Fabry-Pérot resonances properties for a spectral measurement setup. In a power measurement scheme, sensitivities are approximately 1500 dB/RIU and 2435 dB/RIU yielding LODs of 6.7×10^{-5} RIU and 4.1×10^{-5} RIU for the

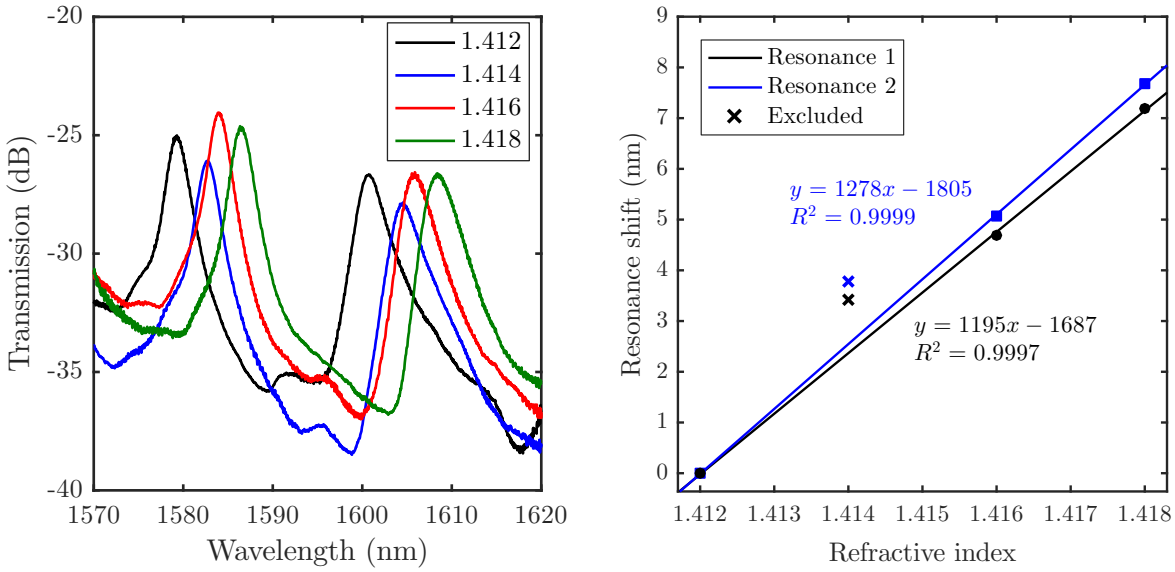

Figure 4.12 (a) Measured Fabry-Pérot spectra in function of the oil refractive index. The $n = 1.412$ spectrum has been substituted by a second measurement. (b) Fitted linear sensitivities for each resonance.

first and second resonance respectively. These experimental power setup LODs are in line with the theory presented in Chapter 3.

Table 4.2 Experimental Fabry-Pérot resonances properties for $n_{oil} = 1.412$.

	Resonance #1	Resonance #2
Loss at maximum (dB)	-25.0	-26.7
FWHM (nm)	3.33	4.51
FSR (nm)	21.5	21.5
Finesse	6.4	4.8
Sensitivity (nm/RIU)	1195	1278
LOD (RIU)	1.3×10^{-5}	1.2×10^{-5}

Intriguingly, the experimental spectral setup sensitivities are larger than the maximum theoretical ones. Indeed, as seen in the previous chapter, the theoretical sensitivity is $S_{theo} = \lambda/n_{oil}$. For an oil of $n_{oil} = 1.412$, theoretical sensitivities are 1119 nm/RIU and 1134 nm/RIU for the first and second resonance respectively. Both sensitivities correspond to a LOD of 1.3×10^{-5}. These slight differences could be due to artificially increased shifts caused by the presence of spectral non-uniformity. As presented in the above published results, some spectral variations still exists in the fabricated rib waveguides due to the propagation of higher order modes. Hence, varying the optical length in the cavity changes the fraction of optical power in the fundamental mode at the end facet of the waveguide and thus can induce additional artificial shifts. In Chapters 5 and 6, the second generation of rib waveguides optimized for single-mode propagation report sensitivities smaller than the maximum theoretical ones using the same oils.

CHAPTER 5 ARTICLE 2 - HIGH-THROUGHPUT REFRACTIVE INDEX-BASED MICROPHOTONIC SENSOR FOR ENHANCED CELLULAR DISCRIMINATION

This chapter is a reproduction of an article published in Sensors and Actuators B: Chemical.[1] It details the fabrication, experimental setups, inertial microfluidic focusing of cells and optical operating principles of the on-chip Fabry-Pérot microcavity cell sensor presented in this thesis. Importantly, this chapter establishes the first enhanced myeloid cells discrimination using refractive index information when compared to flow cytometry. This chapter also introduces the use of the *overlaprate* (OLR) coefficient as a quantifying tool of the observed discrimination. The detailed mathematical procedure to calculate the OLR can be found in Annex C. Some terms in this chapter have been replaced to consistently preserve the definitions presented in the previous chapters.

5.1 Authors and affiliations

Antoine Leblanc-Hotte,[a,*] Geneviève Chabot-Roy,[b] Livia Odagiu,[b,c] Manon Richaud,[d] Sylvie Lesage,[b,c] Jean-Sébastien Delisle,[d,e,f] Yves-Alain Peter[a]

[a] *Department of Engineering Physics, Polytechnique Montreal, 2500, Chemin de Polytechnique, Montreal, Québec, Canada, H3T 1J4.*

[b] *Cellular Immunogenetics Laboratory, Maisonneuve-Rosemont Hospital Research Center, 5415, Boulevard de l'Assomption, Montreal, Québec, Canada, H1T 2M4.*

[c] *Département de microbiologie, infectiologie et immunologie, Université de Montréal, C.P. 6128, succursale Centre-ville, Montreal, Québec, Canada, H3C 3J7.*

[d] *Cancer and Transplantation Immunology Laboratory, Maisonneuve-Rosemont Hospital Research Center, 5415, Boulevard de l'Assomption, Montreal, Québec, Canada, H1T 2M4.*

[e] *Department of medicine, Université de Montréal, C.P. 6128, succursale Centre-ville, Montreal, Québec, Canada, H3C 3J7.*

[f] *Hemato-oncology service, Maisonneuve-Rosemont Hospital, 5415, Boulevard de l'Assomption, Montreal, Québec, Canada, H1T 2M4.*

[1] A. Leblanc-Hotte, G. Chabot-Roy, L. Odagiu, M. Richaud, S. Lesage. J.-S. Delisle and Y.-A. Peter, "High-throughput refractive index-based microphotonic sensor for enhanced cellular discrimination," *Sensors and Actuators B: Chemical*, vol. 266, pp. 255–262, aug 2018. DOI: 10.1016/j.snb.2018.03.087

5.2 Abstract

This paper presents a novel microphotonic sensor based on silicon technologies for high-throughput single cell measurements. It employs a highly sensitive Fabry-Pérot resonant cavity to extract cellular refractive index information. The integrated large cross-section rib waveguides provide a single-mode like behavior important for resonant cell sensing. Differentiated myeloid cells derived from a promyelocytic leukemia cell line were injected in a microchannel, sheathlessly focused using inertial forces and analyzed while flowing through the resonant cavity volume. Results were compared against a commercial flow cytometer and showed a substantial improvement on cellular discrimination. Thus, this sensor has the ability to discriminate cell populations, usually identified using fluorescent parameters, without any dyes and can reach measurement rate as high as 2000 cells per second. By harnessing the cell's effective volume refractive index, our device offers complementary measurements readily improving actual technologies and thus providing crucial information for research and clinical professionals.

Keywords–Microphotonic, Fabry-Pérot, Optical microcavity, Refractive index, Microfluidic, Cell sorting, Sensor.

5.3 Introduction

Complete blood counts are essential to monitor a patient general health by measuring the number and quality of white blood cells, red blood cells and platelets. These tests performed in many hospitals and research centers rely on hematology analyzers which include flow cytometers and Coulter counters. While the Coulter principle is an electrical impedance measurement used to count the types of cells, flow cytometry uses interaction of light with cells to qualify their type. Owing to its measurement rate in the order of 10 000 cells per second, it is a tool of choice amongst clinical and research professionals.

In flow cytometry, cells are tightly focused in a fluid stream and cross a perpendicular laser beam. Detectors placed at strategic angles measure forward scattered light (FSC) and side scattered light (SSC). Forward scattered light is influenced by the size of the cell and side scattered light is influenced by the granularity of the cell. FSC/SSC measurements are mainly used to identify living cells and exclude dead cells or doublets. Furthermore, flow cytometers constantly improve their selectivity using fluorescent parameters [171]. Pretreatment with an antibody-fluorophore complex targets specific features of the cells while monochromatic lasers optically excite each individual type of complex on their flowing course. Expression levels of these specific features are fundamental to medical professionals diagnostic and interpretation.

Polychromatic flow cytometry can now yield 20 to 30 different fluorescent channels owing to the conjunction of quantum dots and organic fluorophores [172–174] and major manufacturing companies are aiming to reach 50 channels in a near future. However, these dyes can be very expensive, the necessary pretreatment procedures can be time consuming in addition to increase cell death and measurements need carefully calibrated software compensations to account for overlapping fluorescence spectra. Additionally, benchtop flow cytometers have a high cost, are space consuming, lack portability and require trained operating personnel.

On the other hand, numerous integrated miniaturized flow cytometers measuring scattered light, fluorescence or attenuation, have been developed to mimic their benchtop equivalent in a point-of-care manner [81, 82, 91, 96, 98, 175]. These miniaturized systems are a promising alternative considering their lower cost and portability. Although reporting very good performances, these systems measure the same physical and fluorescent parameters as flow cytometry. However, the integration of microphotonics and microfluidics components on a single device can harness different cellular physical properties. In particular, refractive index of single cells has attracted a lot of interest recently and fueled recent microsystems developments. Microfabricated surface refractometers using whispering gallery modes in different configurations [132, 157, 158], photonic crystal cavities [138], surface plasmon resonance [176] and evanescent wave interaction in gratings [126] or interferometers [110] reported high sensitivity and small limit of detection (LOD) around 10^{-6} to 10^{-8} refractive index unit (RIU) but they all lack depth of interaction required for whole cell characterization. Microfabricated Fabry-Pérot resonators are sensitive to the medium inside their cavity and thus are good volume refractometer candidates, even if reporting smaller LOD around 10^{-5} RIU [141, 145, 148].

Whole cell refractive index analyses were reported previously using forward scattered light from two-beam laser trap [8], an external laser resonant cavity [5] and optical fiber Fabry-Pérot cavities [6, 7]. In these studies, single effective refractive index is used as critical parameter to identify various cancer cells from the kidney, cervix, adrenal medulla, breast and lymphocytes. It has also been shown by others that the refractive index could help diagnose certain infections, malaria and anemia [9]. Another study reported an out-of-plane integrated Fabry-Pérot cavity using cell-generated secondary optical transverse modes to differentiate lymphoma from lymphocytes with high specificity and sensitivity [4]. Although providing important information on a cell's refractive index related to its state or specific pathology, no dynamic or high-throughput measurement of large cellular population have been demonstrated by any of these microsystems.

Nevertheless, there is a high demand amongst biomedical technologists for use and improve-

ments in polychromatic flow cytometry equipment. Clinical and research professionals both strive to obtain cutting-edge technologies that offer high-throughput, multiparametric and diversified single-cell measurement, ideally in a single system. The proposed device directly mitigates this shortcoming by offering new non-fluorescent discrimination parameter in a high-throughput manner. This report presents a novel microphotonic sensor based on silicon technologies for high-throughput single cells measurement. It employs a highly sensitive Fabry-Pérot resonant cavity, $\Delta n = 1.6 \times 10^{-5}$, reported in previous work [144, 148, 164] to extract cellular refractive index information. The integrated large cross-section rib waveguides provide a single-mode like behavior important for resonant cell sensing [148]. Differentiated myeloid cells derived from a promyelocytic leukemia cell line were injected in a microchannel, sheathlessly focused using inertial forces and analyzed while flowing through the resonant cavity volume. This dynamic measurement of a cell's effective volume refractive index enables new parameters for cellular population discrimination. Furthermore, this microsystem does not require any dye treatment of the cells, accepts any cell shape and can reach measurement rate of 2000 cells per second. Results were compared against a commercial flow cytometer and showed a substantial improvement on cellular population discrimination. Indeed, FSC-SSC based flow cytometry could not distinguish between any of the three differentiated myeloid cells populations whereas the microsystem could distinguish two of these cell types. We believe such microphotonic system represents an important step towards distinguishing different cell types and could be integrated in flow cytometry instruments and cell counter devices.

5.4 Materials and methods

5.4.1 Microfabrication

The device was fabricated by conventional silicon micromachining using photolithography and deep reactive ion etching (DRIE) as core processes. We used a silicon-on-insulator (SOI) wafer comprising a handle layer of 600 μm, a buried oxide (BOX) layer of 0.5 μm and a device layer of 15 μm. First, microfluidic channels and distributed Bragg reflectors (DBRs) were patterned using a positive photoresist. DBRs were designed according to previously published work [164] to achieve a Fabry-Pérot cavity with resonances in the near infrared (NIR) region. These structures were etched in the silicon device layer down to the buried oxide (BOX) using a DRIE-BOSCH process with alternating SF_6 and C_4F_8 plasmas. Then, similarly, rib waveguides were photolitographically defined and etched to a lower height. Microstructured SOI wafers were cut into separate chips using a dicing saw (ADT, Provectus 7100) and an engineered resin/diamond blade for optical quality facets with low scattering losses. This

dicing method previously reported a mean roughness value of 5.5 nm [148]. Manufactured and diced Pyrex plates with holes of 760 μm in diameter were anodically bonded on top of the chips to seal the microfluidic channels. Tygon microbore tubings were then connected to the microchannels entries and exits and bonded using ultraviolet reactive glue. Figure 5.1a shows a 3D rendering of the assembled microphotonic cell sensor device and Fig. 5.1b reports a scanning electron microscopy (SEM) image of the fabricated device showing the rib waveguides, DBRs, Fabry-Pérot cavities and microfluidic channel. Verticality of DBRs trenches were measured using transverse scanning electron microscopy (SEM) images and reported a value of $90.0 \pm 0.2°$.

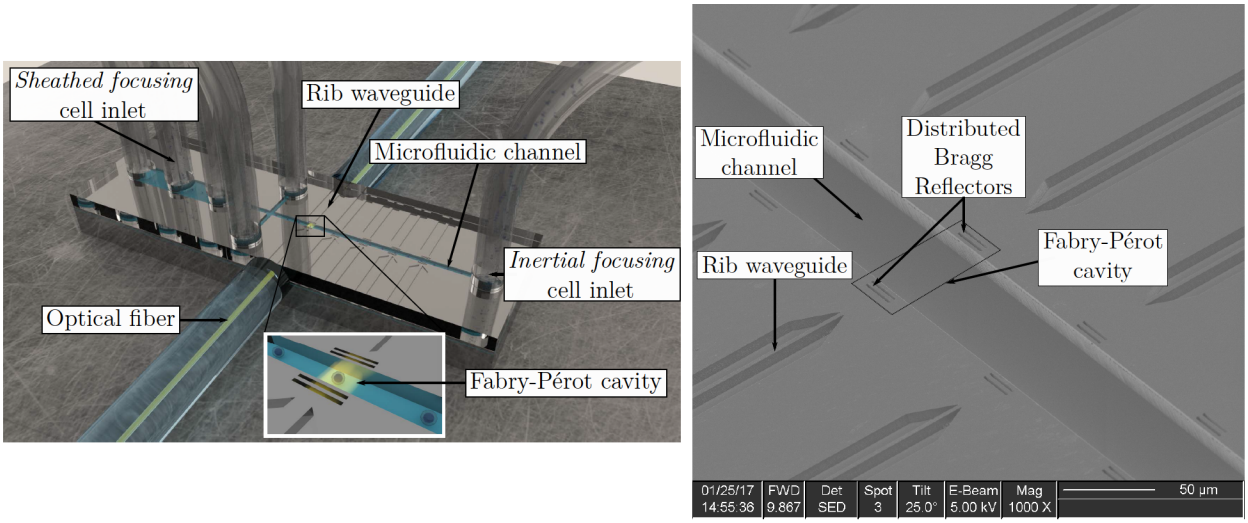

a) b)

Figure 5.1 Illustrations of the microphotonic cell sensor with (a) 3D rendering of the assembled device using Blender Software and (b) SEM image of the microfabricated rib waveguides, DBRs, Fabry-Pérot cavities and microfluidic channel.

5.4.2 Single-mode like Rib waveguide

Geometries of the rib waveguides were designed according to previously published work to yield a single-mode like propagation [148]. Briefly, we calculated higher order optical modes attenuations for several rib waveguide dimensions at different wavelengths. We used a finite difference (FD) method and a direct matrix solver with perfectly matched layer (PML) as boundary conditions to compute supported modes. The imaginary part of the complex refractive index for each computed mode, *i.e.* the extinction coefficient, was converted into an attenuation coefficient. This technique yielded an attenuation map showing regions of interest corresponding to single-mode like behavior. Figure 5.2 shows the combined attenuation

map for modes HE_{10}, HE_{20}, HE_{30} and HE_{40} at wavelengths of $\lambda = 1.50\ \mu m$, $1.575\ \mu m$ and $1.65\ \mu m$ with onsets showing a schematic of the rib waveguide cross-section with corresponding variables and the single-mode like NIR output mode profile of a $5.5\ \mu m$ rib waveguide after $5.85 \pm 0.01\ mm$ of propagation. Experimental setup used to analyze the NIR output mode profile is described in *Section 5.4.5*. Fabricated rib waveguides were chosen to be $5.0\ \mu m$ and $5.5\ \mu m$ in width and $9.5\ \mu m$ in height, represented by the white dots in Fig. 5.2.

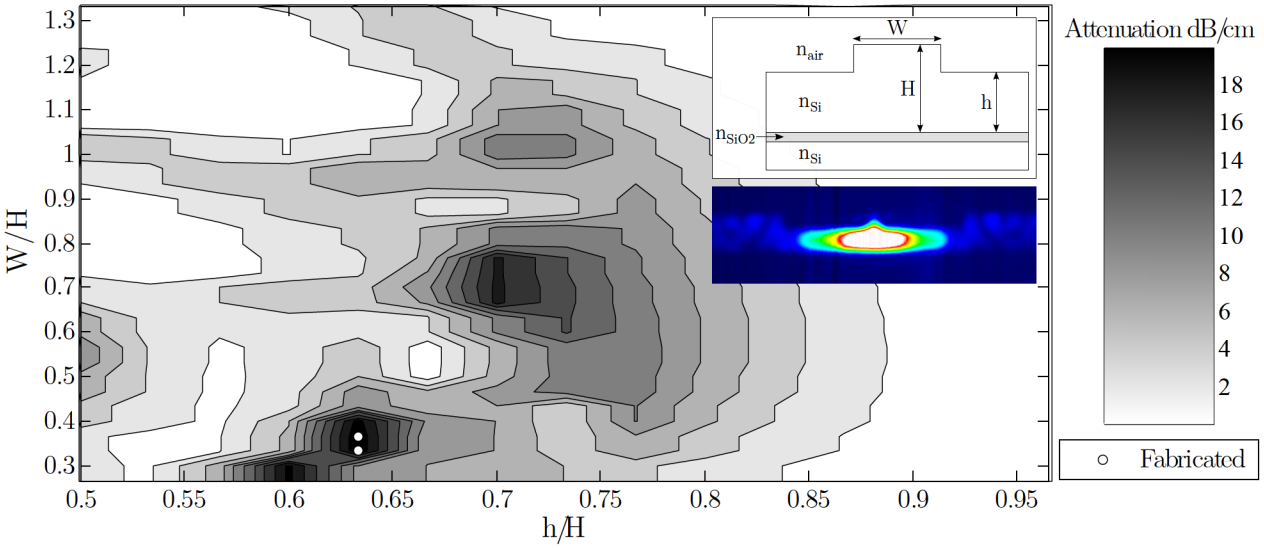

Figure 5.2 Combined attenuation map for modes HE_{10}, HE_{20}, HE_{30} and HE_{40} at wavelengths of $\lambda = 1.50\ \mu m$, $1.575\ \mu m$ and $1.65\ \mu m$. Onsets showing a schematic of the rib waveguide cross-section with corresponding variables and the single-mode like NIR output mode profile of the fabricated $5.5\ \mu m$ rib waveguide.

5.4.3 Microfluidic operation

Samples injection were made using a syringe pump (Harvard Apparatus, Pump 11 Pico Plus Elite) connected to the inertial focusing cell inlet tube (Fig. 5.1a) at a flow rate of $5\ \mu l/min$.

It is worth mentioning that since the resonant cavity does not have a focal point, position of cells along the width of the microchannel had a negligible impact on the output signal. Nevertheless, the two-stages sheathless inertial focusing as reported by Zhou and Papautsky will affect cells position flowing through the microchannel [58]. Indeed, particles flowing through a rectangular microchannel will focus to four distinct lateral equilibrium positions due to the inertial lift forces involved, the shear-induced lift force, the wall-induced lift force and the rotation-induced lift force. In the first stage, fast migration of cells toward channel walls is caused by the shear-induced and wall-induced lift forces balance whereas in

the second stage slow migration of cells to center points of walls is caused by the rotation-induced lift force. This is true for confined flows at finite Reynolds number. However, with increasing channel aspect ratio, equilibrium positions on short faces disappear leaving only two equilibrium positions centered at the long face of the channel. For flowing lengths higher than the complete focusing length, cells will remain focused to the equilibrium positions and ordered with preferred interparticle spacing [55]. The complete focusing length required for particle migration is

$$L = \frac{3\pi\mu {D_h}^2}{4\rho U_f a^3}\left(\frac{H}{{C_L}^-} + \frac{W}{{C_L}^+}\right), W > H \tag{5.1}$$

where μ and ρ are the fluid viscosity and density, D_h is the hydraulic diameter, U_f is the average flow velocity, a is the particle diameter, H and W are the channel height and width respectively and ${C_L}^-$ and ${C_L}^+$ are the negative and positive lift coefficients estimated through the authors data. ${C_L}^-$ is associated to the migration away from the center points of walls (fast migration in stage I) and ${C_L}^+$ is associated to the migration toward the center points of walls (slow migration in stage II). In the present study the microchannel dimensions are $H = 15\ \mu m$ and $W = 35\ \mu m$, cell diameter is 12 μm, flow rate is $Q = 5\ \mu l/min$ and fluid properties are approximated to the ones of water. ${C_L}^-$ is estimated to be 0.19 and ${C_L}^+$ estimated to 0.023. This yields a complete focusing length $L = 6\ mm$. The cavity used in this study was placed 1.2 mm away from the inlet. Thus, cells will be partially focused around the equilibrium positions with a spread of 29 μm in the direction of the width. Larger cells require less length to be completely focused, as shown in Eq. 5.1. This might lead larger cells to yield a less scattered population and thus create an inertial focusing contribution to the discrimination capability of the device. However, cell with the same size distributions, as for these experiments, will behave similarly. Furthermore, since planar DBRs are used, the sensing cross-section of the optical resonant profile is uniform along the cavity axis. Thus, position of the cells in this axis should have negligible impact on the output signal. Lateral hydrodynamic focusing used in a previous device [177] does not suggest a significant difference on population spreading compared to inertial focusing. Still, devices were designed with multiple entries as shown in Fig. 5.1a to keep open the possibility of sheathed 3D hydrodynamic focusing when cells were too small to be confined in height solely by this phenomenon.

5.4.4 Cell culture

The HL-60 cell line was obtained from the ATCC (#CCL-240), maintained in RPMI containing 20% fetal calf serum (FCS) and kept in a humid chamber at 37°C with 5% CO_2. HL-60 is a promyelocytic leukemia cell line that can be differentiated into various myeloid cell types

depending on the culture condition. We opted to differentiate the HL-60 cells into basophils and neutrophils. HL-60 cells were passaged in differentiation media, in RPMI containing 10% FCS with 1% HEPES (baseline condition). To obtain neutrophils, 2×10^5 HL-60 cells per ml were cultured with 1.25% dimethylsulfoxide (DMSO, Sigma) for seven days [178]. To obtain basophils, 2×10^5 HL-60 cells per ml were maintained for seven days in the absence of serum [179].

At day 7 of culture, the HL-60 cells were harvested, washed in phosphate buffered saline (PBS) containing 2% FCS and 1 mM EDTA. The cells were counted and resuspended in PBS (2% FCS, 1 mM EDTA) at a concentration of 2 million cells per ml. Cell aggregation is prevented using 1 mM EDTA (Ethylenediaminetetraacetic acid) a known chelating agent binding to calcium and hindering calcium specific adhesion (cadherins) and thus preventing cell clumping. Nevertheless, cell aggregation can still occur. In both the flow cytometer and microphotonic sensor, data from small cell clusters are readily excluded by the amplitude or width of the signal, whereas larger cell clusters tend to block the device, which must then be cleaned prior to further data acquisition. Samples where cell viability was below 50% were excluded from further analyses. 150 000 cells were placed on a slide by cytospin and subjected to Wright-Giemsa staining. The data was acquired on a microscope (Zeiss, AxioImager Z2) using a 63X oil immersion objective. All solutions were divided into two separate tubes, one for data acquisition with flow cytometry and one for data acquisition with the microsystem.

5.4.5 Experimental setups

In this study, three different experimental setups were used: one to analyze the NIR output mode profile, one to analyze the spectral response from the rib waveguides alone as well as coupled to the Fabry-Pérot cavity and finally one to register optical power variation in time at a fixed wavelength for single cell analysis.

NIR mode profile of rib waveguides were assessed using a standard SMF-28 fiber butt coupling light from a wide band laser source (Newport, BBS-430) in the inlet facet. Outputted light was collected on an InGaAs camera (VDS Vosskhler GmbH, NIR-610PGE) through an objective lens using a 45°angled mirror. For the spectral analysis setup, an optical spectrum analyzer (Hewlett Packard, 86142A) collected the outputted NIR light through a butt coupled optical fiber and recorded the normalized spectrum. The raw spectrum was normalized using the wide band laser source as a reference. Stand-alone rib waveguides and Fabry-Pérot coupled rib waveguides were assessed. Certified refractive index oils were used to measure the resonance peak sensitivity. The optical power variation measurement setup fixed the propagating wavelength at the top of the Fabry-Pérot resonance using a tunable laser source

(Agilent, 8164B). As a cell flew through the Fabry-Pérot cavity, the resonance peak shifted towards longer wavelength because the refractive index of the cell is higher than the surrounding liquid (PBS). A fast InGaAs infrared photodetector (Thorlabs, DET01CFC) recorded optical power variations at the output and relayed it to a high speed digitizer (National Instruments, NI-PXI 5114). A LabView program was developed to allow for fast acquisition of the relayed voltage variation in time.

5.4.6 Flow cytometry measurements

Three sub-parameters, height, width and area, were automatically extracted from FSC and SSC measurements. 50 000 cells of the basophils and neutrophils solutions were processed for data acquisition on the same BDCANTO flow cytometer. Flow cytometry samples were analyzed using FlowJo software. *Overlaprate* (OLR) coefficients were computed in parallel using equation 5.2, as detailed below.

5.4.7 Single cell analysis

Distinctively from FSC and SSC, sensor measurements are influenced by the effective volume refractive index of the cells. Single cell curves were analyzed and compared against each others based on multiple extracted parameters using a custom made MatLab visualization algorithm. As for flow cytometry, OLR coefficients were computed in parallel using equation 5.2.

To confirm that two scatter populations, *i.e.* clusters, are indeed distinguishable we computed the *overlaprate* (OLR) coefficient as reported by Sun and Wang in equation 5.2 [180]. This coefficient is calculated as the ratio of the probability density function (PDF) value at the saddle point and the PDF value at the lowest local maximum. Authors also developed an algorithm to find the saddle point of the PDF in any number of dimensions. Essentially, it solves a set of differential equations allowing to find a curve which always contains the maxima and saddle point. Qualitatively, two cluster are well separated if the OLR is less than 0.6, partially overlapping in the interval [0.6, 0.8] and strongly overlapping if greater than 0.8. A value of 1 indicates that no saddle point could be found and that the two clusters are completely overlapping.

$$OLR = \frac{p(X_{Saddle})}{p(X_{Submax})} \tag{5.2}$$

We computed the OLR by fitting a Gaussian distribution over each measured cell popula-

tion for each parameter and applied an affine transformation on the entire set of data to simultaneously diagonalize both population's covariance matrices [181]. Using this technique gave us a set of real functions with a single dependent variable in each one. However, extracted parameters are correlated in the same population since there is only one physical measurement, i.e. the displacement of the resonance peak in time. We found that a 4 to 5 dimension PDF gave us enough precision to asses clusters separation while minimizing the computing error due to the simultaneous diagonalization of these correlated parameters. In particular, parameters that do not have linear covariances, such as height, width and area altogether in FSC or SSC, are badly approximated by a Gaussian distribution. Thus, height sub-parameters were excluded from the OLR computation.

5.5 Results and discussion

5.5.1 Single-mode like Rib Waveguides

Spectral measurements of the 5.0 μm and 5.5 μm rib waveguides for propagation lengths of 5.85, 7.35, 9.85 and 15.84 mm reported total coupling losses of -15.5 dB and propagation losses ≤ 1.5 dB/cm for both width. Intensity variation along wavelengths between $\lambda = [1475,\ 1675]$ nm reported a mean standard deviation of 0.9 dB and 0.8 dB for rib widths of 5.0 μm and 5.5 μm respectively. Based on these results and the NIR output mode profile shown in Fig. 5.2, fabricated rib waveguides built from the theory developed in previous work [148] are indeed single-mode like.

5.5.2 Resonant cavity sensing

Figure 5.3a shows the experimental spectrum of the Fabry-Pérot cavity with DBRs widths of 2.0 μm, microchannel width of 35 μm and rib waveguide width of 5.5 μm. The red line represents the wavelength at which the tunable laser was locked for optical power variation measurements.

Noticeably, the spectrum presents two distinct peaks per expected resonance. Further experiments are necessary to precisely determine the underlying phenomena responsible for these "double peaks". However, FD simulations results yielded fundamental transverse electric (TE) and transverse magnetic (TM) modes propagating with slightly different modal indices $\Delta n \sim 5 \times 10^{-5}$ ($n_{TM} < n_{TE}$), attenuation coefficients $\Delta\alpha \sim 0.25$ dB/cm ($\alpha_{TM} < \alpha_{TE}$) and mode sizes ($size_{TM} < size_{TE}$). Additionally, standard optical transfer matrix simulations with an incident Gaussian beam revealed that two-period DBRs (air-silicon-air-silicon) better fits the resonance's full width at half maximum (FWHM), *i.e.* the overall reflectivity of

the DBRs. Furthermore, these "double peaks" can be well fitted with cavity gaps of different optical lengths. The best fit was found for cavities having a geometrical length difference of 115 nm and a refractive index difference of 5×10^{-5} RIU. Thus, it is reasonable to consider that TE and TM modes would exhibit distinct peaks in the spectrum due to the combined effect of their difference in modal index, attenuation coefficients and mode size. For future reference, we will use the term *"TE cavity"* to describe the resonances corresponding to a cavity gap with a higher refractive index and a shorter length whereas *"TM cavity"* will be for a cavity gap with a lower refractive index and a longer length. Simulated *TE* and *TM cavities* as well as their combination can be found in Fig. 5.3a. Deviation between experimental and simulated spectra can be partially justified when considering the effects of the rib waveguides. As reported previously, fabricated single-mode like rib waveguides do not yield an experimentally flat spectrum due to small energy transfer of the fundamental mode to higher optical modes [148]. Furthermore, simulations do not accommodate for multimode resonance in the cavity nor multimode coupling behavior with the optical fiber. Additionally, simulated roughness of the interfaces, approximated by an absorption layer, and effective thickness of the Bragg layers might differ slightly from the experimental device. Still, the overall simulated and experimental spectra are in good accordance.

Sensitivity and LOD were measured using a different cavity to avoid hindering by oil residue on the microchannel walls. Figure 5.3b shows the measured spectra with certified refractive index oils used to determine the resonance peaks shifts and Fig. 5.3c shows the linear regression fit used to calculate the *TE* and *TM cavities* sensitivities. Sensitivity and LOD values should be roughly the same between cavities since dimensions of DBRs and microchannels are very close and made simultaneously on the same SOI. Table 5.1 reports pertinent parameters of these cavities where FSR is the free spectral range and the finesse is calculated as $FSR/FWHM$. LOD values were calculated considering an accuracy of $3\sigma = 0.015$ nm [148].

Figure 5.3d shows a typical signal in dB scale with the corresponding extracted parameters. FWHM is the full width at half maximum, FWTM is the full width at one third of the maximum, Area HM is the area under the curve at half maximum, Area TM is the area under the curve at one third of the maximum and FW is the full width. Supplementary computed parameters correspond to the following ratios: Rising Time/Falling Time, Slope In/Slope Out, Rising Area/Falling Area, Maximum/full width (FW), Maximum/FWHM, Maximum/full width at one third of the maximum (FWTM), FWHM/FWTM, FWHM/FW and FWTM/FW. Considering a perfectly organized train of cells, the signal shown in Fig. 5.3d would repeat every 3 to 5×10^{-4} s, corresponding to rates of 3333 to 2000 cells/s respectively. The measurement rate is limited to these values due to the imposed flow rate

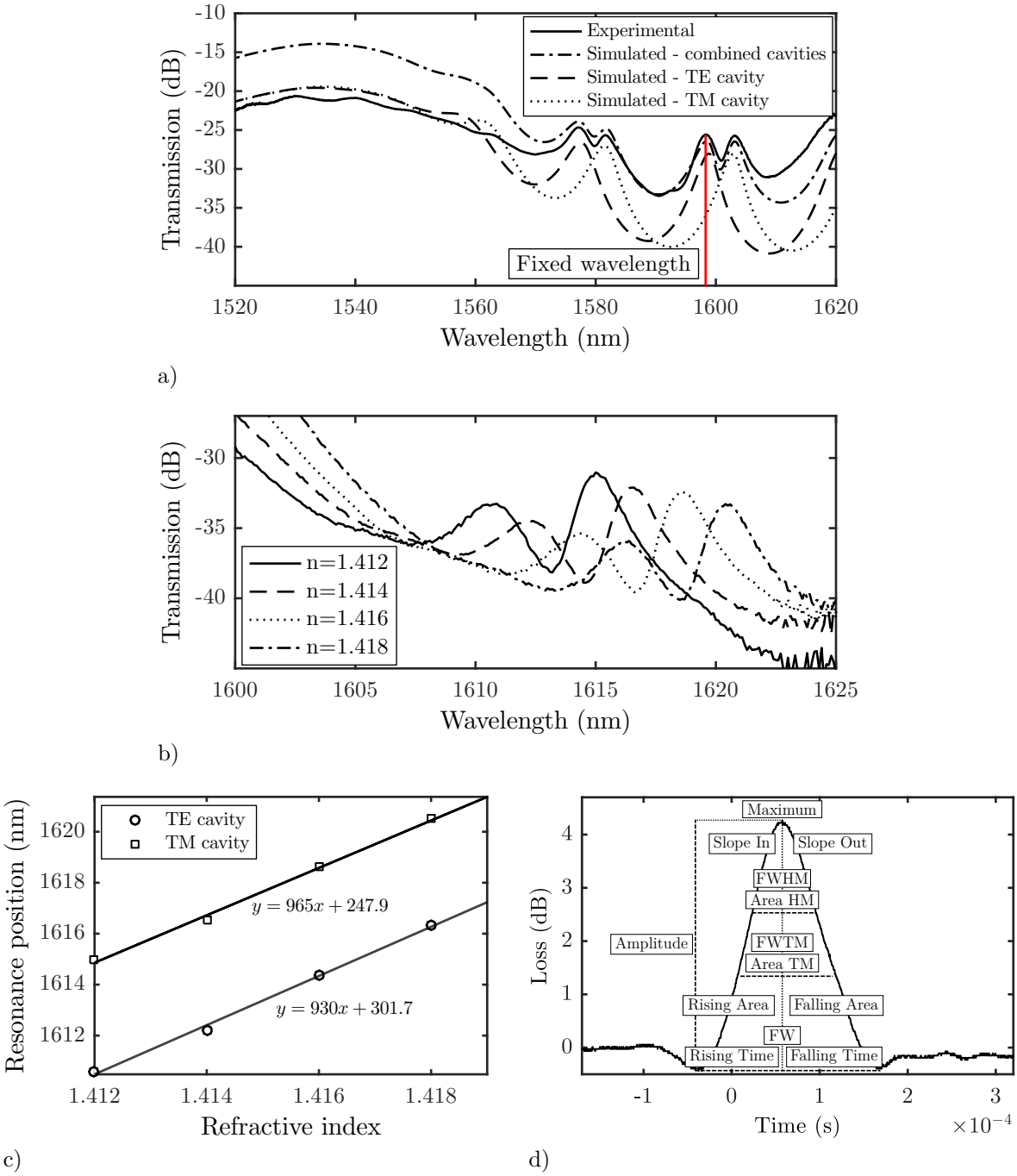

Figure 5.3 (a) Experimental spectrum of the Fabry-Pérot cavity with DBRs widths of 2.0 μm, microchannel width of 35 μm and rib waveguide width of 5.5 μm (solid line) and simulated spectra for the *TE cavity* (dashed line), *TM cavity* (dotted line) and combined cavities (dashed-dotted line). (b) Superimposed spectra of the Fabry-Pérot resonance peaks shifts with corresponding refractive index value and (c) fitted linear regressions used to calculate the sensitivity of the *TE* and *TM cavities*. (d) Typical voltage variation in time curve for a single cell passage with corresponding extracted parameters.

of 5 $\mu l/min$. Higher flows will increase the velocity of cells in the cavity but cell deforming forces also rise. In particular, narrowing microchannels induce an elongation force which can rupture the cellular membrane above a certain threshold, thus limiting the operating flow rate.

Table 5.1 Fabry-Pérot resonances properties calculated from experimental spectra for the *TE* and *TM cavities*

	TE cavity	TM cavity
Loss at Maximum (dB)	-25.6	-25.7
FWHM (nm)	4.16	4.18
FSR (nm)	21.2	21.55
Finesse	5.1	5.2
Sensitivity (nm/RIU)	965	930
LOD (RIU)	1.55×10^{-5}	1.61×10^{-5}

5.5.3 Promyelocytic leukemia biological model

The HL-60 cells were differentiated into neutrophils and basophils based on two distinct cell culture conditions. The efficacy of the differentiation was monitored by performing a Wright-Giemsa staining. Expectedly, the neutrophils exhibited segmented nuclei, while the basophils presented with vacuoles (Fig. 5.4d). As all samples presented distinct characteristics, we then aimed to determine if non-fluorescent parameters were sufficient to separate the cells by flow cytometry. As depicted in Fig. 5.4a, these cell culture conditions yielded cells with similar FSC-SSC profiles, such that they could not be readily discriminated by flow cytometry. Indeed, in the culture condition promoting neutrophil differentiation, the HL-60 cells tended to be a bit smaller and less dense than both undifferentiated cells and basophils. Still, overlay graphical representation of HL-60 in neutrophil promoting conditions over undifferentiated HL-60 cells (Fig. 5.4b blue vs green, respectively) or over HL-60 cells cultures in basophil-promoting conditions (Fig. 5.4c blue vs red, respectively) demonstrates that these conditions cannot be effectively separated based on either FSC or SSC and even when using both FSC and SSC as dot plot representation (Fig. 5.4a). To that effect, computed OLRs on flow cytometry data using equation 5.2 returned values of 1 for all combined cellular populations (see Table 5.2), validating that no discrimination could be established between these conditions.

On the other hand, microsystem measurements demonstrate a clear discrimination between some cellular populations. Fig. 5.3e shows baseline culture conditions, neutrophils and basophils solutions measured separately with the gated main population and bottom panel

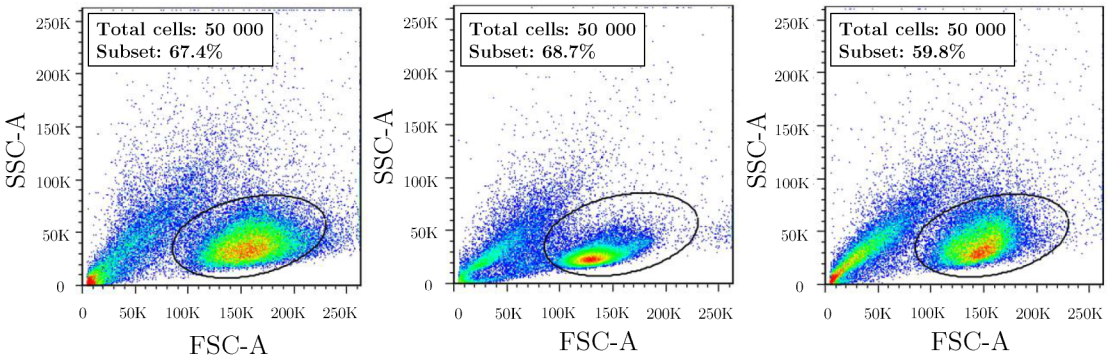
Total cells: 50 000
Subset: 67.4%
Total cells: 50 000
Subset: 68.7%
Total cells: 50 000
Subset: 59.8%
SSC-A
FSC-A
0
50K
100K
150K
200K
250K

a)

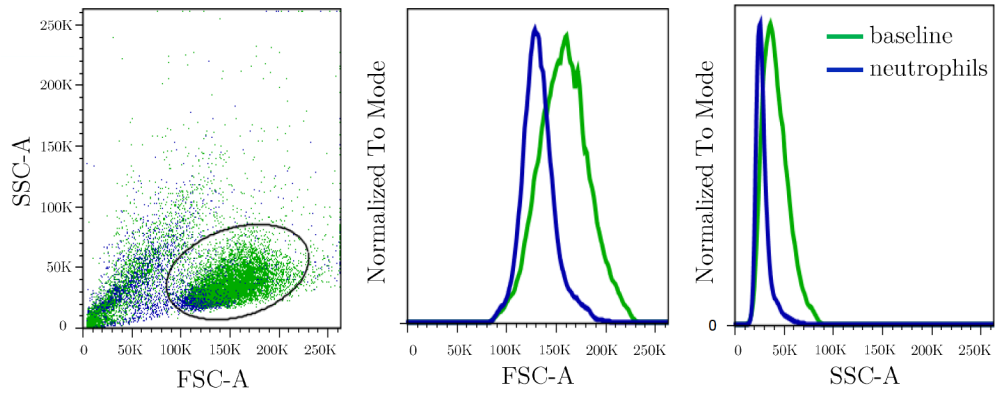
SSC-A
FSC-A
Normalized To Mode
baseline
neutrophils
SSC-A
0
50K
100K
150K
200K
250K

b)

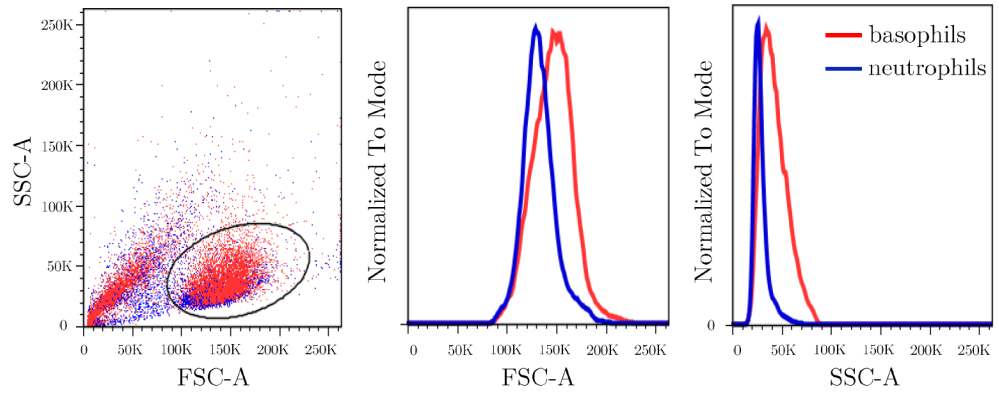
SSC-A
FSC-A
Normalized To Mode
basophils
neutrophils
SSC-A
0
50K
100K
150K
200K
250K

c)

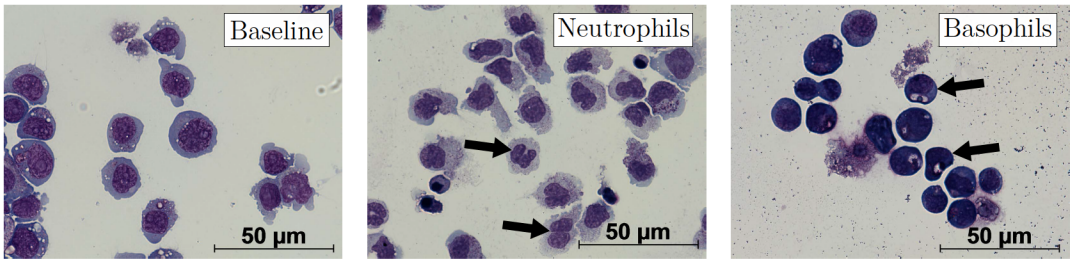
Baseline
Neutrophils
Basophils
50 µm

d)

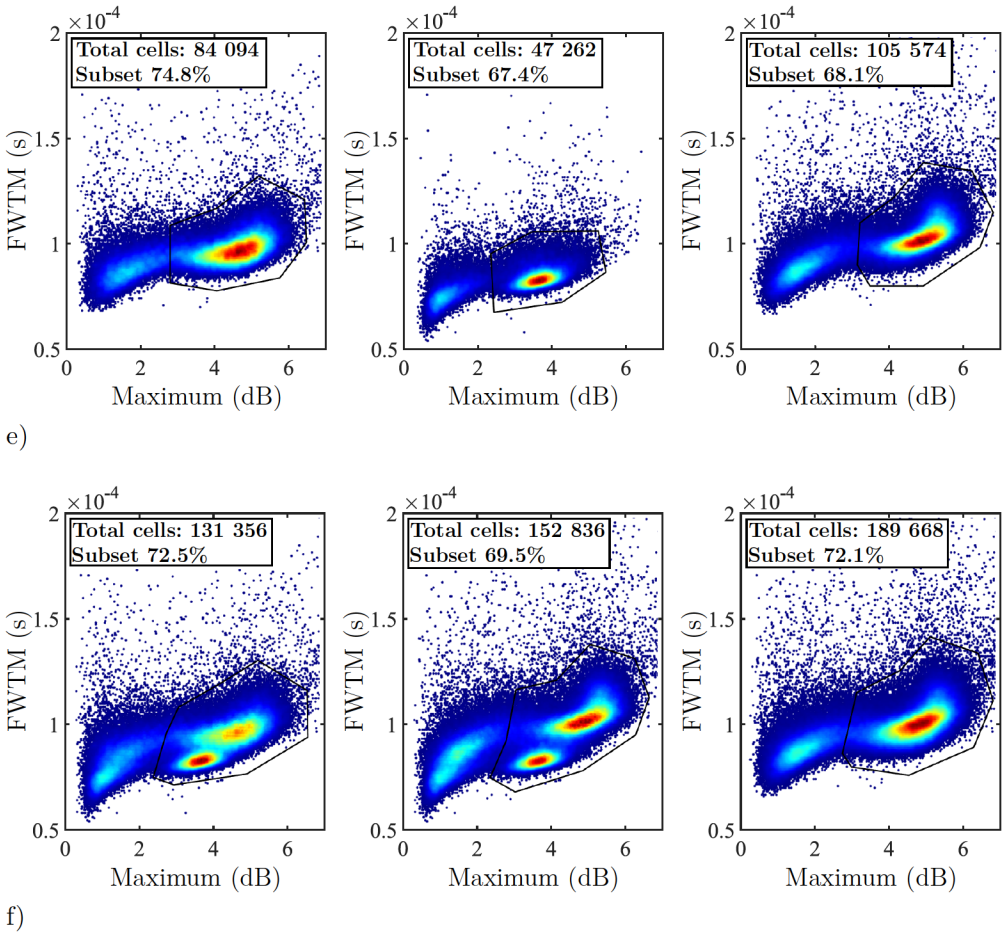

Figure 5.3 HL-60 differentiated into basophils and neutrophils cannot be distinguished by typical FSC-SSC flow cytometry profiles. (a) Typical FSC-SSC profiles of HL-60 cells differentiated neutrophils (middle) or basophils (right). The baseline culture condition is also shown (left). The total number of measured cells and the percentage of gated cells is shown. (b) and (c) respectively depict overlays for baseline vs neutrophil-differentiating conditions and basophil- vs neutrophil-differentiating conditions; in dot plot (left), in FSC histogram (middle) and in SSC histogram (right) for baseline in green, neutrophils in blue and basophils in red. One representative of at least three experiments. (d) HL-60 cells were differentiated for 7 days into neutrophils (middle) or basophils (right). The baseline culture condition is also shown (left). Arrows on the right panel point to cells bearing vacuoles, typical of basophils, while arrows on the middle panel point to cells bearing a segmented nucleus characteristic of neutrophils. One representative of at least three experiments. (e) Color-coded density scatter plots in function of Maximum and FWTM for separately measured baseline culture conditions (left), HL-60 cells differentiated neutrophils (middle) and basophils (right) solutions and (f) combined cellular populations for baseline vs neutrophil-differentiating conditions (left), basophil- vs neutrophil-differentiating conditions (middle) and baseline vs basophil-differentiating conditions (right). The total number of measured cells and the percentage of gated cells is shown. One representative of at least two experiments.

shows all combinations of these cellular populations. Discrimination occurs for baseline culture condition over neutrophil-differentiating conditions (Fig. 5.3f left, $OLR < 0.4$) as well as basophil- over neutrophil-differentiating conditions (Fig. 5.3f middle, $OLR < 0.4$). Discrimination between baseline culture condition over basophils-differentiating conditions could not be established (Fig. 5.3f right, $OLR = 1$). Axes on Fig. 5.3e and 5.3f were chosen for both simple association with optical power variation signal and better graphical visualization.

Table 5.2 reports the computed OLRs on each combination of HL-60 cellular populations for the flow cytometer and the microsystem. The parameters used to compute the flow cytometry OLR are FSC-A, FSC-W, SSC-A and SSC-W whereas the parameters for the microsystem OLR are FWHM, FWTM, Rising time, Falling time and FW in the first experiment and Maximum, FWHM, FW, Maximum/FW and Maximum/FWHM in the second experiment. Optimal OLR parameters are not exactly the same between experiments since the five linearly covariant parameters yielding the lowest OLR were chosen in each case. Thereupon, variation of biophysical properties between experiments as well as resonance peak profile variations due to re-coupling are factors inducing changes in optimal parameters for OLR computation. Nevertheless, cell populations with at least one two-parameter OLR less than 0.8 are always distinguishable whereas the ones with all two-parameters OLRs equal to 1 are never distinguishable, no matter which parameters are used. Conveniently, OLR parameters can be chosen for each set of experiments to palliate for variations without hindering the overall discrimination capability of the device. Consequently, FSC-SSC based flow cytometry could not distinguish between any of the HL-60 cells populations whereas the microsystem could distinguish between both neutrophil-differentiating conditions and undifferentiated HL-60 cells as well as neutrophil- and basophil-differentiating conditions in each experiment. Since FSC measurements reported no significant difference regarding the cell sizes, sensor measurements are confirmed to rely predominantly on the effective volume refractive index of the cells. These results confirm that our novel microphotonic sensor grants a substantial improvement on cellular population discrimination. It can be used complementar-

Table 5.2 OLR coefficients comparison between the flow cytometer and the microsystem for each experiment

	Flow cytometry		**Microsystem**	
Experiment	#1	#2	#1	#2
Baseline - Neutrophils	1	1	0.13	0.36
Basophils - Neutrophils	1	1	0.003	0.36
Baseline - Basophils	1	1	1	1

ily to flow cytometry, enhancing its sorting capabilities, and thus provide crucial information for research and clinical professionals.

5.6 Conclusion

We described a novel microphotonic system based on cellular refractive index measurement which represents an added value to actual cell counters and flow cytometry because of its improved ability to discriminate cell populations. Identification of HL-60 cells differentiated into neutrophils and basophils as well as a baseline culture was investigated and proved to be indistinguishable using FSC-SSC based flow cytometry while being distinguishable with our microsystem in the cases of baseline vs neutrophils and basophils vs neutrophils. Thus, this device represents an important step towards better cellular measurement capabilities. Furthermore, this microsystem does not require any dye treatment, accepts any cell shape and can reach measurement rate of several thousand cells per second.

Acknowledgments

The authors wish to thank the clinical hematology laboratory staff at Hôpital Maisonneuve-Rosemont for technical support with the Wright-Giemsa staining, the staff at Polytechnique Montreal's Laboratory of Microfabrication for technical support with microfabrication processes and Dr. Claire Viallard for technical support with imaging. This work is supported in part by the Natural Sciences and Engineering Research Council of Canada (NSERC) [grant number PGSD3-445848-2014], the Fonds de recherche du Québec – Nature et technologies (FRQNT) [grant numbers Equipe 173638 and RQMP 187779]. S. Lesage and J.-S. Delisle hold respectively a Senior and Junior II career award from the Fonds de recherche du Québec – Santé (FRQS).

CHAPTER 6 ARTICLE 3 - ON-CHIP REFRACTIVE INDEX CYTOMETRY FOR WHOLE-CELL DEFORMABILITY DISCRIMINATION

This chapter is a reproduction of an article published in Lab on a Chip.[1] Importantly, this final article included in this thesis demonstrates the exploitation of whole-cell deformability for unprecedented discrimination based on physical cellular properties. This chapter also introduces a signal replication simulation model from which effects of cell deformation and nucleus positioning are comprehensively described. Sections 6.1–6.6 are reproduction of the main manuscript whereas section 6.7 is a reproduction of the published electronic supplementary information (ESI). References to objects in ESI are identified by the symbol † in the main manuscript. Some terms in this chapter have been replaced to consistently preserve the definitions presented in the previous chapters.

6.1 Authors and affiliations

Antoine Leblanc-Hotte,[a,*] Nadine Sen Nkwe,[b] Geneviève Chabot-Roy,[c] El Bachir Affar,[b] Sylvie Lesage,[c,d] Jean-Sébastien Delisle,[e,f,g] and Yves-Alain Peter [a]

[a] *Department of Engineering Physics, Polytechnique Montreal, Montreal, QC H3T 1J4, Canada.*

[b] *Maisonneuve-Rosemont Hospital Research Center, Department of Medicine, University of Montreal, Montreal, QC H1T 2M4, Canada.*

[c] *Cellular Immunogenetics Laboratory, Maisonneuve-Rosemont Hospital Research Center, Montreal, QC H1T 2M4, Canada.*

[d] *Département de microbiologie, infectiologie et immunologie, University of Montreal, Montreal, QC H3C 3J7, Canada.*

[e] *Cancer and Transplantation Immunology Laboratory, Maisonneuve-Rosemont Hospital Research Center, Montreal, QC H1T 2M4, Canada.*

[f] *Department of Medicine, University of Montreal, Montreal, QC H3C 3J7, Canada.*

[g] *Hemato-oncology service, Maisonneuve-Rosemont Hospital, Montreal, QC H1T 2M4, Canada.*

[1] A. Leblanc-Hotte, N. Sen Nkwe, G. Chabot-Roy, E. B. Affar, S. Lesage, J.-S. Delisle, and Y.-A. Peter, "On-chip refractive index cytometry for whole-cell deformability discrimination," *Lab on a Chip*, vol. 19, no. 3, pp. 464–474, 2019 – Reproduced by permission of The Royal Society of Chemistry. DOI: 10.1039/C8LC00938D

6.2 Abstract

On-chip high-throughput phenotyping of single cells has gained a lot of interest recently due to the discrimination capability of label-free biomarkers such as whole-cell deformability and refractive index. Here we present on-chip refractive index cytometry (RIC) for whole-cell deformability at a high measurement rate. We have further exploited a previously published on-chip optical characterization method which enhances cellular discrimination through the refractive index measurement of single cells. The proposed on-chip RIC can simultaneously probe the cellular refractive index, effective volume and whole-cell deformability while reaching a measurement rate up to 5000 cells per second. Additionally, the relative position of the nucleus inside the cell is reflected by the asymmetry of the measured curve. This particular finding is confirmed by our numerical simulation model and emphasized by a modified cytoskeleton HL-60 cells model. Furthermore, the proposed device discriminated HL-60 derived myeloid cells such as neutrophils, basophils and promyelocytes, which are indistinguishable using flow cytometry. To our knowledge, this is the first integrated device to simultaneously characterize the cellular refractive index and whole-cell deformability, yielding enhanced discrimination of large myeloid cell populations.

6.3 Introduction

The emergence of novel label-free biomarkers such as whole-cell deformability and refractive index (RI) stimulates substantial interest for integration onto on-chip single-cell phenotyping devices. Red blood cells (RBC) were one of the first type of cells to be extensively mechanically studied. Their lack of nucleus makes them a simpler cellular model and their large elasticity allows them to pass through capillaries smaller than their diameter. For RBC, whole-cell deformability has proven to be a specific biomarker for numerous pathologies such as malaria, anemia, diabetes and more [14]. Lately, more focus was put on white blood cells (WBC) whole-cell deformability measurement as a marker for disease such as chronic lymphocytic leukemia [15] as well as changes in cytoskeleton [16] and nuclear organization such as cell cycle phases and cellular differentiation [17–20]. Concurrently, mechanical phenotyping of other cell lines has shown the potential to discriminate malignant progression stages, lineage and even aging [182, 183]. Microfluidic devices are ideal candidates for measurement of single cells mechanical properties at high rates because of their small structures and controllable flow characteristics. Many devices use high-speed cameras to get the cells shape in different pinched [19] or extensional flow geometries [17, 20, 184–186]. These deformability cytometry (DC) platforms need off-line images analysis to extract mechanical

properties. However, later development of real-time deformability cytometry (RT-DC) has provided continuous in-line measurement of large cell populations [16–18, 183]. Still, most of these systems are limited by the camera frame rate (∼100 000 frames per second) and physically by the cell resting time at the stagnation or imagery point to a few thousands cells per second [20, 184]. Moreover, whole-cell deformability measurements by means of imagery may suffer from out-of-focus images caused by cell drifting at the stagnation point. Overcoming low throughputs, Dudani et al. reported a DC device analyzing 65 000 cells per second using a pinched-flow scheme and a very high frame rate. This device appears to be limited only by the maximum concentration of cells that can be focused [19]. While this reported measurement rate exceeds that of most flow cytometers and thus can provide complementary measurements if integrated, such addition would be costly. Overcoming cell drifting, Deng et al. reported a RT-DC cell stretcher device which collides inertially focused cells against the wall of a T-junction yielding a throughput around 500 cells per second [183]. Other devices have used transition time measurement of cells in a narrow microchannel but are inherently limited by the cells passage time to a few hundred cells per second [15, 182, 187, 188]. Recently published transition sensing microdevices established conditions allowing to account for cell size and surface adhesion [182, 188] previously criticized in these devices [20]. Optical stretching, atomic force microscopy (AFM) and micropipette aspiration of single cells has also reported insightful mechanical properties, although their measurement rate is limited to very few cells per minute [14, 18, 20, 189]. Furthermore, optical stretchers are limited to small forces and thus small deformation, AFM measurements cannot extend to whole-cell properties and micropipette aspiration is not suited for cells with a large nucleus/cytoplasm ratio.

Undoubtedly, deformation kinetics of eukaryotic cells inside a given microchannel is a complex and intricate phenomenon. whole-cell deformability is guided by the characteristics of the membrane, cytoskeleton (microfilaments, microtubules and intermediate filaments), nucleus, organelles and cytoplasm [182, 190]. Each of these entities have intrinsic physical properties such as tension, stiffness, shear modulus, elasticity, viscosity, shear-thinning, etc. Most studies report significantly different values of these properties. For example, the elastic modulus measured by AFM or by optical stretching report differences ranging above one order of magnitude [188]. For sake of comparison to most device, we herein measure whole-cell deformability using on-chip RIC.

To understand the mechanical properties of cells and predict their behavior in flows, deformation models have been thoroughly investigated using thin-shell homogeneous capsules in either square [191] or rectangular [192, 193] microchannels. Although providing the first insights on how capsule deformation is related to its mechanical properties, in particular

the elasticity, eukaryotic cells have a much more complex organization. More recent and intricate studies, triggered by the rise of RT-DC, have numerically simulated cells modeled as a viscoelastic material surrounded by a thin-shell with [190] or without [18] the influence of the deformed cell on the fluid flow. These models allowed to decouple the effect of the thin-shell from the bulk elasticity on the deformation and are the most accepted models for steady-state cell deformation in a straight channel. However, they do not include the effect of the nucleus, which has been shown to have an important contribution to the observed deformation of cells [183, 188]. The most comprehensive WBC simulation model was developed by Tatsumi et al. in which the cell nucleus was modeled as a second droplet inside the cell and which also considered shear-thinning effects of these non-Newtonian fluids [194]. It established that the size and position of the nucleus considerably affects the deformed shape of the cell. Simulations were performed in a contraction region where elongation forces are important and did not study the steady-state behavior.

On-chip measurement of single cell RI has also been investigated through various microsystems. It is a known label-free biomarker for identification of various cancer cells [4–8] as well as infections, malaria and anemia [9]. Recently, Schürmann et al. reported surprising findings showing that the RI of the nucleus is smaller than the cytoplasm [12], which disagreed with the established common perception of the cell organization and current literature [10, 11]. Their results, using quantitative phase microscopy (QPM) and assuming a spherical shape of the cells, were later confirmed by another group using the same technique [13]. Schürmann et al. later combined rotating cells inside a microchannel, QPM and fluorescence to quantitatively measure the 3D RI of HL-60 cells and further improved our understanding of the cell organization [150]. While these technologies are undoubtedly powerful, they do not provide the high measurement rate necessary for large cell population measurement. Combining 2D QPM and fluorescence on assumed ellipsoid-shaped single cells has the potential to achieve this high measurement rate [151]. However, the authors did not report large cell population measurements. Other integrated devices have been used for RI sensing at high measurement rates, reporting limit of detection (LOD) around 10^{-6} to 10^{-8} refractive index unit (RIU), using whispering gallery modes cavities, photonic crystals, surface plasmon and evanescent wave but all lack the depth of interaction required for whole cell characterization [195]. To overcome these limitations, we previously reported a microfabricated Fabry-Pérot resonator allowing larger volume interaction and thus better suited for single cell RI measurement at a high measurement rate [195]. Our approach significantly improved discrimination of cell populations when compared to flow cytometry but still did not distinguish all analyzed WBC solely on the basis of RI measurements.

In this study, we present on-chip refractive index cytometry (RIC) repurposed for whole-cell

deformability evaluation of single cells at a high measurement rate. We have further exploited the previously presented on-chip optical characterization method which has proven to enhance cellular discrimination through the RI measurement of single cells [195]. The presented on-chip RIC can additionally measure whole-cell deformability which, in this case, includes the relative position of the nucleus inside of the cell. Indeed, the first experiment on HL-60 cells treated with cytochalasin B, which breaks actin filaments formation, expectedly reported larger whole-cell deformability compared to the control population. To help understand the effect of deformation on the measured output curve, we developed a simple numerical simulation model in which the cell and the nucleus are modeled by ellipsoids. The model confirms that the proposed on-chip RIC can simultaneously probe the RI, effective volume and whole-cell deformability of single cells. Furthermore, one particular parameter related to the asymmetry of the curve, the ratio time, reflects the relative position of the nucleus inside the cell. Subsequently, the proposed device discriminated HL-60 derived myeloid cells such as neutrophils, basophils and promyelocytes, which are indistinguishable using flow cytometry. To our knowledge, this is the first integrated device to simultaneously characterize two distinct cellular physical characteristics, RI and whole-cell deformability, yielding enhanced discrimination of large myeloid cell populations while reaching a measurement rate up to 5000 cells per second. The proposed device has an interaction depth and a measurement rate suited for whole cell measurement of large cell populations while operating with potentially cheap and compact equipment thus offering possible integration into flow cytometers.

6.4 Materials and methods

6.4.1 RIC devices

The silicon-on-insulator (SOI) devices used for RIC in these experiments were presented in previous work [195]. Briefly, they were fabricated using conventional silicon micromachining using photolithography and deep reactive ion etching (DRIE). Distributed Bragg reflectors (DBRs) composing the Fabry-Pérot cavity were designed to achieve resonances in the near infrared (NIR). Rib waveguides were designed according to previously published work to yield a single-mode like propagation [148]. Devices were cut with optical quality facets, sealed with anodically bonded pyrex plates and tubing was glued at entry and exit points. The microfabricated devices batch yielded similar optical spectra and sensitivities around 950 nm/RIU. Fig. 6.1 shows a 3D rendering of the RIC device.

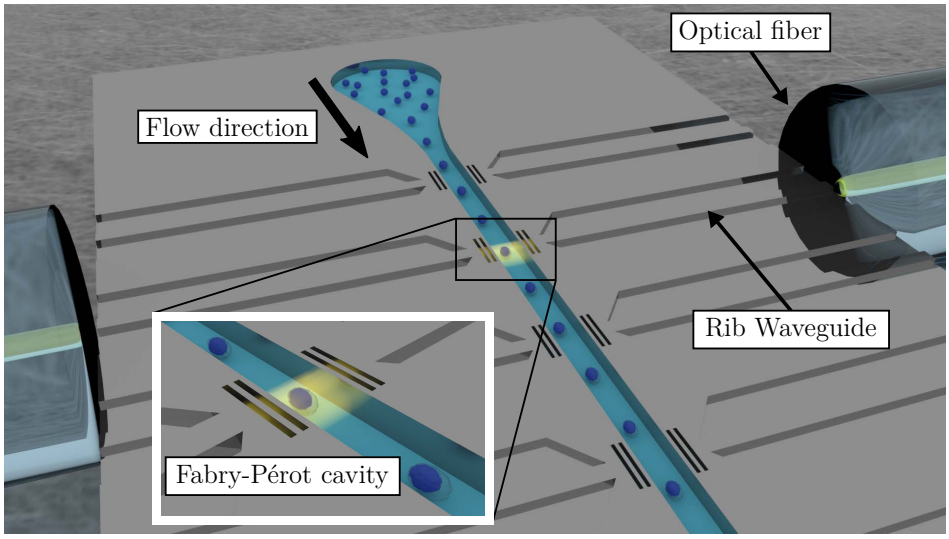

Figure 6.1 3D rendering of the silicon-on-insulator (SOI) RIC device.

6.4.2 Cell culture

For the first cellular model, HL-60 cell line (ATCC #CCL-240) was maintained in RPMI-1640 medium (Thermo Fisher Scientific) supplemented with 10% fetal bovine serum (FBS) in a humidified, 5% CO_2, air atmosphere. The media was supplemented with 1% penicillin/streptomycin and 1% L-glutamine. Cells were resuspended in PBS containing 2% FBS and 1 mM EDTA (Ethylenediaminetetraacetic acid) to prevent cell aggregation and treated with 30 μM cytochalasin B (MilliporeSigma) for 10 min at room temperature which strongly inhibits actin filaments formation. Cells were then collected and kept on ice prior to RIC measurement or flow cytometry. For immunostaining, 50 000 cytochalasin B treated and control cells were separately centrifuged on glass slides using a cytospin apparatus and fixed for 20 min using 3% paraformaldehyde. Cells were permeabilized in PBS containing 0.5% NP-40 for 30 min followed by incubation in a blocking solution (PBS with 0.1% NP-40 and 10% FBS). Then, F-actin was stained with the Alexa Fluor 488 phalloidin for 30 min and nuclei were stained with DAPI. Cells on the microscope slides were imaged using an inverted confocal fluorescence microscope (Olympus FV1000 LSM) with a 60X oil immersion objective lens. For cell size measurement, the cells were resuspended in a trypan blue solution and placed in a hemocytometer. Cells on the hemocytometer were imaged using an upright bright field microscope (Zeiss AxioImager Z2) with a 40X objective lens and equipped with a color CCD camera. Collected images were processed through Fiji distribution of ImageJ.

For the second cellular model, HL-60 cells were maintained in RPMI containing 20% fetal calf serum (FCS) and kept in a humidified, 5% CO_2, air atmosphere. Cells were passaged in

differentiation media, RPMI containing 10% FCS with 1% HEPES (baseline condition). To obtain neutrophils, 2×10^5 cells per ml were cultured with 1.25% dimethylsulfoxide (DMSO, Sigma) for seven days. To obtain basophils, 2×10^5 cells per ml were maintained for seven days in the absence of serum. At day 7 of culture, cells were harvested, washed in phosphate buffered saline (PBS) containing 2% FCS and 1 mM EDTA. The cells were counted and resuspended in PBS (2% FCS, 1 mM EDTA) at a concentration of 2 million cells per ml. All solutions, for both cellular models, were divided into two separate tubes, one for data acquisition with flow cytometry and one for data acquisition with RIC.

6.4.3 Single cell analysis

Cells were injected into the microchannel at a flow rate between 5 and 30 μl/min using a syringe pump (Harvard Apparatus, Pump 11 Pico Plus Elite) and focused using inertial effects. Cells were ordered with preferred interparticle spacing through repulsive viscous forces [55, 57]. In the presented experiments on cytochalasin B treated HL-60 cells, microchannel dimensions were H=15 μm and W=40 μm whereas for the HL-60 differentiated cells, microchannel dimensions were H=15 μm and W=30 μm. The cavities are placed 1.2 mm away from the beginning of the straight channel for both cellular model experiments. These cavities were chosen because their resonance peak exhibited the smallest loss and full width at half maximum. Cells traveling through the Fabry-Pérot cavity shift the resonance peak towards longer wavelength because of their larger RI than the surrounding fluid. A tunable laser source (Agilent, 8164B) fixed the propagating wavelength at the top of the Fabry-Pérot resonance, a fast InGaAs infrared photodetector (Thorlabs, DET01CFC) recorded optical power variations and relayed it to a high speed digitizer (National Instruments, NI-PXI 5114). Recorded curve analysis is done off-line using a custom MatLab algorithm.

6.4.4 Cellular population discrimination

An important characteristic of any flow cytometry device is its ability to discriminate cell populations. To evaluate the discrimination of our device, we introduce a discrimination coefficient, the *overlaprate* (OLR), as reported by Sun and Wang [180]. It quantifies the separation of two populations using their probability density functions [195]. This coefficient is preferred to conventional statistical tests, such as t-test or Mann-Whitney U test, since they reported very small p-values even when the populations are clearly not discriminated. This is due to the large number of samples and skewness of the population distributions. Furthermore, typical statistical tests can highlight differences between two populations but may not always reflect the discrimination capability. Thus, the OLR is better suited to

quantify discrimination in clinical use where cell populations are mixed.

The OLR is the ratio of the probability density function (PDF) value at the saddle point over the PDF value at the lowest local maximum.

$$OLR = \frac{PDF(X_{saddle})}{PDF(X_{lowest\ max})} \tag{6.1}$$

An OLR value of 1 indicates that the two populations cannot be discriminated. An OLR value greater than 0.8 indicates that the two populations are overlapping but still discriminated. Smaller OLR values indicate weakly overlapping populations and thus clear discrimination. Importantly, the OLR can be computed in any number of dimensions.

6.4.5 Numerical simulations

To better understand the effects of a cell deformation on the measured output curve, we developed a simple 3D numerical simulation model, shown in Fig. 6.2. The origin is located at the center point of the cavity where the x-axis is along the flowing direction, the y-axis is along the height of the microchannel and the z-axis is along the optical cavity width. The cell membrane and the nucleus were modeled as ellipsoids with varying radii. While volumes of each ellipsoid did not change, axial radii were allowed to vary as well as the x-axis offset of the nucleus. To match the mean calculated suspended sphere radius of HL-60 cells reported in Section 6.5.2, the spherical radius of the cell membrane was set to $R_{cell} = 6\ \mu m$. To match a $600 \pm 300\ \mu\text{m}^3$ HL-60 nucleus volume [12], the spherical radius of the nucleus was set to $R_{nuc} = 5.45\ \mu m$, corresponding to a realistic 0.75 volume ratio [188]. Based on results reported by Schürmann et al., the RI of HL-60 nucleus was set to $n_{nuc} = 1.355$ whereas the average RI of the whole cell was set to $n_{cell} = 1.378$. Considering the 0.75 volume ratio of the nucleus, the cytoplasm RI is calculated to be $n_{cyt} = 1.447$. The surrounding RI was set to the one of PBS ($n_{PBS} = 1.335$). Although the exact shape of the cell and nucleus in steady-state are approximated by ellipsoids, this model yields a simple yet effective description of the measured output curve.

The intensity profile of the optical mode inside of the cavity was modeled as a two-dimensional Gaussian of $3\sigma = 20\ \mu m$ in the x-axis and $3\sigma = 7.5\ \mu m$ in the y-axis and constant over the 35 μm width between the DBRs in the z-axis [195]. For each step of the cell flowing through the cavity, the volume overlap between the cell and the cavity mode intensity was numerically calculated and then projected onto the LP_{01} optical mode of a fiber with a diameter of 8.2 μm modeled using Bessel functions. This method approximates well the light portion collected at the output by the butt coupled single mode fiber and projected onto

the 2D photodetector area. The effective RI was calculated as the sum of the projected RIs weighted by their respective area ratios on the LP_{01} mode. Finally, the variation of RI from n_{PBS}, corresponding to an absence of cell, was plotted against time. The measured optical power curves are in good agreement with this effective RI numerical simulation over time (see Fig. 6.9† for examples of simulated curve).

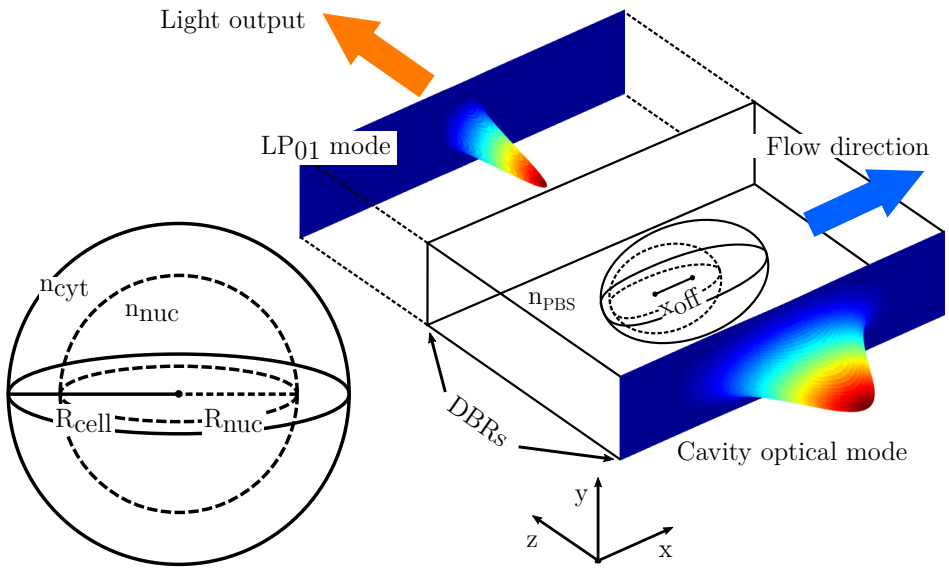

Figure 6.2 Numerical simulation scheme of the cell interaction with optical modes and the reference spherical cell.

6.5 Results and discussion

6.5.1 Single cell analysis

Microchannels dimensions and specific flow rates may yield cells spread around the inertial equilibrium positions in some experiments. However, planar DBRs do not generate a focal point, thus position of cells along the width of the microchannel had a negligible impact on the output signal. In the worst-case scenario (flow rate of 5 μl/min in the H=15 μm and W=40 μm channel), the focusing spread is 27.9 μm in width whereas in the best case (15 μl/min in the H=15 μm and W=30 μm channel), the spread is 12.5 μm. In this latter condition, considering a cell size of 12 μm, the cell centers are separated by 0.5 μm, thus yielding a good inertial focusing. The inertial focusing length equation from Zhou and Papautsky used for calculations and the resulting focusing spreads at different flow rates (Tables 6.2 and 6.3) can be found in ESI [58].†

For each acquired curve, meaningful parameters were extracted to compare the different

cellular populations. In particular, the full width (FW) represents the deformed length of the cell in the flowing direction (x-axis), the maximum (Max) corresponds to the largest effective RI measured and the area under the curve (Area) relates to the effective RI volume of the cell. The FW parameter is divided into two contributions, the rising time (RT) and the falling time (FT), from which the ratio time parameter is calculated as ratio time=RT/FT. The ratio time parameter reflects the relative position of the nucleus in the cell, as explained below. Measurements of losses vs time for single cells at different velocities are shown in Fig. 6.3. Fig. 6.3a corresponds to a cell at higher velocity, yielding a ratio time < 1, Fig. 6.3b to a cell at midrange velocity, yielding a ratio time ~ 1 and Fig. 6.3c to the particular case of cytochalasin B treated HL-60 cells at smaller velocity, yielding a ratio time > 1.

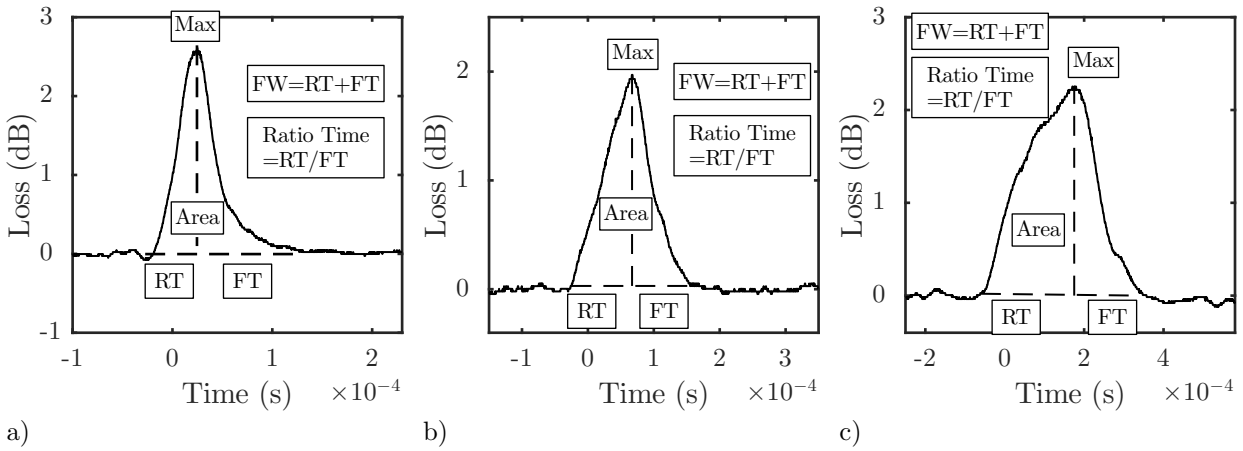

Figure 6.3 Measurement of losses vs time showing (a) a typical single cell at higher velocity corresponding to a ratio time < 1 (15 μl/min in a 15 μm $\times$ 30 μm channel cross-section, average flow velocity 0.56 m/s, average cell velocity 0.22 m/s), (b) a single cell at midrange velocity corresponding to a ratio time ~ 1 (10 μl/min in a 15 μm $\times$ 40 μm channel cross-section, average flow velocity 0.28 m/s, average cell velocity 0.13 m/s) and (c) the particular case of a single cell at lower velocity corresponding to a ratio time > 1 (5 μl/min in a 15 μm $\times$ 40 μm channel cross-section, average flow velocity 0.14 m/s, average cell velocity 0.06 m/s). Average cell velocities are approximated using a conversion factor from the average flow velocities $U_p = \gamma U_f$, where γ =0.45 for 12 μm cells in a 15 μm $\times$ 40 μm channel and γ =0.40 for a 15 μm $\times$ 30 μm channel. See ESI for derivation.†

For a given cell length in the flowing direction (FW), the position of the Max determines both the RT and FT, thus the ratio time. A symmetric cellular RI distribution yields a Max positioned at the midpoint of the curve (Fig. 6.3b), thus a ratio time of 1. Conversely, an asymmetric cellular RI distribution yields a shifted Max position (Fig. 6.3a and 6.3c). Numerical simulations reveal that the Max position is influenced by the amount of cytoplasm measured alone. This is explained by the larger RI of the cytoplasm ($n_{cyt} = 1.447$) compared

to the nucleus ($n_{nuc} = 1.355$). Two possible effects are assumed to impact the relative localization of the cytoplasm in the cell: the displacement and the deformation of the nucleus. To decouple these effects, two sets of simulations were implemented. In the first case, the position of the nucleus was varied while no deformation was imposed on either the cell or the nucleus. Computed ratio time values for each nucleus position are reported in Fig. 6.4a. The relative offset of the nucleus is $x_{off}/(dx_{cell} - dx_{nuc})$ where x_{off} is the absolute offset of the nucleus from the center of the cell ($x_{off} < 0$ is towards the trailing end fo the cell) and dx_{cell} and dx_{nuc} are the diameter of the cell and nucleus in the flowing direction (x-axis) respectively. In this case, $dx_{cell} = 2R_{cell}$ and $dx_{nuc} = 2R_{nuc}$ since there is no deformation imposed. For $x_{off} = 0$, the RI distribution is symmetric thus yielding a ratio time of 1.

In the second case, the position of the nucleus was set to the trailing end of the cell ($x_{off}/(dx_{cell} - dx_{nuc}) = -0.9$) while deformation of the nucleus in the x-axis was varied. Computed ratio time values for each step of nucleus deformation are reported in Fig. 6.4b. Fixed 10% contraction and 4% expansion deformations of the cell membrane ellipsoid in the y-axis and x-axis were imposed respectively. Y-axis contraction mimics the shear-stress generated by the channel top and bottom walls whereas x-axis expansion allows a symmetric range of nucleus deformations to be simulated. The nucleus radius was matched to the one of the cell in the y-axis by a 0.9% contraction deformation. The relative deformation of the

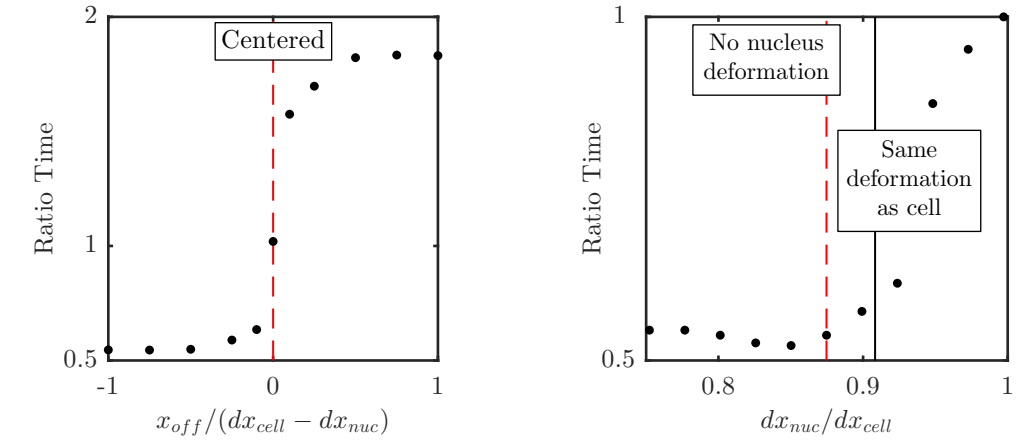

Figure 6.4 Computed ratio time values from simulated curve when varying (a) the nucleus offset in the x-axis and (b) the nucleus deformation in the x-axis. Red dashed lines mark the centered nucleus position in (a) and the undeformed nucleus in (b). Full black line marks the equal 4% deformation of the nucleus and the cell in the x-axis. Each steps in (a) are 25% offset except for the two points closest to the centered position which are ±10%. Each steps in (b) are 2.5% deformation.

nucleus in the x-axis is dx_{nuc}/dx_{cell}. An undeformed nucleus in the x-axis corresponds to a relative deformation of ∼0.875 and a 4% deformed nucleus (same as imposed on the cell) corresponds to a relative deformation of ∼ 0.91. These values are identified by the red dashed and full black vertical lines in Fig. 6.4b respectively. The bounding limits, $dx_{nuc}/dx_{cell} = 1$ and $dx_{nuc}/dx_{cell} \sim 0.75$, correspond to a nucleus the same length as the cell in the x-axis and to a nucleus the same length as the cell in the z-axis respectively. For $dx_{nuc}/dx_{cell} = 1$, the RI distribution is symmetric thus yielding a ratio time of 1.

An asymmetric cellular RI distribution, leading to ratio time values greater or smaller than 1, can only appear if the nucleus is displaced relatively to the cytoplasm. Simulation results clearly indicate that the offset of the nucleus has a predominant impact on the measured ratio time. Indeed, for small relative offset of the nucleus the ratio time value varies rapidly. Contrarily, small relative nucleus deformation have a weak impact on the ratio time. Importantly, relative nucleus deformation in the x-axis larger than $R_{nuc}/R_{cell} \sim 0.91$ implies that the nucleus has a greater deformation than the cell (imposed at 4% in the simulations). This behavior is not realistic, especially considering that the nucleus is stiffer than the surrounding cytoplasm [188]. Thus, based on the simulation model, the relative position of the nucleus in the cell predominantly influence the ratio time value and the impact of the nucleus deformation is negligible. Curve parameters (Max, FW, Area, RT and FT) dependencies in function of the relative nucleus position can be found in Fig. 6.11.†

Ultimately, for discrimination of cells, the ratio time and FW parameters can both reflect the whole-cell deformability. Softer cells deform more and yield larger FW values which inevitably yield smaller ratio time values, when considering a similar relative position of the nucleus. Indeed, for similar relative nucleus positions >±10%, the rising time value of softer and stiffer cells is approximately the same (Fig. 6.12d†). Since the FW is larger for softer cells (Fig. 6.12b†), the Falling time is inevitably larger (Fig. 6.12e†) and thus the ratio time is smaller (Fig. 6.12f†). Computed curve parameters dependencies to deformed cell length are reported in Fig. 6.12.†

6.5.2 Cytochalasin B treated HL-60 cells model

A known drug employed to study the role of cytoskeleton on HL-60 whole-cell deformability is cytochalasin [16, 17, 188, 196]. This agent disrupts filamentous actin formation within cells and thus allows for increased whole-cell deformability. Indeed, actin filaments are crucial for the cells to maintain their shape [182]. Thus, treating cells with cytochalasin allows cellular mechanical phenotyping since the modified cytoskeleton, specifically microfilaments composed of actin, directly impacts whole-cell deformability. Therefore, we treated HL-60

cells with cytochalasin B and evaluated the variation in whole-cell deformability by cytospin [197, 198]. Cytospun cells projected onto a microscopic slide spread more or less depending on their whole-cell deformability. Confocal fluorescence microscopy images (Fig. 6.13†) show that treated cells present clumps of phalloidine fluorescence. These clumps are associated to grouped broken-down actin filaments, responsible for the larger whole-cell deformability. Also, treated cells reported a larger mean area and a smaller mean height, as expected. Importantly, the calculated mean volumes of treated and control cells completely overlap thus confirming that the drug treatment did not affect the size of the cells. Furthermore, measured suspended cell sizes using conventional microscopy confirms an undeformed radius of approximately 6 μm for both control and cytochalasin B treated cells. Table 6.1 reports the calculated mean area, height and volume of both control and cytochalasin B treated HL-60 cells using confocal fluorescence microscopy images as well as the measured suspended cell radius using bright field images. Cells from confocal fluorescence microscopy were approximated as cylindrical shaped since the cytospin method has made them lose their spherical geometry.

Table 6.1 Calculated areas, heights, volumes and suspended sphere radii (mean ± standard deviation) of cytospun ($N = 5$) control and ($N = 5$) cytochalasin B treated HL-60 cells using confocal fluorescence microscopy images. Measured suspended cell radius of ($N = 336$) control and ($N = 379$) cytochalasin B treated HL-60 cells using bright field images. Coefficients of variation (CV) are reported for suspended cells radii. P-values are from t-test.

	Control	Cytochalasin B treated	P-value
Area (μm^2)	148 ± 14	195 ± 29	0.02
Height (μm)	6.0 ± 0.5	4.6 ± 0.5	< 0.01
Volume (μm^3)	883 ± 104	895 ± 163	0.89
Sphere radius (μm)	5.9 ± 0.2	6.0 ± 0.3	0.92
Cell radius (μm)	6.2 ± 0.8	6.3 ± 0.9	0.05
CV	12.7%	14.3%	N/A

To further confirm that the drug treatment only altered the whole-cell deformability, we measured both populations using flow cytometry. It is clear that the cytochalasin B treated cells cannot be discriminated from the non-treated control using flow cytometry FSC-SSC measurements (2D OLR=1, Fig. 6.14†). The histograms (Fig. 6.14b and 6.14c†) confirm once more that the size (FSC) and granularity (FSC) of the two cell populations completely overlap.

To determine whether our RIC device could discriminate cells based on whole-cell deformability at a high measurement rate, we proceeded to assess the two cell populations. The time window necessary to measure a single cell at the imposed flow rate of 15 μl/min was 3×10^{-4}

s. Considering a perfect train of cells, this yields a measurement rate around 3000 cells per second. Fig. 6.5a reports the density-colored dot plot combination of the RIC measurements for control and cytochalasin B treated HL-60 cells in function of the Area and ratio time parameters. Fig. 6.5b and 6.5c report the Area and ratio time histograms for both cell populations respectively. The Area parameter of both cell populations is approximately the same, confirming that the effective RI volume of the cells is similar. This agrees well with the calculated volumes in Table 6.1 and FSC results (Fig. 6.14b†). Contrarily, the ratio time parameter shows a significant difference between the two populations which suggest distinct cellular behavior. The computed OLR for control and Cytochalasin B treated HL-60 cell populations presented in Fig. 6.5a is 0.3, indicating a clear discrimination. Calculated coefficients of variation (CV) for flow cytometry and RIC are reported in Tables 6.7 and 6.8† respectively. CV of RIC measurement for the Area parameter (Table 6.8†), which has the largest values, are similar to the biological variation observed on the size measurement in Table 6.1. Thus the device induces very small additional variation and the position of the cells in the channel has limited effect on the measurements.

To understand the effects yielding a smaller ratio time value of cytochalasin treated cells, FW, RT and FT parameters are compared. Fig. 6.5d, 6.5e and 6.5f show the histograms of FW, RT and FT for both cell populations respectively. First, cytochalasin treated cells show larger mean values of FW. This indicates cells that are more deformed in the flowing direction (x-axis). Furthermore, the larger FW of treated cells is due to the larger FT since the RT is similar. This explains the smaller ratio time value of treated cells. As predicted by our numerical simulation model, for similar relative position of the nucleus, more deformed cells yield smaller ratio time values. Indeed, at this flow rate, both cell populations have mean ratio time values smaller than 1, indicating a nucleus positioned at the trailing side of the cell.

However, small differences in the relative position of the nucleus are not accurately measured by the RT and FT (Fig. 6.11d and 6.11e†). Contrarily, in our simulations, the Max parameter showed increasing values for increasing relative position of the nucleus (Fig. 6.11a†). Thus, in this experiment, the larger Max value for treated cells, showed in Fig. 6.5g, is suspected to come mainly from the increase in relative position of the nucleus. The contribution to the Max value from adding cytochalasin B into the cell cytoplasm is negligible since the effective RI volume variation is negligible (Area parameter in Fig. 6.5b). Overall, the cytochalasin B treated HL-60 cells lack actin filaments which act to maintain the cell shape. These cells undergo more deformation due to the flow induced forces compared to the control population. Thus, cytochalasin B treated HL-60 cells have a larger FW value and a smaller ratio time value than HL-60 control cells, in line with their higher degree of whole-cell deformability.

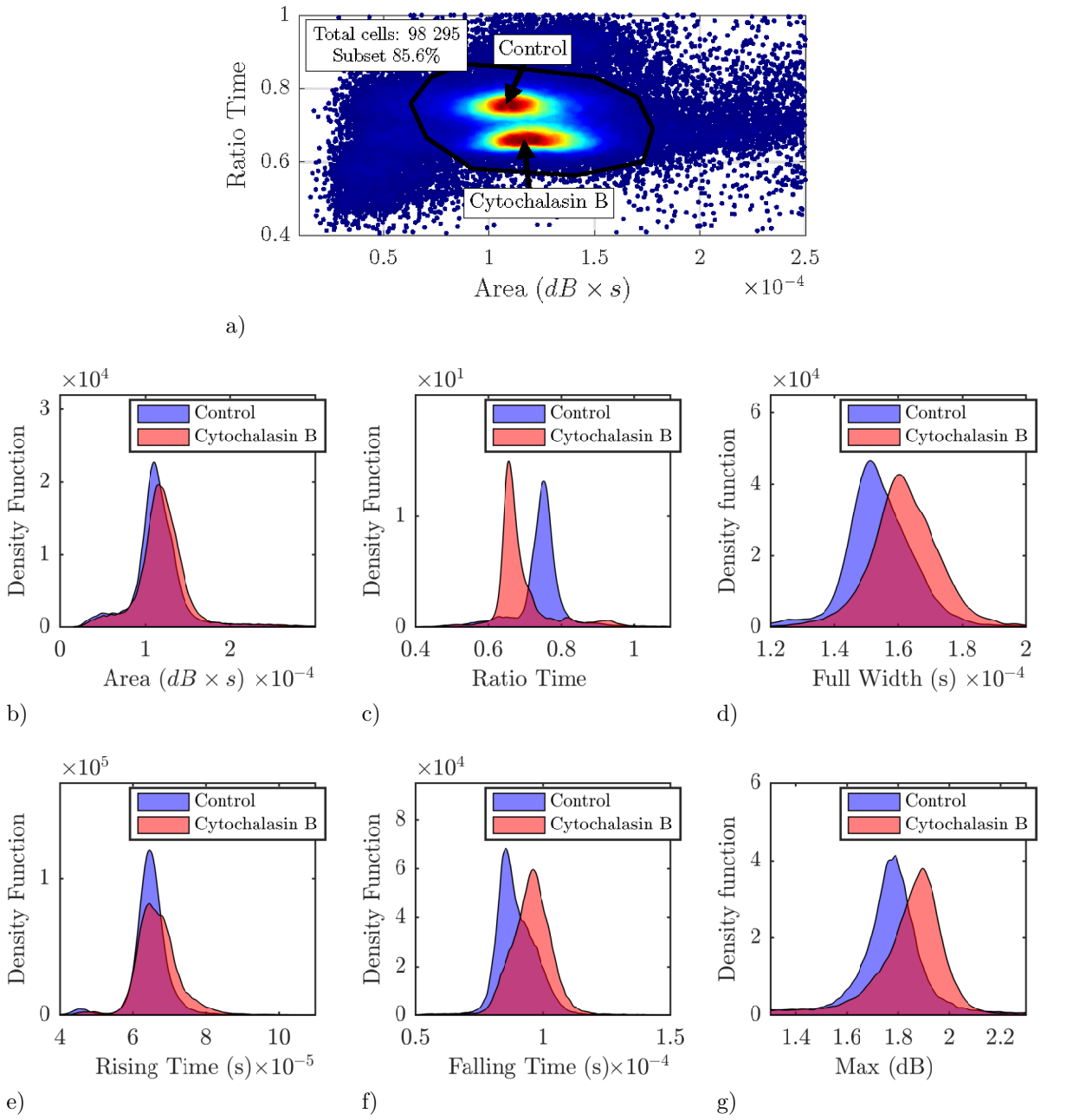

Figure 6.5 (a) RIC Area and ratio time density-colored dot plot combination for control and Cytochalasin B treated HL-60 cells (2D OLR=0.3) at a flow rate of 15 μl/min. Cytochalasin B treated HL-60 cells have a smaller ratio time value than HL-60 control cells, in line with their higher degree of whole-cell deformability. Histograms of control and Cytochalasin B treated HL-60 cells for (b) Area (1D OLR=1), (c) ratio time (1D OLR=0.4), (d) full width (FW) (1D OLR=1), (e) rising time (RT) (1D OLR=1), (f) falling time (FT) (1D OLR=1) and (g) Max (1D OLR=1). Subset is used for OLR calculations. One representative of at least four experiments.

6.5.3 Parameters variations with flow

We then proceeded to evaluate each parameter dependency to flow rate to verify our numerical simulation model predictions for varying deformed cell length (Fig. 6.12†). Larger flow rates implies larger forces acting on the cell thus more deformation is anticipated. As expected, all parameters followed the predicted tendencies for both control and cytochalasin treated HL-60 cells (Fig. 6.15†). In particular, increasing flow rates lead to increasing values of FW and FT while values of RT and Area are relatively constant. Thus, larger flow rates exert larger fluidic forces on the cells which in turn yield larger deformation in the flowing direction.

Interestingly, at a flow of 5 μl/min (particle velocity $U_p = 0.06$ m/s), both cell populations report signals yielding a ratio time value > 1, similar to the curve presented in Fig. 6.3c. This indicates a nucleus positioned at the leading side of the cell rather than at the trailing side. At a flow of 10 μl/min ($U_p = 0.13$ m/s), the ratio time is very close to or slightly larger than 1, indicating near-symmetric RI distribution and a centered nucleus. For flows > 15 μl/min ($U_p > 0.19$ m/s), ratio time values are < 1 indicating a nucleus positioned at the trailing side of the cell. These results suggest a transition between 5 and 15 μl/min for the nucleus to be placed at the leading or trailing side of the cell. The derivation methods for particle velocities, their related Reynolds number at each flow rate and a potential explanation for this transition based on particle Reynolds number can be found in ESI.†

Subsequently to this ratio time transition, parameters according discrimination for these cellular populations are not the same at all flows. At flows of 5 and 10 μl/min, the larger rising time values of cytochalasin B treated cells can be used to discriminate them from the control (1D OLR of 0.90 and 0.92 respectively, Fig. 6.15d†). Conversely to the analysis presented at 15 μl/min in the previous section, the larger FW of treated cells is now due to the larger RT since the FT is similar at each of these flow rates. This explains the larger ratio time value of treated cells. Again our numerical simulation model predicts that more deformed cells yield larger ratio time values when the nucleus is similarly positioned towards the leading side. Indeed, at this flow rate, cytochalasin B treated cells have ratio time values larger than 1, indicating a nucleus positioned at the leading side of the cell. At 15 μl/min, the FT of cytochalasin B treated cells is larger leading to a lower ratio time, as previously shown in Fig. 6.5. At a flow of 20 μl/min, no parameters allow for discrimination of cell populations. In particular, the FW of both cell populations is similar (Fig. 6.15b†). This suggest that forces acting on the cells reached the actin cytoskeleton limit to influence significantly the deformed shape of the cells. Thus, in the cytochalasin B treated HL-60 cells case, there exist a limit for cell deformation after which increasing the flow rate does not promote discrimination based on whole-cell deformability. For the largest flow of 30 μl/min, cytochalasin B treated cells

teared apart, blocked the microchannel and greatly affected data acquisition. Measured cells are suspected to be considerably damaged, as suggests the significantly lower Area parameter value (Fig. 6.15c†) and should not be considered for discrimination purposes in this case. Cell tearing is suspected to come from strong elongation forces induced by contraction regions prior to the beginning of the straight channel which can be engineered to be more gentle. In contrast, control cells did not tear, probably due to their actin cytoskeleton protection, and reported a measurement rate of 5000 cells per second.

6.5.4 Differentiated cells model

Once the whole-cell deformability discrimination capability of our RIC device was confirmed, we desired to test whether it could readily separate cells known to be undiscriminated by flow cytometry. This is usually the case for granulocytes, namely basophils, neutrophils and eosinophils. Thus, HL-60 cells maintained in baseline conditions and differentiated into neutrophils and basophils were analyzed by flow cytometry and RIC. Fig. 6.6 reports the flow cytometry measurements of these three cell populations. The superimposed dot plot in Fig. 6.6a shows that neutrophils, basophils and baseline conditions are strongly overlapping and thus no discrimination occurs (2D OLR neutrophils-basophils=1, neutrophils-baseline=1 and basophils-baseline=1). FSC-A and FSC-A histograms reported in Fig. 6.6b and 6.6c respectively show that even if neutrophils are slightly smaller in size (FSC-A) and have less granularity (FSC-A) they cannot be distinguished. Also, basophils show a slightly larger FSC-A value but still strongly overlap with the baseline conditions and their FSC-A histograms almost completely overlap.

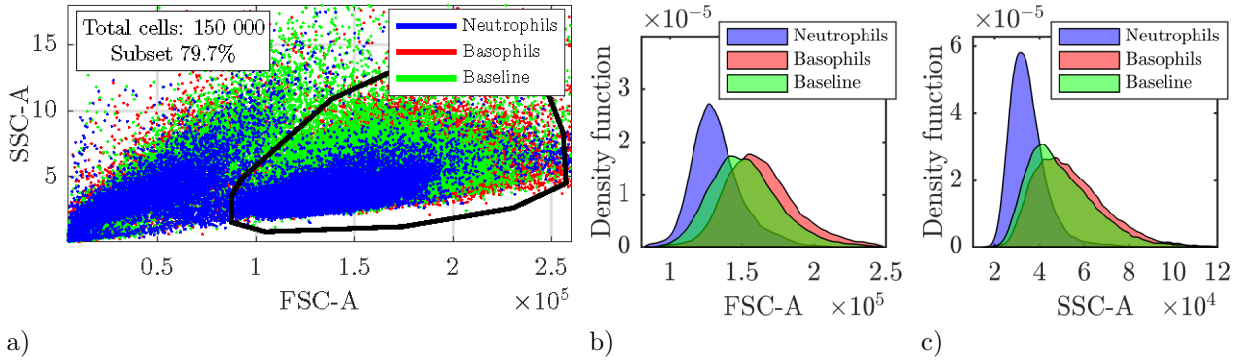

Figure 6.6 (a) Flow cytometry FSC-A and SSC-A dot plot superimposition of HL-60 cells maintained in baseline conditions and differentiated into neutrophils and basophils. (b) FSC-A histograms and (c) SSC-A histograms of subsets. 2D OLR for any combination of two myeloid cell populations is 1. One representative of at least three experiments.

In contrary, RIC measurements grants simultaneous discrimination of all three cell populations. Fig. 6.7 reports the density-colored dot plots of the RIC measurements for the three cell populations in function of the ratio Max/FW and rising time. Neutrophil-differentiating conditions are reported in Fig. 6.7a, basophil-differentiating conditions in Fig. 6.7b, baseline culture conditions in Fig. 6.7c and the combination of all three conditions in Fig. 6.7d. The parameters for each axis of the dot plot were chosen so that the three populations are simultaneously visually separated when combined without major correlation. Computed OLR in those axes for all combination of myeloid cell populations do not yield values smaller than 1 in all cases (2D OLR neutrophils-basophils=0.91, neutrophils-baseline=0.89 and basophils-

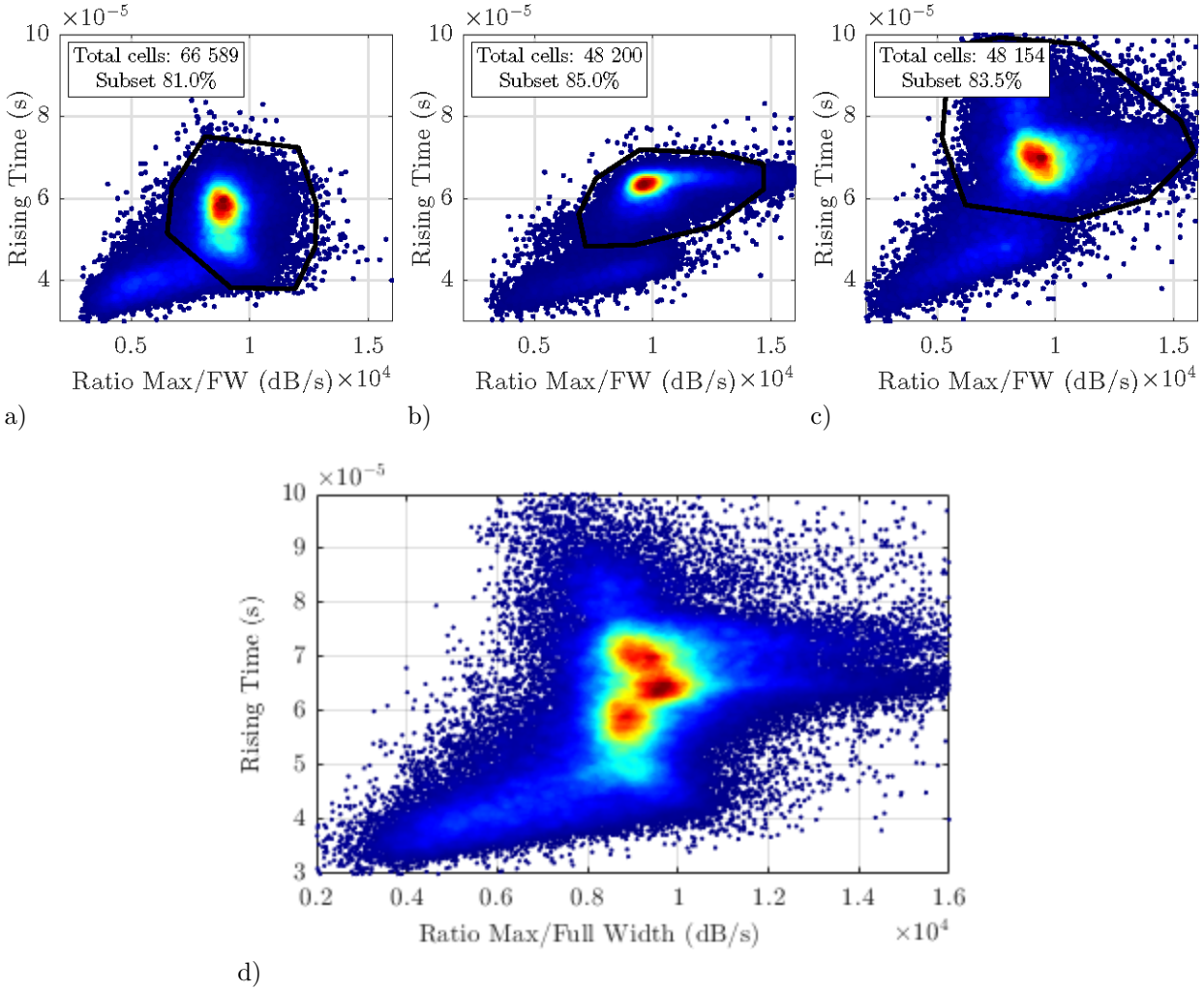

Figure 6.7 RIC ratio Max/FW and rising time density-colored dot plot at a flow rate of 15 μl/min for (a) HL-60 differentiated into neutrophils, (b) HL-60 differentiated into basophils, (c) HL-60 baseline conditions and (d) combination. One representative of at least three experiments.

baseline=1). The ratio Max/FW might provide good visual separation in the dot plot but it does not provide good separation alone. However, OLR computed in 3D using the FW, RT and FT are all below 1 (3D OLR neutrophils-basophils=0.41, neutrophils-baseline=0.82 and basophils-baseline=0.66). Thus, using the right combination of parameters, cell populations can be easily discriminated. One-dimensional OLR values of all combinations of myeloid cells discrimination can be found in Table 6.11.† The average time window necessary to measure a single cell at the imposed flow rate of 15 μl/min ($U_p = 0.22$ m/s) is 2×10^{-4} s, yielding a measurement rate of 5000 cells per second.

To fully characterize these myeloid cells, in depth analysis of each calculated curve parameter is necessary. Fig. 6.8 reports the RIC parameters histograms for all three cell populations. The Max histogram in Fig. 6.8a reveals that neutrophils have a significant smaller value

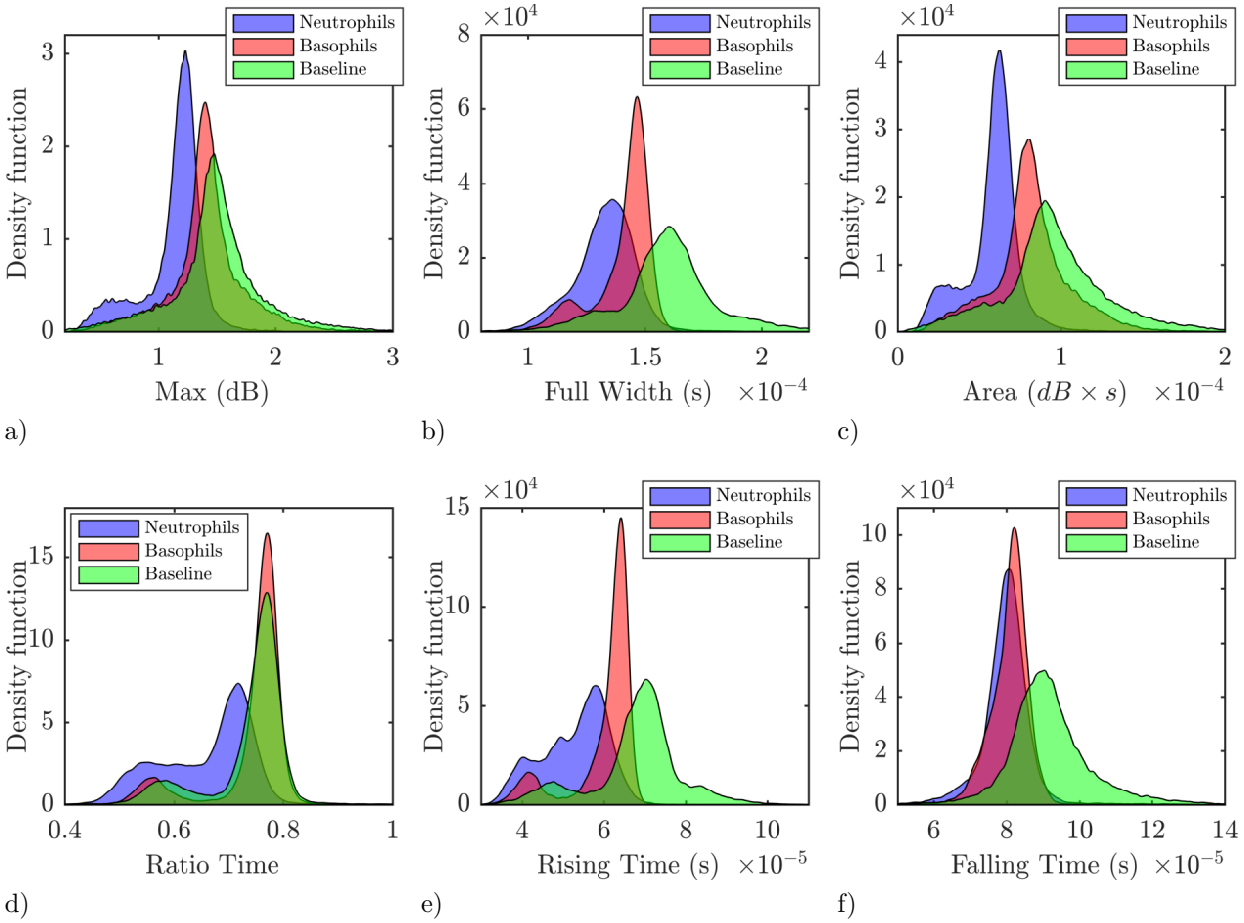

Figure 6.8 Histograms of HL-60 cells maintained in baseline conditions (total cells: 48 154) and differentiated into neutrophils (total cells: 66 589) and basophils (total cells: 48 200) at a flow rate of 15 μl/min for (a) maximum, (b) full width, (c) Area, (d) ratio time, (e) rising time and (f) falling time.

than basophils and baseline conditions cells. This result was expected since these cells reported a smaller size with flow cytometry as well as a smaller Max value in our previous work [195]. It also explains the smaller FW and Area values in Fig. 6.8b and Fig. 6.8c respectively. Moreover, basophils and baseline conditions cells show strongly overlapping Max and Area histograms, corresponding to the same largest measured RI and effective RI volume respectively. In contrast, the FW histogram in Fig. 6.8b shows a smaller mean value for the basophils compared to the baseline, corresponding to less deformed cells in the flowing direction (x-axis). Interestingly, the ratio time histograms of basophils and baseline conditions cells completely overlap in Fig. 6.8d. Based on our numerical simulation model, the similar Max and ratio time values indicate a similar nucleus relative position at the trailing side. However for basophils, FW, RT and FT, Fig. 6.8b, Fig. 6.8e and 6.8f respectively, have all decreased such that the ratio time is similar to the baseline. Thus, in this case only the FW parameter can discriminate basophils from baseline cells based on whole-cell deformability. This effect cannot be explained by our numerical simulation model. Basophils are much more structurally complex than our simple ellipsoids model since they typically have a multilobed nucleus and large cytoplasmic granules. These unconsidered entities clearly impact the calculated parameters in ways not yet included in our numerical simulation model. Still, the presented RIC method encloses rich information on cells RI and whole-cell deformability which allows enhanced and clear discrimination of HL-60 derived myeloid cells at high measurement rate.

6.6 Conclusion

In conclusion, we reported a new method to extract whole-cell deformability of single cells through Refractive Index Cytometry. We have developed a simple 3D ellipsoid numerical simulation model to help understand how the cells behavior in our device impact the measured parameters. We have demonstrated that our on-chip RIC can simultaneously probe the cells RI, effective volume and whole-cell deformability. Furthermore, one particular parameter, the ratio time, reflects the relative position of the nucleus inside the cell. Using these parameters, we have showed that HL-60 cells treated with cytochalasin B reported larger whole-cell deformability compared to the control population. Additionally, HL-60 maintained in baseline conditions and differentiated into neutrophils and basophils cells were all clearly discriminated.

The small foot-print and high measurement rate of approximately 5000 cells per second makes this device an ideal candidate for integration in existing flow cytometers. Integration and packaging of the device would reduce the cost and time of design and microfabrication as well

as preclude the need for off-line analysis and thus deliver near real-time throughput. The complementary parameters proposed by our RIC device could potentially benefit research and clinic areas such as rare cell detection, identification of cancerous or precancerous cells, T-cell phenotyping, HIV/AIDS infection research, stem cells research, identification of RBC pathologies, drug treatment analysis to assess efficiency and toxicity or cell cycle analysis.

Author contributions

A. Leblanc-Hotte conceptualization, formal analysis, lead investigation, methodology, software visualization, writing - original draft. N. Sen Nkwe supporting investigation. G. Chabot-Roy supporting investigation. E. B. Affar supporting resources, supporting supervision and writing - review & editing. S. Lesage conceptualization, equal funding acquisition, supporting resources, supporting supervision and writing - review & editing. J.-S. Delisle conceptualization, equal funding acquisition, supporting resources, equal lead supervision and writing - review & editing. Y.-A. Peter conceptualization, equal funding acquisition, lead resources, equal lead supervision and writing - review & editing.

Conflicts of interest

There are no conflicts of interest to declare.

Acknowledgments

The authors wish to thank the Molecular Biology, nucleic acid and animal study group at Polytechnique Montreal for their support on the immunostaining of HL-60 cells, the staff at Polytechnique Montreal's Laboratory of Microfabrication for technical support with microfabrication processes and Mikhail Sergeev, Ph.D., at the Bioimaging Core Facility of the Maisonneuve-Rosemont Hospital (University of Montreal) for resources and technical support with confocal fluorescence imaging and brightfield microscopy. This work is supported in part by the Natural Sciences and Engineering Research Council of Canada (NSERC) [grant number PGSD3-445848-2014], the Fonds de recherche du Québec – Nature et technologies (FRQNT) [grant numbers Equipe 173638, 255414 and RQMP 187779]. S. Lesage and J.-S. Delisle hold respectively a Senior and Junior II career award from the Fonds de recherche du Québec – Santé (FRQS).

6.7 Published electronic supplementary information

6.7.1 Examples of numerical simulation curve

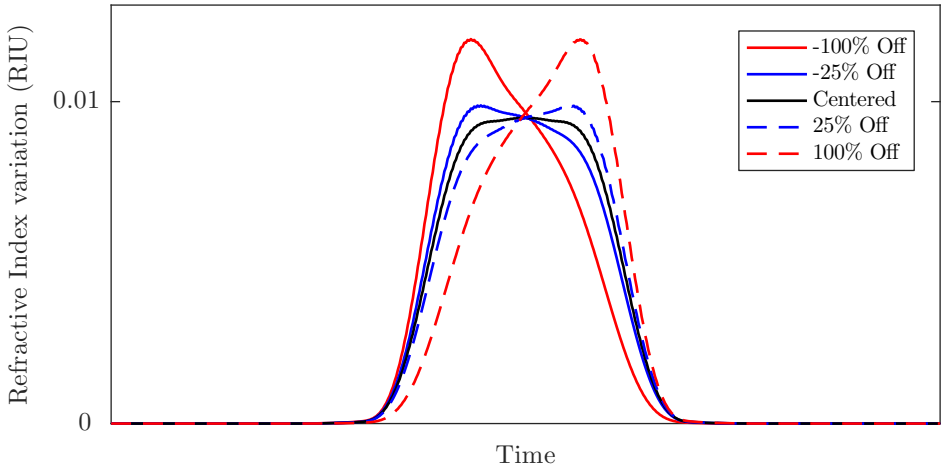

Figure 6.9 Examples of numerically simulated RI variation curve for different relative positions of the nucleus.

The measured optical power curve showed in Fig. 6.3 of the manuscript are in good agreement with this effective RI numerical simulation over time. Indeed, output curve are predominantly shaped by the resonance peak shift dynamics, which is itself dictated by the effective RI variation in time.

The mismatch between the simulated RI variation curve and the measured losses vs time can be justified by the lack of light-matter interaction phenomenon considered by the numerical model. Indeed, the simulation algorithm does not take into account the absorption, diffraction or lens effect of the different parts of the cell. Also, the slope of the resonance peak in the spectrum is not linear and thus will also mold the measured losses curve. Still, this RI variation numerical model gives a good understanding of how the deformation of the cell and the relative position of the nucleus affect the measured curve.

6.7.2 Inertial focusing length and cells spread

The required length for complete inertial focusing in a two-stage scheme as reported by Zhou and Papautsky is:

$$L = \frac{3\pi\mu D_h^2}{4\rho U_f D_{cell}^3}\left(\frac{H}{C_L^-} + \frac{W}{C_L^+}\right) \quad \text{for} \quad W > H$$

where μ and ρ are the fluid viscosity and density respectively, $D_h = 2WH/(W+H)$ is the hydraulic diameter, H and W are the channel height and width respectively, U_f is the average fluid velocity, D_{cell} is the cell diameter and C_L^- and C_L^+ are the negative and positive lift coefficient respectively. Using the data provided by Zhou and Papautsky, the lift coefficients can be approximated [58]. This form is generally more restrictive (outputs longer lengths) than the one proposed by Di Carlo et al. [50]. The table below reports the lift coefficients, the required focusing lengths and the resulting spreads in width W_{spread} for a cavity placed 1.2 mm away from the beginning of the straight channel. Importantly, the cross-section dimensions for cells to be focused are $H - D_{cell}$ and $W - D_{cell}$ in height and width respectively. Also, the calculated spread in width includes the cells diameters as shown in Fig. 6.10.

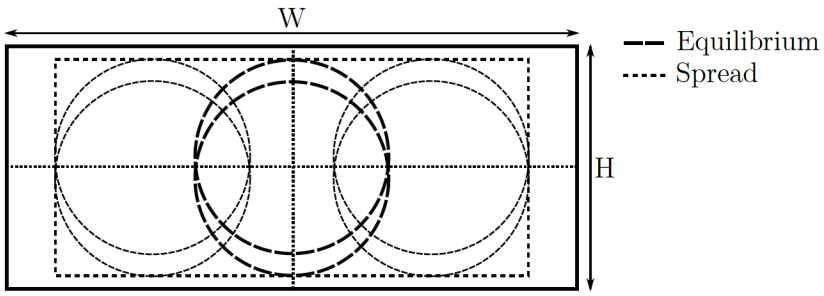

Figure 6.10 Inertial equilibrium positions in a rectangular channel and focusing area due to the spread in width.

Table 6.2 Calculated lift coefficients, required focusing lengths and resulting spreads in width for a cavity placed 1.2 mm away from the beginning of the straight channel for cells of 12 μm in a $W = 40\ \mu m$ by $H = 15\ \mu m$ channel at different flow rates.

Flow rate Q (μl/min)	$\mathbf{C_L^-}$	$\mathbf{C_L^+}$	**L (mm)**	$\mathbf{W_{spread}}$ **(μm)**
5	0.47	0.048	2.7	27.9
10	0.21	0.026	2.6	27.2
15	0.14	0.018	2.5	26.8
20	0.1	0.014	2.5	26.5
30	0.06	0.009	2.4	26.1

Table 6.3 Calculated lift coefficients, required focusing length and resulting spread in width for a cavity placed 1.2 mm away from the beginning of the straight channel for cells of 12 μm in a $W = 30\ \mu m$ by $H = 15\ \mu m$ channel at 15 μl/min.

Flow rate Q (μl/min)	$\mathbf{C_L^-}$	$\mathbf{C_L^+}$	**L (mm)**	$\mathbf{W_{spread}}$ **(μm)**
15	0.11	0.015	1.2	12.5

6.7.3 Curve parameters dependencies to relative nucleus position

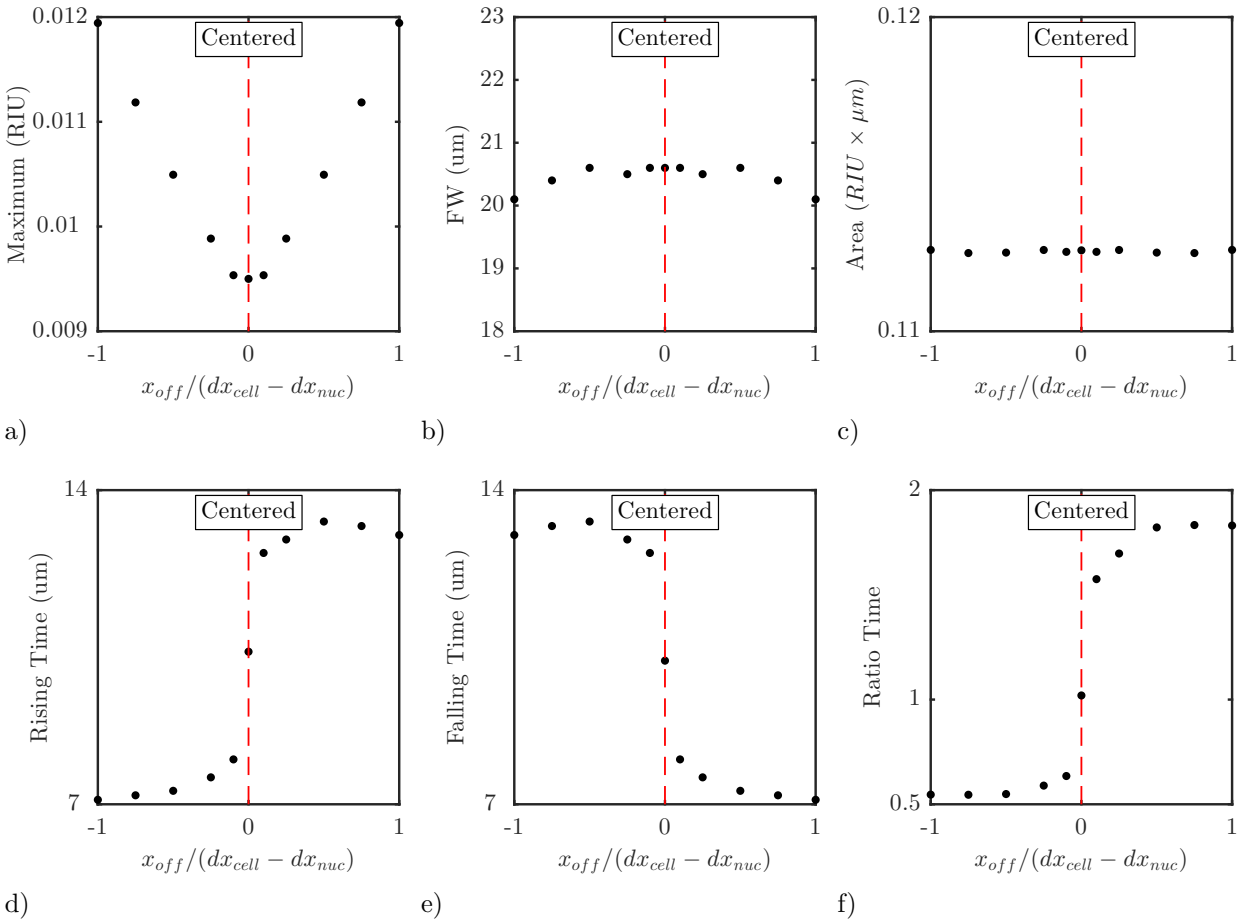

Figure 6.11 Computed parameter values from simulated curve when varying the relative nucleus position for (a) max, (b) full width (FW), (c) Area, (d) rising time (RT), (e) falling time (FT) and (f) ratio time. Red dashed lines indicates a centered nucleus position. Each steps are 25% offset except for the two points closest to the centered position which are ±10%.

6.7.4 Curve parameters dependencies to deformed cell length

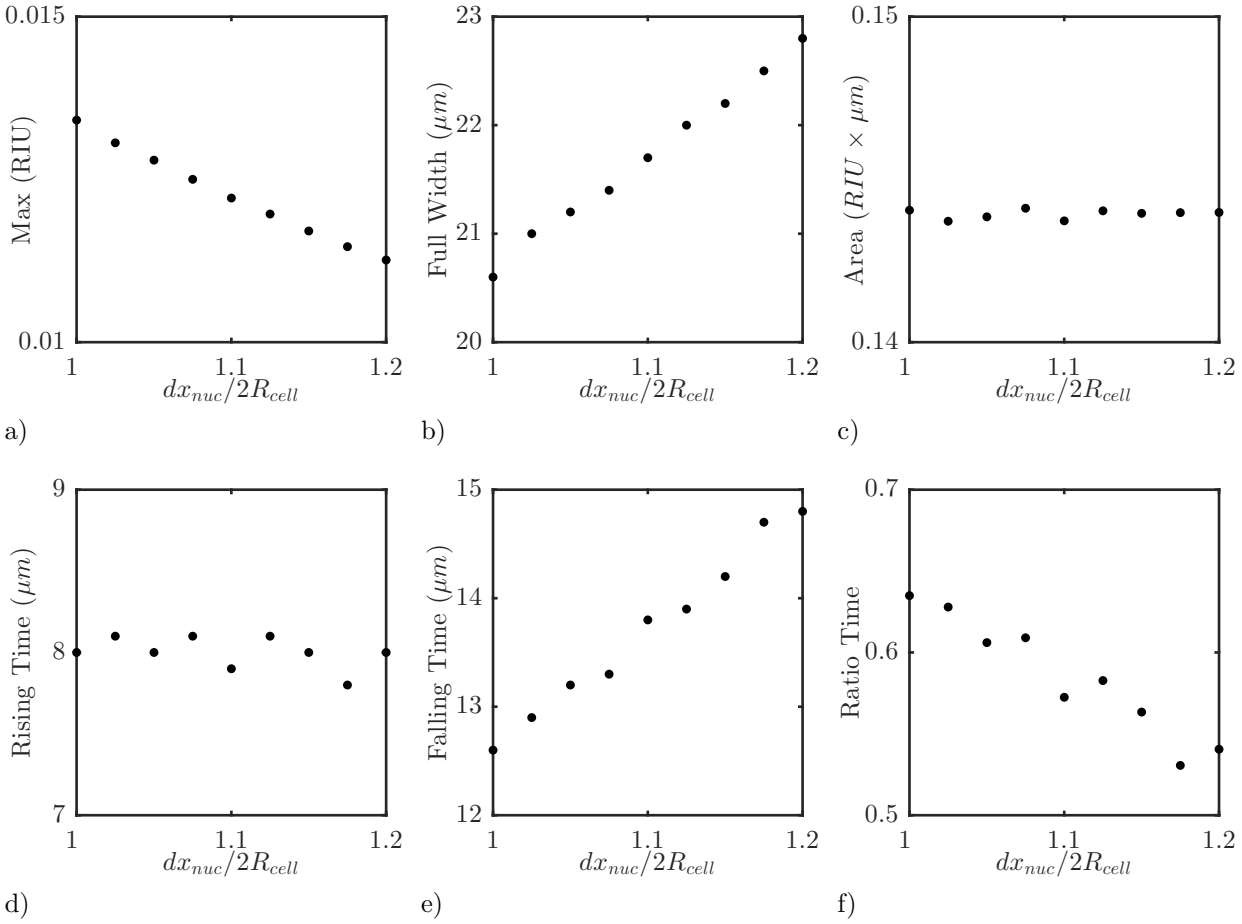

Figure 6.12 Computed parameter values from simulated curve when varying the deformed cell length in the x-axis for (a) max, (b) full width (FW), (c) Area, (d) rising time (RT), (e) falling time (FT) and (f) ratio time. Deformed cell length is $dx_{cell}/2R_{cell}$ where dx_{cell} is the diameter of the cell ellipsoid in the x-axis. A fixed 10% contraction deformation was imposed on the cell membrane ellipsoid in the y-axis. The nucleus radius was matched to the one of the cell in the y-axis by a 0.9% contraction deformation. For each step of 2.5% deformation, both the cell and the nucleus ellipsoids were deformed in the x-axis. The nucleus relative position was kept at $x_{off}/(dx_{cell} - dx_{nuc}) = -0.5$. Other nucleus relative position yielded similar results.

6.7.5 Confocal microscopy

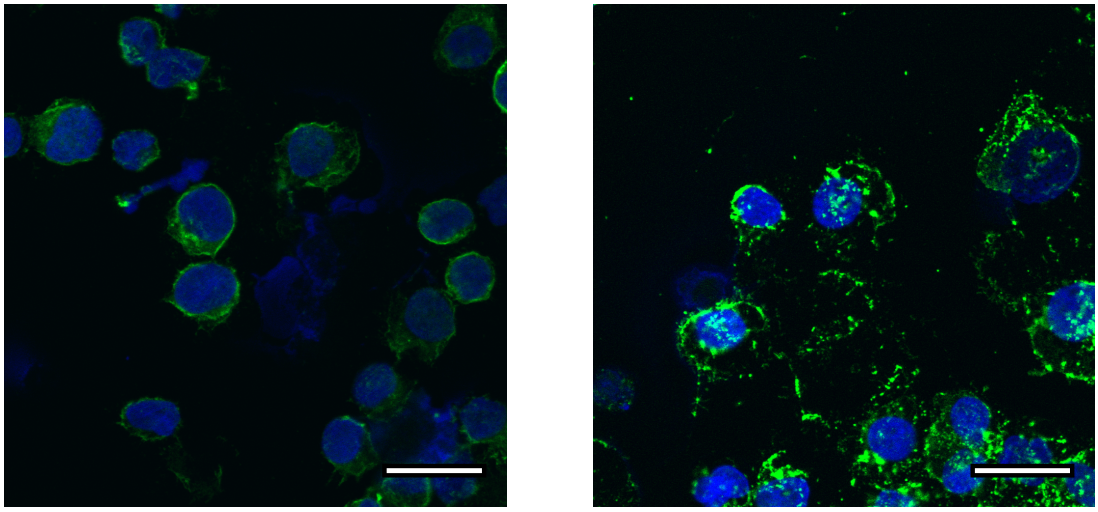

a) b)

Figure 6.13 Confocal fluorescence microscopy images of cytospun immunostained control and cytochalasin B treated HL-60 cells. F-actin is stained with Alexa Fluor 488 phalloidin (green) and nuclei is stained with DAPI (blue). Top view of the fluorescence composite for (a) HL-60 cells control and (b) cytochalasin B treated HL-60 cells. Treated cells present clumps of phalloidine fluorescence associated to grouped broken-down actin filaments, responsible for the larger whole-cell deformability. Scale bars are 20 μm.

6.7.6 Flow cytometry measurement of control and cytochalasin B treated HL-60 cells

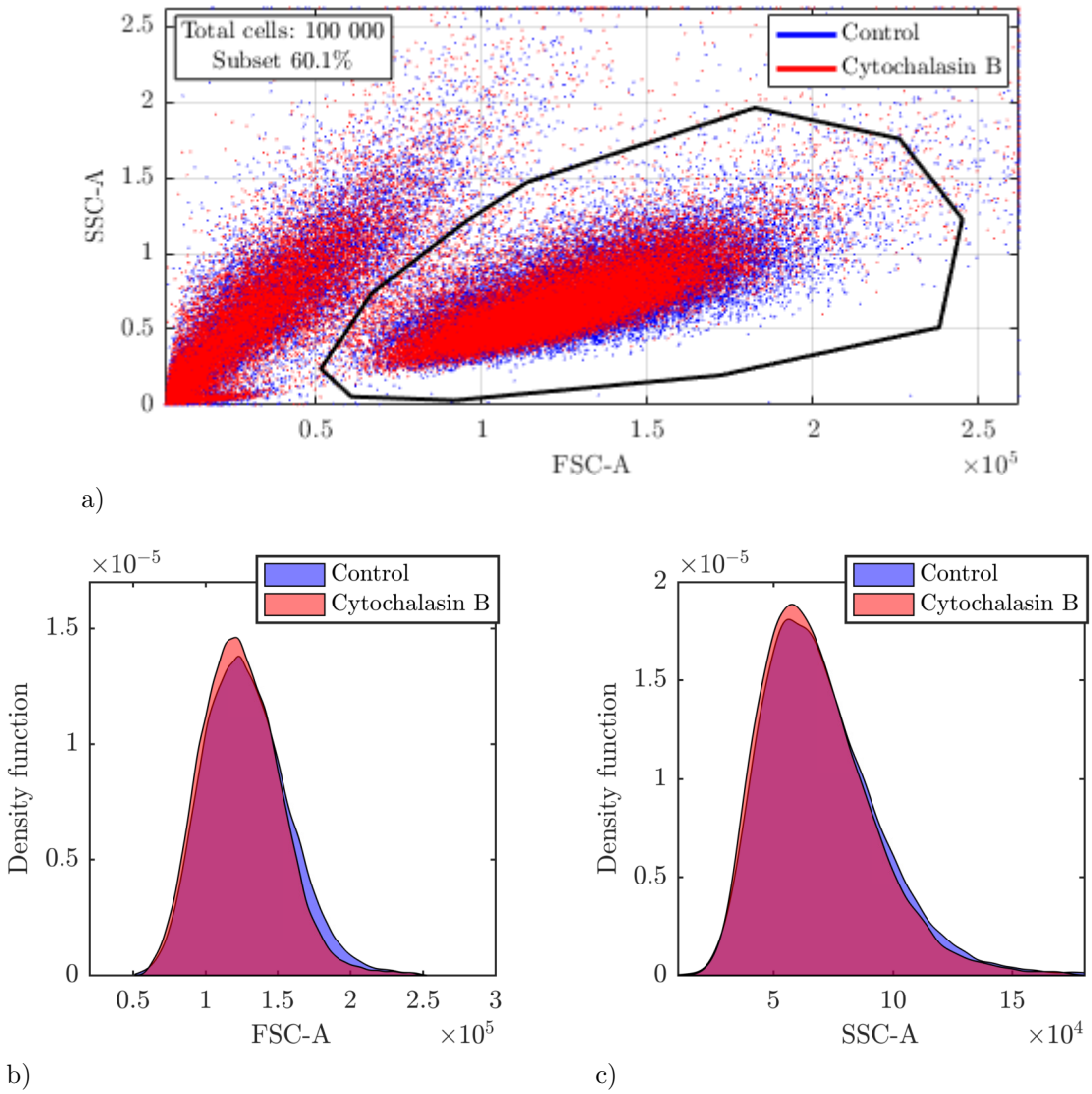

Figure 6.14 Flow cytometry measurements of control and cytochalasin B treated HL-60 cells. (a) Flow cytometry FSC-A and SSC-A dot plot superimposition (2D OLR=1). (b) FSC-A histogram (1D OLR=1) and (c) SSC-A histogram (1D OLR=1) of subsets. One representative of at least two experiments.

6.7.7 Measured curve parameters dependencies to flow rate

Larger flow rates implies larger forces acting on the cell thus more deformation is anticipated along the flowing direction. All parameters follow the predicted tendencies for both control and cytochalasin treated HL-60 cells (Fig. 6.12). Expectedly, FW values increase with

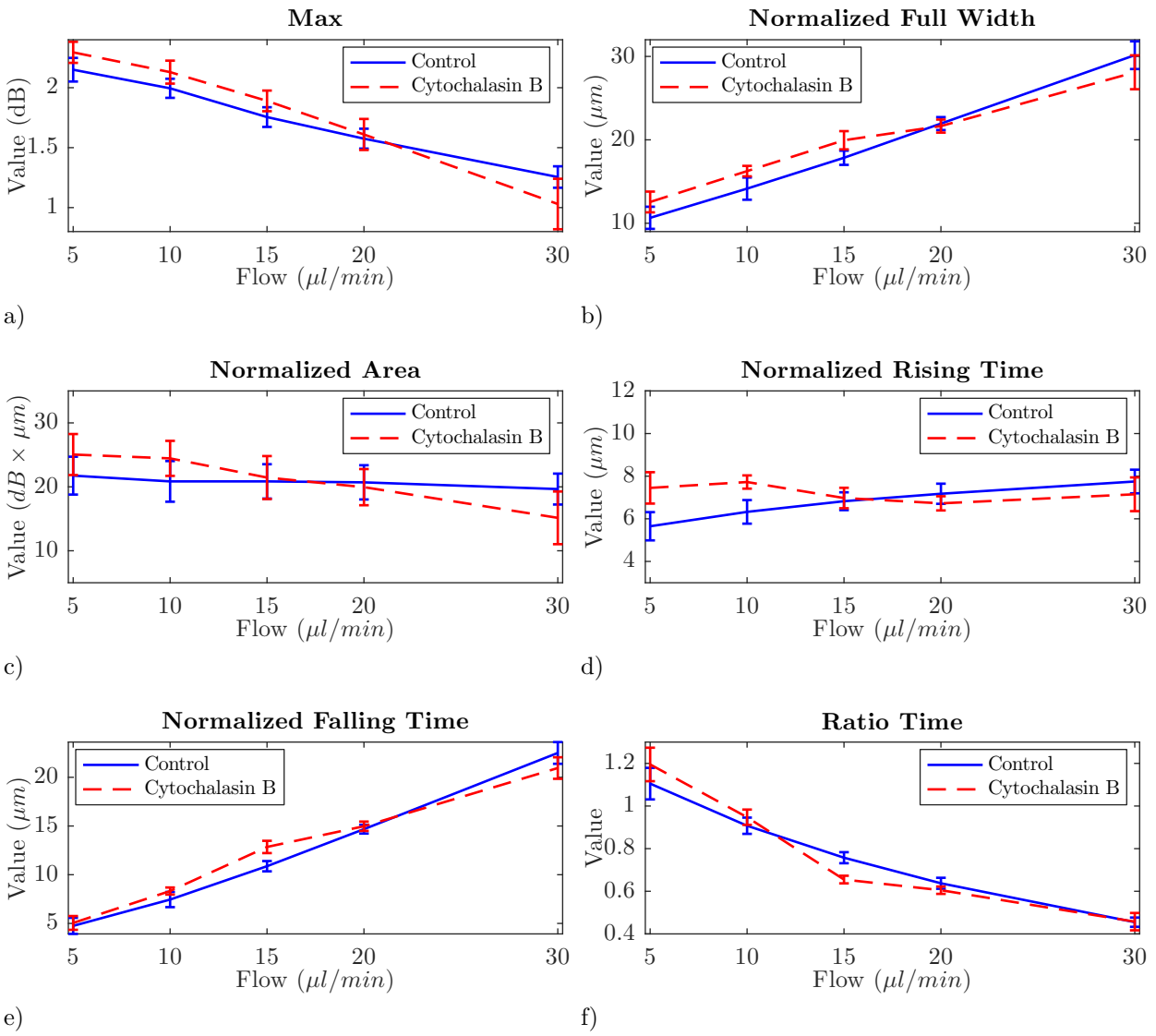

Figure 6.15 Measured curve parameters dependencies to flow rate for (a) max, (b) full width (FW) normalized by velocity, (c) Area normalized by velocity, (d) rising time (RT) normalized by velocity, (e) falling time (FT) normalized by velocity and (f) ratio time. Each error bar is $\pm$ one standard deviation derived from the normal distribution fitted over the corresponding parameter at a particular flow rate for a specific cell type. Parameters with time dependence, FW, Area, RT and FT were multiplied by the particle velocity to represent values in terms of length rather then time. The total mode field diameter (MFD) of the fiber, or a fraction for RT and FT, was subsequently subtracted. Total number of cells and subset at each flow rate for control and Cytochalasin B treated HL-60 cells are reported in Tab. 6.4.

increasing flow rates whereas Max values decrease and normalized Area values stay constant as shown in Fig. 6.15b, 6.15a and 6.15c respectively. Since the total effective RI volume (Area) stays constant the volume ratio of the cell to the cavity is smaller and thus yields

smaller measured maximal RI variation (Max). Variation of ratio time in function of flow rates reported in Fig. 6.15f shows decreasing values with increasing flow, rising time, Fig. 6.15d, shows relatively constant values whereas falling time, Fig. 6.15e, shows increasing values.

Interestingly, at a flow of 5 μl/min (particle velocity $U_p = 0.06$ m/s), both cell populations report signals yielding a ratio time value > 1. This indicates that the nucleus is positioned at the leading side of the cell rather than at the trailing side. At a flow of 10 μl/min ($U_p = 0.13$ m/s), the ratio time is very close to or slightly larger than 1, indicating near-symmetric RI distribution and a centered nucleus. For flows > 15 μl/min ($U_p > 0.19$ m/s), ratio time values are < 1 indicating a nucleus positioned at the trailing side of the cell. These results suggest a transition between 5 and 15 μl/min for the nucleus to be placed at the leading or trailing side of the cell.

These flows coincide to particle Reynolds number $Re_p = Re(2R_{cell}/D_h)^2$ of 0.9 and 2.75 respectively, where Re is the channel Reynolds number and D_h is the hydraulic diameter of the channel. At $Re_p = 1$, namely the transition point between stokes and turbulent drag, the flow rate is 5.5 μl/min ($U_p = 0.07$ m/s). The transition of the particle Reynolds number from smaller to larger than 1 might be related to the ratio time transition, thus the relative position of the nucleus from trailing to leading. Indeed, a turbulent drag near the cell might promote the deformation of the membrane towards the leading side. Further investigation is required to confirm this theory.

Table 6.4 Total number of cells and subset at each flow rate for control and Cytochalasin B treated HL-60 cells.

	Control		**Cytochalasin B**	
	Total	**Subset**	**Total**	**Subset**
Q=5 μl/min	48 057	80.0%	45 835	75.4%
Q=10 μl/min	47 879	85.8%	36 518	54.9%
Q=15 μl/min	47 536	65.2%	50 759	62.8%
Q=20 μl/min	46 780	85.7%	51 081	46.6%
Q=30 μl/min	10 188	68.0%	49 864	85.7%

6.7.8 Derivation of particle velocities

The average particle velocity U_p is set to a fraction of the average fluid velocity in the microchannel $U_p = \gamma \times U_f$. The factor γ is experimentally derived as follows:

$$\gamma = \frac{U_p}{U_f} \qquad \text{where} \qquad U_f = \frac{Q}{W \times H} \qquad \text{and} \qquad U_p = \frac{D_{cell} + MFD}{\overline{FW}}$$

$$\gamma = \frac{D_{cell} + MFD}{\overline{FW} \times U_f} = \frac{(D_{cell} + MFD)(W \times H)}{\overline{FW} \times Q}$$

where Q is the flow rate, W and H are the channel width and height respectively, $D_{cell} = 12\ \mu m$ is the cell diameter, $MFD = 10.4\ \mu m$ is the mode field diameter of the SMF-28 optical fiber and $\overline{FW}$ is the average measured full width (FW) at the specific flow Q. This equation is valid for undeformed cells, at flows of 5 and 10 μl/min where the Ratio Time value is ≥ 1. At Q=5 μl/min in a $W = 40\ \mu m$ by $H = 15\ \mu m$ channel, $\overline{FW} = 3.37 \times 10^{-4}$ and yields a factor $\gamma = 0.48$ whereas at Q=10 μl/min, $\overline{FW} = 1.95 \times 10^{-4}$ and yields a factor $\gamma = 0.41$. Thus, the γ factor was set to an average of 0.45.

The theoretical derivation of the factor γ yields an equivalent value. Comparing the two forms of the particle Reynolds number Re_p:

$$Re_p = Re\left(\frac{D_{cell}}{D_h}\right)^2 \quad \Leftrightarrow \quad Re_p = \frac{\rho\,(U_f - U_p)\,D_{cell}}{\mu}$$

$$Re_p = \frac{\rho U_f D_h}{\mu}\left(\frac{D_{cell}}{D_h}\right)^2 \quad \Leftrightarrow \quad Re_p = \frac{\rho U_f\,(1-\gamma)\,D_{cell}}{\mu}$$

$$\gamma = 1 - \frac{D_{cell}}{D_h}$$

where $D_h = 2WH/(W+H)$ is the hydraulic diameter and ρ and μ are the fluid density and viscosity respectively. For the considered channel dimensions and cell diameter, $\gamma = 0.45$. Average fluid velocities, particle velocities, Re and Re_p calculated in a $W = 40\ \mu m$ by $H = 15\ \mu m$ channel at the different imposed flow rates using this factor are reported in Tab. 6.5. The same quantities in a $W = 30\ \mu m$ by $H = 15\ \mu m$ channel at a flow rate of 15 μl/min using $\gamma = 0.40$ are reported in Tab. 6.6.

Table 6.5 Calculated average fluid and particle velocities, Re and Re_p at the different imposed flow rates for $W = 40\ \mu m$, $H = 15\ \mu m$ and $D_{cell} = 12\ \mu m$ using $\gamma = 0.45$.

Flow rate Q (μl/min)	5	10	15	20	30
Fluid velocity U_f (m/s)	0.14	0.28	0.42	0.56	0.83
Reynolds number (Re)	3	6	9	12	18
Particle velocity U_p (m/s)	0.0625	0.125	0.1875	0.25	0.375
Particle Reynolds number (Re_p)	0.9	1.8	2.75	3.7	5.5

Table 6.6 Calculated average fluid and particle velocities, Re and Re_p at a flow rate of 15 μl/min for $W = 30\ \mu m$, $H = 15\ \mu m$ and $D_{cell} = 12\ \mu m$ using $\gamma = 0.40$.

Flow rate Q (μl/min)	15
Fluid velocity U_f (m/s)	0.56
Reynolds number (Re)	11
Particle velocity U_p (m/s)	0.22
Particle Reynolds number (Re_p)	4.0

6.7.9 Coefficients of variation of flow cytometry and RIC measurements

Table 6.7 Calculated coefficients of variation of FSC-A and SSC-A measurements for control and Cytochalasin B treated HL-60 cells.

	FSC-A	**SSC-A**
Control	22.6%	34.7%
Cytochalasin B	21.8%	33.8%

Table 6.8 Calculated coefficients of variation of Max, FW, Area, RT, FT and Ratio Time measurements for control and Cytochalasin B treated HL-60 cells at all flow rates.

	Flow rate Q (μl/min)	**Max**	**FW**	**Area**	**RT**	**FT**	**Ratio Time**
Control	5	10.6%	7.5%	17.5%	9.8%	13.6%	14.8%
	10	7.9%	6.8%	16.1%	7.6%	8.3%	8.0%
	15	7.5%	5.4%	15.6%	5.6%	6.8%	6.4%
	20	7.8%	3.8%	14.6%	5.8%	3.8%	5.5%
	30	9.6%	4.2%	14.0%	7.1%	5.4%	9.7%
Cytochalasin B	5	4.9%	6.6%	12.6%	7.7%	9.5%	9.6%
	10	8.2%	3.6%	13.9%	4.0%	5.4%	6.1%
	15	14.0%	5.4%	22.3%	6.0%	5.5%	3.6%
	20	18.9%	4.0%	22.7%	4.3%	4.6%	4.2%
	30	22.1%	6.2%	29.1%	10.3%	7.0%	11.5%

Table 6.9 Calculated coefficients of variation of FSC-A and SSC-A measurements for neutrophils, basophils and baseline conditions.

	FSC-A	**SSC-A**
Neutrophils	13.2%	23.2%
Basophils	15.6%	29.9%
Baseline	15.7%	30.4%

Table 6.10 Calculated coefficients of variation of Max, FW, Area, RT, FT and Ratio Time measurements for neutrophils, basophils and baseline conditions at a flow rate of 15 μl/min.

	Max	**FW**	**Area**	**RT**	**FT**	**Ratio Time**
Neutrophils	9.2%	5.7%	12.8%	7.6%	5.0%	5.1%
Basophils	9.4%	4.0%	13.3%	4.5%	4.1%	2.5%
Baseline	11.8%	8.4%	16.8%	8.6%	8.4%	3.2%

6.7.10 OLR of myeloid cells populations

Table 6.11 Calculated 1D OLR values of all combinations of myeloid cells for discrimination.

	Neutrophils vs Basophils	**Neutrophils vs Baseline**	**Basophils vs Baseline**
Max	1	1	1
Full width (FW)	1	0.91	1
Area	1	0.90	1
Rising time (RT)	0.98	0.83	1
Falling time (FT)	1	1	0.998
Ratio time	1	1	1

1D OLR are not smaller than 1 in all cases. However, using the right combination of parameters, cell populations can be easily discriminated. Indeed, OLR computed in 3D using the FW, RT and FT are all below 1 (3D OLR neutrophils-basophils=0.41, neutrophils-baseline=0.82 and basophils-baseline=0.66).

CHAPTER 7 GENERAL DISCUSSION – LIMITATIONS AND POSSIBILITIES OF ON-CHIP REFRACTIVE INDEX CYTOMETRY

This chapter discuss elements excluded from the published articles presented in Chapters 4 – 6 but which are relevant to this thesis. These elements are: device performance, integration into flow cytometry and biological applications. Device performance is further divided to comment specifically on the polarization of propagating modes, the deformation profile of cells in microchannels and the smallest detectable particle.

7.1 Device performance

7.1.1 *TE* and *TM* propagating modes

Fundamental *TE* and *TM* modes propagating in the fabricated SOI rib waveguides have different properties, as suggested in Chapter 5. The difference in modal indices $\Delta n \sim 5 \times 10^{-5}$ ($n_{TM} < n_{TE}$), attenuation coefficients $\Delta\alpha \sim 0.25\ dB/cm$ ($\alpha_{TM} < \alpha_{TE}$) and mode sizes ($size_{TM} < size_{TE}$) can explain the two resonances observed in a close spectral range, (see Fig. 5.3a). While the device reports enhanced discrimination abilities, the performance might be further improved if a single polarization propagates.

To eliminate or dramatically extinguish one of the fundamental polarized modes, two solutions are discussed. The first one consist of a polarized filter prior to input in the rib and the second one to integrate an on-chip filter prior to the Fabry-Pérot cavity. Adding a polarized filter does not require design and fabrication of another generation of devices. To excite only the *TE* or *TM* mode, the s- or p-polarized input light, respectively, must be perfectly aligned to the incident plane. However, slight imperfections of the incident plane or the rib boundaries can alter the polarization at input or along propagation and thus excite both modes. Hence, this solution should prove laborious to implement due to imperfections inherent to the microfabrication process.

Integrating an on-chip filter could selectively extinct the *TE* or *TM* mode along propagation. The horizontally polarized *TE* fundamental mode (HE_{00}) usually extend more over the sidewalls of the waveguide whereas the vertically polarized *TM* fundamental mode (EH_{00}) extend more over the top and bottom of the waveguide. Long-period Bragg gratings defined on the sidewalls of silicon waveguides have been shown to yield extinction ratio of the *TE* mode around 30 dB [199]. Similarly, periodically etched low profile holes on top of silicon waveguides have been shown to yield extinction ratio of the *TM* mode around 25 dB [199].

Other techniques use a secondary metallic waveguide on top of the primary silicon waveguide to extinguish the *TM* mode [200, 201]. However, all of these integrated filters were only investigated on top of very small ($\sim$ 200 $nm \times$ 500 nm), highly confined and single-mode rectangular waveguides. The rib waveguides presented in this thesis have very large cross-sections thus their fundamental *TE* and *TM* modes do not extend as much across the boundaries. This might greatly limit the efficiency of these on-chip filter. As such, geometrical variations of rib waveguides could instead excite higher order modes or produce extinction ratios dependent on the wavelength. Clearly, in depth modal propagation analysis is required before integrating such on-chip polarization filters in large cross-section SOI rib waveguides.

7.1.2 Cellular deformation profile

Cells and elastic capsules in a rectangular or cylindrical channel deform into a bullet-like shape if the particles size is comparable to the dimensions of the channel ($a/H >\sim 0.8$). This has been shown by numerous simulations and experimental results as previously stated in Chapter 6. However, this bullet-like deformation profile yields a circularity usually close to the one of an undeformed cell. This has raised interrogations regarding the reported elongation along the flowing direction in the latest published article (Chapter 6). If a cell in a microfluidic channel adopts a bullet-like deformed profile, how can a cell having its cytoskeleton modified report such a larger deformed length compared to the control.

First, circularity usually reports smaller relative deformation values compared to the deformed length measurement, *i.e.* the FW. The circularity c of a cell inside a microfluidic channel is:

$$c = \frac{2\sqrt{\pi A}}{P}$$

where A and P are the area and perimeter of a cell, respectively, on a recorded image. Consider a cell adopting an elliptic shape with a major axis extended by 10% from its spherical area-equivalent. This extension is similar to some measurements reported in Chapter 6. The circularity is approximately 0.99, corresponding to a relative deformation of 1%, whereas the relative FW deformation is 10%. Thus, although the circularity of this elliptic cell is close to the one of an undeformed cell, the relative deformed length value is much larger.

Then, cells treated to have a weaker cytoskeleton using cytochalasin B deform more than the control cells, as reported in Fig. 6.5. Likewise, a recently published article reported smaller circularity values of HL-60 cells after cytoskeleton modification using cytochalasin D [202]. Favorably to the argument above, the slight variation of circularity between populations, although proven to be statistically significant, does not allow for discrimination based on an

OLR coefficient.

On a related note, recent simulations in rectangular channels of aspect ratio $W/H = 2$, such as the ones presented in this thesis, have shown distinct deformation profiles compared to axisymmetric channels [203]. While the bullet-like profile was preserved in the more confined channel dimension, the profile in the other dimensions depended on the simulated surface tension behavior. Membranes having variable surface tension showed ellipsoids extended along the width whereas membranes having constant surface tension showed ellipsoids extended along the flowing direction. Importantly, their findings suggest that experimentally observed deformation profiles of RBCs are due to the inner cytoskeleton rather than to the outer lipid bilayer. Thus, it is reasonable to suppose this will also be the case for WBC such as HL-60 cells.

7.1.3 Small particle detection

A fundamental interrogation on the performance of the presented RIC device concerns the smallest particle which can be detected. As extensively detailed, the presented biosensor detects a relative variation in optical length inside its Fabry-Pérot cavity. Thus, intuitively, a smaller cavity length should detect smaller particles. However, it was shown in Chapter 3 that sensitivities depend on the cavity length. Indeed, for spectral measurements (based on the position of the resonance), smaller cavities have resonance modes which extend more into the DBRs thus yield smaller sensitivities and larger LOD. For power measurements (based on the transmitted power at a fixed wavelength), smaller cavities have larger FWHM, less steep slopes thus also yield smaller sensitivities and larger LOD. Furthermore, power measurements sensitivities also depend on the spectral position of the interrogating wavelength on the slope (see Fig. 3.5b).

To understand the effect of cavity length on LODs of both spectral and power measurement setups, simulations were carried out. First, transfer matrices were used to simulate the spectra of Fabry-Pérot cavities having integers ranging from $m_{cav} = 2$ to $m_{cav} = 50$, corresponding to cavity lengths ranging from $l_{cav} = 1.2\ \mu m$ to $l_{cav} = 30.0\ \mu m$ ($m_{air} = 5$, $m_{Si} = 17$, $n_{cav} = n_{H_2O}$ and $\lambda_0 = 1600\ nm$). Then, the spectral sensitivity of each cavity was computed by identifying the resonance positions when varying the RI. The power sensitivity of each cavity was computed by recording the transmitted power when varying the RI. For spectral measurements, sensitivities are linear with the RI variation, as previously shown in Fig. 5.3c. Contrarily, for power measurements, the sensitivities are optimized for a precise RI variation or for the purpose of this study, a position on the resonance slope, as previously shown in Fig. 3.5b. Subsequent calculations are realized using an interrogation wavelength set to

the optimized sensitivity, which is different for each cavity. Finally, LOD of each cavity was calculated considering an accuracy of $3\sigma = 0.015\ nm$ and $3\sigma = 0.1\ dB$ for spectral and power measurements respectively. Figure 7.1a shows the LOD in function of the cavity length l_{cav} for the spectral and power setups. As expected, in both cases, longer cavities are associated to larger sensitivities thus smaller LODs. Also, as previously described in Chapter 3, spectral measurements show smaller LODs for all cavity lengths. For very small cavities, the difference in LODs can be as much as one order of magnitude. However, the difference quickly decreases and reach a stable value around 3×10^{-5} RIU for longer cavities.

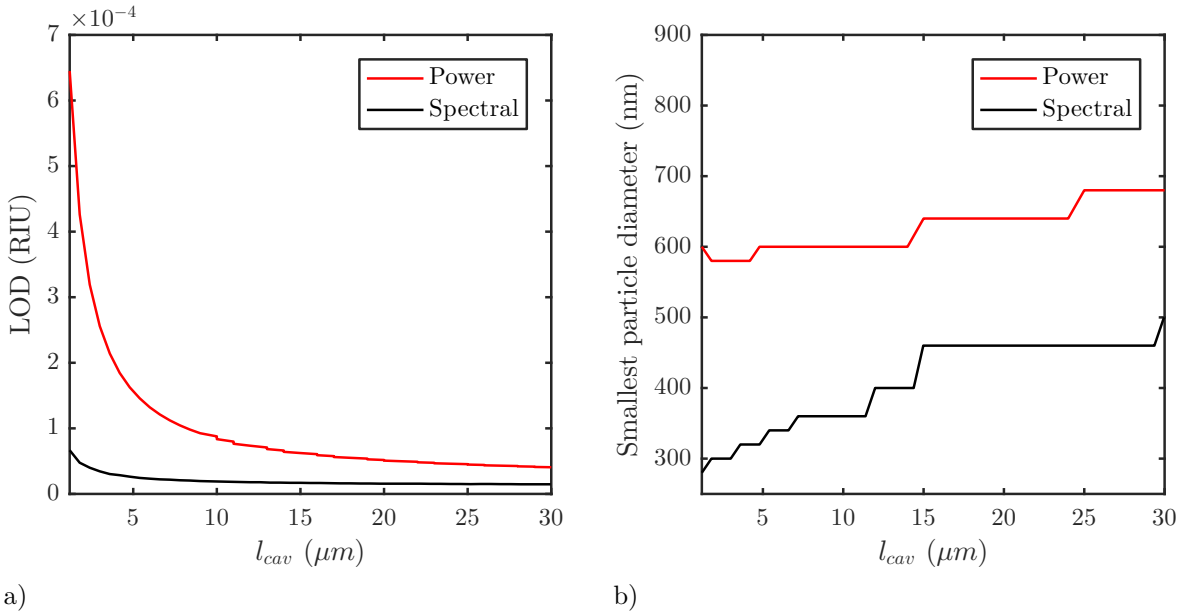

Figure 7.1 Spectral and power measurements comparison in function of the cavity length l_{cav} based on (a) the LOD and (b) the smallest detectable particle diameter having an RI of $n_{cyt} = 1.447$.

To understand the effect of cavity length on the minimum detectable particle size for both spectral and power measurement setups, results from the previous simulations were assigned in a second set of simulations. First, using the predictive RI curve simulation model presented in Chapter 6, the maximal RI variations induced by particles having a diameter ranging from 200 nm to 800 nm in cavity lengths ranging from $l_{cav} = 1.2\ \mu m$ to $l_{cav} = 30.0\ \mu m$ was computed. The particles RI was set to $n_{cyt} = 1.447$ to mimic typical vesicles of cytoplasmic contents. Then, the particle diameter for which the maximal RI variation matched the previously computed LOD in function of the cavity length was recorded. Figure 7.1b shows the minimum particle diameter detectable for spectral and power measurements. Again, as expected, the minimum detectable particle sizes for spectral measurements are smaller than

the ones for power measurements for all cavity lengths. Moreover, since the LOD curve of the spectral setup is relatively constant, the smallest detectable particle size increases with the cavity length. Indeed, the particle size must be larger to induce the same RI variation (LOD) in a longer cavity. Interestingly, for the power setup, it seems that the LOD curve and particle RI variation in function of the cavity length balance each other to yield a more constant minimum particle size. However, the LOD curve of the power setup reaches a constant value for cavities longer than 30 μm and thus, similarly to spectral measurements, the smallest detectable particle size will only increase for longer cavities.

To answer the original interrogation, two possibilities are considered. For flowing particles, the time spent in the cavity is to short to be spectrally measured, thus power measurements are required. In this case, it is safe to claim that the minimum detectable particle size is between 600 nm to 700 nm. If particles can be trapped in the resonant cavity enough time to complete a spectral measurement, then the minimum detectable size is between 300 nm to 500 nm. Importantly, particle sizes speculated here are for detection only and may not allow discrimination based on physical properties. Indeed, in these configurations, both setups are working at their detection limit. Also, particles having smaller RI would need to have larger diameters to be detected.

7.2 Towards integration in flow cytometry

The proposed RIC device is a serious candidate for integration in existing flow cytometers due to its high measurement rate and complementary physical parameters. Integration of supplementary optical, fluidic and electronic components should not cause major problems. Indeed monochromatic NIR lasers, detectors and optical fibers are all compact equipment available at reasonable prices. Also, fluidic pumps and electronic hardware are already provided by flow cytometry manufacturers. However, the device integration into a flow cytometer measurement cell will require further design and testing to ensure compatibility of both systems. In the scope of preliminary integration, compatibility issues are grouped into three categories: cellular viability, fluidic operation and measurements association.

Naturally, the RIC device should ideally not impact cellular viability or at least have less repercussion than labeling procedures using fluorescent antibody complexes. This is especially important for deformability characterization which applies fluidic forces that can be destructive, as experienced at larger flows. As mentioned in Chapter 6, "*Cell tearing is suspected to come from strong elongation forces induced by contraction regions prior to the beginning of the straight channel which can be engineered to be more gentle*". A simple solution consist of modifying the curve profile of the contraction region to generate a smaller

and constant elongation force. This is achieved for contraction curves having hyperbolic profiles, as extensively studied in ref. [204, 205]. Otherwise, cells can be considered to be healthy after being processed through the RIC device as no chemical treatment is employed. A colorimetric test should confirm cells viability post-processing.

The next issue involves the difference in fluidic operation between flow cytometry and the RIC device. In flow cytometry, cells are hydrodynamically focused using of sheath fluids whereas in the RIC device cells are inertially focused. The large amount of sheath fluids required in flow cytometry greatly dilutes the cell solution. Thus RIC measurements should be performed prior to sheath focusing to maintain its high measurement rate. Also, microfluidic design of the RIC device should be adjusted to fit the driving pressure in flow cytometry. Briefly, measurement rate in flow cytometry can be as high as 35 000 cells/s whereas in RIC it is around 5 000 cells/s. Thus, cell velocity is approximately 7 times faster. Additionally, flow cytometry tubes are at least one order of magnitude larger than the device microchannels. Jointly, this implies a flow rate larger by at least three orders of magnitudes. Fortunately, the hydrodynamic resistance R_h of the flow cytometry system is much smaller than the one the RIC device due to the strong dependence on the hydraulic diameter. Thus for constant driving pressure ΔP, a larger hydrodynamic resistance yields a smaller flow rate Q as described in the equation below:

$$\Delta P = R_h Q \qquad \text{where} \qquad R_h = \frac{8\mu L}{\pi R_h^4}.$$

To achieve a smaller flow rate in the RIC device, carefully designed microfluidic channels could be added prior to the sensing resonant cavity. Contrarily, to achieve a larger flow rate, if the driving pressure is not large enough, a secondary pressure pump could be added before the device to push fluid or after the device to pull fluid.

The above proposed solutions imply that RIC measurements are realized either in parallel or prior to the ones of flow cytometry. A parallel configuration provides precious information but is similar to processing the cells in separate systems: data cannot be correlated to each single cell. A markedly more powerful method is to associate both the RIC and flow cytometry measurements to each single cell, providing unprecedented cellular information. In a serial configuration, this would require precise timing, control and stability over the cells dynamics. Fortunately, the proposed microfluidic system allows for such a control. However, the hydrodynamic sheath focusing employed in flow cytometry might not preserve the cells order. A straightforward solution is to maintain the RIC inertial focusing further along the measurement line thus eliminating the need for sheaths. Such a configuration would allow to

precisely determine cells positions at any time, knowing their velocity, and thus enable RIC and flow cytometry measurements correlation.

The ultimate configuration is to perform both measurements simultaneously on each single cell. However, this configuration is the most challenging to integrate. Indeed, the RIC device is built in silicon which is not transparent in the visible spectrum. Even if the top and bottom layers would be made out of glass, flow cytometry SSC and fluorescent signals are collected perpendicularly to the main beam direction. Separate glass waveguides could be integrated on-chip but most of these already weak perpendicular signals would be lost. This configuration calls for ingenious design and is not recommended for a first attempt of integration into flow cytometry systems.

7.3 Biological applications

In this thesis, investigated biological applications only targeted differentiated myelocytes or modified cytoskeleton cells. Although these biological models demonstrated the applicability of our RIC device, the proposed complementary cellular parameters are of interest in other research fields. The brief list below enumerates some contemporary and relevant biological applications accompanied by short descriptions of their problematic. In these potential cellular applications, RI and deformability are believed to be specific label-free measurands from which current methods could benefit.

Cancer diagnostic accuracy

Some cancer cannot always be accurately diagnosed, even when using multiple tools. This is the case for thyroid carcinoma. Follicular cells of the thyroid gland identified as suspicious of a neoplasm by cytological examination prove to be malignant in only 15 to 30 % of the cases [206]. However, following this diagnostic a thyroidectomy is generally recommended. Patients who undergo this surgery, which includes risks, are medicated for the rest of their lives.

Precancerous cell detection

Early detection of cancer could limit the damages engendered by this pathology. Cancers which are commonly asymptomatic at early stages include oral, gastric, cervical and colorectal [207–210]. Additionally, some cancer must be diagnosed at early stages to be operable. This is the case for pancreatic cancer where 80 to 85 % of patients cannot be surgically treated at the time of diagnostic [211].

Chemotherapy efficiency

Contemporary chemotherapy drugs such as docetaxel and paclitaxel prevent cellular mitosis by stabilizing microtubules, a cytoskeleton component. These plant-derived drugs are used to treat ovarian, breast, lung, cervical, prostate and pancreatic cancers among others. The efficiency of similar chemotherapy drugs under development could be monitored through whole-cell deformability.

T lymphocytes phenotyping

Discrimination of T lymphocytes sub-populations is an active research field. Understanding their functions and roles has implications in cell-based treatments for numerous pathologies such as cancer, HIV/AIDS, primary immune deficiencies and autoimmune diseases. Currently, T lymphocyte phenotyping is realized by complex fluorescent labelling which identifies specific surface proteins: cluster of differentiation (CD). This method carries serious challenges and issues as discussed in Chapter 1.

T lymphocytes therapy

Remarkable interest is directed towards T lymphocytes therapy to treat cancer, transplantation rejection and autoimmunity. In fact, the 2018 Nobel Prize in Physiology or Medicine was attributed to James P. Allison and Tasuku Honjo for their discovery of cancer therapy by inhibition of negative immune regulation. Eminent researches also revealed that specific phenotypes of donor T lymphocytes have the potential to cure hematological malignancies in hosts without triggering widespread alloreactivity [212, 213]. The culture, isolation and control *in vitro* of these specific T lymphocytes may benefit from the proposed complementary physical parameters measurement.

Dendritic cells discrimination

Dendritic cells process antigens and then stimulates T lymphocytes to trigger an immune response. However, myeloid and lymphoid dendritic cells discrimination from monocytes and plasma cells, respectively, requires fluorescent labelling. Moreover, there is a lack of knowledge concerning their functions and interactions. RIC holds great potential to discriminate these dendritic cells and may provide further insight on their biomechanical characteristics.

WBC pathology

Many health conditions can be indirectly identified by a quantitative leukocytes analysis, *i.e.* the counts of neutrophils, lymphocytes, monocytes, eosinophils and basophils, as mentioned in Chapter 1. Nonetheless, a qualitative analysis can reveal disorders related to leukocytes functions. For instance, some pathologies can affect neutrophils

ability to kill other cells, adhere to the endothelium, migrate using chemotaxis, perform phagocytis or to release their granules content [214]. These pathologies cannot be identified using flow cytometry and require more invasive or complex tests. However, RI and deformability characterization could help identify some of these WBC pathologies.

Cell cycle analysis

Cell cycle analysis is routinely performed based on their labelled DNA content. However, each phase (G_1, S, G_2 and M) is associated to major changes in cytoplasmic composition and cytoskeleton organization. Indeed, in the G_1 phase cell size increases to prepare for DNA replication occurring in the S phase. In the G_2 phase, cell size increases further and microtubules reorganize to prepare for mitosis occurring in the M phase. Furthermore, G_2 and M cells are not discriminated based on their DNA content and thus require additional labeling. RIC preliminary results show promising label-free discrimination of all phases [215].

CHAPTER 8 CONCLUSIONS AND RECOMMENDATIONS

To conclude, achievements presented in this thesis are synthesized under each objectives and original contributions are highlighted. Then, some crucial upcoming challenges are briefly described and personal recommendations for the future of this research are imparted.

The first objective of this thesis was to develop an integrated biosensor which can achieve a small LOD on whole-cell measurement as well as a high-throughput. To realize such a sensor, an in-plane Fabry-Pérot cavity made of air-silicon DBRs has been integrated on-chip. Previous work laid the geometrical requirements necessary to achieve resonances in the NIR. Such a resonant cavity provided a larger interaction with the sample under interrogation which is well suited for whole-cell characterization. LODs of 1.2×10^{-5} RIU and 4.1×10^{-5} RIU were obtained, for the spectral and power measurement setups respectively, even if the integrated sensor yielded small Q factor and finesse $\mathcal{F}$. Other technologies based on evanescent field sensing may achieve smaller LOD but do not have penetration depth large enough to measure whole cells. Oppositely, other volume sensors based on interference have either larger LOD, out-of-plane setups not appropriate for integrated solutions or suffer from difficult integration into microfluidic structures. As for throughput, the adopted inertial focusing scheme allowed for a measurement rate of 5000 cells/s. Although similar to most on-chip flow cytometry devices, this throughput is still far from what commercial flow cytometry can achieve. However, inertial focusing does not require large amounts of fluids, naturally provides regular interparticle spacing and can accommodate small or large cells.

Under this first objective, the engineering of large cross-section rib waveguides exhibiting single-mode like behavior embodies an explicit original contribution. For resonant sensing applications, control of propagating light properties, in particular the absence of higher order modes, is of utmost importance. Through experimental validation, it was clearly demonstrated that *"satisfying the previously established design formulas is not in itself sufficient to ensure effective single-mode operation"*. Thereupon, the attenuation maps reported in this thesis act as modernized design guidelines for these single-mode like rib waveguides.

The second objective was to characterize single cells based on their RI and deformability. At small flow rates, fluidic shear forces are not large enough to deform significantly the cells. In these cases, cells are characterized based on their RI alone and thus present relatively symmetric curve of losses in time. Oppositely, at large flow rates, cells experience stronger shear forces which induce deformation. The curves then become asymmetric and, using relevant parameters, cells can also be characterized based on their deformability. Notably,

shear stress induced on cells can be tuned to either promote or inhibit deformation. Among the numerous parameters extracted from these curves, the Max corresponds to the largest effective RI measured, the FW represents the length of the cell in the flowing direction, the Area relates to the effective RI volume and the ratio time, which relates to the degree of asymmetry of the curve, reflects the spatial RI distribution along the flowing direction. As such, the ratio time indicates the relative position of the nucleus in the cell. A ratio time > 1, indicates a nucleus positioned at the leading side of the cell whereas a ratio time < 1 is associated to a trailing side position. Moreover, the transition from leading to trailing is believed to be influenced by the transition of the particle Reynolds number (Re_p) from smaller to larger than 1. Ultimately, both the ratio time and FW parameters are relevant to characterize whole-cell deformability. Indeed, softer cells deform more and yield larger FW values which in turn yield more asymmetric curves, when considering a similar positioning of the nucleus, thus smaller ratio time values. Under this objective, specific original contributions consist of simultaneous cellular RI and deformability characterization of single cells as well as the establishment of a nucleus position indicator.

The third and last objective was to realize enhanced discrimination of myeloid cells. This was unequivocally proved in chapter 6 where the integrated biosensor characterized cells based on specific physical properties: the RI and deformability. It was shown that WBC populations indiscriminated by flow cytometry FSC-SSC measurements, specifically neutrophils, basophils and promyelocytes, are readily distinguished by the RIC device. The efficiency of discrimination was assessed using the OLR coefficient. It quantified the separation of two populations using their probability density function and thus validated the capacity of the device. This OLR coefficient is preferred to traditional statistical tests which can highlight differences between populations but may not always reflect the discrimination capability. Characterization using cellular RI alone has yielded intermediate discrimination efficiency. Only neutrophils were fully discriminated from basophils and promyelocytes. However, simultaneous characterization of the cellular RI and deformability yielded complete and unprecedented discrimination of all myeloid cells under investigation. This central original contribution has extensive impact on cellular characterization tools, one of which is flow cytometry.

Notwithstanding to the discrimination capacity of the presented RIC device, some challenges still reside for the next generation of prototypes. In particular, the throughput should be further improved to attain an operational rate similar to flow cytometry. To reach such a high-throughput, development efforts are two-fold. First, the raw measurement rate should be increased and then a fully automated data analysis should be implemented. From the theoretical analysis exposed in this thesis, a larger microfluidic channel would allow for larger

measurement rates while not hindering the sensitivity or the LOD of the resonant cavity. Optimizing the cellular concentration of the sample solution as well as the length of the inertial focusing channel prior to the cavity should yield a regular and optimal interparticle spacing. Subsequently, an automated analysis would provide a data calculation rate close to real-time, much like flow cytometry. As such, it should only report the six most relevant curve parameters: Max, FW, Area, RT, FT and ratio time, as exposed in the latest published article. On a related remark, processing the acquired data sets through an artificial intelligence algorithm might be a promising avenue which could provide unsuspected methods to discriminate populations.

Moreover, to reach the maximal measurement rate, cell tearing due to elongation forces must be completely eliminated, as mentioned previously. In that mindset, a thorough simulation model of eukaryotic cells deformation in a rectangular channel should be performed. Such a deformation model is missing from the current literature. It could indicate the optimized design and operational parameters for which cells would undergo optimal deformation and thus provide more sensitive deformability measurement. Additionally, a comprehensive model may allow correlation to some apparent rheology parameters such as the Young's modulus and viscosity. Due to the advancement of deformability cytometry (DC), these parameters are growing as a standardized base of comparison.

Lastly, the scope of applications should be clearly defined to strengthen the applicability of the RIC device. Focusing on a precise range of research and clinical applications may help to promote business and collaborative opportunities important for the future of this project. As a final recommendation, I would suggest to target cell cycle analysis, 5-part WBC count and T lymphocytes phenotyping for therapy. First, a complete cell cycle analysis should be readily accessible based on the results presented in this thesis. Indeed, each cell cycle phase has unique characteristics which should be reflected in a RI and deformability measurement. This would be advantageous for a broad spectrum of biological research and clinical fields. Secondly, considering lymphocytes and monocytes are already distinguished by flow cytometry and neutrophils and basophils by the RIC device, only eosinophils are yet to be discriminated to achieve a 5-part WBC count. Ideally, it should be performed on human cells acquired from a blood donation. This would demonstrate the applicability over healthy human cells as opposed to the immortal cell lines processed in this thesis. Thirdly, T lymphocytes phenotyping for therapy is a promising and contemporary research field which may hold the solution for cancer treatment. Needless to say, contributing to the development of such a novel and vital treatment option is the dream of many scientists.

REFERENCES

[1] D. Köhler, P. Bacher, A. Scheffold, M. Assenmacher, and M. Herber, "High-sensitivity detection and analysis of rare cells by integrated magnetic enrichment and flow cytometry using the MACSQuant ® Analyzer," *MACS&more*, vol. 14, no. 1, pp. 19–21, 2012.

[2] R. Hulspas, M. R. O'Gorman, B. L. Wood, J. W. Gratama, and D. Robert Sutherland, "Considerations for the control of background fluorescence in clinical flow cytometry," *Cytometry Part B - Clinical Cytometry*, vol. 76B, pp. 355–364, 2009.

[3] H. T. Maecker and J. Trotter, "Flow Cytometry Controls, Instrument Setup, and the Determination of Positivity," *Cytometry Part A*, vol. 69A, pp. 1037–1042, 2006.

[4] W. Wang, D. W. Kisker, D. H. Thamm, H. Shao, and K. L. Lear, "Optofluidic intracavity spectroscopy of canine hemangiosarcoma." *IEEE transactions on bio-medical engineering*, vol. 58, no. 4, pp. 853–60, apr 2011.

[5] X. Liang, a.Q. Liu, C. Lim, T. Ayi, and P. Yap, "Determining refractive index of single living cell using an integrated microchip," *Sensors and Actuators A: Physical*, vol. 133, no. 2, pp. 349–354, feb 2007.

[6] L. K. Chin, A. Q. Liu, C. S. Lim, X. M. Zhang, J. H. Ng, J. Z. Hao, and S. Takahashi, "Differential single living cell refractometry using grating resonant cavity with optical trap," *Applied Physics Letters*, vol. 91, no. 24, pp. 89–92, 2007.

[7] W. Z. Song, X. M. Zhang, a. Q. Liu, C. S. Lim, P. H. Yap, and H. M. M. Hosseini, "Refractive index measurement of single living cells using on-chip Fabry-Pérot cavity," *Applied Physics Letters*, vol. 89, no. 20, p. 203901, 2006.

[8] R. A. Flynn, B. Shao, M. Chachisvilis, M. Ozkan, and S. C. Esener, "Two-beam optical traps: Refractive index and size measurements of microscale objects," *Biomedical Microdevices*, vol. 7, no. 2, pp. 93–97, 2005.

[9] P. Y. Liu, L. K. Chin, W. Ser, H. F. Chen, C.-M. Hsieh, C.-H. Lee, K.-B. Sung, T. C. Ayi, P. H. Yap, B. Liedberg, K. Wang, T. Bourouina, and Y. Leprince-Wang, "Cell refractive index for cell biology and disease diagnosis: past, present and future." *Lab on a chip*, vol. 16, pp. 634–644, 2016.

[10] M. M. Villone, P. Memmolo, F. Merola, M. Mugnano, L. Miccio, P. L. Maffettone, and P. Ferraro, "Full-angle tomographic phase microscopy of flowing quasi-spherical cells," *Lab on a Chip*, vol. 18, no. 1, pp. 126–131, 2018.

[11] Q. Zhang, L. Zhong, P. Tang, Y. Yuan, S. Liu, J. Tian, and X. Lu, "Quantitative refractive index distribution of single cell by combining phase-shifting interferometry and AFM imaging," *Scientific Reports*, vol. 7, no. 1, pp. 1–10, 2017.

[12] M. Schürmann, J. Scholze, P. Müller, J. Guck, and C. J. Chan, "Cell nuclei have lower refractive index and mass density than cytoplasm," *Journal of biophotonics*, vol. 9, no. 10, pp. 1068–1076, 2016.

[13] Z. A. Steelman, W. J. Eldridge, J. B. Weintraub, and A. Wax, "Is the nuclear refractive index lower than cytoplasm? Validation of phase measurements and implications for light scattering technologies," *Journal of Biophotonics*, vol. 10, no. 12, pp. 1714–1722, 2017.

[14] G. Tomaiuolo, "Biomechanical properties of red blood cells in health and disease towards microfluidics," *Biomicrofluidics*, vol. 8, no. 5, pp. 1–19, 2014.

[15] Y. Zheng, J. Wen, J. Nguyen, M. A. Cachia, C. Wang, and Y. Sun, "Decreased deformability of lymphocytes in chronic lymphocytic leukemia," *Scientific Reports*, vol. 5, no. 7613, pp. 1–5, 2015.

[16] S. Golfier, P. Rosendahl, A. Mietke, M. Herbig, J. Guck, and O. Otto, "High-throughput cell mechanical phenotyping for label-free titration assays of cytoskeletal modifications," *Cytoskeleton*, vol. 74, no. 8, pp. 283–296, 2017.

[17] O. Otto, P. Rosendahl, A. Mietke, S. Golfier, C. Herold, D. Klaue, S. Girardo, S. Pagliara, A. Ekpenyong, A. Jacobi, M. Wobus, N. Töpfner, U. F. Keyser, J. Mansfeld, E. Fischer-Friedrich, and J. Guck, "Real-time deformability cytometry: on-the-fly cell mechanical phenotyping." *Nature Methods*, vol. 12, no. 3, pp. 199–202, 4 p following 202, 2015.

[18] A. Mietke, O. Otto, S. Girardo, P. Rosendahl, A. Taubenberger, S. Golfier, E. Ulbricht, S. Aland, J. Guck, and E. Fischer-Friedrich, "Extracting Cell Stiffness from Real-Time Deformability Cytometry: Theory and Experiment," *Biophysical Journal*, vol. 109, no. 10, pp. 2023–2036, 2015.

[19] J. S. Dudani, D. R. Gossett, H. T. K. Tse, and D. Di Carlo, "Pinched-flow hydrodynamic stretching of single-cells," *Lab on a Chip*, vol. 13, no. 18, p. 3728, 2013.

[20] D. R. Gossett, H. T. K. Tse, S. A. Lee, Y. Ying, A. G. Lindgren, O. O. Yang, J. Rao, A. T. Clark, and D. Di Carlo, "Hydrodynamic stretching of single cells for large population mechanical phenotyping," *Proceedings of the National Academy of Sciences*, vol. 109, no. 20, pp. 7630–7635, 2012.

[21] J. Knight, A. Vishwanath, J. Brody, and R. Austin, "Hydrodynamic Focusing on a Silicon Chip: Mixing Nanoliters in Microseconds," *Physical Review Letters*, vol. 80, no. 17, pp. 3863–3866, apr 1998.

[22] G.-B. Lee, C.-I. Hung, B.-J. Ke, G.-R. Huang, B.-H. Hwei, and H.-F. Lai, "Hydrodynamic Focusing for a Micromachined Flow Cytometer," *Journal of Fluids Engineering*, vol. 123, no. 3, p. 672, 2001.

[23] G.-B. Lee, C.-C. Chang, S.-B. Huang, and R.-J. Yang, "The hydrodynamic focusing effect inside rectangular microchannels," *Journal of Micromechanics and Microengineering*, vol. 16, no. 5, pp. 1024–1032, may 2006.

[24] Z. Wu and N.-T. Nguyen, "Hydrodynamic focusing in microchannels under consideration of diffusive dispersion: theories and experiments," *Sensors and Actuators B: Chemical*, vol. 107, no. 2, pp. 965–974, jun 2005.

[25] Y. J. Chiu, S. H. Cho, Z. Mei, V. Lien, T. F. Wu, and Y. H. Lo, "Universally applicable three-dimensional hydrodynamic microfluidic flow focusing," *Lab on a Chip*, vol. 13, no. 9, pp. 1803–1809, 2013.

[26] L. Jiang, W. Wang, Y. Chau, and S. Yao, "Controllable formation of aromatic nanoparticles in a three-dimensional hydrodynamic flow focusing microfluidic device," *RSC Advances*, vol. 3, no. 39, pp. 17 762–17 769, 2013.

[27] J. M. Lim, N. Bertrand, P. M. Valencia, M. Rhee, R. Langer, S. Jon, O. C. Farokhzad, and R. Karnik, "Parallel microfluidic synthesis of size-tunable polymeric nanoparticles using 3D flow focusing towards in vivo study," *Nanomedicine: Nanotechnology, Biology, and Medicine*, vol. 10, no. 2, pp. 401–409, 2014.

[28] K. I. Min, D. J. Im, H. J. Lee, and D. P. Kim, "Three-dimensional flash flow microreactor for scale-up production of monodisperse PEG-PLGA nanoparticles," *Lab on a Chip*, vol. 14, no. 20, pp. 3987–3992, 2014.

[29] G. Eluru, L. A. N. Julius, and S. S. Gorthi, "Single-layer microfluidic device to realize hydrodynamic 3D flow focusing," *Lab on a Chip*, vol. 16, no. 21, pp. 4133–4141, 2016.

[30] P. Paiè, F. Bragheri, R. M. Vazquez, and R. Osellame, "Straightforward 3D hydrodynamic focusing in femtosecond laser fabricated microfluidic channels," *Lab on a Chip*, vol. 14, no. 11, pp. 1826–1833, 2014.

[31] M. Rhee, P. M. Valencia, M. I. Rodriguez, R. Langer, O. C. Farokhzad, and R. Karnik, "Synthesis of size-tunable polymeric nanoparticles enabled by 3D hydrodynamic flow focusing in single-layer microchannels," *Advanced Materials*, vol. 23, no. 12, pp. 79–83, 2011.

[32] W. R. Dean M. A., "XVI. Note on the motion of fluid in a curved pipe," *The London, Edinburgh, and Dublin Philosophical Magazine and Journal of Science*, vol. 4, no. 20, pp. 208–223, 1927.

[33] D. Di Carlo, "Inertial microfluidics," *Lab on a Chip*, vol. 9, no. 21, pp. 3038–3046, 2009.

[34] X. Mao, J. R. Waldeisen, and T. J. Huang, ""Microfluidic drifting"–implementing three-dimensional hydrodynamic focusing with a single-layer planar microfluidic device." *Lab on a chip*, vol. 7, no. 10, pp. 1260–2, oct 2007.

[35] B. H. Ha, K. S. Lee, J. H. Jung, and H. J. Sung, "Three-dimensional hydrodynamic flow and particle focusing using four vortices Dean flow," *Microfluidics and Nanofluidics*, vol. 17, no. 4, pp. 647–655, 2014.

[36] A. A. Nawaz, X. Zhang, X. Mao, J. Rufo, S. C. S. Lin, F. Guo, Y. Zhao, M. Lapsley, P. Li, J. P. McCoy, S. J. Levine, and T. J. Huang, "Sub-micrometer-precision, three-dimensional (3D) hydrodynamic focusing via "microfluidic drifting"," *Lab on a Chip*, vol. 14, no. 2, pp. 415–423, 2014.

[37] M. G. Lee, S. Choi, and J. K. Park, "Three-dimensional hydrodynamic focusing with a single sheath flow in a single-layer microfluidic device," *Lab on a Chip*, vol. 9, no. 21, pp. 3155–3160, 2009.

[38] J. Zhang, M. Li, W. H. Li, and G. Alici, "Inertial focusing in a straight channel with asymmetrical expansion-contraction cavity arrays using two secondary flows," *Journal of Micromechanics and Microengineering*, vol. 23, no. 8, 2013.

[39] A. J. Chung, D. R. Gossett, and D. Di Carlo, "Three dimensional, sheathless, and high-throughput microparticle inertial focusing through geometry-induced secondary flows," *Small*, vol. 9, no. 5, pp. 685–690, 2013.

[40] L. L. Fan, X. K. He, Y. Han, J. Zhe, and L. Zhao, "Continuous 3D particle focusing in a microchannel with curved and symmetric sharp corner structures," *Journal of Micromechanics and Microengineering*, vol. 25, no. 3, 2015.

[41] D. H. Yoon, J. B. Ha, Y. K. Bahk, T. Arakawa, S. Shoji, and J. S. Go, "Size-selective separation of micro beads by utilizing secondary flow in a curved rectangular microchannel." *Lab on a chip*, vol. 9, no. 1, pp. 87–90, jan 2009.

[42] S. S. Kuntaegowdanahalli, A. A. S. Bhagat, G. Kumar, and I. Papautsky, "Inertial microfluidics for continuous particle separation in spiral microchannels." *Lab on a chip*, vol. 9, no. 20, pp. 2973–80, oct 2009.

[43] M. G. Lee, S. Choi, and J. K. Park, "Inertial separation in a contraction-expansion array microchannel," *Journal of Chromatography A*, vol. 1218, no. 27, pp. 4138–4143, 2011.

[44] I. D. Johnston, M. B. McDonnell, C. K. Tan, D. K. McCluskey, M. J. Davies, and M. C. Tracey, "Dean flow focusing and separation of small microspheres within a narrow size range," *Microfluidics and Nanofluidics*, vol. 17, no. 3, pp. 509–518, 2014.

[45] S. Tripathi, A. Kumar, Y. V. Bala Varun Kumar, and A. Agrawal, "Three-dimensional hydrodynamic flow focusing of dye, particles and cells in a microfluidic device by employing two bends of opposite curvature," *Microfluidics and Nanofluidics*, vol. 20, no. 2, pp. 1–14, 2016.

[46] G. Segré and A. Silberberg, "Radial Particle Displacements in Poiseuille Flow of Suspensions," *Nature*, vol. 189, p. 209, 1961.

[47] J. A. Schonberg and E. J. Hinch, "Inertial migration of a sphere in poiseuille flow," *Journal of Fluid Mechanics*, vol. 203, p. 517–524, 1989.

[48] E. S. Asmolov, "The inertial lift on a spherical particle in plane Poiseuille flow at large Reynolds number," *Journal of Fluid Mechanics*, vol. 381, no. 1999, pp. 63–87, 1999.

[49] J. P. Matas, J. F. Morris, and É. Guazzelli, "Inertial migration of rigid spherical particles in Poiseuille flow," *Journal of Fluid Mechanics*, vol. 515, pp. 171–195, 2004.

[50] D. Di Carlo, J. F. Edd, K. J. Humphry, H. A. Stone, and M. Toner, "Particle segregation and dynamics in confined flows," *Physical Review Letters*, vol. 102, no. 9, pp. 1–4, 2009.

[51] B. Chun and A. J. C. Ladd, "Inertial migration of neutrally buoyant particles in a square duct: An investigation of multiple equilibrium positions," *Physics of Fluids*, vol. 18, no. 3, pp. 1–5, 2006.

[52] Y. S. Choi, K. W. Seo, and S. J. Lee, "Lateral and cross-lateral focusing of spherical particles in a square microchannel," *Lab on a Chip*, vol. 11, no. 3, pp. 460–465, 2011.

[53] K. J. Humphry, P. M. Kulkarni, D. A. Weitz, J. F. Morris, and H. A. Stone, "Axial and lateral particle ordering in finite Reynolds number channel flows," *Physics of Fluids*, vol. 22, no. 8, pp. 1–5, 2010.

[54] S. C. Hur, H. T. K. Tse, and D. Di Carlo, "Sheathless inertial cell ordering for extreme throughput flow cytometry." *Lab on a chip*, vol. 10, no. 3, pp. 274–280, 2010.

[55] W. Lee, H. Amini, H. A. Stone, and D. Di Carlo, "Dynamic self-assembly and control of microfluidic particle crystals." *Proceedings of the National Academy of Sciences of the United States of America*, vol. 107, no. 52, pp. 22 413–8, 2010.

[56] J. Zhou, P. V. Giridhar, S. Kasper, and I. Papautsky, "Modulation of aspect ratio for complete separation in an inertial microfluidic channel," *Lab on a Chip*, vol. 13, no. 10, pp. 1919–1929, 2013.

[57] A. E. Reece and J. Oakeya, "Long-range forces affecting equilibrium inertial focusing behavior in straight high aspect ratio microfluidic channels," *Physics of Fluids*, vol. 28, no. 4, pp. 1–10, 2016.

[58] J. Zhou and I. Papautsky, "Fundamentals of inertial focusing in microchannels." *Lab on a chip*, vol. 13, no. 6, pp. 1121–32, 2013.

[59] J. P. Matas, V. Glezer, É. Guazzelli, and J. F. Morris, "Trains of particles in finite-Reynolds-number pipe flow," *Physics of Fluids*, vol. 16, no. 11, pp. 4192–4195, 2004.

[60] D. Di Carlo, D. Irimia, R. G. Tompkins, and M. Toner, "Continuous inertial focusing, ordering, and separation of particles in microchannels," *Proceedings of the National Academy of Sciences*, vol. 104, no. 48, pp. 18 892–18 897, 2007.

[61] A. J. Mach and D. di Carlo, "Continuous scalable blood filtration device using inertial microfluidics," *Biotechnology and Bioengineering*, vol. 107, no. 2, pp. 302–311, 2010.

[62] S. C. Hur, T. Z. Brinckerhoff, C. M. Walthers, J. C. Dunn, and D. Di Carlo, "Label-Free Enrichment of Adrenal Cortical Progenitor Cells Using Inertial Microfluidics," *PLoS ONE*, vol. 7, no. 10, 2012.

[63] J. Sun, C. Liu, M. Li, J. Wang, Y. Xianyu, G. Hu, and X. Jiang, "Size-based hydrodynamic rare tumor cell separation in curved microfluidic channels," *Biomicrofluidics*, vol. 7, no. 1, pp. 1–11, 2013.

[64] M. E. Warkiani, G. Guan, K. B. Luan, W. C. Lee, A. A. S. Bhagat, P. Kant Chaudhuri, D. S. W. Tan, W. T. Lim, S. C. Lee, P. C. Chen, C. T. Lim, and J. Han, "Slanted spiral microfluidics for the ultra-fast, label-free isolation of circulating tumor cells," *Lab on a Chip*, vol. 14, no. 1, pp. 128–137, 2014.

[65] M. E. Warkiani, A. K. P. Tay, G. Guan, and J. Han, "Membrane-less microfiltration using inertial microfluidics," *Scientific Reports*, vol. 5, pp. 1–10, 2015.

[66] J. Zhang, W. Li, M. Li, G. Alici, and N. T. Nguyen, "Particle inertial focusing and its mechanism in a serpentine microchannel," *Microfluidics and Nanofluidics*, vol. 17, no. 2, pp. 305–316, 2014.

[67] J. M. Martel and M. Toner, "Inertial Focusing in Microfluidcs," *Annual Review of Biomedical Engineering*, vol. 16, pp. 371–396, 2014.

[68] J. Zhang, S. Yan, D. Yuan, G. Alici, N. T. Nguyen, M. Ebrahimi Warkiani, and W. Li, "Fundamentals and applications of inertial microfluidics: A review," *Lab on a Chip*, vol. 16, no. 1, pp. 10–34, 2016.

[69] S. Yang, J. Y. Kim, S. J. Lee, S. S. Lee, and J. M. Kim, "Sheathless elasto-inertial particle focusing and continuous separation in a straight rectangular microchannel," *Lab on a Chip*, vol. 11, no. 2, pp. 266–273, 2011.

[70] G. D'Avino, G. Romeo, M. M. Villone, F. Greco, P. A. Netti, and P. L. Maffettone, "Single line particle focusing induced by viscoelasticity of the suspending liquid: Theory, experiments and simulations to design a micropipe flow-focuser," *Lab on a Chip*, vol. 12, no. 9, pp. 1638–1645, 2012.

[71] J. Nam, H. Lim, D. Kim, H. Jung, and S. Shin, "Continuous separation of microparticles in a microfluidic channel via the elasto-inertial effect of non-Newtonian fluid," *Lab on a Chip*, vol. 12, no. 7, pp. 1347–1354, 2012.

[72] F. Del Giudice, G. Romeo, G. D'Avino, F. Greco, P. A. Netti, and P. L. Maffettone, "Particle alignment in a viscoelastic liquid flowing in a square-shaped microchannel," *Lab on a Chip*, vol. 13, no. 21, pp. 4263–4271, 2013.

[73] K. W. Seo, H. J. Byeon, H. K. Huh, and S. J. Lee, "Particle migration and single-line particle focusing in microscale pipe flow of viscoelastic fluids," *RSC Advances*, vol. 4, no. 7, pp. 3512–3520, 2014.

[74] G. Holzner, S. Stavrakis, and A. DeMello, "Elasto-Inertial Focusing of Mammalian Cells and Bacteria Using Low Molecular, Low Viscosity PEO Solutions," *Analytical Chemistry*, p. acs.analchem.7b03093, 2017.

[75] G. Li, G. H. McKinley, and A. M. Ardekani, "Dynamics of particle migration in channel flow of viscoelastic fluids," *Journal of Fluid Mechanics*, vol. 785, pp. 486–505, 2015.

[76] A. Wolff, I. R. Perch-Nielsen, U. D. Larsen, P. Friis, G. Goranovic, C. R. Poulsen, J. P. Kutter, and P. Telleman, "Integrating advanced functionality in a microfabricated high-throughput fluorescent-activated cell sorter," *Lab on a Chip*, vol. 3, pp. 22–27, 2003.

[77] C. Simonnet and A. Groisman, "High-throughput and high-resolution flow cytometry in molded microfluidic devices," *Analytical Chemistry*, vol. 78, no. 16, pp. 5653–5663, 2006.

[78] J. Oakey, R. W. Applegate Jr, E. Arellano, D. Di Carlo, S. W. Graves, and M. Toner, "Particle Focusing in Staged Inertial Microfluidic Devices for Flow Cytometry," *Analytical Chemistry*, vol. 82, no. 9, pp. 3862–3867, 2010.

[79] M. E. Piyasena, P. P. A. Suthanthiraraj, R. W. Applegate, A. M. Goumas, T. A. Woods, G. P. López, and S. W. Graves, "Multinode acoustic focusing for parallel flow cytometry," *Analytical Chemistry*, vol. 84, no. 4, pp. 1831–1839, 2012.

[80] P. P. Austin Suthanthiraraj, M. E. Piyasena, T. A. Woods, M. A. Naivar, G. P. Ĺpez, and S. W. Graves, "One-dimensional acoustic standing waves in rectangular channels for flow cytometry," *Methods*, vol. 57, no. 3, pp. 259–271, 2012.

[81] L.-M. Fu and Y.-N. Wang, "Optical microflow cytometer based on external total reflection," *Electrophoresis*, vol. 33, no. 21, pp. 3229–3235, 2012.

[82] M. Frankowski, J. Theisen, A. Kummrow, P. Simon, H. Ragusch, N. Bock, M. Schmidt, and J. Neukammer, "Microflow cytometers with integrated hydrodynamic focusing." *Sensors (Basel, Switzerland)*, vol. 13, no. 4, pp. 4674–4693, 2013.

[83] J. Skommer, J. Akagi, K. Takeda, Y. Fujimura, K. Khoshmanesh, and D. Wlodkowic, "Multiparameter Lab-on-a-Chip flow cytometry of the cell cycle," *Biosensors and Bioelectronics*, vol. 42, no. 1, pp. 586–591, 2013.

[84] X. Wang, M. Zandi, C. C. Ho, N. Kaval, and I. Papautsky, "Single stream inertial focusing in a straight microchannel," *Lab on a Chip*, vol. 15, no. 8, pp. 1812–1821, 2015.

[85] P. Simon, M. Frankowski, N. Bock, and J. Neukammer, "Label-free whole blood cell differentiation based on multiple frequency AC impedance and light scattering analysis in a micro flow cytometer," *Lab on a Chip*, vol. 16, pp. 2326–2338, 2016.

[86] J. Zhao and Z. You, "A microflow cytometer with a rectangular Quasi-flat-top laser spot," *Sensors (Switzerland)*, vol. 16, no. 9, pp. 1–12, 2016.

[87] Y. C. Tung, M. Zhang, C. T. Lin, K. Kurabayashi, and S. J. Skerlos, "PDMS-based opto-fluidic micro flow cytometer with two-color, multi-angle fluorescence detection capability using PIN photodiodes," *Sensors and Actuators, B: Chemical*, vol. 98, pp. 356–367, 2004.

[88] A. Kummrow, J. Theisen, M. Frankowski, A. Tuchscheerer, H. Yildirim, K. Brattke, M. Schmidt, and J. Neukammer, "Microfluidic structures for flow cytometric analysis of hydrodynamically focussed blood cells fabricated by ultraprecision micromachining," *Lab on a Chip*, vol. 9, no. 7, pp. 972–981, 2009.

[89] D. Schafer, E. A. Gibson, E. A. Salim, A. E. Palmer, and R. Jimenez, "Microfluidic cell counter with embedded optical fibers fabricated by femtosecond laser ablation and anodic bonding," *Optics Express*, vol. 17, no. 8, pp. 6068–6073, 2009.

[90] J. P. Golden, J. S. Kim, J. S. Erickson, L. R. Hilliard, P. B. Howell, G. P. Anderson, M. Nasir, and F. S. Ligler, "Multi-wavelength microflow cytometer using groove-generated sheath flow," *Lab on a Chip*, vol. 9, no. 13, pp. 1942–1950, 2009.

[91] X. Mao, A. A. Nawaz, S. C. S. Lin, M. I. Lapsley, Y. Zhao, J. P. McCoy, W. S. El-Deiry, and T. J. Huang, "An integrated, multiparametric flow cytometry chip using "microfluidic drifting" based three-dimensional hydrodynamic focusing," *Biomicrofluidics*, vol. 6, no. 2, p. 24113, 2012.

[92] G. Testa, G. Persichetti, and R. Bernini, "Micro flow cytometer with self-aligned 3D hydrodynamic focusing," *Biomedical Optics Express*, vol. 6, no. 1, pp. 54–62, 2015.

[93] S. Etcheverry, A. Faridi, H. Ramachandraiah, T. Kumar, W. Margulis, F. Laurell, and A. Russom, "High performance micro-flow cytometer based on optical fibres," *Scientific Reports*, vol. 7, pp. 1–8, 2017.

[94] Z. Wang, J. El-Ali, M. Engelund, T. Gotsaed, I. R. Perch-Nielsen, K. B. Mogensen, D. Snakenborg, J. P. Kutter, and A. Wolff, "Measurements of scattered light on a microchip flow cytometer with integrated polymer based optical elements RID E-3256-2010 RID B-7601-2011," *Lab on a Chip*, vol. 4, pp. 372–377, 2004.

[95] J. Godin and Y.-H. Lo, "Two-parameter angular light scatter collection for microfluidic flow cytometry by unique waveguide structures," *Biomedical Optics Express*, vol. 1, no. 5, pp. 1472–1479, 2010.

[96] M. Rosenauer, W. Buchegger, I. Finoulst, P. Verhaert, and M. Vellekoop, "Miniaturized flow cytometer with 3D hydrodynamic particle focusing and integrated optical elements applying silicon photodiodes," *Microfluidics and Nanofluidics*, vol. 10, no. 4, pp. 761–771, 2011.

[97] K. T. Kotz, A. C. Petrofsky, R. Haghgooie, R. Granier, M. Toner, and R. G. Tompkins, "Inertial focusing cytometer with integrated optics for particle characterization," *Technology*, vol. 1, no. 1, pp. 27–36, 2013.

[98] B. R. Watts, Z. Zhang, C. Q. Xu, X. Cao, and M. Lin, "Scattering detection using a photonic-microfluidic integrated device with on-chip collection capabilities," *Electrophoresis*, vol. 35, no. 2-3, pp. 271–281, 2014.

[99] D. Spencer, G. Elliott, and H. Morgan, "A sheath-less combined optical and impedance micro-cytometer," *Lab on a Chip*, vol. 14, no. 16, pp. 3064–3073, 2014.

[100] A. S. Rane, J. Rutkauskaite, A. DeMello, and S. Stavrakis, "High-Throughput Multiparametric Imaging Flow Cytometry," *Chem*, vol. 3, no. 4, pp. 588–602, 2017.

[101] D. M. Kalb, F. A. Fencl, T. A. Woods, A. Swanson, G. C. Maestas, J. J. Juárez, B. S. Edwards, A. P. Shreve, and S. W. Graves, "Line-Focused Optical Excitation of Parallel Acoustic Focused Sample Streams for High Volumetric and Analytical Rate Flow Cytometry," *Analytical Chemistry*, vol. 89, no. 18, pp. 9967–9975, 2017.

[102] Y. Han, Y. Gu, A. C. Zhang, and Y.-H. Lo, "Review: Imaging Technologies for Flow Cytometry," *Lab on a chip*, vol. 16, no. 24, pp. 4639–4647, 2016.

[103] R. J. Yang, L. M. Fu, and H. H. Hou, "Review and perspectives on microfluidic flow cytometers," *Sensors and Actuators, B: Chemical*, vol. 266, pp. 26–45, 2018.

[104] S. Stavrakis, G. Holzner, J. Choo, and A. DeMello, "High-throughput microfluidic imaging flow cytometry," *Current Opinion in Biotechnology*, vol. 55, pp. 36–43, 2019.

[105] R. E. Green, H. M. Sosik, R. J. Olson, and M. D. DuRand, "Flow cytometric determination of size and complex refractive index for marine particles: comparison with independent and bulk estimates," *Applied Optics*, vol. 42, no. 3, p. 526, 2003.

[106] S. G. Ackleson and R. W. Spinrad, "Size and refractive index of individual marine particulates: a flow cytometric approach," *Applied Optics*, vol. 27, no. 7, p. 1270, 1988.

[107] V. P. Maltsev, "Scanning flow cytometry for individual particle analysis," *Review of Scientific Instruments*, vol. 71, no. 1, pp. 243–255, 2000.

[108] V. Maselli, J. R. Grenier, S. Ho, and P. R. Herman, "Femtosecond laser written optofluidic sensor: Bragg grating waveguide evanescent probing of microfluidic channel," *Optics Express*, vol. 17, no. 14, p. 11719, 2009.

[109] A. Densmore, D. X. Xu, P. Waldron, S. Janz, P. Cheben, J. Lapointe, a. Delâge, B. Lamontagne, J. H. Schmid, and E. Post, "A silicon-on-insulator photonic wire based evanescent field sensor," *IEEE Photonics Technology Letters*, vol. 18, no. 23, pp. 2520–2522, 2006.

[110] A. Ymeti, J. S. Kanger, J. Greve, G. A. Besselink, P. V. Lambeck, R. Wijn, and R. G. Heideman, "Integration of microfluidics with a four-channel integrated optical Young interferometer immunosensor," *Biosensors and Bioelectronics*, vol. 20, no. 7, pp. 1417–1421, 2005.

[111] D. Patko, K. Cottier, A. Hamori, and R. Horvath, "Single beam grating coupled interferometry: high resolution miniaturized label-free sensor for plate based parallel screening," *Optics Express*, vol. 20, no. 21, pp. 23 162–23 173, 2012.

[112] K. Schmitt, B. Schirmer, C. Hoffmann, A. Brandenburg, and P. Meyrueis, "Interferometric biosensor based on planar optical waveguide sensor chips for label-free detection of surface bound bioreactions," *Biosensors and Bioelectronics*, vol. 22, no. 11, pp. 2591–2597, 2007.

[113] P. Kozma, F. Kehl, E. Ehrentreich-Förster, C. Stamm, and F. F. Bier, "Integrated planar optical waveguide interferometer biosensors: A comparative review," *Biosensors and Bioelectronics*, vol. 58, pp. 287–307, 2014.

[114] P. Polynkin, A. Polynkin, N. Peyghambarian, and M. Mansuripur, "Evanescent field-based optical fiber sensing device for measuring the refractive index of liquids in microfluidic channels," *Optics Letters*, vol. 30, no. 11, p. 1273, 2005.

[115] Q. Wang and G. Farrell, "All-fiber multimode-interference-based refractometer sensor: proposal and design." *Optics letters*, vol. 31, no. 3, pp. 317–319, 2006.

[116] Y. Liu, W. Peng, X. Zhang, and S. Qian, "Optical fiber sensor based on capillary wall for highly-sensitive refractive index measurement," *Optics Communications*, vol. 319, pp. 106–109, 2014.

[117] Q. Wu, Y. Semenova, P. Wang, and G. Farrell, "High sensitivity SMS fiber structure based refractometer – analysis and experiment," *Optics Express*, vol. 19, no. 9, p. 7937, 2011.

[118] Y. Zhang, B. Lin, S. C. Tjin, H. Zhang, G. Wang, P. Shum, and X. Zhang, "Refractive index sensing based on higher-order mode reflection of a microfiber Bragg grating," *Optics Express*, vol. 18, no. 25, p. 26345, 2010.

[119] Y. Ran, Y.-N. Tan, L.-P. Sun, S. Gao, J. Li, L. Jin, and B.-O. Guan, "193nm excimer laser inscribed Bragg gratings in microfibers for refractive index sensing," *Optics Express*, vol. 19, no. 19, p. 18577, 2011.

[120] X. Fang, C. R. Liao, and D. N. Wang, "Femtosecond laser fabricated fiber Bragg grating in microfiber for refractive index sensing," *Optics Letters*, vol. 35, no. 7, p. 1007, 2010.

[121] A. Iadicicco, S. Campopiano, A. Cutolo, M. Giordano, and A. Cusano, "Refractive index sensor based on microstructured fiber Bragg grating," *IEEE Photonics Technology Letters*, vol. 17, no. 6, pp. 1250–1252, 2005.

[122] S. Sahu, J. Ali, P. P. Yupapin, and G. Singh, "Porous Silicon Based Bragg-Grating Resonator for Refractive Index Biosensor," *Photonic Sensors*, vol. 8, no. 3, pp. 248–254, 2018.

[123] W. Liang, Y. Huang, Y. Xu, R. K. Lee, and A. Yariv, "Highly sensitive fiber Bragg grating refractive index sensors," *Applied Physics Letters*, vol. 86, no. 15, pp. 1–3, 2005.

[124] J. H. Chong, P. Shum, H. Haryono, A. Yohana, M. K. Rao, C. Lu, and Y. Zhu, "Measurements of refractive index sensitivity using long-period grating refractometer," *Optics Communications*, vol. 229, no. 1-6, pp. 65–69, 2004.

[125] T. Zhu, Y.-j. Rao, and Q.-j. Mo, "Simultaneous Measurement of Refractive Index and Temperature Using a Single," *IEEE Photonics Technology Letters*, vol. 17, no. 12, pp. 2700–2702, 2005.

[126] G. Quero, A. Crescitelli, D. Paladino, M. Consales, A. Buosciolo, M. Giordano, A. Cutolo, and A. Cusano, "Evanescent wave long-period fiber grating within D-shaped optical fibers for high sensitivity refractive index detection," *Sensors and Actuators B: Chemical*, vol. 152, no. 2, pp. 196–205, 2011.

[127] P. Bhatia and B. D. Gupta, "Surface-plasmon-resonance-based fiber-optic refractive index sensor: sensitivity enhancement," *Applied Optics*, vol. 50, no. 14, p. 2032, 2011.

[128] Z. Xiao, H. Dai, and X. Chen, "Ultrasensitive optofluidic resonator refractive index sensor," *Optics Letters*, vol. 43, no. 17, pp. 4216–4219, 2018.

[129] D. Monzón-Hernández and J. Villatoro, "High-resolution refractive index sensing by means of a multiple-peak surface plasmon resonance optical fiber sensor," *Sensors and Actuators, B: Chemical*, vol. 115, no. 1, pp. 227–231, 2006.

[130] M. Piliarik, L. Párová, and J. Homola, "High-throughput SPR sensor for food safety," *Biosensors and Bioelectronics*, vol. 24, no. 5, pp. 1399–1404, 2009.

[131] R. Slavík and J. Homola, "Ultrahigh resolution long range surface plasmon-based sensor," *Sensors and Actuators, B: Chemical*, vol. 123, no. 1, pp. 10–12, 2007.

[132] M. Iqbal, M. A. Gleeson, B. Spaugh, F. Tybor, W. G. Gunn, M. Hochberg, T. Baehr-Jones, R. C. Bailey, and L. C. Gunn, "Label-free biosensor arrays based on silicon ring resonators and high-speed optical scanning instrumentation," *IEEE Journal of Selected Topics in Quantum Electronics*, vol. 16, no. 3, pp. 654–661, 2010.

[133] G. Besselink, R. Heideman, E. Schreuder, L. Wevers, F. Falke, and H. Van den Vlekkert, "Performance of Arrayed Microring Resonator Sensors with the TriPleX Platform," *Journal of Biosensors & Bioelectronics*, vol. 7, no. 2, 2016.

[134] L. Gounaridis, P. Groumas, E. Schreuder, G. Tsekenis, A. Marousis, R. Heideman, H. Avramopoulos, and C. Kouloumentas, "High performance refractive index sensor based on low Q-factor ring resonators and FFT processing of wavelength scanning data," *Optics Express*, vol. 25, no. 7, pp. 134–142, 2017.

[135] N. Lin, L. Jiang, S. Wang, H. Xiao, Y. Lu, and H. Tsai, "Thermostable refractive index sensors based on whispering gallery modes in a microsphere coated with poly(methyl methacrylate)," *Applied Optics*, vol. 50, no. 7, p. 992, 2011.

[136] K. Chaitavon, S. Sumriddetchkajorn, and J. Nukeaw, "Highly sensitive refractive index measurement with a sandwiched single-flow-channel microfluidic chip," *RSC Advances*, no. d, 2013.

[137] N. Xie, H. Zhang, B. Liu, H. Liu, T. Liu, and C. Wang, "In-Line Microfiber-Assisted Mach–Zehnder Interferometer for Microfluidic Highly Sensitive Measurement of Salinity," *IEEE Sensors Journal*, vol. 18, no. 21, pp. 8767–8772, nov 2018.

[138] Y. N. Zhang, Y. Zhao, and R. Q. Lv, "A review for optical sensors based on photonic crystal cavities," *Sensors and Actuators A: Physical*, vol. 233, pp. 374–389, 2015.

[139] X. Zhang, G. Zhou, P. Shi, H. Du, T. Lin, J. Teng, and F. S. Chau, "On-chip integrated optofluidic complex refractive index sensing using silicon photonic crystal nanobeam cavities," *Optics Letters*, vol. 41, no. 6, p. 1197, 2016.

[140] L. K. Chin, A. Q. Liu, C. S. Lim, C. L. Lin, T. C. Ayi, and P. H. Yap, "An optofluidic volume refractometer using Fabry–Pérot resonator with tunable liquid microlenses," *Biomicrofluidics*, vol. 4, no. 2, p. 24107, jan 2010.

[141] R. Gao, Y. Jiang, W. Ding, Z. Wang, and D. Liu, "Filmed extrinsic Fabry-Perot interferometric sensors for the measurement of arbitrary refractive index of liquid," *Sensors and Actuators B: Chemical*, vol. 177, pp. 924–928, 2013.

[142] L.-X. Kong, Y.-X. Zhang, W.-G. Zhang, Z. Li, Y.-S. Zhang, T.-Y. Yan, and P.-C. Geng, "Temperature-Independent Micro-Refractometer Based on Cascaded In-Fiber Air Cavities With Strain-Error Correction," *IEEE Sensors Journal*, vol. 18, no. 21, pp. 8773–8780, 2018.

[143] P. Liu, H. Huang, T. Cao, Z. Tang, X. Liu, Z. Qi, M. Ren, and H. Wu, "An optofluidics biosensor consisted of high-finesse Fabry-Pérot resonator and micro-fluidic channel," *Applied Physics Letters*, vol. 100, no. 23, pp. 233 704–233 705, 2012.

[144] R. St-Gelais, J. Masson, and Y.-A. Peter, "All-silicon integrated Fabry–Pérot cavity for volume refractive index measurement in microfluidic systems," *Applied Physics Letters*, vol. 94, no. 24, p. 243905, 2009.

[145] N. Gaber, Y. Sabry, M. Erfan, F. Marty, and T. Bourouina, "High-Q Fabry–Pérot Micro-Cavities for High-Sensitivity Volume Refractometry," *Micromachines*, vol. 9, no. 2, p. 54, 2018.

[146] H. Zhu, J. J. He, L. Shao, and M. Li, "Ultra-high sensitivity optical sensors based on cascaded two Fabry-Perot interferometers," *Sensors and Actuators, B: Chemical*, vol. 277, no. September, pp. 152–156, 2018.

[147] H. Wu, H. Huang, M. Bai, P. Liu, M. Chao, J. Hu, J. Hao, and T. Cao, "An ultra-low detection-limit optofluidic biosensor based on all glass Fabry-Perot cavity," *Optics Express*, vol. 22, no. 26, p. 31977, dec 2014.

[148] A. Leblanc-Hotte, J.-S. Delisle, S. Lesage, and Y.-A. Peter, "The Importance of Single-Mode Behavior in Silicon-On-Insulator Rib Waveguides With Very Large Cross Section for Resonant Sensing Applications," *IEEE Journal of Selected Topics in Quantum Electronics*, vol. 22, no. 6, pp. 241–248, nov 2016.

[149] W. J. Choi, D. I. Jeon, S.-G. Ahn, J.-H. Yoon, S. Kim, and B. H. Lee, "Full-field optical coherence microscopy for identifying live cancer cells by quantitative measurement of refractive index distribution." *Optics express*, vol. 18, no. 22, pp. 23 285–95, oct 2010.

[150] M. Schürmann, G. Cojoc, S. Girardo, E. Ulbricht, J. Guck, and P. Müller, "Three-dimensional correlative single-cell imaging utilizing fluorescence and refractive index tomography," *Journal of Biophotonics*, vol. 11, no. 3, pp. 1–11, 2018.

[151] G. Dardikman, Y. Nygate, I. Barnea, N. Turko, G. Singh, B. Javidi, and N. Shaked, "Integral refractive index imaging of flowing cell nuclei using quantitative phase microscopy combined with fluorescence microscopy," *Biomedical Optics Express*, vol. 9, no. 3, pp. 88–92, 2018.

[152] I. M. White and X. Fan, "On the performance quantification of resonant refractive index sensors," *Optics Express*, vol. 16, no. 2, pp. 1020–1028, 2008.

[153] A. Ganjoo, H. Jain, C. Yu, R. Song, J. V. Ryan, J. Irudayaraj, Y. J. Ding, and C. G. Pantano, "Planar chalcogenide glass waveguides for IR evanescent wave sensors," *Journal of Non-Crystalline Solids*, vol. 352, no. 6-7 SPEC. ISS., pp. 584–588, 2006.

[154] M. Piliarik and J. Homola, "Surface plasmon resonance (SPR) sensors: approaching their limits?" *Optics Express*, vol. 17, no. 19, p. 16505, 2009.

[155] A. W. Peterson, M. Halter, A. Tona, and A. L. Plant, "High resolution surface plasmon resonance imaging for single cells," *BMC Cell Biology*, vol. 15, no. 1, p. 35, 2014.

[156] B. Dong, J. Hao, T. Zhang, and J. L. Lim, "High sensitive fiber-optic liquid refractive index tip sensor based on a simple inline hollow glass micro-sphere," *Sensors and Actuators, B: Chemical*, vol. 171-172, pp. 405–408, 2012.

[157] S. M. Harazim, V. A. Bolaños Quiñones, S. Kiravittaya, S. Sanchez, and O. G. Schmidt, "Lab-in-a-tube: on-chip integration of glass optofluidic ring resonators for label-free sensing applications," *Lab on a Chip*, vol. 12, no. 15, p. 2649, 2012.

[158] F. Vollmer and S. Arnold, "Whispering-gallery-mode biosensing: Label-free detection down to single molecules," *Nature Methods*, vol. 5, no. 7, pp. 591–596, 2008.

[159] D. Yang, H. Tian, and Y. Ji, "High-Q and high-sensitivity width-modulated photonic crystal single nanobeam air-mode cavity for refractive index sensing," *Applied Optics*, vol. 54, no. 1, pp. 1–5, jan 2015.

[160] H. Shao, S. Member, D. Kumar, and K. L. Lear, "Single-Cell Detection Using Optofluidic Intracavity Spectroscopy," *IEEE Sensors Journal*, vol. 6, no. 6, pp. 1543–1550, 2006.

[161] Y. Zheng, L. H. Chen, J. Yang, R. Raghunandhan, X. Dong, P. L. So, and C. C. Chan, "Fiber optic Fabry-Perot optofluidic sensor with a focused ion beam ablated microslot for fast refractive index and magnetic field measurement," *IEEE Journal of Selected Topics in Quantum Electronics*, vol. 23, no. 2, 2017.

[162] P. Domachuk, I. C. Littler, M. Cronin-Golomb, and B. J. Eggleton, "Compact resonant integrated microfluidic refractometer," *Applied Physics Letters*, vol. 88, no. 9, pp. 1–4, 2006.

[163] N. Gaber, Y. M. Sabry, F. Marty, and T. Bourouina, "Optofluidic Fabry-Perot microcavities comprising curved surfaces for homogeneous liquid refractometry-design, simulation, and experimental performance assessment," *Micromachines*, vol. 7, no. 4, 2016.

[164] R. St-Gelais, A. Poulin, and Y.-A. Peter, "Advances in Modeling , Design, and Fabrication of Deep-Etched Multilayer Resonators," *Journal of Lightwave Technology*, vol. 30, no. 12, pp. 1900–1908, 2012.

[165] R. A. Soref, J. Schmidtchen, and K. Petermann, "Large single-mode rib waveguides in GeSi and Si-on-SiO2," *Journal of Lightwave Technology*, vol. 9, no. 8, pp. 1971–1974, 1991.

[166] S. P. Pogossian, L. Vescan, and A. Vonsovici, "The single-mode condition for semiconductor rib waveguides with large cross section," *Journal of Lightwave Technology*, vol. 16, no. 10, pp. 1851–1853, 1998.

[167] T. Claes, W. Bogaerts, and P. Bienstman, "Vernier-cascade label-free biosensor with integrated arrayed waveguide grating for wavelength interrogation with low-cost broadband source." *Optics letters*, vol. 36, no. 17, pp. 3320–3322, 2011.

[168] C. J. Smith, R. Shankar, M. Laderer, M. B. Frish, M. Loncar, and M. G. Allen, "Sensing nitrous oxide with QCL-coupled silicon-on-sapphire ring resonators," *Optics Express*, vol. 23, no. 5, p. 5491, 2015.

[169] A. Leblanc-Hotte, R. St-Gelais, and Y.-A. Peter, "Optofluidic device for high resolution volume refractive index measurement of single cell," in *16th International Conference on Miniaturized Systems for Chemistry and Life Sciences*, Okinawa, Japan, 2012.

[170] J. Lousteau, D. Furniss, a. B. Seddon, T. M. Benson, a. Vukovic, and P. Sewell, "The single-mode condition for silicon-on-insulator optical rib waveguides with large cross section," *Journal of Lightwave Technology*, vol. 22, no. 8, pp. 1923–1929, 2004.

[171] S. P. Perfetto, P. K. Chattopadhyay, and M. Roederer, "Seventeen-colour flow cytometry: unravelling the immune system," *Nature Reviews Immunology*, vol. 4, no. 8, pp. 648–655, 2004.

[172] P. K. Chattopadhyay, D. A. Price, T. F. Harper, M. R. Betts, J. Yu, E. Gostick, S. P. Perfetto, P. Goepfert, R. A. Koup, S. C. De Rosa, M. P. Bruchez, and M. Roederer, "Quantum dot semiconductor nanocrystals for immunophenotyping by polychromatic flow cytometry," *Nature medicine*, vol. 12, no. 8, pp. 972–977, 2006.

[173] P. K. Chattopadhyay, T. M. Gierahn, M. Roederer, and J. C. Love, "Single-cell technologies for monitoring immune systems," *Nature immunology*, vol. 15, no. 2, pp. 128–135, 2014.

[174] P. K. Chattopadhyay and M. Roederer, "A mine is a terrible thing to waste: High content, single cell technologies for comprehensive immune analysis," *American Journal of Transplantation*, vol. 15, no. 5, pp. 1155–1161, 2015.

[175] C.-H. Lin and G.-B. Lee, "Micromachined flow cytometers with embedded etched optic fibers for optical detection," *Journal of Micromechanics and Microengineering*, vol. 13, no. 3, pp. 447–453, 2003.

[176] K. A. Willets and R. P. Van Duyne, "Localized Surface Plasmon Resonance Spectroscopy and Sensing," *Annual Review of Physical Chemistry*, vol. 58, no. 1, pp. 267–297, 2007.

[177] A. Leblanc-Hotte, J.-S. Delisle, S. Lesage, and Y.-A. Peter, "Optofluidic device for high resolution and multiparametric measurement of single biological cells," in *Solid-State Sensors, Actuators and Microsystems Workshop*, Hilton Head Island, South Carolina, USA, 2014.

[178] S. J. Collins, F. W. Ruscetti, R. E. Gallagher, and R. C. Gallo, "Terminal differentiation of human promyelocytic leukemia cells induced by dimethyl sulfoxide and other polar compounds," *Proceedings of the National Academy of Sciences of the United States of America*, vol. 75, no. 5, pp. 2458–2462, 1978.

[179] K. Muroi, R. Sasaki, Y. Miura, and K. Ohyashiki, "Medium pH determines the differentiation of human promyelocytic leukemia cells to basophils or eosinophils by culturing in a protein- and serum-free medium," *Leukemia Research*, vol. 13, no. 2, pp. 157–163, jan 1989.

[180] H. Sun and S. Wang, "Measuring the component overlapping in the Gaussian mixture model," *Data Mining and Knowledge Discovery*, vol. 23, no. 3, pp. 479–502, 2011.

[181] K. Fukunaga, *Introduction to statistical pattern recognition*, 2nd ed. San Francisco: Morgan Kaufmann, 1990.

[182] J. Kim, S. Han, A. Lei, M. Miyano, J. Bloom, V. Srivastava, M. R. Stampfer, Z. J. Gartner, M. A. LaBarge, and L. L. Sohn, "Characterizing cellular mechanical phenotypes with mechano-node-pore sensing," *Microsystems & Nanoengineering*, vol. 4, no. October 2017, p. 17091, 2018.

[183] Y. Deng, S. P. Davis, F. Yang, K. S. Paulsen, M. Kumar, R. Sinnott DeVaux, X. Wang, D. S. Conklin, A. Oberai, J. I. Herschkowitz, and A. J. Chung, "Inertial Microfluidic Cell Stretcher (iMCS): Fully Automated, High-Throughput, and Near Real-Time Cell Mechanotyping," *Small*, vol. 13, no. 28, pp. 1–11, 2017.

[184] J. Lin, D. Kim, H. T. Tse, P. Tseng, L. Peng, M. Dhar, S. Karumbayaram, and D. Di Carlo, "High-throughput physical phenotyping of cell differentiation," *Microsystems & Nanoengineering*, vol. 3, no. December 2016, p. 17013, 2017.

[185] M. Masaeli, D. Gupta, S. O'Byrne, H. T. Tse, D. R. Gossett, P. Tseng, A. S. Utada, H. J. Jung, S. Young, A. T. Clark, and D. Di Carlo, "Multiparameter mechanical and morphometric screening of cells," *Scientific Reports*, vol. 6, no. December, pp. 1–11, 2016.

[186] V. Faustino, D. Pinho, T. Yaginuma, R. C. Calhelha, I. C. Ferreira, and R. Lima, "Extensional flow-based microfluidic device: Deformability assessment of red blood cells in contact with tumor cells," *Biochip Journal*, vol. 8, no. 1, pp. 42–47, 2014.

[187] J. Chen, Y. Zheng, Q. Tan, E. Shojaei-Baghini, Y. L. Zhang, J. Li, P. Prasad, L. You, X. Y. Wu, and Y. Sun, "Classification of cell types using a microfluidic device for

mechanical and electrical measurement on single cells," *Lab on a Chip*, vol. 11, no. 18, p. 3174, 2011.

[188] K. D. Nyberg, K. H. Hu, S. H. Kleinman, D. B. Khismatullin, M. J. Butte, and A. C. Rowat, "Quantitative Deformability Cytometry: Rapid, Calibrated Measurements of Cell Mechanical Properties," *Biophysical Journal*, vol. 113, no. 7, pp. 1574–1584, 2017.

[189] I. Sraj, C. D. Eggleton, R. Jimenez, E. Hoover, J. Squier, J. Chichester, and D. W. M. Marr, "Cell deformation cytometry using diode-bar optical stretchers." *Journal of biomedical optics*, vol. 15, no. 4, p. 047010, 2013.

[190] M. Mokbel, D. Mokbel, A. Mietke, N. Träber, S. Girardo, O. Otto, J. Guck, and S. Aland, "Numerical Simulation of Real-Time Deformability Cytometry to Extract Cell Mechanical Properties," *ACS Biomaterials Science and Engineering*, vol. 3, no. 11, pp. 2962–2973, 2017.

[191] X. Q. Hu, B. Sévénié, A. V. Salsac, E. Leclerc, and D. Barthès-Biesel, "Characterizing the membrane properties of capsules flowing in a square-section microfluidic channel: Effects of the membrane constitutive law," *Physical Review E - Statistical, Nonlinear, and Soft Matter Physics*, vol. 87, no. 6, pp. 1–9, 2013.

[192] B. Sévénié, A.-V. Salsac, and D. Barthès-Biesel, "Characterization of Capsule Membrane Properties using a Microfluidic Photolithographied Channel: Consequences of Tube Non-squareness," *Procedia IUTAM*, vol. 16, pp. 106–114, 2015.

[193] C. Dupont, P. Le Tallec, D. Barthès-Biesel, M. Vidrascu, and A.-V. Salsac, "Dynamics of a spherical capsule in a planar hyperbolic flow: influence of bending resistance," in *Procedia IUTAM*, vol. 16, 2015, pp. 70–79.

[194] K. Tatsumi, K. Haizumi, K. Sugimoto, and K. Nakabe, "Measurement and Analysis of Lymphocyte Deformation in Microchannel Contraction Flows Using a Compound Drop Model," *Flow, Turbulence and Combustion*, vol. 96, no. 1, pp. 245–260, 2016.

[195] A. Leblanc-Hotte, G. Chabot-Roy, L. Odagiu, M. Richaud, S. Lesage, J.-S. Delisle, and Y.-A. Peter, "High-throughput refractive index-based microphotonic sensor for enhanced cellular discrimination," *Sensors and Actuators B: Chemical*, vol. 266, pp. 255–262, aug 2018.

[196] M. A. Tsai, R. E. Waugh, and P. C. Keng, "Cell cycle-dependence of HL-60 cell deformability," *Biophysical Journal*, vol. 70, no. 4, pp. 2023–2029, 1996.

[197] F. Van Meir, "Planimetry of bronchoalveolar macrophages. Importance of preparation and staining techniques." *Analytical and quantitative cytology and histology*, vol. 13, no. 4, pp. 261–8, aug 1991.

[198] B. O. Stokes, "Principles of Cytocentrifugation," *Laboratory Medicine*, vol. 35, no. 7, pp. 434–437, 2004.

[199] C. Klitis, G. Cantarella, M. J. Strain, and M. Sorel, "High-extinction-ratio TE/TM selective Bragg grating filters on silicon-on-insulator," *Optics Letters*, vol. 42, no. 15, p. 3040, aug 2017.

[200] X. Sun, M. Z. Alam, S. J. Wagner, J. S. Aitchison, and M. Mojahedi, "Experimental demonstration of a hybrid plasmonic transverse electric pass polarizer for a silicon-on-insulator platform," *Optics Letters*, vol. 37, no. 23, p. 4814, dec 2012.

[201] H. Zhu, R. Hao, and E. Li, "Ridge waveguide assisted highly efficient transverse-electric-pass polarizer based on a hybrid plasmonic waveguide," *Applied Optics*, vol. 57, no. 19, p. 5533, jul 2018.

[202] B. Fregin, F. Czerwinski, D. Biedenweg, S. Girardo, S. Gross, K. Aurich, and O. Otto, "High-throughput single-cell rheology in complex samples by dynamic real-time deformability cytometry," *Nature Communications*, vol. 10, no. 1, p. 415, dec 2019.

[203] S. Kuriakose and P. Dimitrakopoulos, "Deformation of an elastic capsule in a rectangular microfluidic channel," *Soft Matter*, vol. 9, no. 16, pp. 4284–4296, 2013.

[204] T. Yaginuma, M. S. N. Oliveira, R. Lima, T. Ishikawa, and T. Yamaguchi, "Human red blood cell behavior under homogeneous extensional flow in a hyperbolic-shaped microchannel," *Biomicrofluidics*, vol. 7, no. 5, p. 054110, sep 2013.

[205] M. Nyström, H. R. Tamaddon Jahromi, M. Stading, and M. F. Webster, "Hyperbolic contraction measuring systems for extensional flow," *Mechanics of Time-Dependent Materials*, vol. 21, no. 3, pp. 455–479, aug 2017.

[206] E. S. Cibas and S. Z. Ali, "The Bethesda System for Reporting Thyroid Cytopathology," *American Journal of Clinical Pathology*, vol. 132, no. 5, pp. 658–665, nov 2009.

[207] D. V. Messadi, "Diagnostic aids for detection of oral precancerous conditions," *International Journal of Oral Science*, vol. 5, no. 2, pp. 59–65, jun 2013.

[208] H. Amal, M. Leja, K. Funka, R. Skapars, A. Sivins, G. Ancans, I. Liepniece-Karele, I. Kikuste, I. Lasina, and H. Haick, "Detection of precancerous gastric lesions and gastric cancer through exhaled breath," *Gut*, vol. 65, no. 3, pp. 400–407, 2016.

[209] B. Stewart and C. Wild, *World Cancer Report 2014*, ser. International Agency for Research on Cancer. International Agency for Research on Cancer, 2014.

[210] V. Conteduca, D. Sansonno, S. Russi, and F. Dammacco, "Precancerous colorectal lesions," *International Journal of Oncology*, vol. 43, no. 4, pp. 973–984, oct 2013.

[211] L. Ge, B. Pan, F. Song, J. Ma, D. Zeraatkar, J. Zhou, and J. Tian, "Comparing the diagnostic accuracy of five common tumour biomarkers and CA19-9 for pancreatic cancer: a protocol for a network meta-analysis of diagnostic test accuracy," *BMJ Open*, vol. 7, no. 12, p. e018175, dec 2017.

[212] V. Janelle, C. Carli, J. Taillefer, J. Orio, and J.-S. Delisle, "Defining novel parameters for the optimal priming and expansion of minor histocompatibility antigen-specific T cells in culture," *Journal of Translational Medicine*, vol. 13, no. 1, p. 123, dec 2015.

[213] E. E. Hillhouse, J.-S. Delisle, and S. Lesage, "Immunoregulatory CD4-CD8- T cells as a potential therapeutic tool for transplantation, autoimmunity, and cancer," *Frontiers in Immunology*, vol. 4, no. JAN, pp. 1–10, 2013.

[214] R. Lakshman and A. Finn, "Neutrophil disorders and their management," *Journal of Clinical Pathology*, vol. 54, no. 1, pp. 7–19, jan 2001.

[215] A. Leblanc-Hotte, J.-S. Delisle, S. Lesage, and Y.-A. Peter, "High-throughput volume refractive index distribution measurement through mechanical deformation of single cells," in *2016 International Conference on Optical MEMS and Nanophotonics (OMN)*, Singapore, 2016.

APPENDIX A LIST OF SCIENTIFIC CONTRIBUTIONS

Refereed journal publications

- **A. Leblanc-Hotte**, N. Sen Nkwe, G. Chabot-Roy, E. B. Affar, S. Lesage, J.-S. Delisle, and Y.-A. Peter, "On-chip refractive index cytometry for whole-cell deformability discrimination," *Lab on a Chip*, vol. 19, no. 3, pp. 464–474, 2019.

- **A. Leblanc-Hotte**, G. Chabot-Roy, L. Odagiu, M. Richaud, S. Lesage. J.-S. Delisle and Y.-A. Peter, "High-throughput refractive index-based microphotonic sensor for enhanced cellular discrimination," *Sensors and Actuators B: Chemical*, vol. 266, pp. 255–262, aug 2018.

- **A. Leblanc-Hotte**, J.-S. Delisle, S. Lesage, and Y.-A. Peter, "The Importance of Single-Mode Behavior in Silicon-On-Insulator Rib Waveguides With Very Large Cross Section for Resonant Sensing Applications," *IEEE Journal of Selected Topics in Quantum Electronics*, vol. 22, no. 6, pp. 241–248, nov 2016.

Refereed journal publications not included in this thesis

- R. St-Gelais, G. Mackey, J. Saunders, J. Zhou, **A. Leblanc-Hotte**, A. Poulin, J.A.Barnes, H.-P. Loock, R. S. Brown, and Y.-A. Peter, "Gas sensing using polymer-functionalized deformable Fabry–Perot interferometers," *Sensors Actuators B Chemical*, vol. 182, pp. 45–52, 2013.

Refereed conference publications

- **A. Leblanc-Hotte**†, G. Chabot-Roy, S. Lesage, J.-S. Delisle, and Y.-A. Peter, "An integrated microphotonic biosensor for simultaneous refractive index and deformability cell discrimination," in *5th International Conference on Microtechnologies in Medicine and Biology*, Monterey, California, USA, 2018.

- **A. Leblanc-Hotte***, G. Chabot-Roy, L. Odagiu, M.Richaud, E. B. Affar, S. Lesage, J.-S. Delisle, and Y.-A. Peter, "Enhanced cellular discrimination using a novel optical microsystem," in *Annual Conference of the European Society for Clinical Cell Analysis*, Thessaloniki, Greece, 2017.

- **A. Leblanc-Hotte**†, J.-S. Delisle, S. Lesage, and Y.-A. Peter, "High-throughput volume refractive index distribution measurement through mechanical deformation of single cells," in *2016 International Conference on Optical MEMS and Nanophotonics (OMN)*, Singapore, 2016.

- **A. Leblanc-Hotte**†, J.-S. Delisle, S. Lesage, and Y.-A. Peter, "Optofluidic device for high resolution and multiparametric measurement of single biological cells," in *Solid-State Sensors, Actuators and Microsystems Workshop*, Hilton Head Island, South Carolina, USA, 2014.

- **A. Leblanc-Hotte**∗, R. St-Gelais, and Y.-A. Peter, "Optofluidic device for high resolution volume refractive index measurement of single cell," in *16th International Conference on Miniaturized Systems for Chemistry and Life Sciences*, Okinawa, Japan, 2012.

- R. St-Gelais, G. Mackey, J. Saunders, J. Zhou, **A. Leblanc-Hotte**, A. Poulin, J.A.Barnes, H.-P. Loock, R. S. Brown, and Y.-A. Peter, "A Fabry-Perot refractometer for chemical vapor sensing by solid-phase microextraction," in *16th International Conference on Optical MEMS and Nanophotonics*, Istanbul, Turkey, 2011.

- R. St-Gelais, G. Mackey, J. Saunders, J. Zhou, **A. Leblanc-Hotte**, J.A.Barnes, H.-P. Loock, Y.-A. Peter, and R. S. Brown, "Functionalized silicon fabry-perot microcavities for chemical vapor sensing," in *Cavity Enhanced Spectroscopy*, Kingston, Ontario, Canada, 2011.

† Oral presentation ∗ Poster presentation

APPENDIX B CELLULAR THROUGHPUT OF SHEATHED HYDRODYNAMIC AND INERTIAL FOCUSING

This annex defines the working range of hydrodynamic and inertial cellular focusing through the derivation of their maximum throughput equation. Lateral sheathed hydrodynamic focusing is derived in the first section, 3D symmetric sheathed hydrodynamic focusing in the second section and inertial focusing in the last section.

Lateral sheathed hydrodynamic focusing

Lateral sheathed hydrodynamic focusing occurs in laminar flows. The laminar flow condition is

$$Re = \frac{\rho U_f L}{\mu} < 1 \quad \rightarrow \quad U_f < \frac{\mu}{\rho L}$$

Considering the minimal distance between the beginning of two adjacent cells is $\Delta x_{cell} = 2a$, where a is the diameter of one cell, and using the velocity ratio $\alpha = U_{foc}/U_f$ yields the throughput T

$$T^{-1} = \frac{\Delta x_{cell}}{U_{foc}} = \frac{2a}{\alpha U_f} \quad \rightarrow \quad U_f = \frac{2Ta}{\alpha}$$

Replacing U_f into the previous equation yields the equation of the throughput T respecting the laminar flow condition

$$T < \frac{\mu}{\rho L} \cdot \frac{\alpha}{2a}$$

For the limit case where no focusing is needed ($L = a = W_o = W_f$), the velocity ratio is $\alpha = 1$ and the maximum throughput is approximately between 5000 and 2200 cells/s, considering typical cells between 10 and 15 μm in diameter respectively. Any applied sheathed hydrodynamic focusing would then result in a smaller throughput. Indeed, focusing the same cells ($W_f = a$) inside a 50 μm $\times$ 50 μm channel ($L = 50\ \mu m$) yields $\alpha = [1.42, 1.4]$ and maximum throughput of 1420 and 930 cells/s respectively.

Vertical and lateral sheathed hydrodynamic focusing

In symmetric 3D sheathed hydrodynamic focusing, Eq. 2.2 is applied first for the vertical focusing and then again for the lateral focusing which yields the following set of equations

$$\frac{Q_{vs}}{Q_i} = \frac{1}{2\alpha_v} \cdot \frac{H_o}{H_f} - \frac{1}{2} \qquad \text{and} \qquad \frac{Q_{ls}}{Q_{i*}} = \frac{1}{2\alpha_l} \cdot \frac{W_o}{W_f} - \frac{1}{2}$$

where Q_{vs} and Q_{ls} are the vertical and lateral sheaths flow rate respectively, α_v and α_l are the vertical and lateral velocity ratios respectively and H_o and H_f are the output channel and focused height respectively. Q_{i*} is the inlet flow rate at the lateral focusing point whereas Q_i is the inlet flow rate at the vertical focusing point. Replacing the output flow rate equation $Q_o = 2Q_{vs} + 2Q_{ls} + Q_i$ and the lateral inlet flow rate equation $Q_{i*} = 2Q_{vs} + Q_i$ into the previous ratios yields

$$Q_o = Q_i \left(\frac{1}{\alpha_v}\frac{H_o}{H_f}\right)\left(\frac{1}{\alpha_l}\frac{W_o}{W_f}\right)$$

Replacing $Q_o = U_f W_o H_o$ and $Q_i = U_{foc} W_f H_f$ into this equation and isolating U_f yields

$$U_f = \frac{U_{foc}}{\alpha_v \alpha_l}$$

Finally, replacing U_f into the same throughput equation respecting the laminar flow condition as in the 2D case yields

$$T < \frac{\mu}{\rho L} \cdot \frac{\alpha_v \alpha_l}{2a}$$

Again, any applied 3D sheathed hydrodynamic focusing would only further reduce the maximum achievable throughput for a given cell size.

Inertial focusing

The inertial condition for particle to be focused onto two equilibrium in a rectangular channel is $1 < Re_p < 5$ [54]. Smaller Re_p values do not promote inertial effects whereas larger values induce supplementary equilibrium positions. The detailed inertial condition is

$$1 < Re\left(\frac{a}{L}\right)^2 < 5 \qquad \rightarrow \qquad 1 < \frac{\rho U_f a^2}{\mu L} < 5$$

Considering that the particle lags behind the flow, the particle velocity is expressed as the average flow velocity times a factor γ such that $U_p = \gamma U_f$. In Chapter 6, this factor was defined as $\gamma = 1 - a/D_h$. Using the same separation between the beginning of two adjacent cells $\Delta x_{cell} = 2a$ yields a throughput T

$$T^{-1} = \frac{\Delta x_{cell}}{U_p} \qquad \rightarrow \qquad T = \frac{\gamma U_f}{2a}$$

Replacing U_f into the inertial condition yields

$$\frac{\gamma \mu L}{2\rho a^3} < T < \frac{5\gamma \mu L}{2\rho a^3}$$

To compare with sheathed hydrodynamic focusing, the same cells of 10 and 15 μm are focused in a $L = D_h = 50\ \mu m$ rectangular channel with an aspect ratio $W/H = 2$. This yields $\gamma = 1 - a/D_h = [0.8, 0.7]$ and maximum throughput of 100 000 and 26 000 cells/s for 10 and 15 μm diameter cells respectively. Thus, the derived equations using simple conditions on flow show that inertial focusing yields much larger maximum throughput than sheathed hydrodynamic focusing.

APPENDIX C *OVERLAPRATE* (OLR) COEFFICIENT

This annex describes the mathematical procedure to calculate the OLR between two cellular populations in N dimensions. The number of measured cells (observations) in each population can be different whereas the number of dimensions (variables), *i.e.* the number of curve parameters such as Max, FWHM, Area, etc., is the same. The populations can be represented as:

$$X_1 = \begin{bmatrix} x_1^1 & x_2^1 & \dots & x_N^1 \end{bmatrix} \qquad \text{and} \qquad X_2 = \begin{bmatrix} x_1^2 & x_2^2 & \dots & x_N^2 \end{bmatrix}$$

where the populations X_i ($i = [1, 2]$) are matrices of all observations for all variables and x_d^i ($d = [1, N]$) are column vectors of observations of a single variable. Since cellular population distributions are skewed, the arithmetic mean may not correspond to the maximum of the population's probability density function (PDF). Thus, Gaussian distributions are fitted such that the modes of each variable (maximum of the PDF on the histogram) become the means of the fitted Gaussians. Then, the standard deviations are calculated as $\sigma = (max(PDF) \cdot \sqrt{2\pi})^{-1}$. This operation yields:

$$M_i = \begin{bmatrix} \mu_1^i & \mu_2^i & \dots & \mu_N^i \end{bmatrix} \qquad \text{and} \qquad \sigma_i = \begin{bmatrix} \sigma_1^i & \sigma_2^i & \dots & \sigma_N^i \end{bmatrix}$$

where M_i and σ_i are row vectors of means and standard deviations of each population respectively. The scalars μ_d^i and σ_d^i represent each variable fitted mean and standard deviation respectively. Subsequently, the covariance matrix of each population is:

$$\Sigma_i = \frac{1}{n_i - 1} (X_i - M_i)^T (X_i - M_i) = \begin{bmatrix} \sigma_{11}^2 & \sigma_{12}^2 & \dots & \sigma_{1N}^2 \\ \sigma_{21}^2 & \sigma_{22}^2 & \dots & \sigma_{2N}^2 \\ \vdots & \vdots & \ddots & \vdots \\ \sigma_{N1}^2 & \sigma_{N2}^2 & \dots & \sigma_{NN}^2 \end{bmatrix}$$

where n_i is the number of observations of each population. To conserve the fitted variances, the covariance matrix is replaced by:

$$\Sigma_i' = [I \cdot \sigma_i] \cdot CORR[\Sigma_i] \cdot [I \cdot \sigma_i]$$

where Σ_i' is the correlated covariance matrix, I is the identity matrix and $CORR[\Sigma_i]$ is the correlation matrix of Σ_i. The fitted means row vectors M_i and covariance matrices Σ_i' are used to generate random Gaussian distributions accurately reproducing the original

populations. These generated data sets do not have a skewed profile which is critical for subsequent operations.

For a mixture of two Gaussian distributions in N dimensions, the population means and stationary points of the PDF (maxima and saddle) fall on the ridge curve. Moreover, the stationary points will always lie on or between the two population means [180]. The ridge curve is defined by the following set of equations:

$$-\left(\Sigma_1'\right)^{-1}\left(\mathcal{X}-M_1\right)^T=\begin{bmatrix}A_{x1}\\A_{x2}\\\vdots\\A_{xN}\end{bmatrix}\qquad\text{and}\qquad-\left(\Sigma_2'\right)^{-1}\left(\mathcal{X}-M_2\right)^T=\begin{bmatrix}B_{x1}\\B_{x2}\\\vdots\\B_{xN}\end{bmatrix}$$

$$\text{Ridge curve}\begin{cases}A_{x1}B_{x2}-B_{x1}A_{x2}=0\\A_{x2}B_{x3}-B_{x2}A_{x3}=0\\\dots\\A_{xN-1}B_{xN}-B_{xN-1}A_{xN}=0\end{cases}$$

where $\mathcal{X}$ is a row vector of symbolic variables $[x_1\ x_2\ \dots\ x_N]$. However, to solve this set of equations, the terms A_{xd} and B_{xd} must be expressions of a single symbolic variable x_d. This can only occur if the Σ_i' are symmetric diagonal matrices. Thus, the following affine transformations must first be applied to simultaneously diagonalize both population covariance matrices Σ_i':

$$X_{tot}=\begin{bmatrix}X_1\\X_2\end{bmatrix}\qquad\rightarrow\qquad\zeta=eigenvectors\left(\Sigma_{tot}^{-1}\Sigma_1'\right)$$

Adjusting the scale of the eigenvectors ζ to make them orthonormal

$$\zeta=\frac{\zeta}{\sqrt{\zeta^T\Sigma_{tot}\zeta}}$$

Simultaneously diagonalizing

$$\zeta^T X_{tot}^T=\left(X_{tot}'\right)^T\qquad\text{where}\qquad X_{tot}'=\begin{bmatrix}X_1'\\X_2'\end{bmatrix}$$

and translating the first population to the origin

$$X_{tot}''=X_{tot}'-M_1'\qquad\text{where}\qquad X_{tot}''=\begin{bmatrix}X_1''\\X_2''\end{bmatrix}$$

and M_1' is the row vector means of the transformed population X_1'. These affine transformations yield populations X_1'' and X_2'' which have means and covariance matrices:

$$\begin{cases} M_1'' = \begin{bmatrix} 0 & 0 & \dots & 0 \end{bmatrix} \quad \text{and} \quad M_2'' = \begin{bmatrix} \mu_1'' & \mu_2'' & \dots & \mu_N'' \end{bmatrix} \\ \\ \Sigma_i'' = \begin{bmatrix} (\sigma_{11}'')^2 & 0 & \dots & 0 \\ 0 & (\sigma_{22}'')^2 & \dots & 0 \\ \vdots & \vdots & \ddots & \vdots \\ 0 & 0 & \dots & (\sigma_{NN}'')^2 \end{bmatrix} \end{cases}$$

for which the ridge curve set of equations can now be solved and yield the simple set of solutions

$$\text{Ridge curve} \begin{cases} x_2 = f(x_1) \\ x_3 = f(x_2) \\ \dots \\ x_N = f(x_{N-1}) \end{cases}$$

The Gaussian mixture total PDF is

$$p(\mathcal{X}) = \alpha_1 G_1 + \alpha_2 G_2$$

where α_i are the proportion of each Gaussian G_i and

$$G_i = \frac{1}{\sqrt{(2\pi)^N |\Sigma_i''|}} exp\left(-\frac{1}{2}(\mathcal{X} - M_i'')(\Sigma_i'')^{-1}(\mathcal{X} - M_i'')^T\right)$$

Thus scanning the $p(\mathcal{X})$ from one population mean to the other using the prescribed ridge curve yields a simple set of PDF values for which the lowest maxima and the saddle are easily identified. Thus, the OLR can be calculated using Eq. 5.2

$$OLR = \frac{p(\mathcal{X}_{saddle})}{p(\mathcal{X}_{lowest\ max})}$$